

JAERI - M
85-075

JAPANESE CONTRIBUTIONS TO IAEA INTOR WORKSHOP,
PHASE TWO A, PART 2
CHAPTER III : IMPURITY CONTROL (ENGINEERING)

July 1985

Masahiro SEKI, Nobuharu MIKI,*¹ Yoji SHIBUTANI*¹
Kaoru FUJIMURA, Jun-ichi ADACHI,*² Kosuke SATO*²
Masaharu FUJII,*² Seiichiro YAMAZAKI*² and Shin-ichi ITOH*³

日 本 原 子 力 研 究 所
Japan Atomic Energy Research Institute

JAERI-Mレポートは、日本原子力研究所が不定期に公刊している研究報告書です。
入手の問合わせは、日本原子力研究所技術情報部情報資料課（〒319-11茨城県那珂郡東海村）あて、お申しこしください。なお、このほかに財団法人原子力弘済会資料センター（〒319-11 茨城県那珂郡東海村日本原子力研究所内）で複写による実費頒布をおこなっております。

JAERI-M reports are issued irregularly.

Inquiries about availability of the reports should be addressed to Information Division
Department of Technical Information, Japan Atomic Energy Research Institute, Tokai-mura, Naka-gun, Ibaraki-ken 319-11, Japan.

©Japan Atomic Energy Research Institute, 1985

編集兼発行	日本原子力研究所
印 刷	いばらき印刷株

Japanese Contributions
to IAEA INTOR Workshop, Phase Two A, Part 2
Chapter III : Impurity Control (Engineering)

Masahiro Seki, Nobuharu Miki^{*1}, Yoji Shibutani^{*1},
Kaoru Fujimura⁺, Jun-ichi Adachi^{*2}, Kosuke Sato^{*2},
Masaharu Fujii^{*2}, Seiichiro Yamazaki^{*2} and Shin-ichi Itoh^{*3}

Department of Large Tokamak Research,
Naka Fusion Research Establishment, JAERI

(Received May 31, 1985)

This report corresponds to the second half of Chapter III of Japanese contribution report to IAEA INTOR Workshop, Phase Two A, Part 2. Data base assessment are made on candidate materials for the divertor, limiter, and the first wall. Engineering trade-off studies are made for the high-recycling and low temperature conditions. The studies include material considerations, configuration, thermohydraulic and stress analysis, disruption, lifetime analysis, and tritium permeation.

Keywords: INTOR, Impurity Control Engineering, Divertor, Limiter, First Wall, Configuration, Thermo-hydraulic, Stress, Disruption, Lifetime Analysis, Tritium Permeation, Tokamak, Assessment

+ Department of High Temperature Engineering, JAERI

*1 Toshiba Corp.

*2 Kawasaki Heavy Industry, Ltd.

*3 Hitachi Ltd.

IAEA INTORワークショップ, フェーズⅡA, パート2 報告書

第Ⅲ章 : 不純物制御 (工学)

日本原子力研究所那珂研究所臨界プラズマ研究部

関 昌弘・三木 信晴^{*1}・渋谷 陽二^{*1}・藤村 薫⁺
安達 潤一^{*2}・佐藤 瓊介^{*2}・藤井 政治^{*2}・山崎 誠一郎^{*2}
伊藤 新一^{*3}

(1985年5月31日受理)

この報告書はIAEA主催のINTORワークショップ, フェーズⅡA, パート2の日本の報告書の第Ⅲ章(後半)に相当するものである。

ダイバータ, リミタ, 第1壁の候補材についてのデータベース評価を行ない, 特に高速中性子による照射効果に関するデータの不足を明らかにした。

高密度低温度条件に対するダイバータの工学設計を行なった。設計にあたっては, 材料選択, 構造概念, 熱流力解析, 応力解析ディスラプション解析, 寿命評価, トリチウム透過の検討を行った。

本報告書は, これら検討評価の結果を述べたものである。

+ 原研 高温工学部

*1 (株) 東 芝

*2 (株) 川崎重工

*3 (株) 日 立

CONTENTS

1. Introduction	1
2. Operating conditions	2
2.1 Common parameters	2
2.2 Engineering specifications for the poloidal divertor	2
2.3 Limiter/first wall	2
3. Mechanical configuration	7
3.1 Limiter	7
3.2 Divertor	7
3.2.1 Plate	7
3.2.2 Chamber	7
4. Materials considerations	38
4.1 Structural materials	38
4.1.1 Physical and mechanical properties	38
4.1.2 Irradiation properties	38
4.1.3 Coolant compatibility	38
4.2 Plasma side materials	39
4.2.1 Physical and mechanical properties	39
4.2.2 Irradiation effects	39
4.2.3 Hydrogen permeation and embrittlement	39
5. Fabrication	48
6. Thermohydraulic and stress analysis	50
6.1 Divertor temperature and stress distribution	50
6.2 Limiter temperature and stress analysis	51
6.3 Alternative coolant for first wall, divertor and limiter ..	51
6.3.1 Thermohydraulic evaluation of helium-cooled first wall	51
6.3.2 Comparison of the performances of water-cooled and helium-cooled first wall	53
7. Electromagnetics	92
8. Disruption	93
8.1 Thermal response	93
8.2 Liquid metal kinetics	93
9. Sputtering erosion/Redeposition	108
10. Life time analysis	109
10.1 Divertor	109
10.2 Limiter	109

10.3	First wall	110
10.4	Benefits of long pulse operation	110
10.4.1	Divertor	110
10.4.2	First wall	111
10.5	Conclusions	111
11.	Tritium permeation through divertor/limiter and first wall ...	127
11.1	Tritium permeation into the primary water coolant	127
11.2	Tritium re-emission from the first wall and limiter surface	128
12.	Vacuum	139
13.	Innovative concepts	139
14.	Data base assessment	140
15.	Conclusions and recommendations	175

目 次

1. 序	1
2. 運転パラメータ	2
2.1 一般パラメータ	2
2.2 ダイバータの工学的仕様	2
2.3 リミタ／第1壁	2
3. 構造概念	7
3.1 リミタ	7
3.2 ダイバータ	7
3.2.1 ダイバータ板	7
3.2.2 ダイバータ室	7
4. 材料選択	38
4.1 構造材料	38
4.1.1 物性値	38
4.1.2 照射効果	38
4.1.3 冷却材との両立性	38
4.2 プラズマに面する材料	39
4.2.1 物理的機械的性質	39
4.2.2 照射効果	39
4.2.3 水素透過とぜい化	39
5. 製 作	48
6. 熱流体および応力解析	50
6.1 ダイバータの温度および応力分布	50
6.2 リミタの温度および応力分布	51
6.3 第1壁、ダイバータ、リミタの代替冷却材	51
6.3.1 ヘリウム冷却第1壁の熱流力的検討	51
6.3.2 水冷却およびヘリウム冷却第1壁の特性の比較	53
7. 電磁気	92
8. ディスラプション	93
8.1 温度応答	93
8.2 溶融金属層の運動	93
9. スパタリング損耗／再付着	108
10. 寿命評価	109
10.1 ダイバータ	109
10.2 リミタ	109

10.3	第1壁	110
10.4	長パルス運転による利得	110
10.4.1	ダイバータ	110
10.4.2	第1壁	111
10.4.3	結 論	111
11.	トリチウム透過	127
11.1	一次冷却水系へのトリチウム透過	127
11.2	第1壁やリミタからのトリチウム再放出	128
12.	真 空	139
13.	進歩的概念	139
14.	データベース評価	140
15.	結 論	175

List of Tables and Figures

Table 2.1	Common parameters
Table 2.2	The operating parameters for divertor
Table 2.3	Heat and particle fluxes for the limiter option
Table 3.1	Heat and particle flux on the modium edge temperature limiter
Table 3.2	Limiter operating conditions used for engineering analysis
Table 3.3	Heat and particle flux on divertor plate
Table 3.4	Divertor operating conditions used for engineering analysis
Table 3.5	Comparison of the reduced channel length divertor with the long channel length divertor
Table 4.1	Properties of divertor plate materials
Table 4.2	Tensile properties of OFHC
Table 4.3	Fatigue of OFHC under stress control condition
Table 4.4	Tensile properties of Cu-0.6 Be-2.5 Co
Table 4.5	Fatigue of Cu-0.6 Be-2.5 Co under stress control condition
Table 6.1	Parameters and Materials used for temperature and stress calculations of the divertor plate with tungsten tiles
Table 6.2	Temperature and thermal stress of divertor plate with 1 mm thick tungsten tile (Heat flux = 2 MW/m^2)
Table 6.3	Temperature and thermal stress of divertor plate with 1 mm thick tungsten tile (Heat flux = 5 MW/m^2)
Table 6.4	Temperature and thermal stress of divertor plate with 3 mm thick tungsten tile (Heat flux = 2 MW/m^2)
Table 6.5	Temperature and thermal stress of divertor plate with 3 mm thick tungsten tile (Heat flux = 5 MW/m^2)
Table 6.6	Temperature and thermal stress of divertor plate with 1 mm thick tungsten tile on copper heat sink (Heat flux = 2 MW/m^2)
Table 6.7	Parameters and materials used for temperature and stress calculations of the limiter plate
Table 6.8	Temperature and thermal stress of limiter plate with beryllium tile on copper heat sink (Heat flux = 3 MW/m^2)
Table 6.9	Temperature and thermal stress of limiter plate with graphite file on copper heat sink (Heat flux = 3 MW/m^2)
Table 6.10	Heat load conditions of INTOR first wall -Divertor Option-
Table 6.11	Conditions for parametric survey of helium cooling
Table 6.12	Comparison of the performance of water-cooled and helium-cooled first wall
Table 8.1	Behavior of divertor surface during major plasma disruption
Table 10.1	Common oparating parameters
Table 10.2	Divertor/Limiter disruption characteristics
Table 10.3	Erosion rate of divertor plate
Table 10.4	Lifetime of divertor plate with copper heat sink for stage III operation
Table 10.5	Lifetime of divertor plate with Cu-0.5 Be-2.5Co heat sink for stage III operation
Table 10.6	Erosion rate of limiter plate at the top surface under a medium edge temperature condition
Table 10.7	Lifetime of limiter plate
Table 10.8	First wall Operating conditions
Table 10.9	Sputtering yield values for stainless steel

Table 10.10	Wall thickness requirement for the first wall
Table 10.11	Parameters for the long pulse operation
Table 10.12	Divertor operating conditions used for comparison of the reference operation and the long pulse operation
Table 10.13	Lifetime of divertor plate with 1 mm thick tungsten tiles
Table 10.14	Wall thickness requirement for the first wall
Table 11.1	Hydrogen diffusivities and solubilities data base for the materials of this analysis
Table 11.2	Hydrogen total detrapping energies data base for the radiation damage material defect of this analysis
Table 11.3	First wall reference parameters
Table 11.4	Limiter/Divertor parameters
Table 14.1	Properties of divertor plate materials
Table 14.2	Tensile properties of OFHC
Table 14.3	Fatigue of OFHC under stress control condition
Table 14.4	Tensile properties of Cu-0.6 Be-2.5 Co
Table 14.5	Fatigue of Cu-0.6 Be-2.5 Co under stress control condition
Table 14.6	Comparison of EBW and diffusion bonding
Table 14.7	Tensile properties of stainless steel at 20 C
Table 14.8	Tensile properties of stainless steel at 400 C
Table 14.9	Condition for TiC film deposition by TP-CVD
Table 14.10	Condition for TiC film deposition by HCD-ARE
Table 14.11	Summary of the outgassing rate of five different materials prior to and after 150 C baking
Table 14.12	Emissivity of TiC coated surface
Table 14.13	Mechanical properties of TiC coated Inconel 625

Fig. 3.1	Pumped limiter configuration options
Fig. 3.2	Shaped limiter
Fig. 3.3	Heat and particle flux to shaped limiter for $T_e=150\text{eV}$
Fig. 3.4	Heat and particle flux to flat limiter for $T_e=150\text{eV}$
Fig. 3.5	Cross section at the top surface of limiter plate
Fig. 3.6	Heat flux distribution perpendicular to the separatrix at the location of the collector plates
Fig. 3.7	Particle flux distribution perpendicular to the separatrix at the location of the collector plates
Fig. 3.8	Profile of the divertor region in the Phase 1 design
Fig. 3.9	Heat flux distribution on divertor plate
Fig. 3.10	Heat flux distribution on divertor plate
Fig. 3.11	Profile of the divertor region for the peak heat load of 2 MW/m^2 The plasma configuration is unchanged from the Phase 1 design
Fig. 3.12	Heat flux distribution on divertor plate
Fig. 3.13	Profile of the divertor region in the Japanese plasma configuration
Fig. 3.14	Heat flux distribution on divertor plate The plasma configuration is based upon the Japanese prediction
Fig. 3.15	Heat flux distribution on divertor plate The plasma configuration is based upon the Japanese prediction

- Fig. 3.16 Divertor plate
- Fig. 3.17 Equilibrium poloidal field configuration for the reduced channel length divertor
- Fig. 3.18 Profile of the divertor region for the reduced channel length divertor
The plasma configuration is unchanged from the Phase 1 design
- Fig. 3.19 Heat flux distribution on divertor plate
The plasma configuration is based upon the Japanese prediction
- Fig. 3.20 Heat flux distribution of divertor plate
The plasma configuration is unchanged from the Phase 1 design
- Fig. 3.21 Profile of the divertor region for the reduced channel length divertor
The plasma configuration is based upon the Japanese prediction
- Fig. 3.22 Heat flux distribution on divertor plate
The plasma configuration is unchanged from the Phase 1 design
- Fig. 3.23 Heat flux distribution on divertor plate
The plasma configuration is based upon the Japanese prediction
- Fig. 4.1 Fatigue data for copper at room temperature
- Fig. 4.2 Total strain range () as a function of cycles to failure (N_f) for OFHC copper tested at 300 C in vacuum
- Fig. 4.3 Effect of irradiation at 80 C on room-temperature tensile properties of copper
- Fig. 4.4 Dependence of void swelling of neutron-irradiation copper on temperature
- Fig. 4.5 Thermal conductivity of tungsten versus temperature
- Fig. 4.6 Specific heat capacity of tungsten versus temperature
- Fig. 4.7 Thermal expansion of tungsten versus temperature
- Fig. 4.8 Modulus of elasticity versus temperature
- Fig. 4.9 Tensile strength of 1 mm thick tungsten sheet at elevated temperatures, strain rate 15%/minute. The upper limiter corresponds to stress relieved and the lower to recrystallized sheet
- Fig. 4.10 Elongation of recrystallized tungsten sheet in relation to the test temperature
- Fig. 4.11 Low cycle fatigue of cross rolled tungsten
- Fig. 6.1 Geometry used for thermal hydraulics and stress analysis (Divertor plate with tungsten tile on copper heat sink)
- Fig. 6.2 Maximum temperature of divertor plate with copper heat sink
- Fig. 6.3 Maximum thermal stress of divertor plate with copper heat sink
- Fig. 6.4 Maximum temperature of divertor plate with copper alloy heat sink
- Fig. 6.5 Maximum thermal stress of divertor plate with Cu-0.5 Be heat sink
- Fig. 6.6 Temperature and stress distribution of divertor plate with 1 mm thick tungsten tile on copper heat sink
- Fig. 6.7 Temperature and stress distribution of divertor plate with 1 mm thick tungsten tile on Cu-0.6 Be heat sink (Heat flux

- = 2 MW/m²)
- Fig. 6.8 Temperature and stress distribution of divertor plate with 1 mm thick tungsten tile on Cu heat sink (Heat flux = 5 MW/m²)
- Fig. 6.9 Temperature and stress distribution of divertor plate with 1 mm thick tungsten tile on Cu-0.6 Be heat sink (Heat flux = 5 MW/m²)
- Fig. 6.10 Temperature and stress distribution of divertor plate with 3 mm thick tungsten tile on Cu heat sink (Heat flux = 2 MW/m²).
- Fig. 6.11 Temperature and stress distribution of divertor plate with 3 mm thick tungsten tile on Cu-0.6 Be heat sink (Heat flux = 2 MW/m²)
- Fig. 6.12 Temperature and stress distribution of divertor plate with 3 mm thick tungsten tile on Cu heat sink (Heat flux = 5 MW/m²)
- Fig. 6.13 Temperature and stress distribution of divertor plate with 3 mm thick tungsten tile on Cu-0.6 Be heat sink (Heat flux = 5 MW/m²)
- Fig. 6.14 Temperature and stress distribution of divertor plate with 1 mm thick tungsten tile on copper heat sink (Heat flux = 2 MW/m², thickness of redeposition (SS) = 2 mm)
- Fig. 6.15 Temperature and stress distribution of divertor plate with 1 mm thick tungsten tile on copper heat sink (Heat flux = 2 MW/m², thickness of redeposition (SS) = 4 mm)
- Fig. 6.16 Limiter plate geometry used for thermal hydraulics and stress analysis (Medium edge temperature limiter)
- Fig. 6.17 Temperature and stress distribution at the top surface of a medium edge temperature limiter with 10 mm thick beryllium tile on copper heat sink (Heat flux = 3 MW/m²)
- Fig. 6.18 Temperature and stress distribution at the top surface of a medium edge temperature limiter with 20 mm thick beryllium tile on copper heat sink (Heat flux = 3 MW/m²)
- Fig. 6.19 Temperature and stress distribution at the top surface of a medium edge temperature limiter with 5 mm thick graphite tile on copper heat sink (Heat flux = 3 MW/m²)
- Fig. 6.20 Temperature and stress distribution at the top surface of a medium edge temperature limiter with 10 mm thick graphite tile on copper heat sink (Heat flux = 3 MW/m²)
- Fig. 6.21 First wall configuration
- Fig. 6.22 Model for thermal-hydraulic analysis
- Fig. 6.23 Temperature rise within first wall
- Fig. 6.24 Maximum wall temperatures, coolant velocities and pressure losses (1) P = 7 MPa
- Fig. 6.25 Maximum wall temperatures, coolant velocities and pressure losses (2) P = 5 MPa
- Fig. 6.26 Maximum wall temperatures, coolant velocities and pressure losses (3) P = 3 MPa
- Fig. 6.27 Maximum wall temperatures, coolant velocities and pressure losses (4) P = 1 MPa
- Fig. 6.28 Acceptable design range for helium-cooled first wall (1) P = 7 MPa
- Fig. 6.29 Acceptable design range for helium-cooled first wall (2) P = 5 MPa
- Fig. 6.30 Acceptable design range for helium-cooled first wall (3) P = 3 MPa
- Fig. 6.31 Acceptable design range for helium-cooled first wall (4) P = 1 MPa

- Fig. 8.1 Divertor surface temperature responses during major plasma disruption
- Fig. 8.2 Divertor surface temperature responses during major plasma disruption
- Fig. 8.3 Melt layer thickness during major plasma disruption
- Fig. 8.4 Melt layer thickness during major plasma disruption
- Fig. 8.5 Vaporized thickness during major plasma disruption
- Fig. 8.6 Vaporized thickness during major plasma disruption
- Fig. 8.7 Physical configuration
- Fig. 8.8 Linear amplification factor vs. inclination
- Fig. 8.9 Net amplification vs. inclination
- Fig.10.1 Temperature distribution in first wall
- Fig.10.2 Thermal stress in first wall
- Fig.10.3 Design fatigue strain range, ϵ_t , for 316SS
- Fig.10.4 Allowable first wall thickness as a function of fatigue life
- Fig.10.5 Temperature distribution in first wall
- Fig.10.6 Allowable first wall thickness as a function of fatigue life
- Fig.11.1 Transient permeation rate as a function of continuous operation time (1)
- Fig.11.2 Transient permeation rate as a function of continuous operation time (2)
- Fig.11.3 Transient permeation rate as a function of continuous operation time (3)
- Fig.11.4 Transient permeation rate as a function of continuous operation time (4)
- Fig.11.5 Reemission rate vs time after shutdown (1)
- Fig.11.6 Reemission rate vs time after shutdown (2)
- Fig.14.1 Fatigue data for copper at room temperature
- Fig.14.2 Total strain range ($\Delta\epsilon_t$) as a function of cycles to failure (N_f) for OFHC copper tested at 300 C in vacuum
- Fig.14.3 Effect of irradiation at 80 C on room temperature tensile properties of copper
- Fig.14.4 Dependence of void swelling of neutron irradiated copper on temperature
- Fig.14.5 Thermal conductivity of tungsten versus temperature
- Fig.14.6 Specific heat capacity of tungsten versus temperature
- Fig.14.7 Thermal expansion of tungsten versus temperature
- Fig.14.8 Modulus of elasticity versus temperature
- Fig.14.9 Tensile strength of 1 mm thick tungsten sheet at elevated temperatures. Strain rate 15%/minute. The upper limit corresponds to stress relieved and the lower to recrystallized sheet
- Fig.14.10 Elongation of recrystallized tungsten sheet in relation to the test temperature
- Fig.14.11 Low cycle fatigue of cross rolled tungsten
- Fig.14.12 Diffusion constant for hydrogen in tungsten
- Fig.14.13 Solubility constant for hydrogen in tungsten
- Fig.14.14 Deuterium solubility at one atmosphere in laminar pyrolytic carbon as a function of temperature
- Fig.14.15 Deuterium solubility at 1300 C in laminar pyrolytic carbon as a function of pressure
- Fig.14.16 Tritium diffusion coefficients in laminar pyrolytic carbon over the temperature range 1150 - 1425 C

- Fig.14.17 Deuterium solubility in silicon carbide and pyrolytic carbon as a function of deuterium partial pressure
- Fig.14.18 Deuterium solubility versus temperature (one atmosphere hydrogen pressure)
- Fig.14.19 Arrhenius plot of the diffusivity
- Fig.14.20 Tensile properties of type 304 stainless steel and welded joints
- Fig.14.21 Effect of welding temperature on tensile strength of diffusion welds
- Fig.14.22 Creep rupture strength of type 304 stainless steel and the welded joints
- Fig.14.23 Critical crack opening displacement values (initiation of stable crack growth)
- Fig.14.24 Pre- and post-irradiation stress versus rupture life relationship for control residual element type 308
- Fig.14.25 The structure of silicon carbide bonded to metal substrates
- Fig.14.26 Schematics of apparatus
- Fig.14.27 Schematic view of HCD-ARE system
- Fig.14.28 ESCA spectra of Ti(2S) from TiC film
- Fig.14.29 ESCA spectrum of the film deposited on Inconel 625 liner
- Fig.14.30 Thermal desorption spectra obtained for TiC coated Mo
- Fig.14.31 Thermal desorption spectra obtained for TiC coated Inconel
- Fig.14.32 Evacuation time vs outgassing rate curves obtained for five different materials
- Fig.14.33 Tensile strength of hot rolled pure molybdenum of 20 mm Thickness
- Fig.14.34 0.2% yield point of hot rolled pure molybdenum of 20 mm thickness
- Fig.14.35 Elongation of hot rolled pure molybdenum of 20 mm thickness

1. Introduction

In the course of the Phase 2A, Part 2 sessions, our efforts have been mainly devoted to "Low Edge Temperature Divertor Design," and "Data Base Assessment".

Design studies of the divertor collector plate were made for the high recycling and low particle temperature operating conditions. The conditions are quite attractive for the engineering design, since little or no sputtering erosion is predicted for high-Z materials at low edge temperatures. The studies included material considerations, configuration, thermo-hydraulic and stress analyses, disruption, lifetime analyses, and tritium permeation.

The divertor collector plates consist of a water cooled copper or copper alloy heat sink which is protected by a tungsten tile bonded to the surface. Two divertor configurations were considered. One is essentially unchanged from the previous INTOR configuration. The heat flux on the inner collector plate was 5 MW/m^2 . The other is the one where the plate is further inclined to limit the surface heat flux less than 2 MW/m^2 . Tungsten tile thickness was taken to be either 1 mm or 3 mm. The effect of bonding methods on the mechanical characteristics of tungsten and copper were discussed.

Thermo-hydraulic and stress analyses were also made for the collector plate with a thin stainless steel layer on it.

Thermal response, melt layer depth, and evaporated thickness due to a plasma disruption were calculated for the tungsten tile covered by a thin stainless steel layer. The situation simulates the case where the stainless steel sputtered at the first wall accumulates on the divertor surface. Stability of the melt layer was analytically treated with the aid of hydrodynamic linear stability theory.

In addition to the studies of the low edge temperature divertor, trade-off studies were made to examine the use of helium gas coolant for the first wall, and the advantages of long pulse operation.

2. Operating conditions

2.1 Common parameters

Common parameters such as plasma performance, operating scenario, are listed in Tab. 2.1.

2.2 Divertor/first wall

The engineering specifications for the divertor are shown in Tab. 2.2.

2.3 Limiter/first wall

The operating parameters for the limiter design are presented in Tab. 2.3.

Table 2.1 Common parameters

Stage	I	II
Plasma		
Thermonuclear power (MW)	620	620
-power (MW)	124	124
Neutron power (MW)	496	496
Neutron wall loading (MW·m ⁻²)	1.3	1.3
Operating senario		
Years of operation	3	10
Availability (%)	13.3	25
Cycle time (s)	146	246
Burn time (s)	100	200
Total burn time (s)	8.7×10 ⁶	64×10 ⁶
Total cycles	8.7×10 ⁴	32×10 ⁴
Total neutron fluence (m ⁻²)	3.6×10 ²⁵	3×10 ²⁶
Integral wall loading (MW·a·m ⁻²)	0.3	2.6
Disruptions		
(Major disruptions)		
Frequency	5×10 ⁻³	10 ⁻³
Disruptions/year	165	32
Total disruptions	495	320
Total energy (MJ)	290	290
Thermal plasma energy (MJ)	230	230
Field energy (MJ)	60	60
Disruption time		
Poloidal field (ms)	20	20
Plasma current (ms)	20	20
Thermal energy (ms)		
Reference	20	20
Alternate	5	5
(Minor disruptions)		
Frequency	10 ⁻²	5×10 ⁻³
Disruption/year	330	160
Total disruptions	990	1600
Total energy to limiter/divertor (MJ)	50	50
Disruption time		
Thermal energy (ms)		
Reference	20	20
Alternate	5	5
Engineering(all stages)		
Plasma chamber surface area (m ²)	380	
Limiter/divertor	Bottom of chamber	
Configuration	24 separately removable modules each weighing 25 Mg	
Pumping system	Compound cryopumps located below nuclear island	
Desired lifetime	< 2 years. 50% availability	
Coolant	H ₂ O, < 100°	

Table 2.2 Engineering Specifications for the High Recycling Regime of the Single-Null Poloidal Divertor

Outer scrape-off layer and divertor targets

Scrape-off temperature (at the separatrix in the main chamber)	$T_e = 130 \text{ eV} \quad T_i = 200 \text{ eV}$	
Scrape-off density (at the separatrix in the main chamber)	$6 \times 10^{19} \text{ m}^{-3}$	
Total power conducted into scrape-off plasma	80 MW	
Peak temperature at target	$T_e = 20 \text{ eV} \quad T_i = 20 \text{ eV}$	
Power to outer divertor throat (conducted)	40 MW	
Total power to each target	34.5 MW	
(a) due to kinetic energy of DT plasma	16.2 MW (peaked)	
(b) due to recombination of DT ions at surface	9.8 MW (peaked)	
(c) radiation from diverted plasma	6.5 MW (uniform)	
(d) radiation from main plasma	2 MW (uniform)	
Peak power load to outer plate (*)	18 MW m^{-2}	
Peak power load to inner plate (*)	14 MW m^{-2}	
Power profile (**)	Outer plate	Inner plate
outboard of separatrix	0.03 m	0.035 m
inboard of separatrix	0.01 m	0.012 m
Total ion flow to each target	$4.5 \times 10^{24} \text{ s}^{-1}$	
Composition - 49% D^+ , 49% T^+ , 2% He^{2+}	$3 \times 10^{24} \text{ m}^{-2} \text{ s}^{-1}$	
Peaked ion flux density (*)	$3 \times 10^{24} \text{ m}^{-2} \text{ s}^{-1}$	
Flux density profile (**) (in direction \perp to magnetic surfaces)	Outer plate	Inner plate
outboard of separatrix	0.094 m	0.11 m
inboard of separatrix	0.015 m	0.018 m
Predicted movement of intersection of separatrix with the target (in direction \perp to magnetic surfaces)	$\pm 0.015 \text{ m}$	

(*) Target perpendicular to magnetic surface

(**) Exp^{-1} decay length perpendicular to magnetic surface

Table 2.2 (cont.)

Divertor chamber walls

Total charge exchange on all divertor walls	2 MW
Total radiation on all divertor walls	3 MW
Both power load and sputtering by charge exchanged DT are small within the chamber. Erosion is due predominantly to helium atoms backscattered from the divertor target.	
Erosion peak - close to the position at the wall which faces the intersection of the separatrix with the target	
Peak erosion rate : SS wall (100% availability)	$3-6 \times 10^{-3} \text{ m a}^{-1}$

First wall (assessment of uniform conditions)

Radiator	49 MW
Charge exchange	1 MW
Total flux density of charge exchange atoms	$5 \times 10^{20} \text{ m}^{-2} \text{ s}^{-1}$
Sputtering rate (from SS wall)	$2.3 \times 10^{18} \text{ atoms m}^{-2} \text{ s}^{-1}$
Sputtering by charged particles	negligible

Table 2.3 Heat and particle fluxes for the limiter option

Parameter	Low T (High radiation)	Medium T	High T
Alpha heating (MW)	124	124	124
Radiation (MW)	112	40	20
Ions to limiter (MW)	8	45	60
Electron to limiter (MW)	4	15	20
Neutrals to limiter	-	20	20
Neutrals to wall (MW)	0.5	4	4
Limiter ion flux (s^{-1})	6×10^{23}	1.25×10^{24}	7.2×10^{22}
Limiter neutral flux (s^{-1})	-	4.2×10^{23}	4.3×10^{22}
Wall neutral flux (s^{-1}) ^a	1.6×10^{23}	8.3×10^{22}	8.6×10^{21}
DT ion energy (eV)	45	675	4300
Neutral energy (eV)	20	300	2900
Edge electron temperature (eV) ^b	10	150	670
Edge density (m^{-3}) ^b	5×10^{19}	2.5×10^{19}	5×10^{18}
e-folding distances (cm)			
Temperature ^c	2	2	2
Power ^c	1.5	1.5	1.5
Density ^c	long	long	long

^a The neutral wall flux falls on two 0.5 m, poloidal-width, strips at each end of the limiter.

^b At the 'point of tangency'.

^c at midplane

3. Mechanical configuration

3.1 Limiter

Several configurations of the pumped limiter was considered in Phase IIA Part 1, and is shown in Fig. 3.1. The curved limiter relevant to the medium edge temperature is shown in Fig. 3.2. The heat and particle flux to the curved limiter is shown in Fig. 3.3. The heat and particle flux to the flat limiter is shown in Fig. 3.4. Table 3.1 summarizes the heat and particle flux on the limiter plate.

The major difference between the flat and curved limiter is the heat load at the top surface of limiter. The curved limiter can reduce the heat load at the top surface in comparison with the flat limiter. The peak heat fluxes on the top surface are 2.1 MW/m^2 and 3 MW/m^2 for the curved and flat limiter, respectively. The curved double-edged limiter is desirable from the view point of the heat load. The curved double-edged limiter was recommended as the reference limiter in Phase IIA Part 1. The results of the analysis for the curved limiter were presented in detail in Phase IIA Part 1. The present study is focused on the flat double-edged limiter. The main purpose of this study is to develop a feasible limiter concept for the flat limiter. The advantage of the flat limiter is that the heat flux on the plate is not more sensitive to plasma displacement or deformation. Table 3.2 shows the limiter operating conditions used for engineering analysis.

The cross section at the top surface of the limiter plate is shown in Fig. 3.5. The limiter plate is composed of a protective material, heat sink and supporting structure. The protective material in the form of tiles is brazed to the copper heat sink. Candidate materials considered for the tiles are beryllium and graphite. The materials for the heat sink and supporting structure are annealed OFHC copper and type 316 stainless steel.

3.2 Divertor

3.2.1 Plate

The distributions of heat and particle fluxes on the two divertor plates are shown in Fig. 3.6 and Fig. 3.7 the for plate perpendicular to the separatrix. The inner and outer plates have the peak heat fluxes of 14 MW/m^2 and 18 MW/m^2 normal to the separatrix, respectively.

Two plasma configurations have been considered for the engineering trade-offs. The first plasma configuration is the same as the Phase I and Phase IIA Part 1 designs. The second plasma configuration is based upon the Japanese physics prediction. The major differences between them are the major radius of null-point (4.8 m compared with 4.6 m) and the angle of outer separatrix line to horizontal axis (45° compared with 60°).

The peak heat flux on the collector plate can reduced by inclining the the divertor plates with respect to the magnetic field lines. Different divertor configurations have been considered, namely:

- at an angle with respect to the Phase I magnetic field lines to limit the peak heat flux to 7 or 5 MW/m^2
- at an angle with respect to the Phase I magnetic field lines to limit the peak heat flux to 2 MW/m^2

- at an angle with respect to the Japanese magnetic field lines to limit the peak heat flux to 7 or 5 MW/m².

For the Japanese plasma configuration, the major radius of null-point is smaller than the Phase I configuration, and the region of the inner divertor plate is reduced. Therefore, it appears to be difficult that the inner plate is set to limit the peak heat flux to 2 MW/m².

The first divertor configuration is essentially unchanged from the Phase I and Phase IIA Part 1 design shown in Fig. 3.8. Length of divertor channel (distance between the null-point and the divertor target) is over 0.95 m.

In the Phase I design, the angle between plate and separatrix is 30° for the inner plate and 14.5° for the outer one. Under these geometrical conditions, the maximum heat flux is 7 MW/m² on the inner plate as shown in Fig. 3.9.

The difference between the first divertor configuration and the Phase I design is the angle between the inner plate and separatrix (20° compared with 30°). Figure 3.10 shows the heat flux distribution on divertor plate for the first divertor configuration. The maximum heat fluxes are about 5 MW/m² on both plates.

The second divertor configuration is shown in Fig. 3.11. The divertor collector plates are set at an angle with respect to the magnetic field lines to limit the peak heat flux to 2 MW/m². The angle between plate and separatrix is 8° for the inner plate and 6° for the outer one. Figure 3.12 shows the heat flux distribution on divertor plate.

The disadvantages of the second configuration would be:

- 1) short length of divertor channel (about 0.3 m in case of ±1.5 cm movement of magnetic field line)
- 2) reduction of the pumping capacity for the inner divertor region
- 3) high sensitivity of surface heat flux for the plasma configuration and displacement, e-folding distance and the divertor plate deformation.

The third divertor configuration is shown in Fig. 3.13. Length of divertor channel is about 0.75 m because of smaller major radius of the null-point. For the inner channel, the plate is placed at different angles to the field line, namely at the angle of 30° or 20°. For the outer channel, the plate is placed at angle of 14.5° to the field line. Heat flux distributions on divertor plate are shown in Fig. 3.14 and Fig. 3.15.

Table 3.3 summarizes the heat and particle fluxes on divertor plate. The parametric analysis of the divertor plate has been carried out in the present engineering study. Table 3.4 shows the divertor operating conditions used for engineering analysis.

The detailed configuration of the divertor plate is shown in Fig. 3.8. The plate is composed of a protective material, heat sink, and supporting structures. The protective material considered in the parametric study is tungsten of 1 mm or 3 mm thicknesses. Two materials, OFHC copper and copper alloy (Cu-0.6Be-2.5Co) have been considered for the heat sink material. The supporting structure material against the electromagnetic force is type 316 stainless steel. The protective tile is brazed or plasma-sprayed to the heat sink.

In order to reduce the electromagnetic force in copper heat sink, the heat sink plate is subdivided into individual cooling channels

which is circumferentially directed.

3.2.2 Chamber

The current experiments and physics predictions indicate that the high recycling region is localized very near (10-20 cm) the neutralizer plate. Furthermore, the measured scrape-off distances are much shorter on the inside of the separatrix than on the outside. Thus the region between the two separatrices past the X point has little or no plasma, and doesn't play a large role in the recycling of plasma near the divertor plates. It should be feasible to reduce the distance between the separatrix and the divertor plates from the current design value of 1 meter to 50 centimeters or less.

The purpose of this section is to examine the engineering trade-offs of a reduced size divertor, and to compare with the reference design (the long channel length divertor). Power and particle flux distributions for the reduced size divertor have been assumed to be the same as the reference design.

Two plasma configurations have been considered for the engineering trade-offs. The first plasma configuration is the same as the Phase I and Phase IIA Part 1 designs. The second plasma configuration (Fig. 3.17) is based upon the Japanese physics prediction.

Length of divertor channel has been taken to be 40 cm for the reduced channel length divertor. The angles between plate and separatrix has remained the same as in the long channel length divertor. Therefore, the peak heat flux is the same as in the long channel length divertor.

A profile of the divertor region is shown in Fig. 3.18 for the Phase I plasma configuration. Heat flux distributions on divertor plate are shown in Fig. 3.19 and Fig. 3.20. The plate is raised from 1.1 m below the null-point to 0.5 m below the null-point. The major radius of the removable module required for the divertor plate replacement is shortened from 6.07 m to 5.45 m.

Figure 3.21 shows a profile of the divertor region for the Japanese plasma configuration. Heat flux distributions on divertor plate are shown in Fig. 3.22 and Fig. 3.23. The plate is raised from 1.1 m below the null-point to 0.65 m below the null-point. The major radius of the removable module required for the divertor plate replacement is shortened from 5.37 m to 5.1 m.

Comparison of the reduced channel length divertor with the long channel length divertor is shown in Table 3.5. The peak heat flux has remained the same as in the long channel length divertor.

Under the Phase I plasma configuration, the reduced channel length divertor gives the decrease of 0.6 m in the height of divertor chamber compared with the long channel length divertor. On the other hand, the reduced channel length divertor with the Japanese plasma configuration gives the decrease of 0.45 m. This divertor has the minimum value in the major radius of the removable module.

Table 3.1 Heat and particle flux on the medium edge temperature limiter

	curved double- edged limiter	Flat double- edged limiter
Total energy to limiter (MW)	60	
Ion flux (s^{-1})	1.25×10^{24}	
Edge electron temperature	150	
Composition of ions(average)	47%D,47%T,5%He,1%Z	
Peak heat flux normal to plate		
Top surface (MW)	2.1	3
Leading edge (MW)	1.1	1.1
Peak ion flux normal to plate		
Top surface ($m^{-2}s^{-1}$)	2.7×10^{22}	4.8×10^{22}
Leading edge ($m^{-2}s^{-1}$)	3.8×10^{22}	4.8×10^{22}
Electron temperature on plate		
Top surface (eV)	140	80
Leading edge (eV)	25	25
Nuclear heating		
Be (W/cc)	8	
Cu (W/cc)	15	
SS (W/cc)	12	

Table 3.2 Limiter operating conditions used for engineering analysis

<u>Heat loads (MW/m²)</u>		
Peak, front surface		3
Peak, leading edge		1.1
First wall		0.12
<u>Particle fluxes (m⁻²s⁻¹)</u>		
Ions, middle of limiter		5 x 10 ²²
Ions, leading edge		5 x 10 ²²
CX, first wall		2 x 10 ²⁰
<u>Engineering</u>		
Limiter configuration	Flat, double-edged limiter plate	
Plasma side material of limiter plate		
Material	Be	C
Thickness (mm)	10, 20	5, 10
Bond type	Brazing	
Heat sink of limiter plate	Cu	
First wall	SS	

Table 3.3 Heat and particle flux on divertor plate

Peak energy flux to divertor plate normal to separatrix			
outboard	(MW/m ²)	18	
inboard	(MW/m ²)	14	
Peak ion flux to divertor plate normal to separatrix			
outboard	(m ⁻² s ⁻¹)	7×10^{23}	
inboard	(m ⁻² s ⁻¹)	7×10^{23}	
Inclination of divertor plate to separatrix			
outboard		14.5°	6°
inboard		20°(30°)	8°
Peak energy flux normal to divertor plate			
outboard	(MW/m ²)	4.5	1.9
inboard	(MW/m ²)	7(4.8)	2.0
Peak ion flux normal to divertor plate			
outboard	(m ⁻² s ⁻¹)	1.8×10^{23}	7.3×10^{22}
inboard	(m ⁻² s ⁻¹)	$3.5(2.4) \times 10^{23}$	9.7×10^{22}

Table 3.4 Divertor operating conditions used for engineering analysis

<u>Engineering</u>		
Plasma side material		
Material	W	
Thickness (mm)	1, 3	
Bond type	Brazing, plasma spraying	
Heat sink material	Cu, Cu-0.6Be-2.5Co	
First wall material	SS	
Inclination of divertor plate to separatrix		
Outboard	14.5°	6°
Inboard	20°	8°
<u>Heat loads (MW/m²)</u>		
Peak, Collector plate surface	5	2
First wall	0.1	0.1
<u>Particle fluxes (m⁻²s⁻¹)</u>		
Ions, Middle of collector plate	2.4×10^{23}	9.7×10^{22}
CX, First wall	5×10^{20}	5×10^{20}

Table 3.5 Comparison of the reduced channel length divertor with the long channel length divertor

	Phase I plasma configuration		Japanese plasma configuration	
	Long channel	Reduced channel	Long channel	Reduced channel
Length of divertor channel (m)	0.95	0.4	0.75	0.4
Peak heat flux (MW/m ²)				
Case 1 (1)	7	7	7	7
Case 2 (1)	5	5	5	5
Max. height between plate and null-point (m)	1.1	0.5	1.1	0.65
Major radius of the removable module required for divertor plate replacement (m)	6.07	5.45	5.37	5.1

(1) Inclination of divertor plate to separatrix

Case 1 : 14.5° (outboard) , 30° (inboard)

Case 2 : 14.5° (outboard) , 20° (inboard)

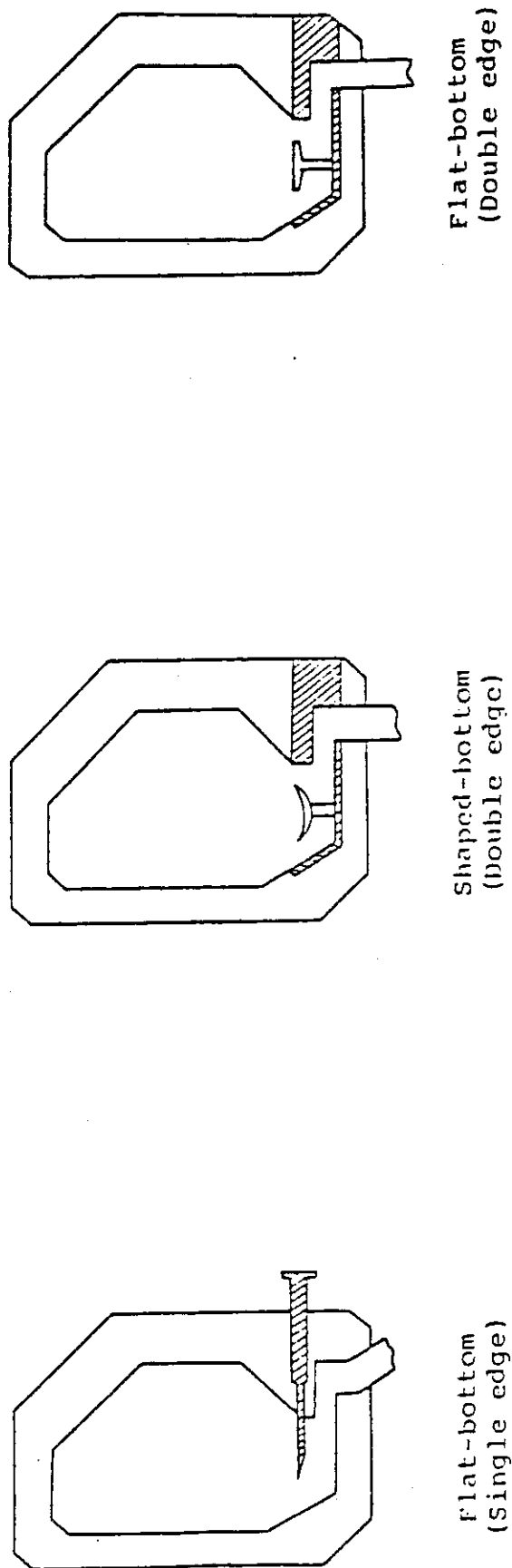


Fig.3.1.1 Pumped limiter configuration options

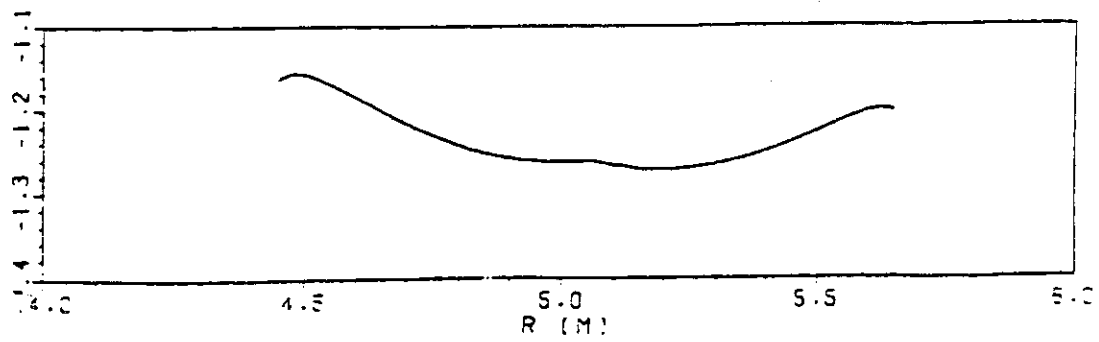
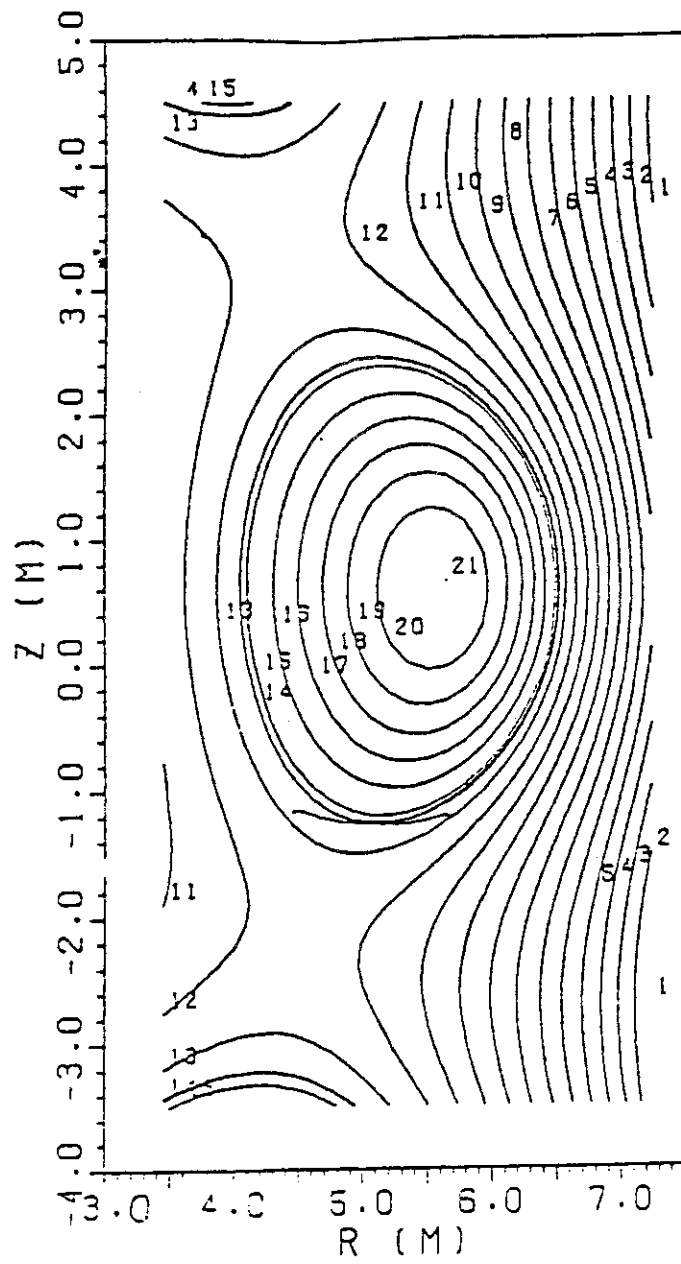


Fig.3.2 Shaped limiter

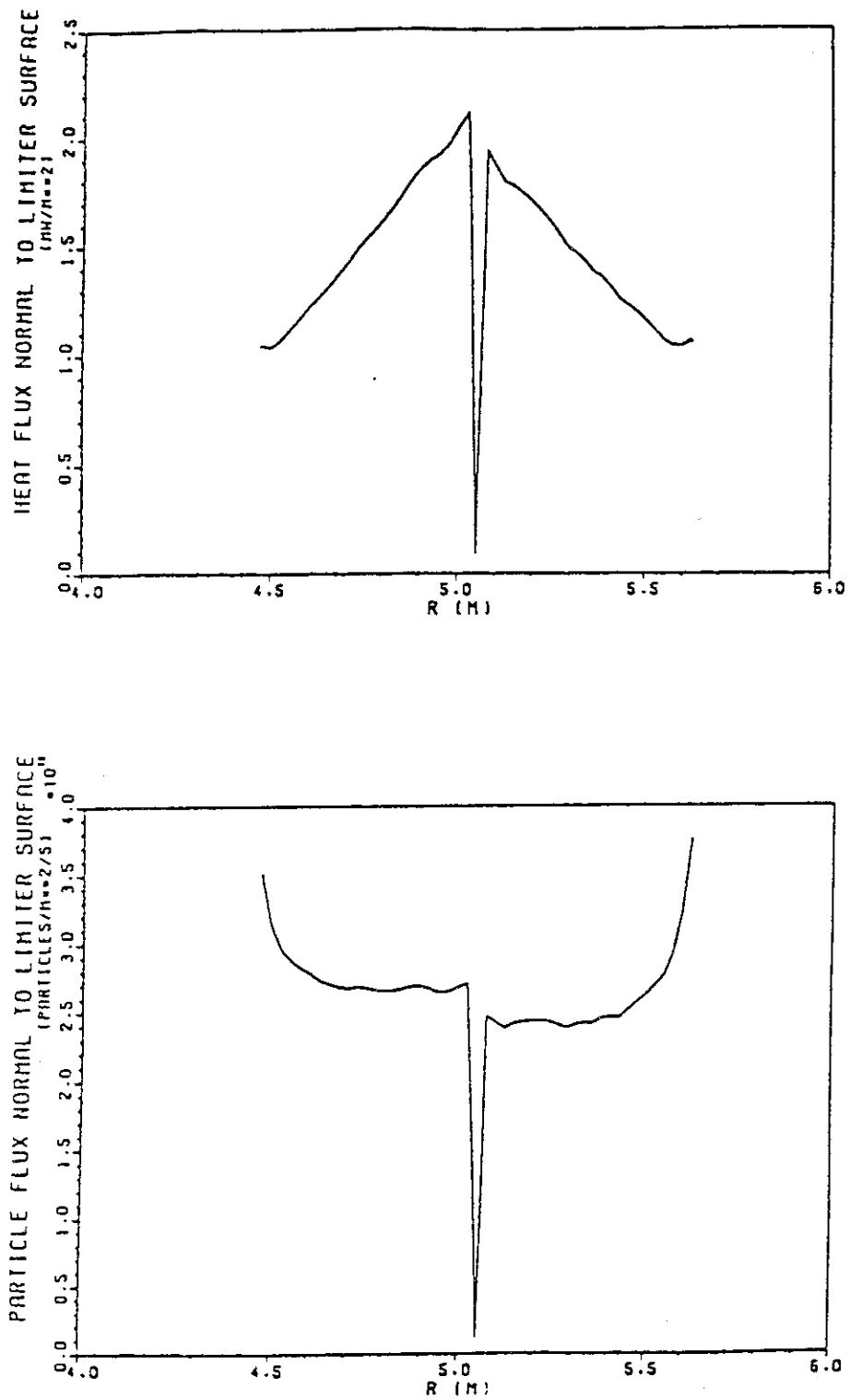


Fig.3.3

Heat and particle flux to
shaped limiter for $T_e = 150 \text{ eV}$

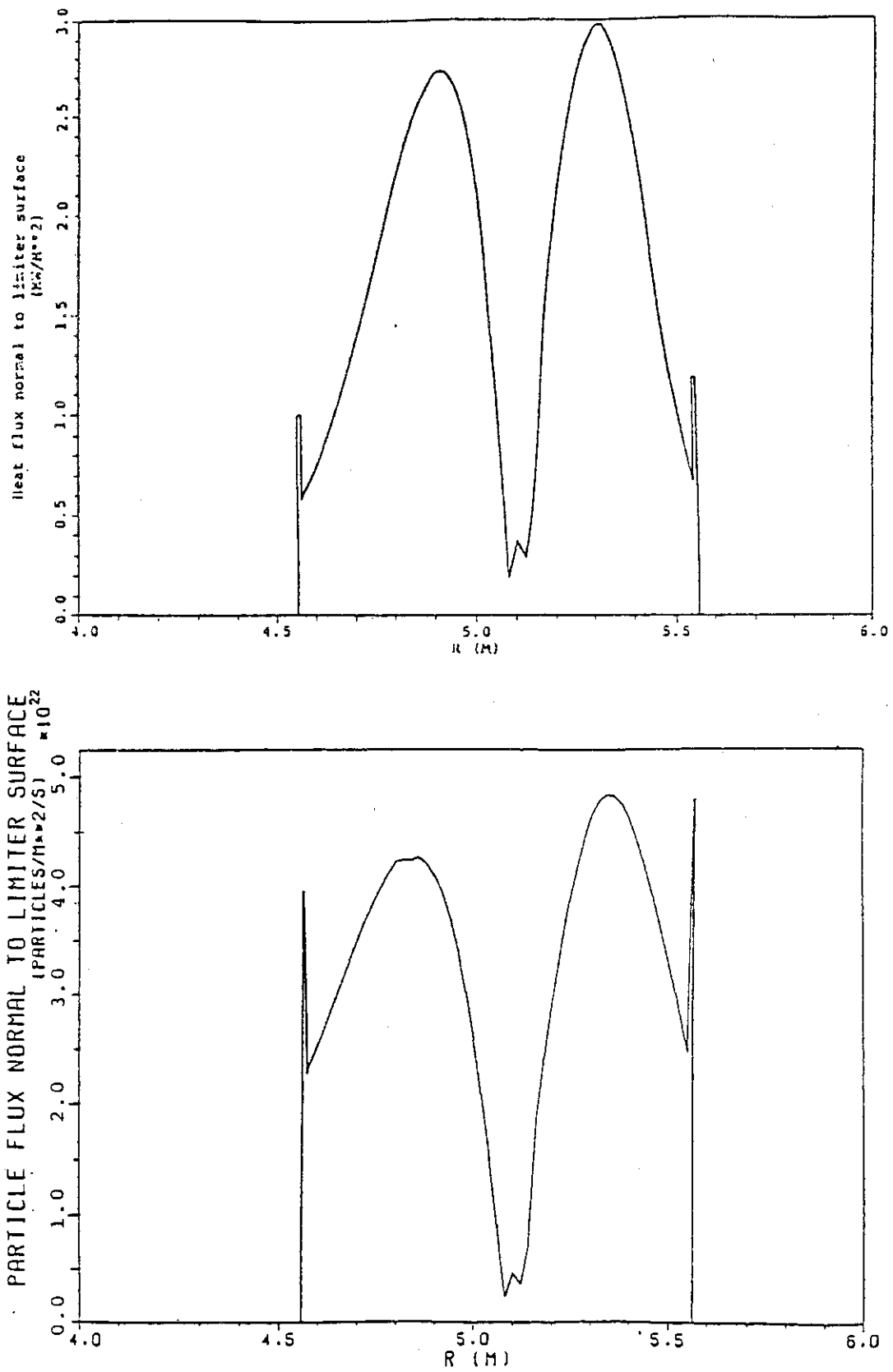


Fig. 3.4 Heat and particle flux to flat limiter for
 $T_e = 150 \text{ eV}$

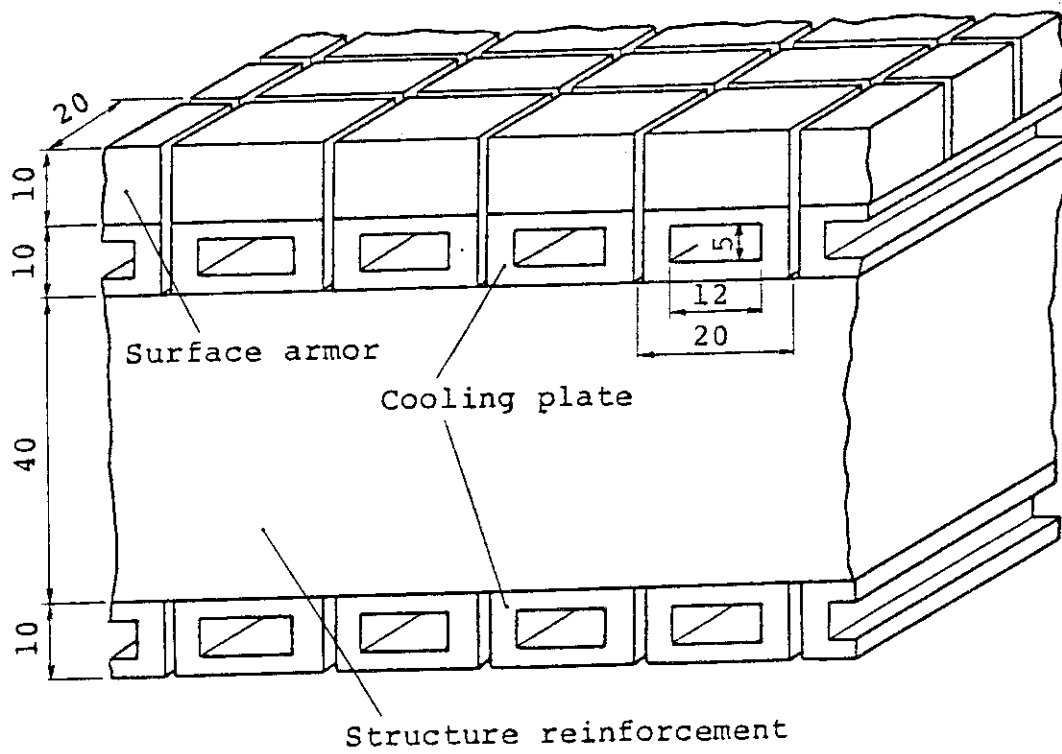


Fig.3.5 Cross section at the top surface of limiter plate

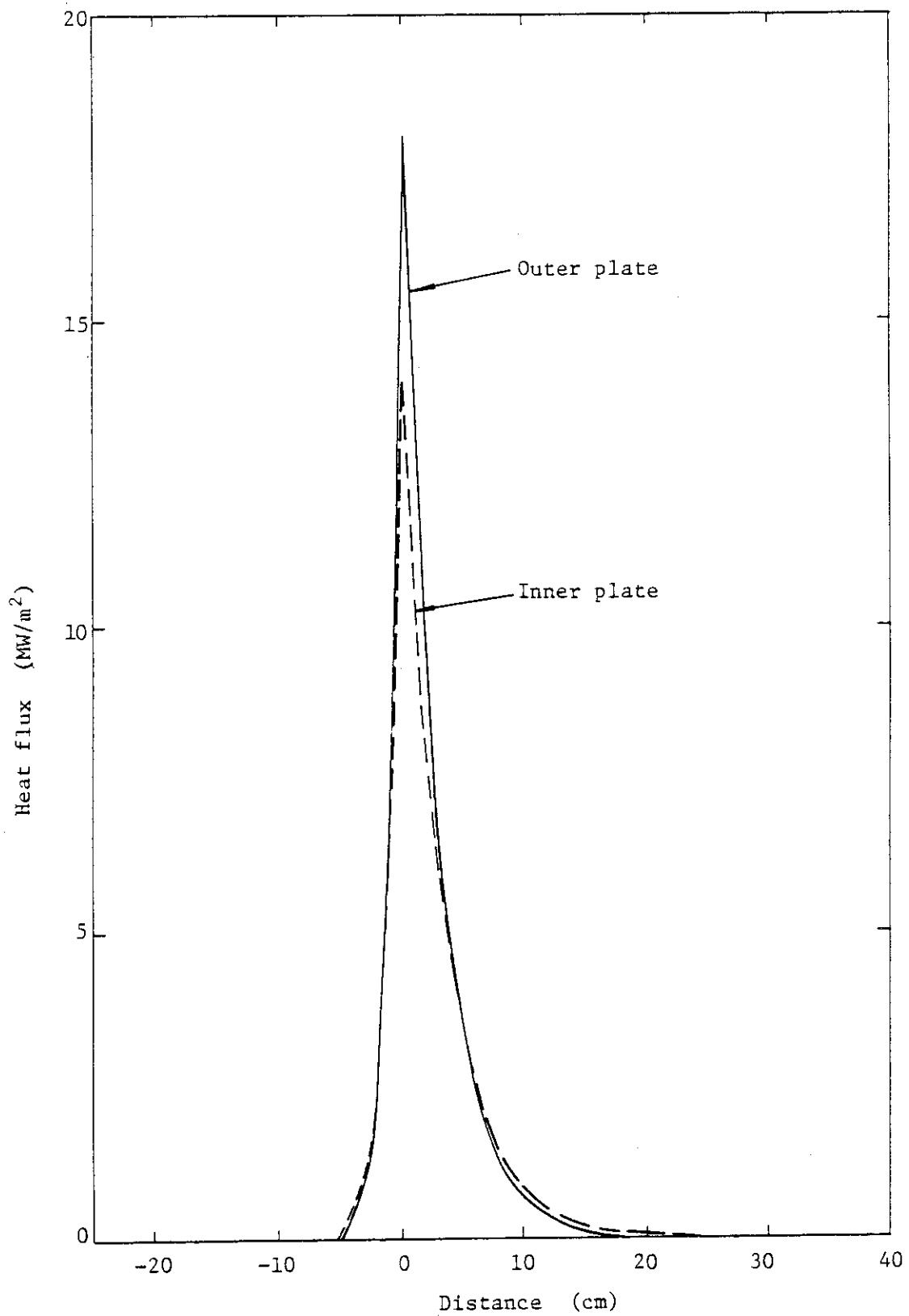


Fig. 3.6 Heat flux distribution perpendicular to the separatrix at the location of the collector plates

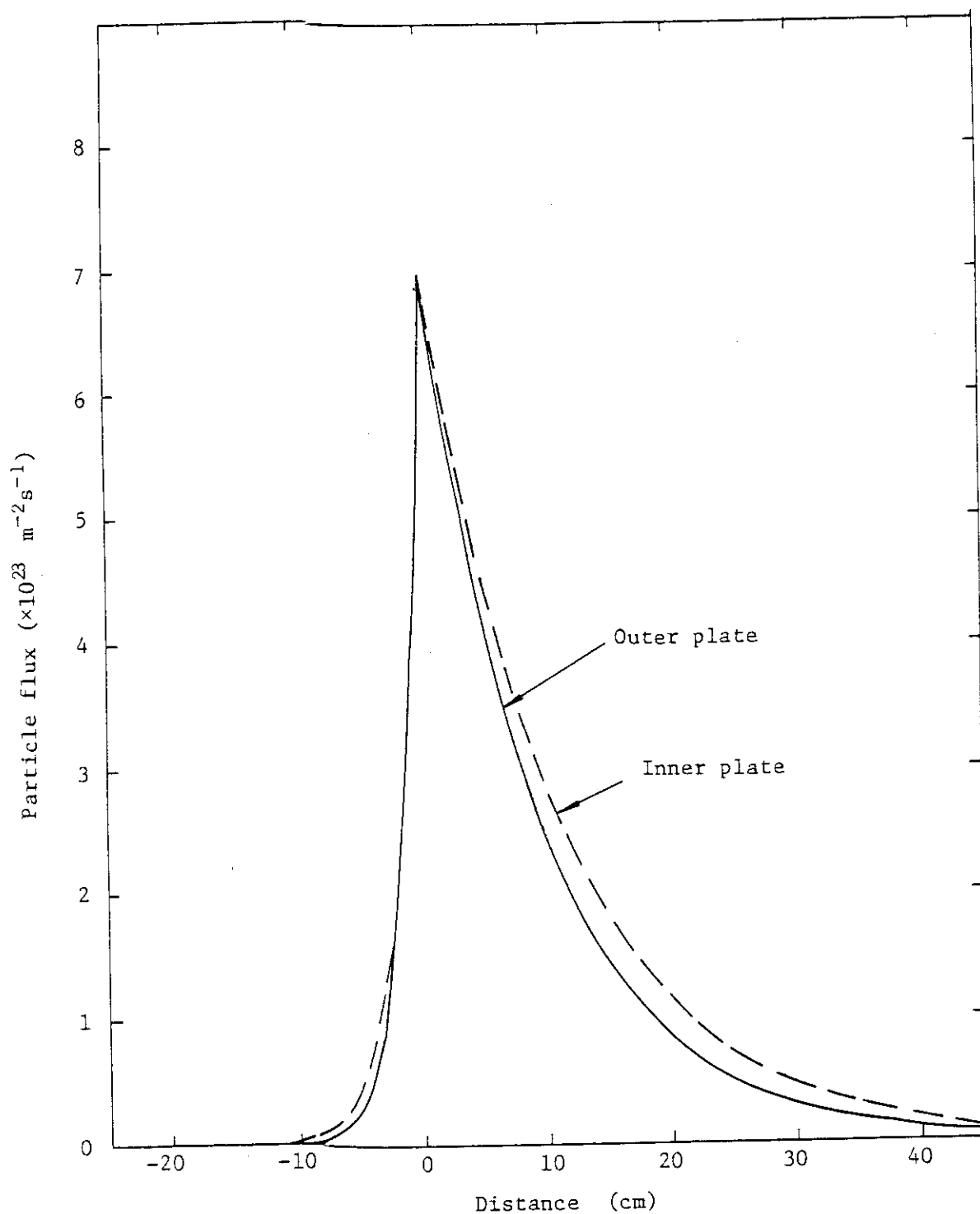


Fig. 3.7 Particle flux distribution perpendicular to the separatrix at the location of the collector plates

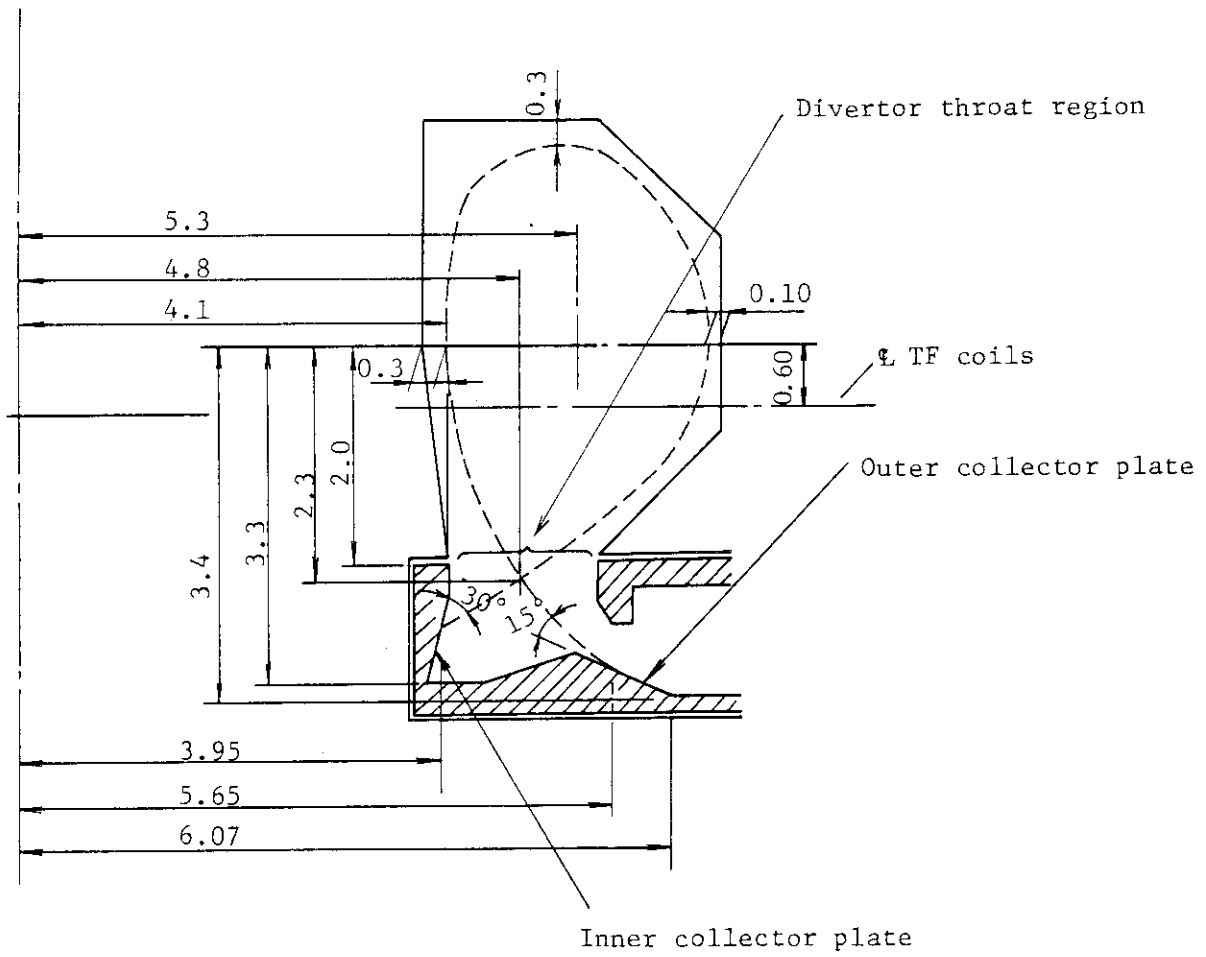


Fig.3.8 Profile of the divertor region in the Phase 1 design

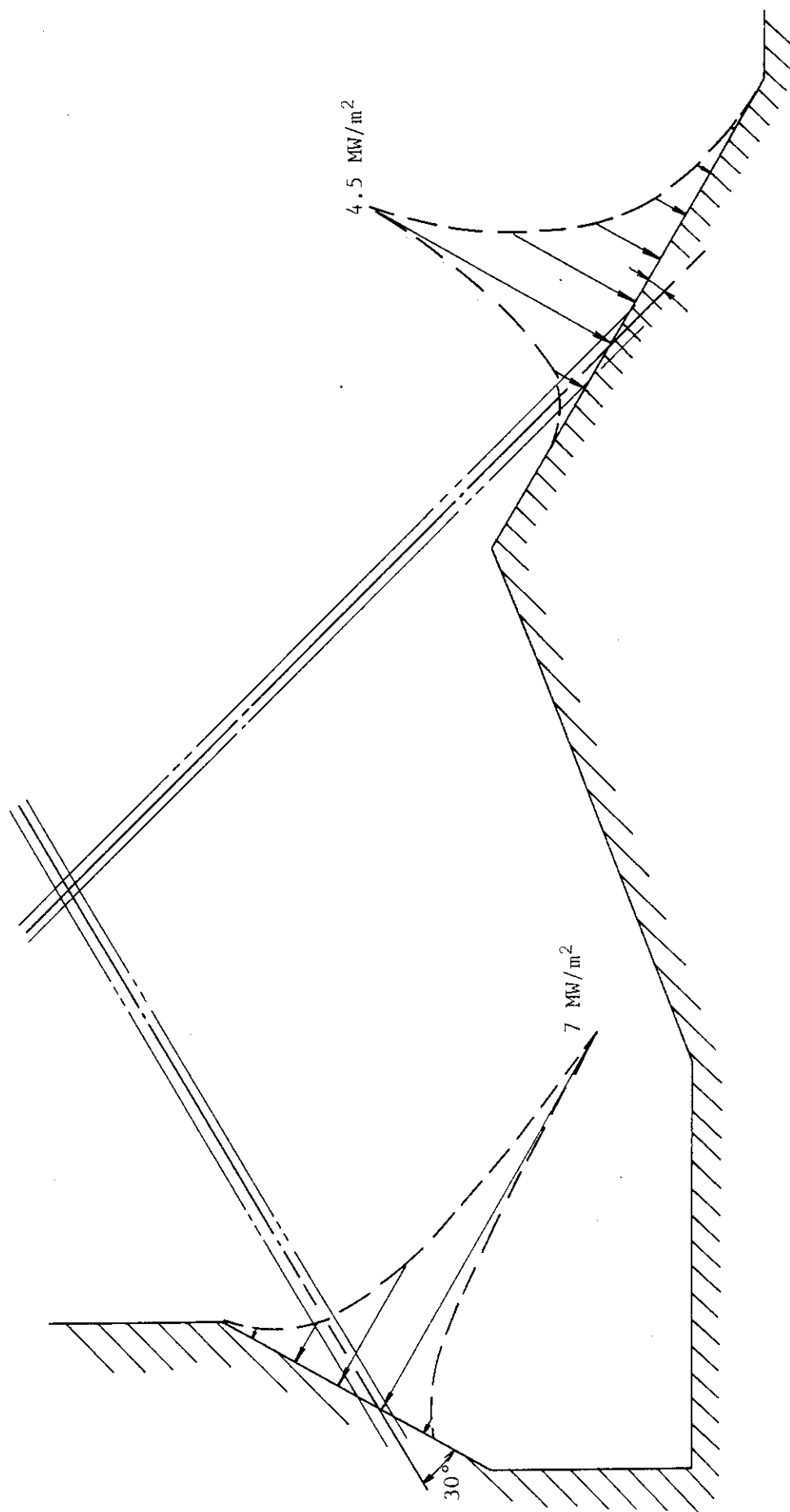


Fig. 3.9 Heat flux distribution on divertor plate

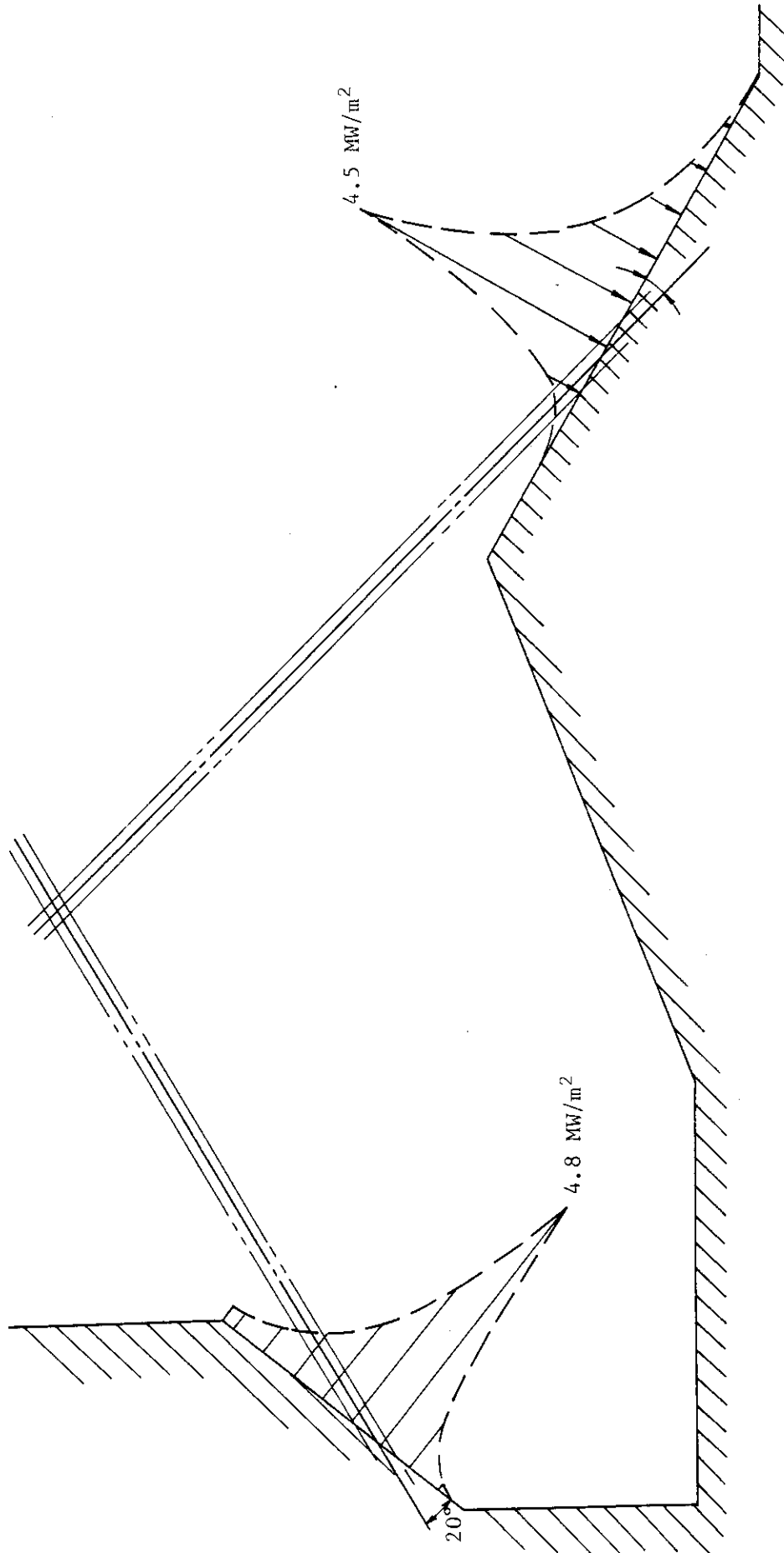


Fig.3.10 Heat flux distribution on divertor plate

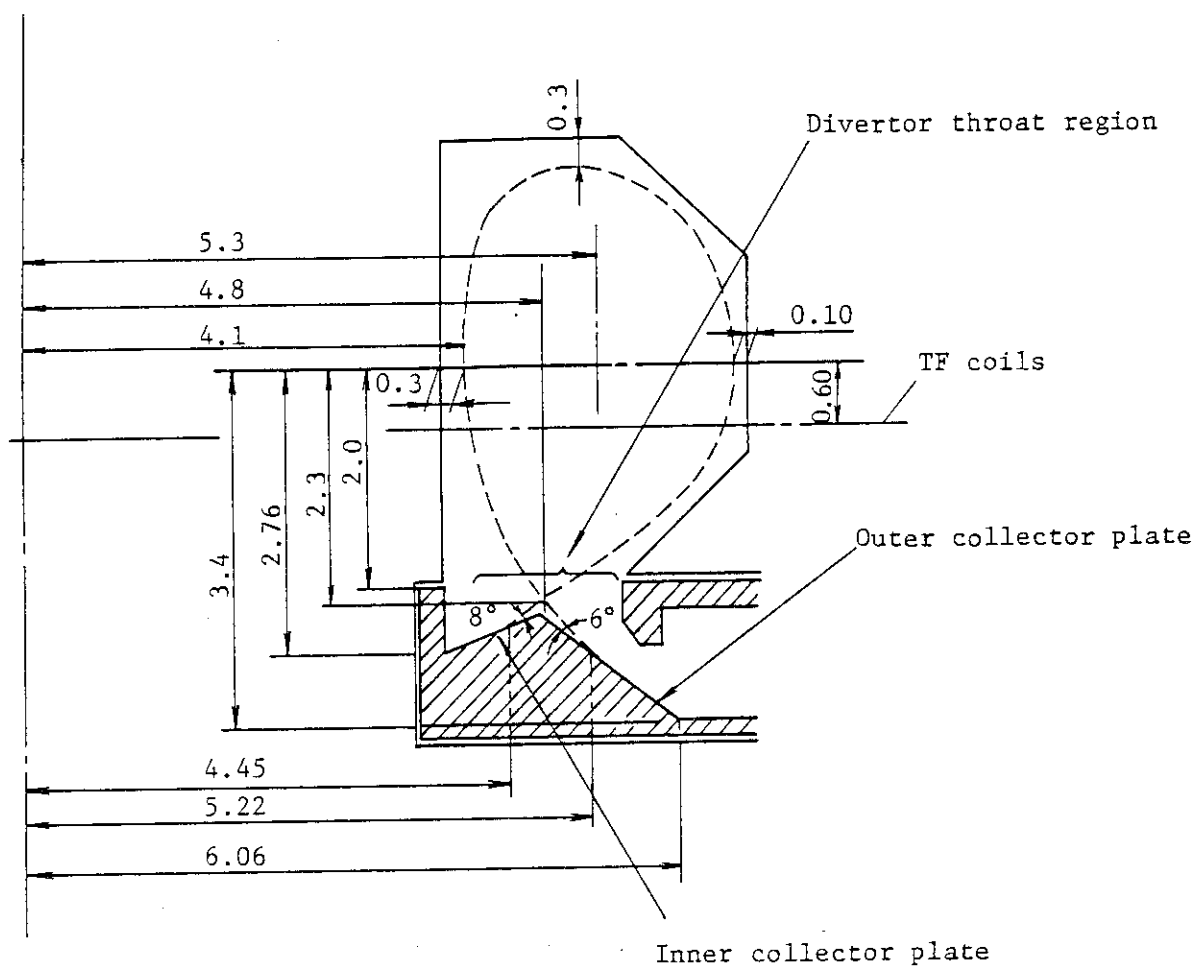


Fig.3.11 Profile of the divertor region for the peak heat load of 2 MW/m^2

The plasma configuration is unchanged from the Phase 1 design.

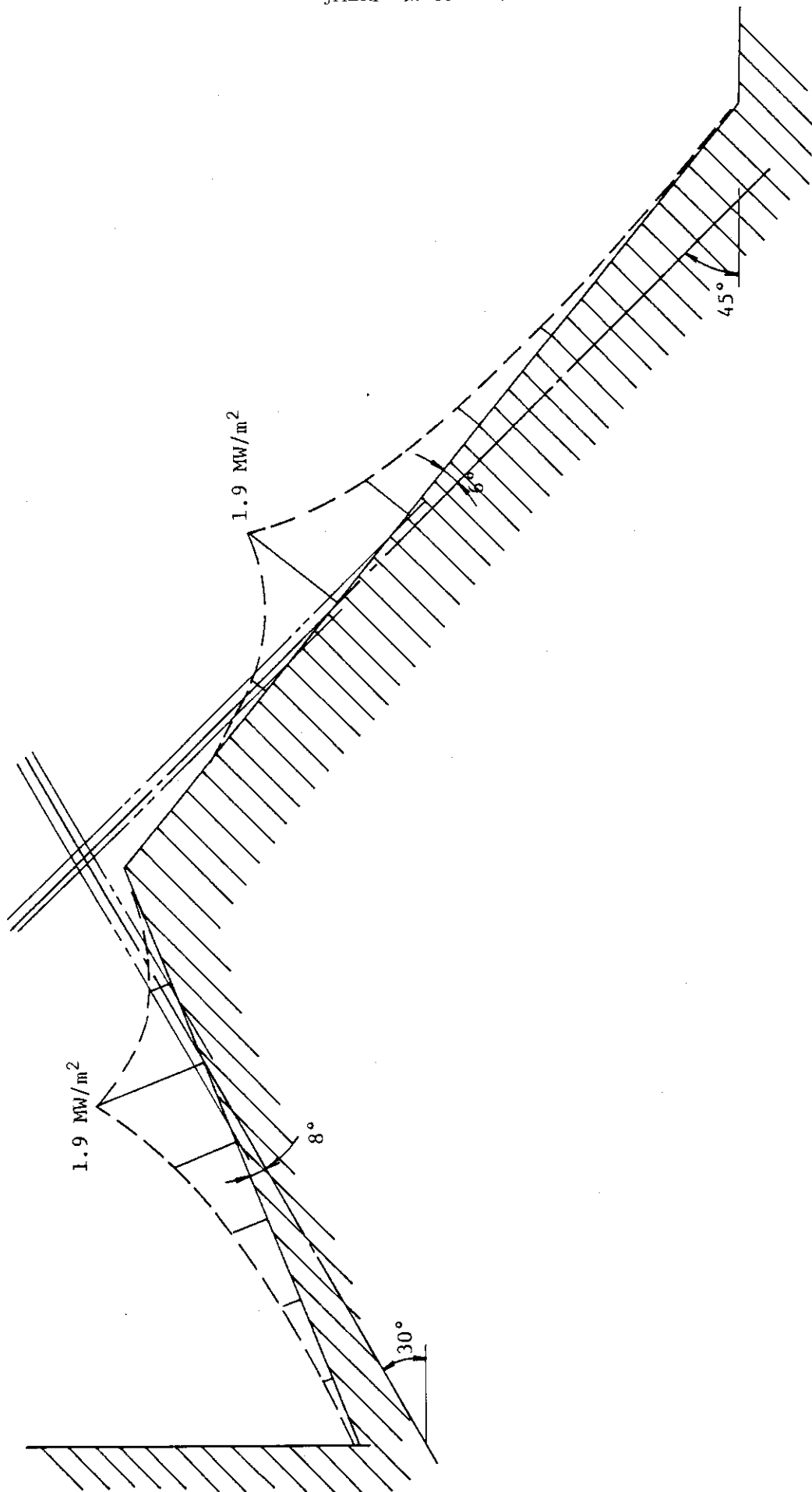


Fig.3.12 Heat flux distribution on divertor plate

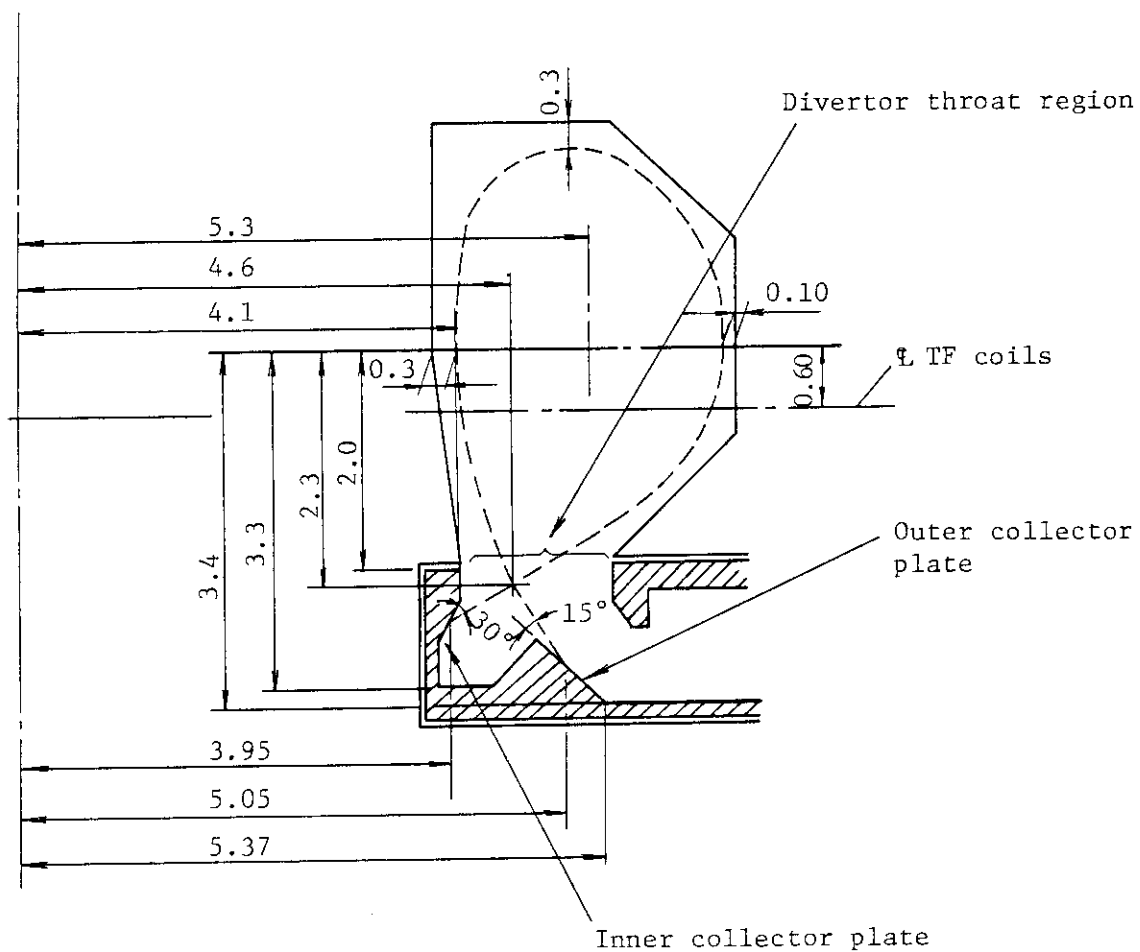


Fig.3.13 Profile of the divertor region in the Japanese plasma configuration

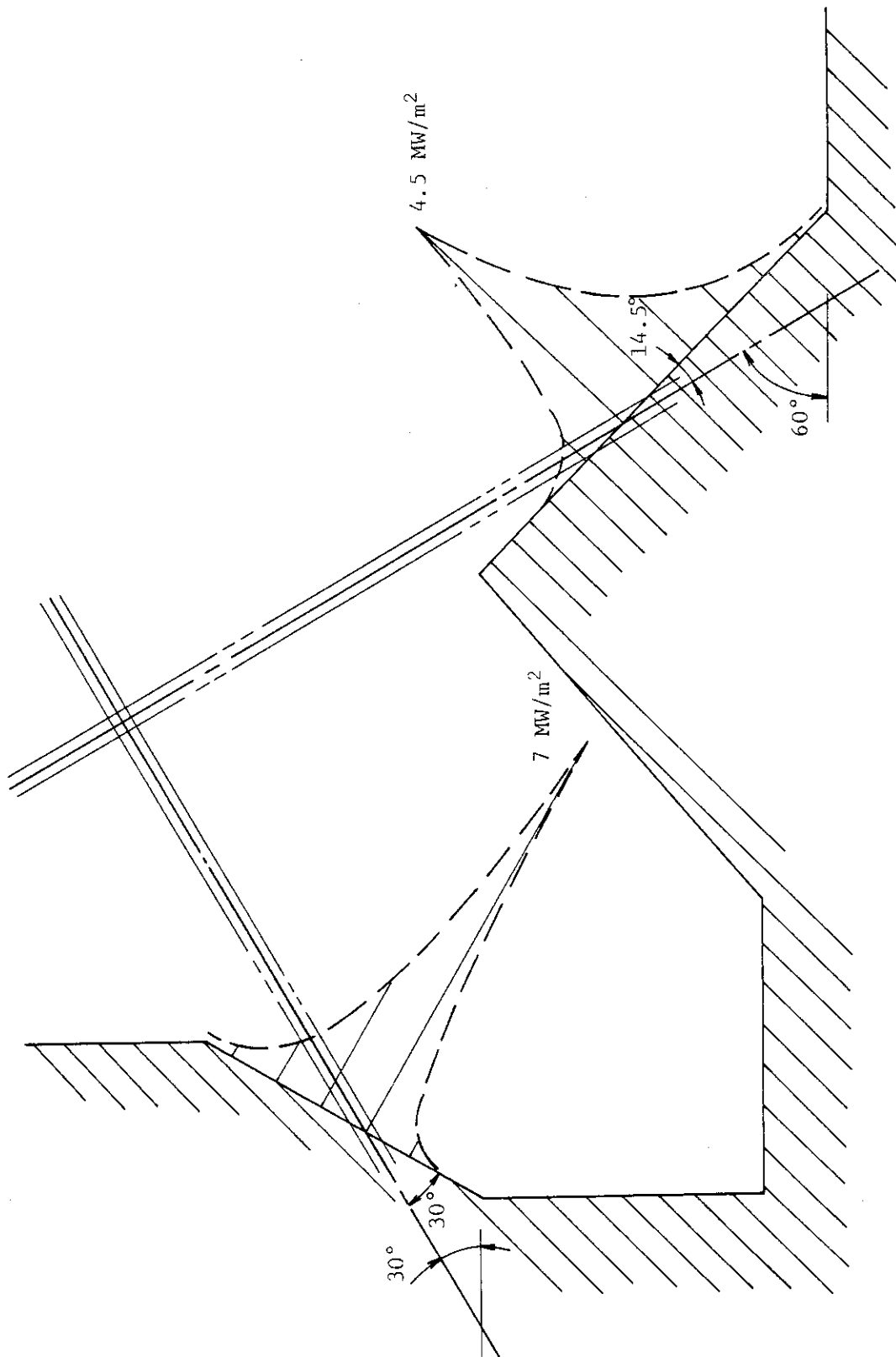


Fig.3.14 Heat flux distribution on divertor plate
The plasma configuration is based upon the
Japanese prediction.

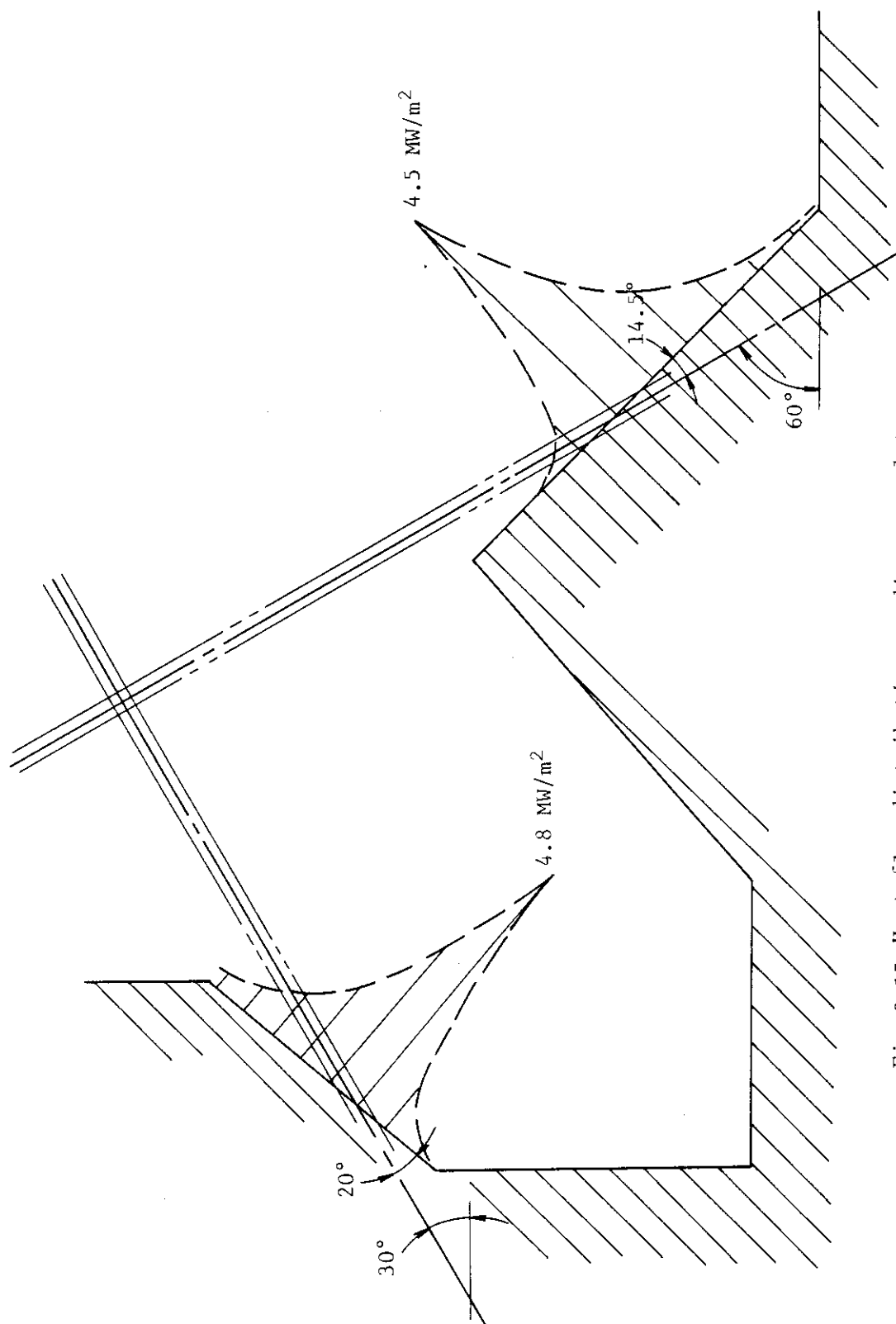


Fig. 3.15 Heat flux distribution on divertor plate

The plasma configuration is based upon the Japanese prediction.

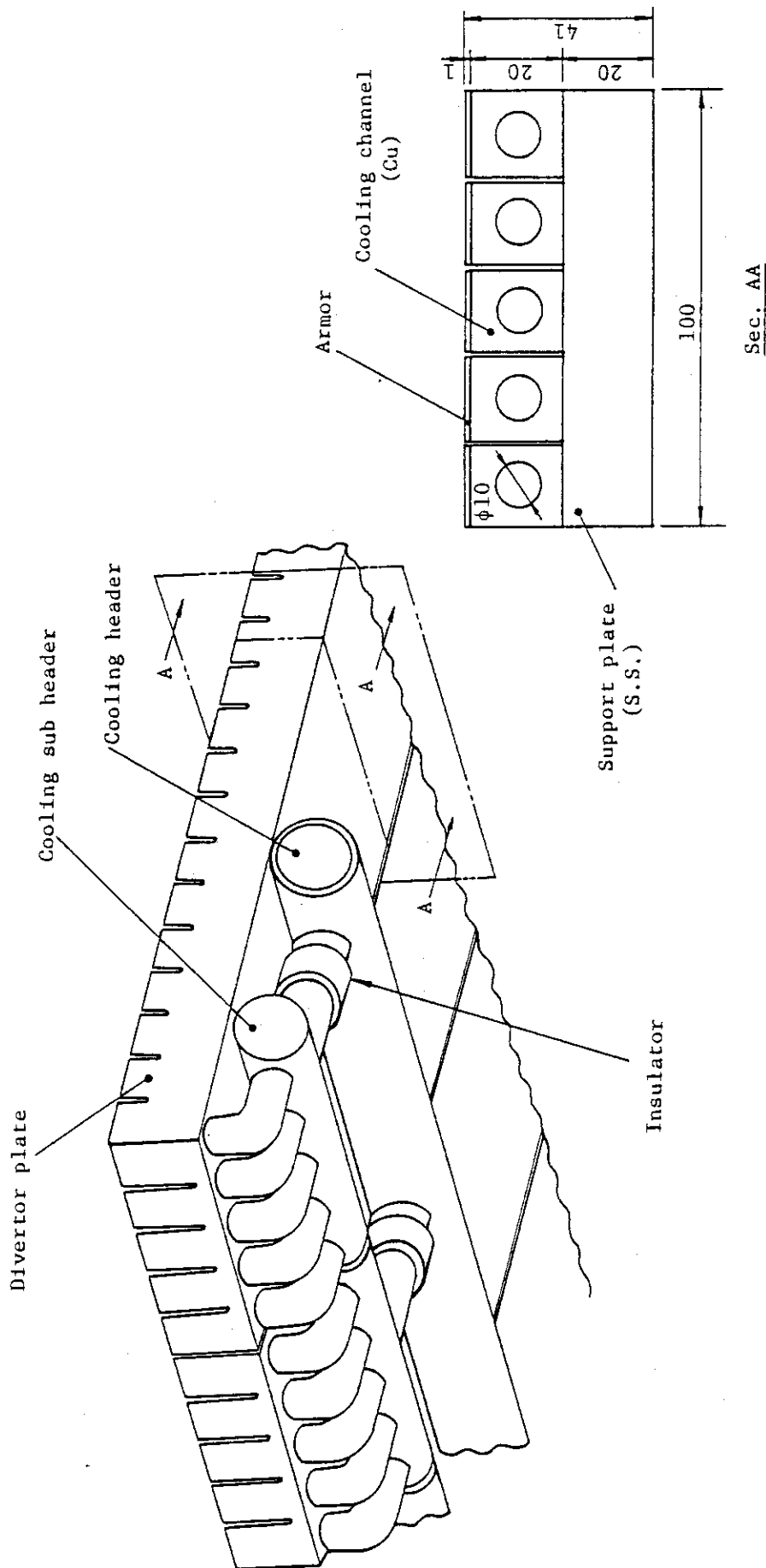


Fig. 3.16 Divertor plate

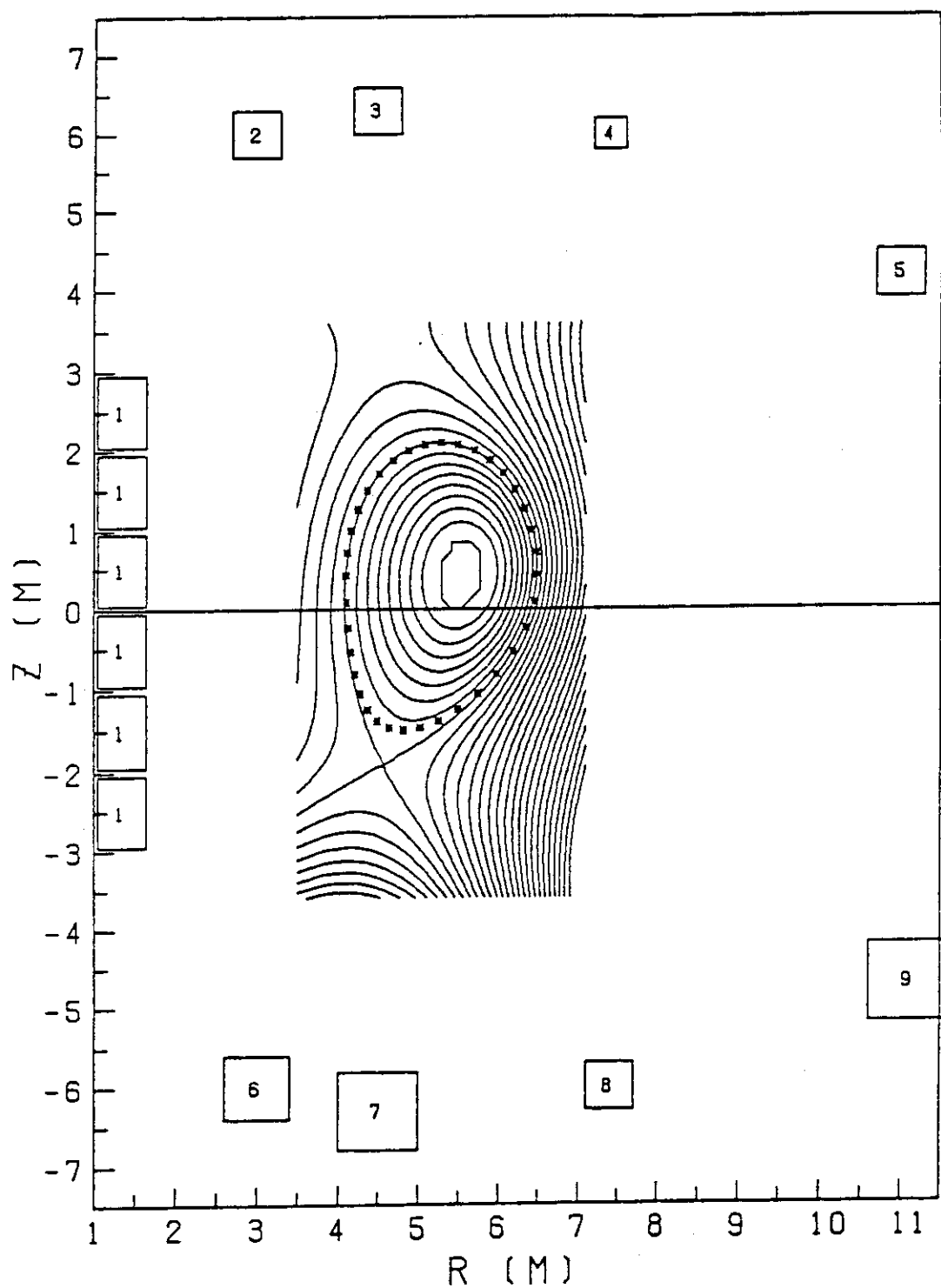


Fig. 3.17 Equilibrium poloidal field configuration for the reduced channel length divertor

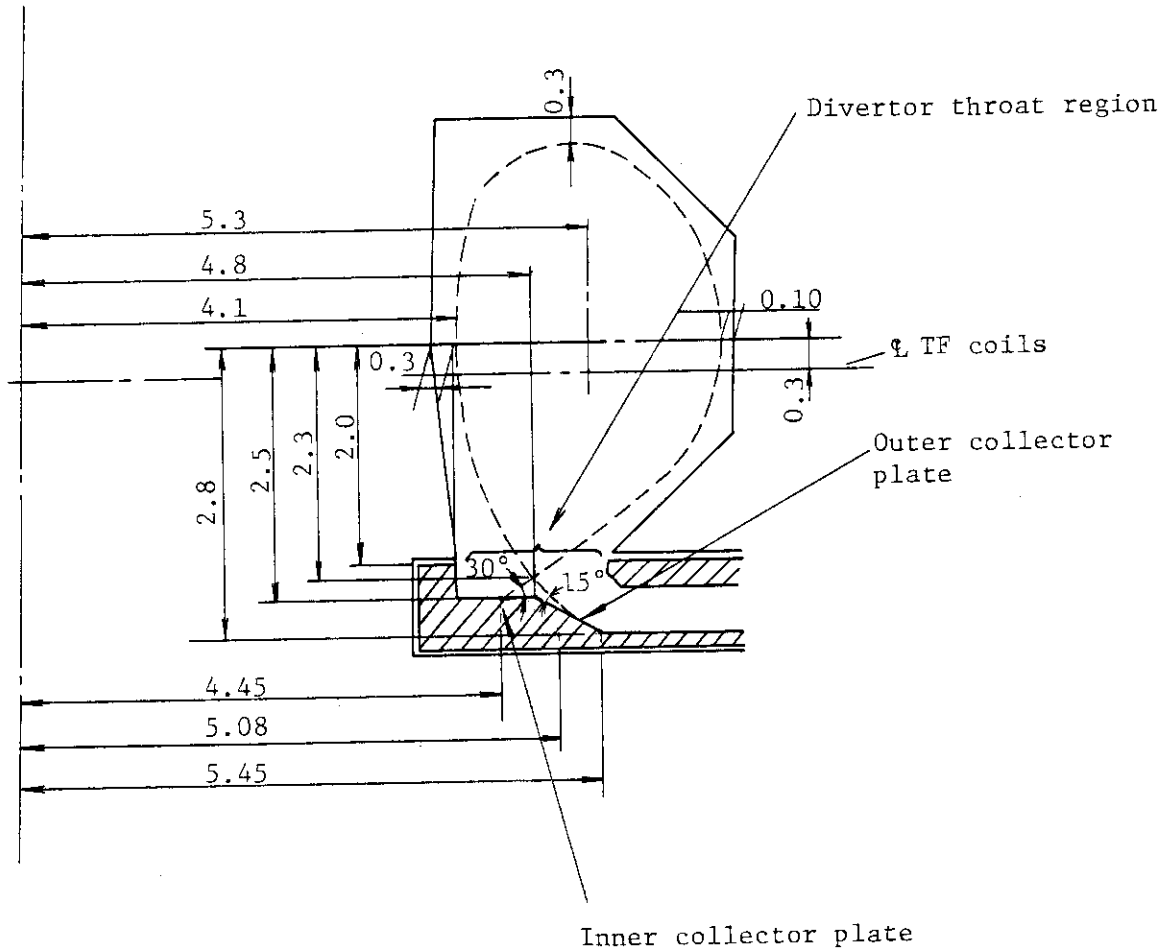


Fig.3.18 Profile of the divertor region for the reduced channel length divertor

The plasma configuration is unchanged from the Phase 1 design.

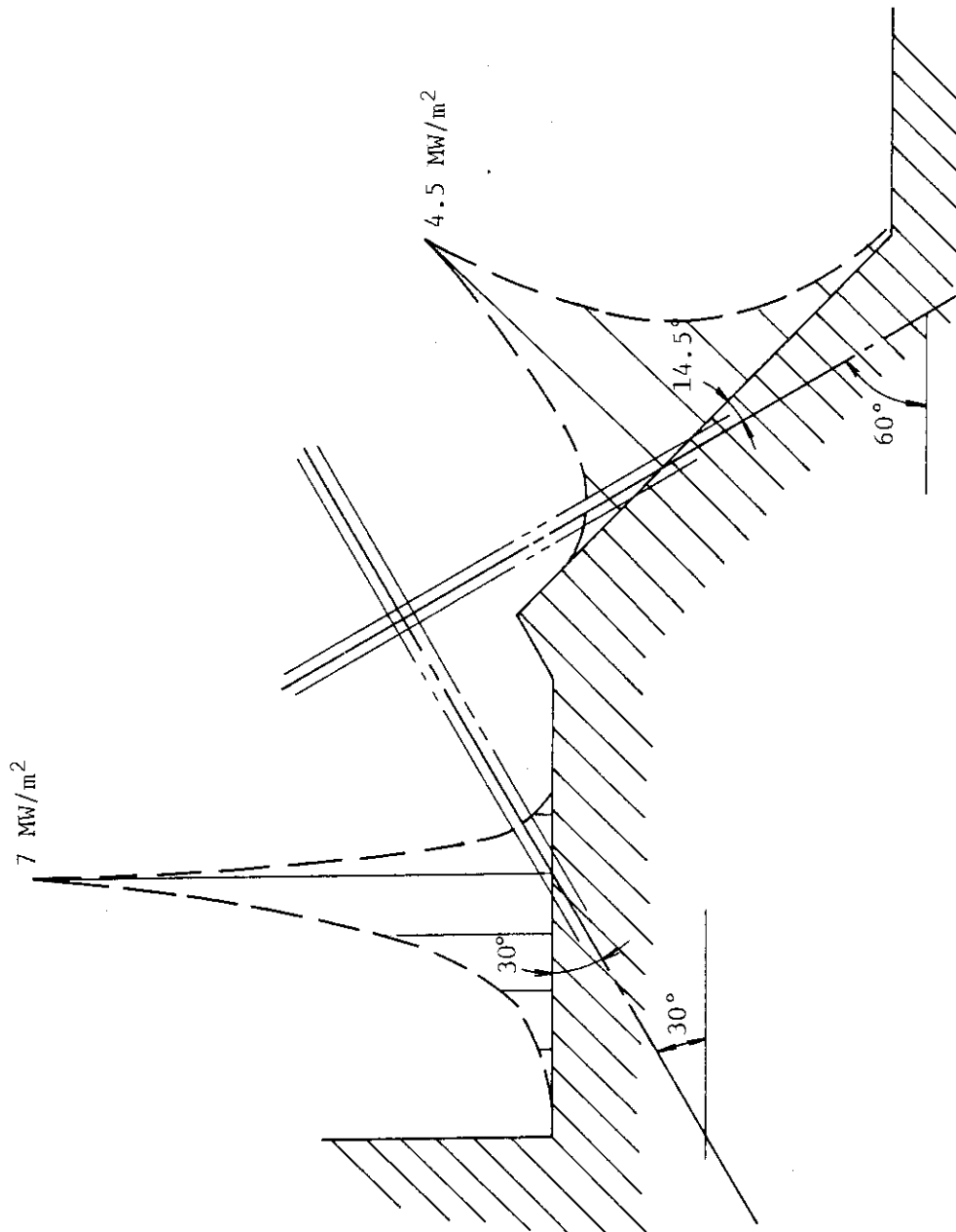


Fig.3.19 Heat flux distribution on divertor plate

The plasma configuration is based upon the Japanese prediction.

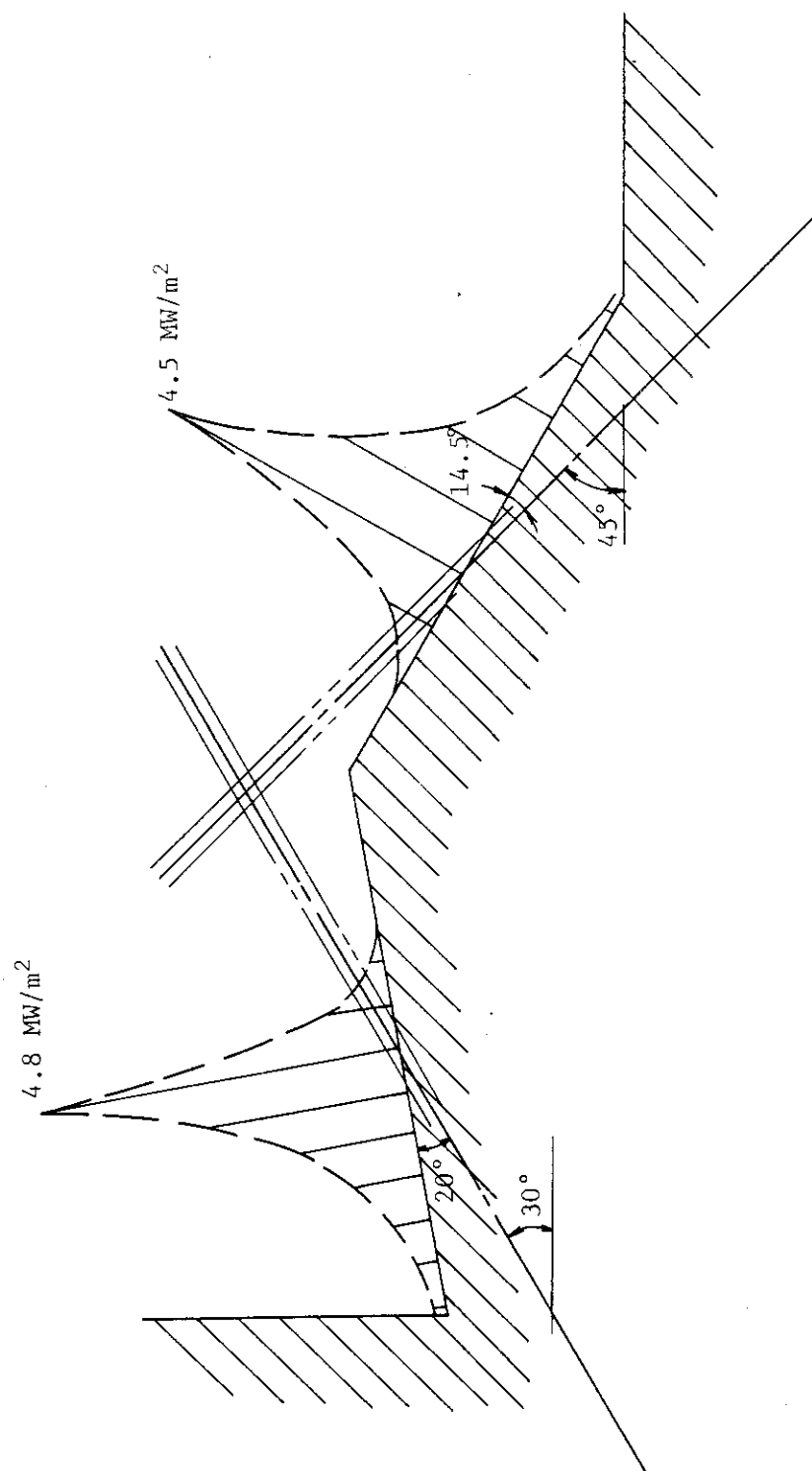


Fig.3.20 Heat flux distribution on divertor plate
The plasma configuration is unchanged from
the Phase 1 design.

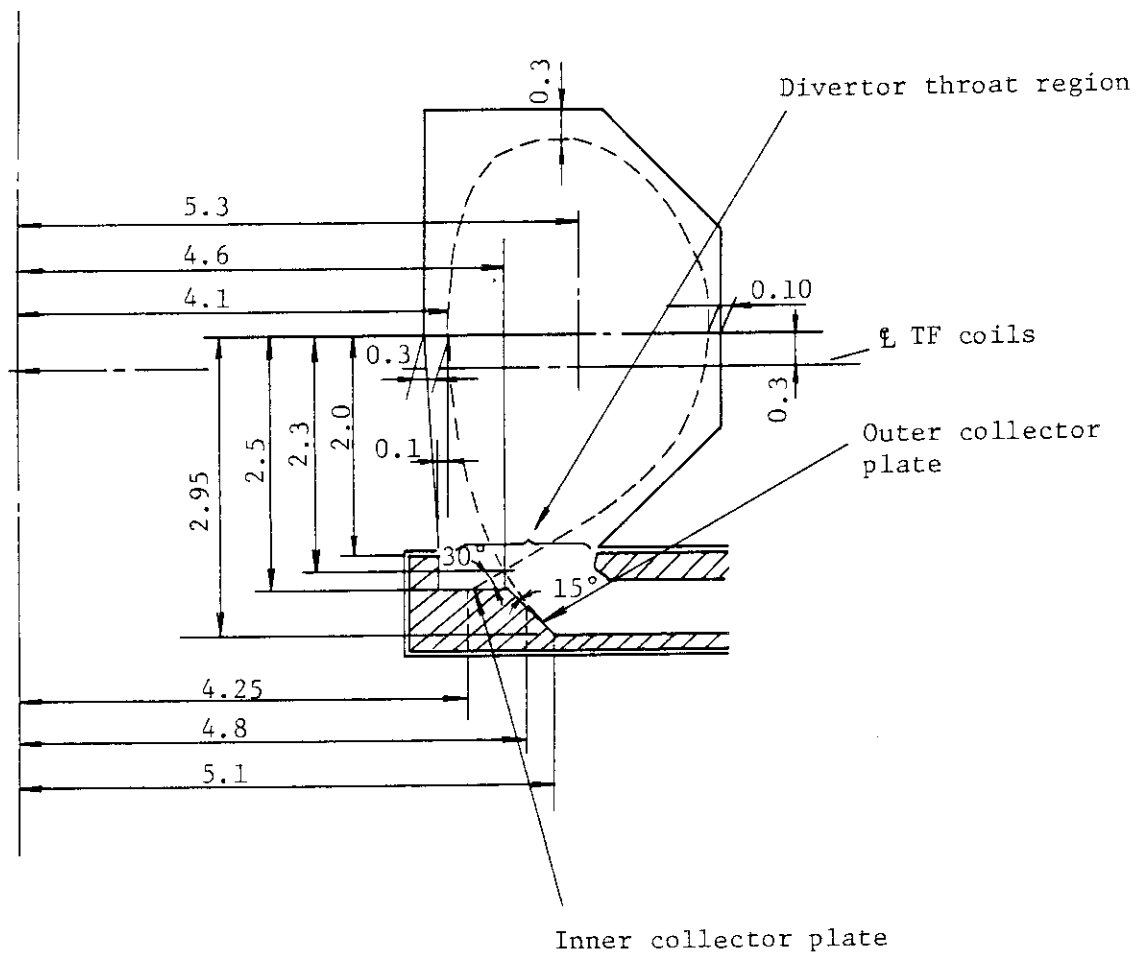


Fig. 3.21 Profile of the divertor region for the reduced channel length divertor

The plasma configuration is based upon the Japanese prediction.

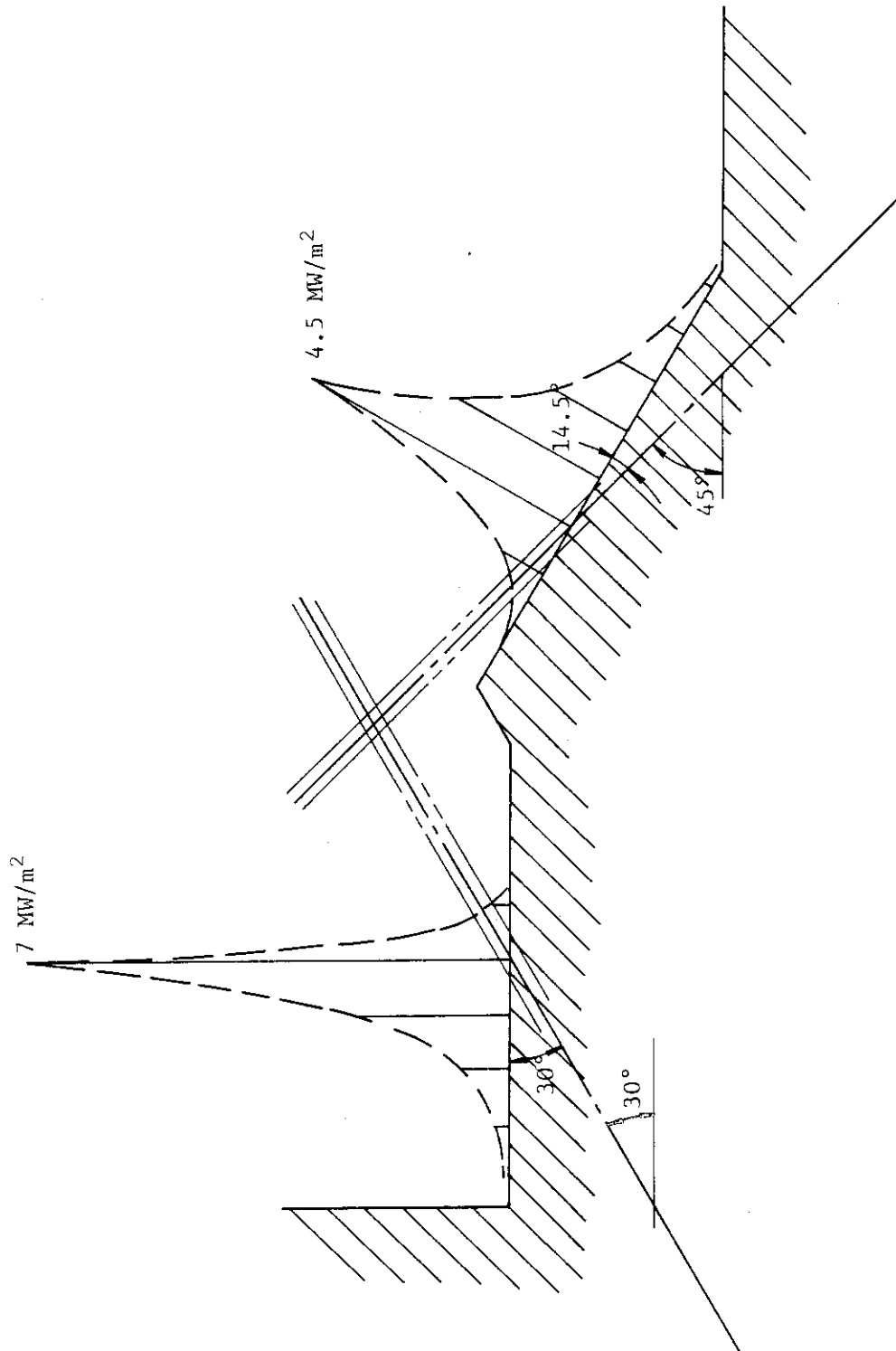


Fig. 3.22 Heat flux distribution on divertor plate

The plasma configuration is unchanged from the Phase 1 design.

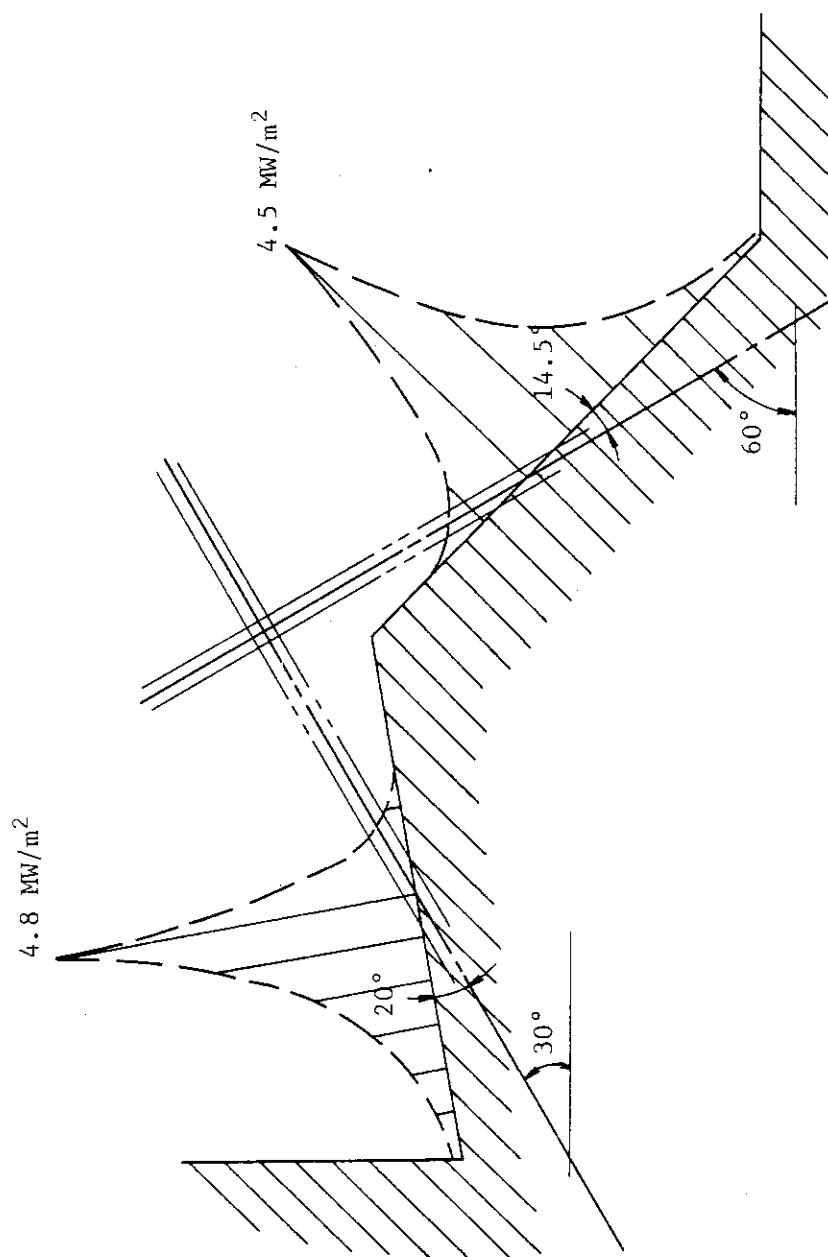


Fig. 3.23 Heat flux distribution on divertor plate
The plasma configuration is based upon the
Japanese prediction.

4. Materials considerations

4.1 Structural materials

4.1.1 Physical and mechanical properties

Pure copper and a copper alloy (Cu-0.6Be-2.5Co) were considered as the heat sink. Type 316 stainless steel was considered for the support structure.

Physical and mechanical properties are given in Table 4.1. The tensile and fatigue properties of OFHC copper and Cu-0.6Be-2.4Co are presented in Table 4.2 to Table 4.5. The strengths in the as-received and the annealed conditions are compared in these tables. Copper and the copper alloy lose the strengths due to annealing.

The room temperature fatigue curve of pure copper under the strain control condition is shown in Fig. 4.1. Figure 4.2 shows the fatigue behavior of OFHC copper at 300 C in high vacuum.

4.1.2 Irradiation properties

(1) Neutron irradiation data on mechanical properties of copper

Fig.4.3 shows the effect of irradiation on mechanical properties of copper, indicating that sharp increase of tensile and yield strength and decrease of elongation in high neutron fluences.

Under the fusion reactor operation at 620 MW, the first wall components are exposed to fast neutron flux of 6×10^{18} n/m².sec, and 9×10^{25} n/m² in 6 months. Copper-made components may suffer severe mechanical property degradation in such high fluence regime. However, high fluence data are not available at this time. It is to be investigated whether high fluence elongation can be extrapolated from the present 10^{24} n/m² data, as shown by the curve in Fig. 4.1.3.

(2) Swelling

Swelling appears at temperatures between 0.35 T_m (=202 C for Cu) and 0.55 T_m (= 473 C), and maximum value of V/V is 0.3-0.5% at 0.45 T_m (= 337 C) at 5×10^{20} n/cm², as shown in Fig. 4.4.

Swelling is represented as a function of fluence up to 10^{20} n/cm². At swelling peak temperature, 335 C, swelling may reach as high as 10% at the irradiation up to 10^{22} n/cm² if void swelling is assumed to be proportional to (fluence)^{0.75}. However, if the temperature is maintained below 250 C, swelling is suppressed lower than 1.9% even at 10^{22} n/cm² irradiation.

Copper swelling could be ignored by following reasons:

- (i) The maximum temperature of the cooling plate is about 200 C.
- (ii) The limiter plate has a loose structure to permit a thermal deformation. This structure will compensate the volume change by the swelling.

4.1.3 Coolant compatibility

The corrosion of the copper heat sink was assumed in the Phase IIA Part 1. The major conclusions are:

- (a) The corrosion rates depend on the conductivity and oxygen content in the water, and the temperature and velocity of water.
- (b) The data of water cooled generator indicate that the corrosion of copper should not be excessive if the water condition is controlled at reasonable levels.
- (c) The corrosion rate of copper may be approximately 0.06 mm/y at 90 C and 5 m/s of water in the conductivity less than 5 S/cm and

the oxygen content of 2 ppm.

4.2 Plasma side materials

4.2.1 Physical and mechanical properties

Tungsten was considered as plasma side material of the divertor plate. Physical and mechanical properties are given in Table 4.1. The elevated temperature properties extracted from PLANSEE bulletin are shown in Fig. 4.5 to Fig. 4.10.

Low-cycle fatigue of cross rolled tungsten is shown in Fig. 4.2.7 for the as-received and recrystallized material conditions. Tungsten in the recrystallized form exhibits the low tensile strength and short fatigue life.

4.2.2 Irradiation effects

Little is known about the irradiation effects on tungsten. Here, we only show the relative damage rates and the damage efficiencies which are obtained at RTNS-II by measuring electrical resistivity at low temperature¹⁾.

	Damage Rate	Damage Efficiency
V	18.01	0.147
Mo	9.47	0.162
W	11.55	0.345
Al	4.18	0.187
Cu	2.48	0.163

Tungsten seems to be unusual, however further work is required to determine the irradiation effects.

4.2.3 Hydrogen permeation and embrittlement

Solution and diffusion of hydrogen in Tungsten are discussed in Ref.2. Solubility and diffusion constants are derived from degassing rates. Comparison to theory indicates that the solubility and diffusion constants are characteristics of interstitially dissolved hydrogen. Transient analysis of tritium migration using these values are seen elsewhere³⁾

- 1) M.W. Guinan and J.H. Kinney, J. Nucl. Mater. 108 & 109 (1982) 95.
- 2) R. Frauenfelder, J. Vac. Sci. Technol. 6 (1969) 388.
- 3) K. Ashibe and K. Ebisawa, to be submitted at 6th Int. Conf. Plasma Wall Interaction, Nagoya, 14-18 May, 1984.

Table 4.1 Properties of divertor plate materials

Property	Temp. [°C]	Tungsten	Copper	Cu-0.6Be-2.5Co	316SS
Thermal Cond. [W/m°C]	20	156	366	209	17.5
	725	110			
Thermal Exp. [$\times 10^{-6}$ /°C]	20	5.0	16.5	17.6	18.6
	300				18.6
	500				20.3
Density [g/cm ³]	20	1.93	8.9	8.75	7.9
Elastic Modulus [GPa]	20	411	129	124	193
	100	408	126		188
	300	400	116		177
	500	392	99.1		159
Tensile Strength [MPa]	20	1500	210	860	590
Poisson's Coef.	20	0.31	0.3	0.3	0.3
Specific Heat [J/kg°C]	20	132	385	377	494
Melting Temp. [°C]		3410	1083	1030~1070	1300

Table 4.2 Tensile properties of OFHC copper

	Test temp.	UTS (MPa)	0.2% YS (MPa)	Elongation (%)
<u>As received</u>	20°C	310	300	18
	100°C	280	260	12
	200°C	250	230	7
<u>850°C×30 min annealed</u>	20°C	220	59	38
	100°C	200	59	36
	200°C	170	59	36

Data presented by Furukawa Metals Co., Ltd. in 1976

Table 4.3 Fatigue of OFHC under stress control condition

	Test temp.	Amplitude of stress (MPa)	
		N = 10 ⁴	N = 10 ⁵
<u>As received</u>	20°C	200	190
	100°C	190	170
	200°C	160	140
<u>850°C×30 min annealed</u>	20°C	170	120
	100°C	150	110 (1)
	200°C	130	98 (1)

(1) Data at 400°C × 30 min annealed condition

Data presented by Furukawa Metals Co., Ltd. in 1976

Table 4.4 Tensile properties of Cu-0.6Be-2.5Co

	Test temp.	UTS (MPa)	0.2% YS (MPa)	Elongation (%)
<u>As received</u>	20°C	860	780	11
	100°C	820	760	11
	200°C	780	720	9
<u>850°C×30 min annealed</u>	20°C	240	130	11
	100°C	210	120	11
	200°C	180	120	9

Data presented by Furukawa Metals Co., Ltd. in 1976

Table 4.5 Fatigue of Cu-0.6Be-2.5Co under stress control condition

	Test temp.	Amplitude of stress (MPa)	
		N = 10 ⁴	N = 10 ⁵
<u>As received</u>	20°C	520	410
	100°C	510	400
	200°C	490	390
<u>850°C×30 min annealed</u>	20°C	200	180
	100°C	200	170
	200°C	180	120

Data presented by Furukawa Metals Co., Ltd. in 1976

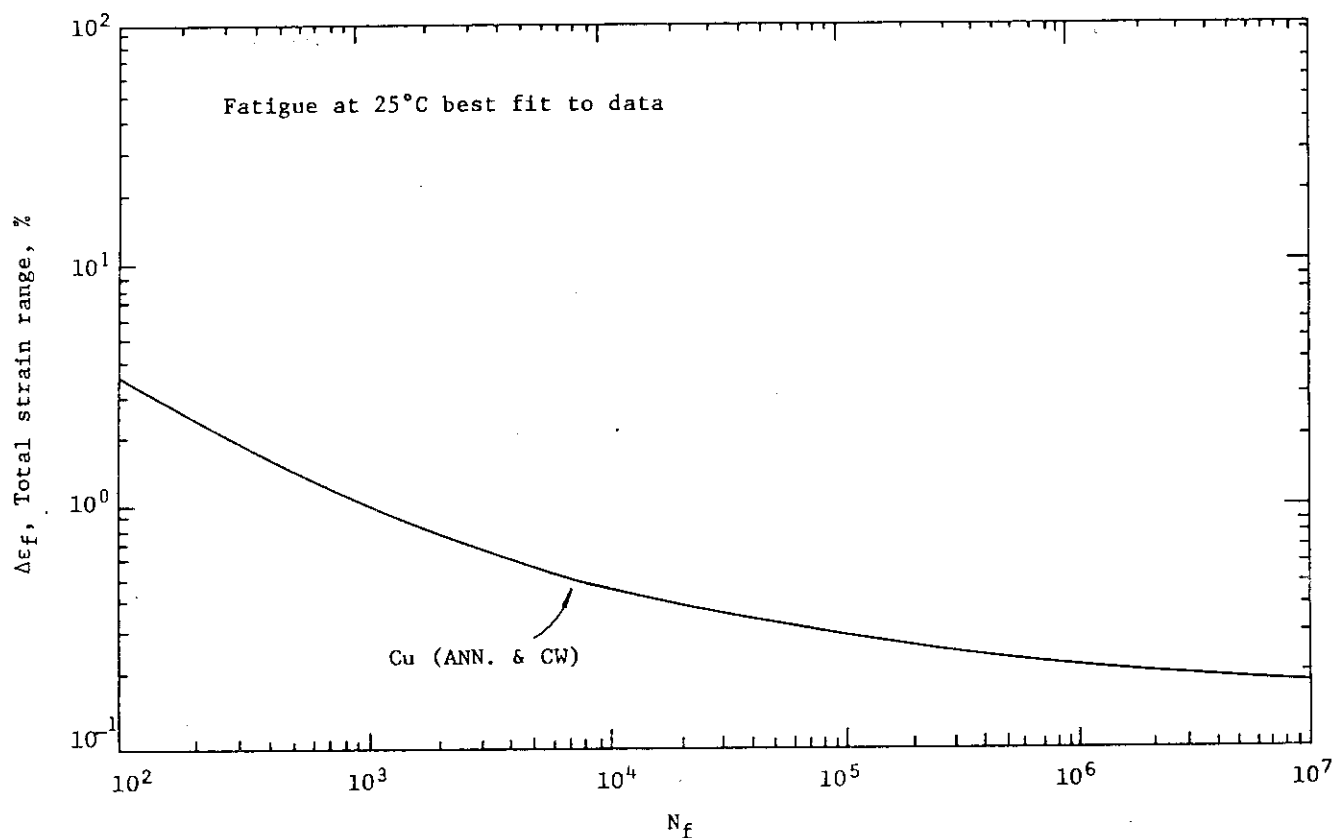


Fig. 4.1. Fatigue data for copper at room temperature

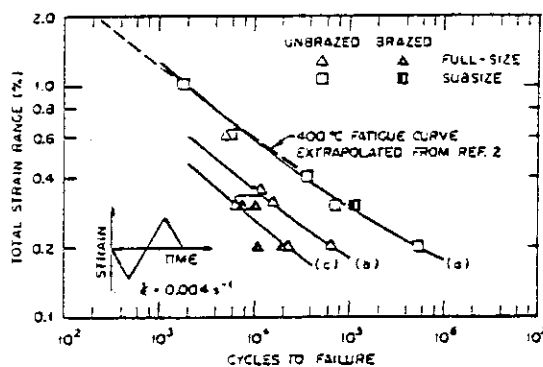


Fig. 4.2 Total strain range ($\Delta\epsilon_t$) as a function of cycles to failure (N_f) for OFHC copper tested at 300°C in vacuum

K.C. Liu and C.M. Loring, Jr. "Low-cycle fatigue Behavior of oxygen-free high-conductivity copper at 300°C in high vacuum", J. Nucl. Mater. 122 & 123 (1984) 783.

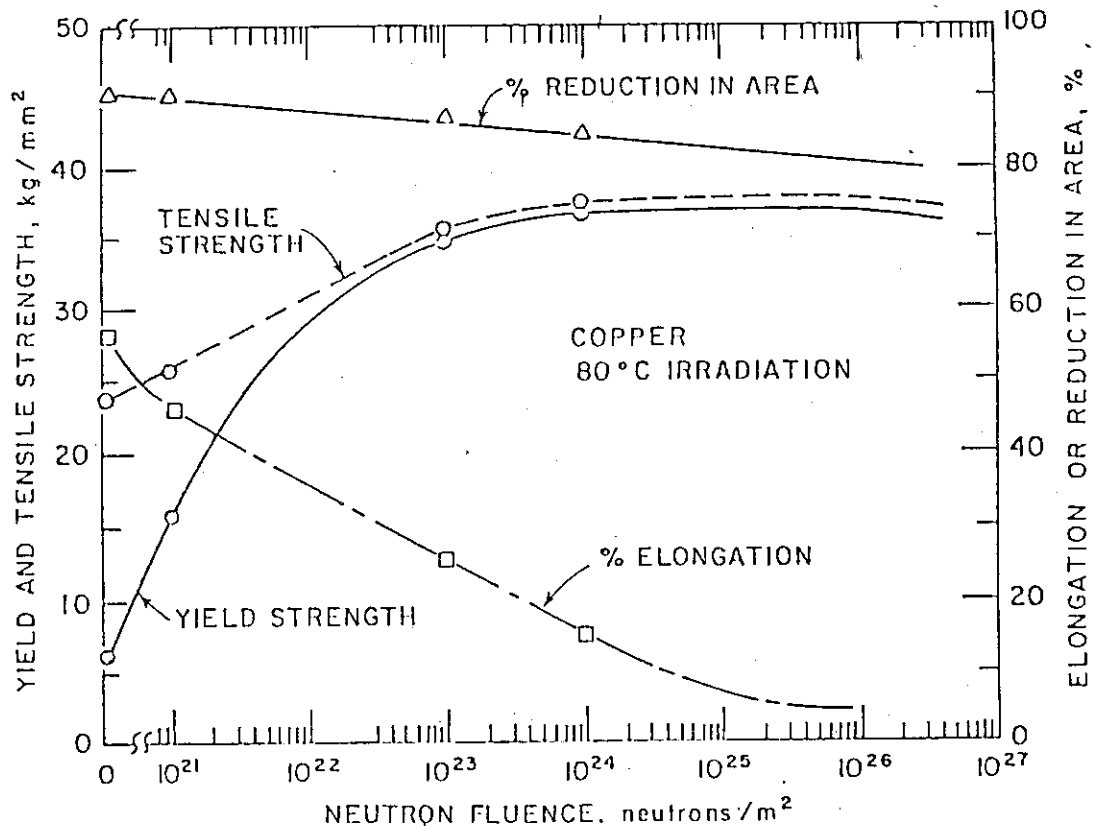


Fig. 4.3 Effect of irradiation at 80°C on room-temperature tensile properties of copper

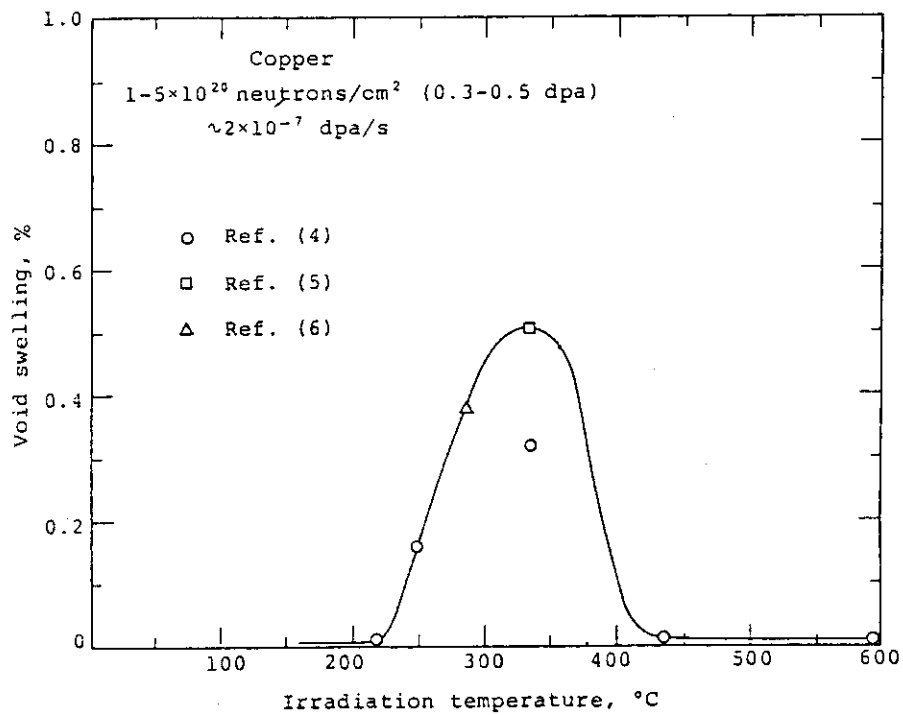


Fig. 4.4 Dependence of void swelling of neutron-irradiated copper on temperature

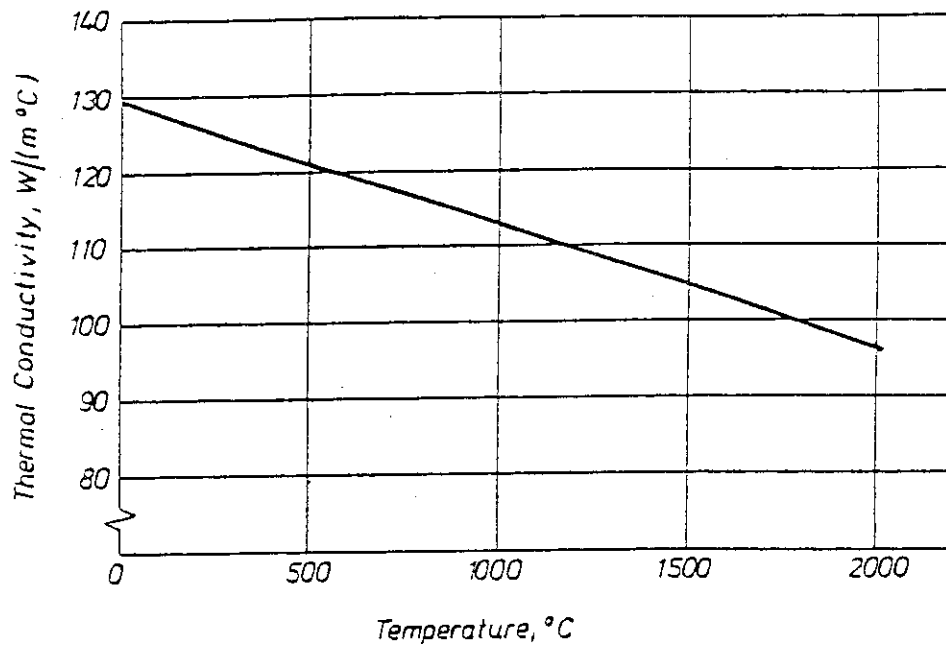


Fig. 4.5 : Thermal conductivity of tungsten versus temperature.

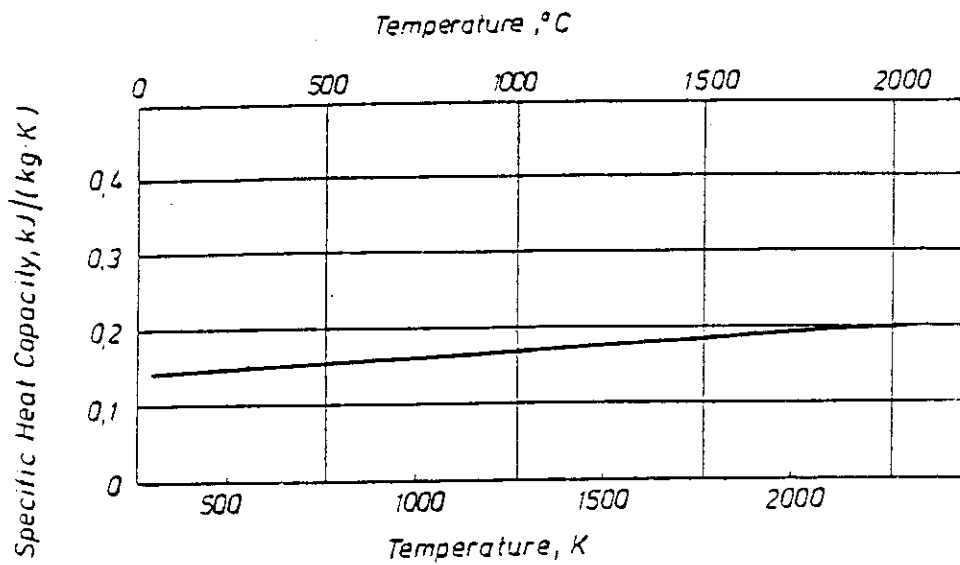


Fig. 4.6 : Specific heat capacity of tungsten versus temperature.

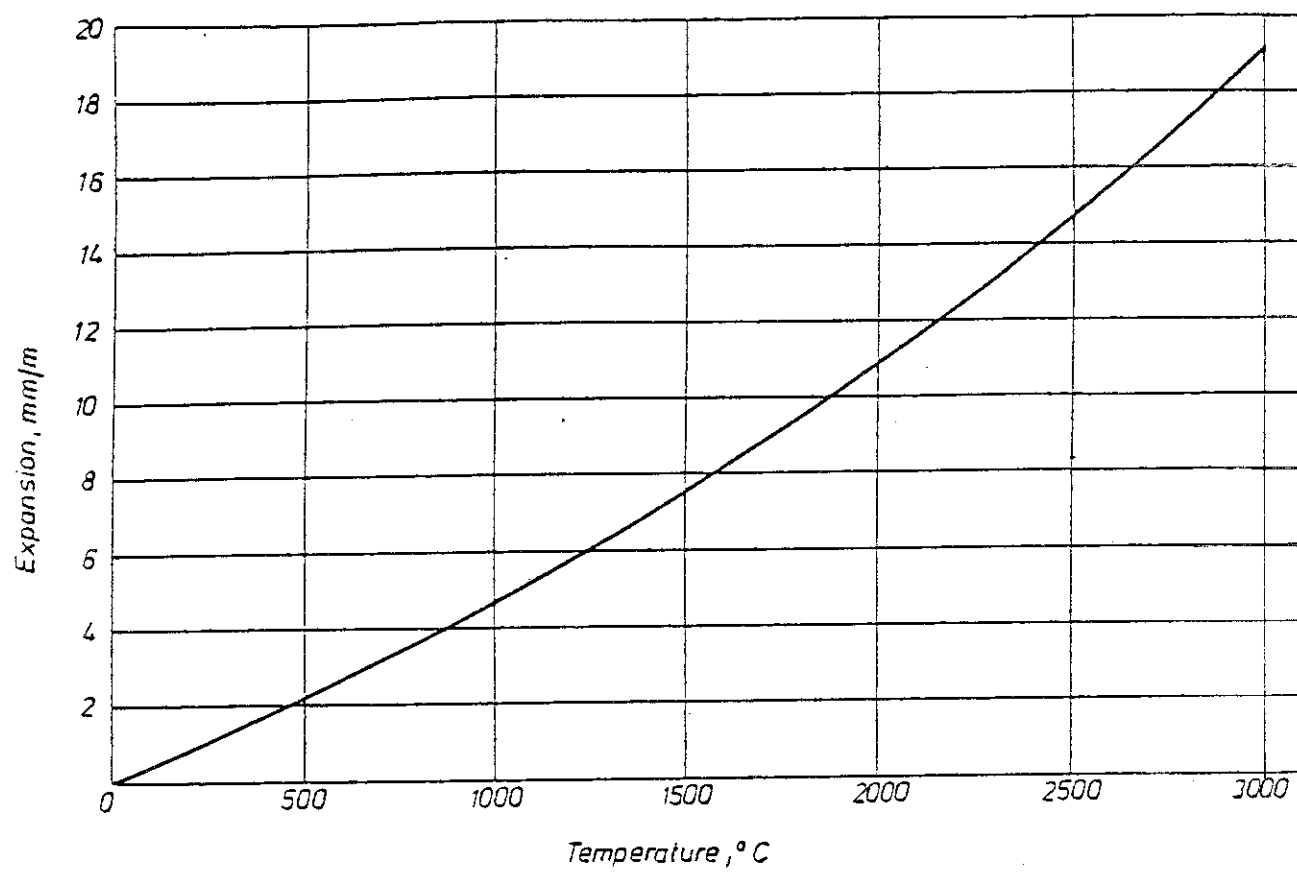


Fig. 4.7 : Thermal expansion of tungsten versus temperature.

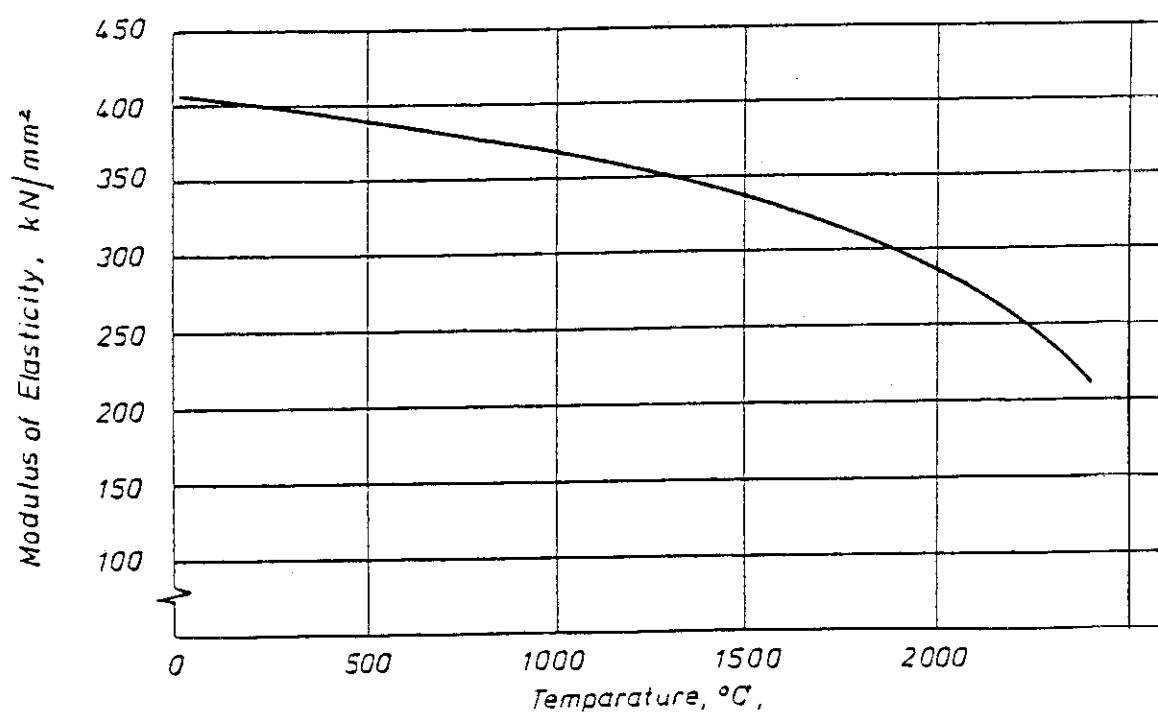


Fig. 4.8 : Modulus of elasticity versus temperature.

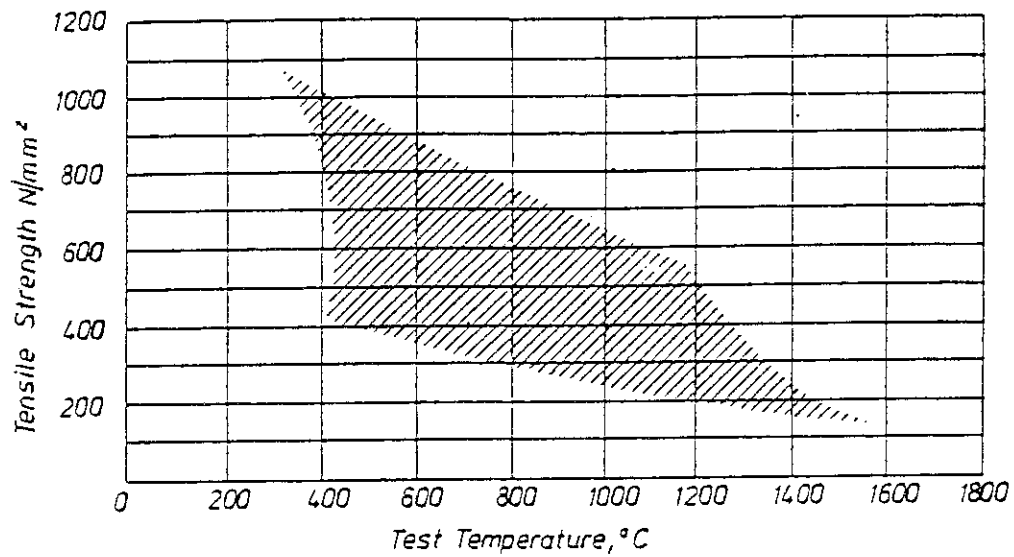


Fig. 4.9 Tensile strength of 1 mm thick tungsten sheet at elevated temperatures, strain rate 15%/minute. The upper limit corresponds to stress relieved and the lower to recrystallized sheet.

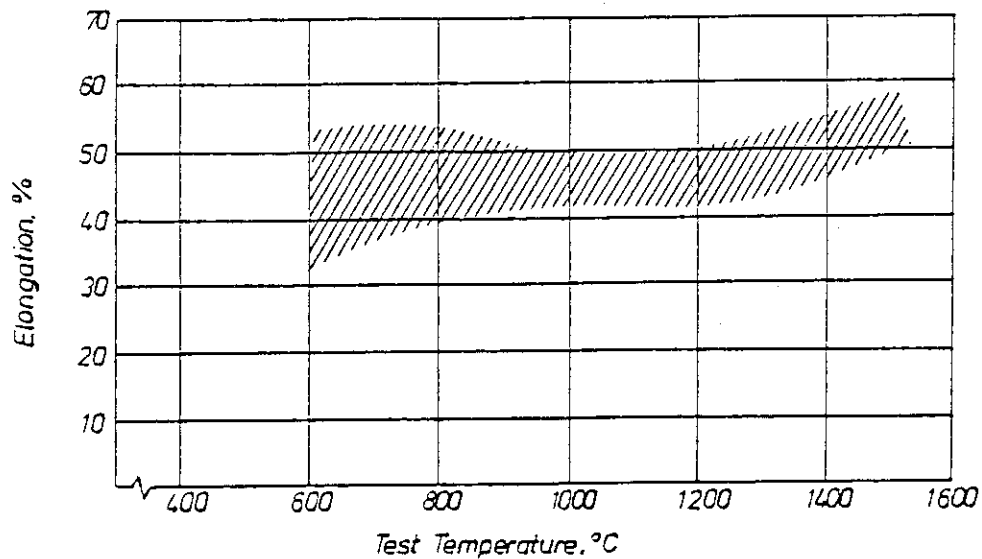


Fig. 4.10 : Elongation of recrystallized tungsten sheet in relation to the test temperature.

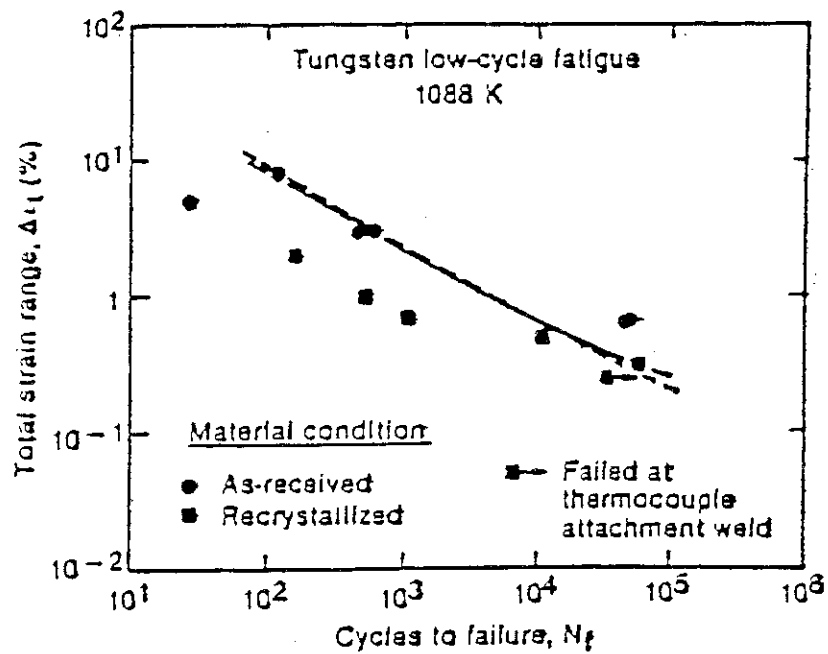
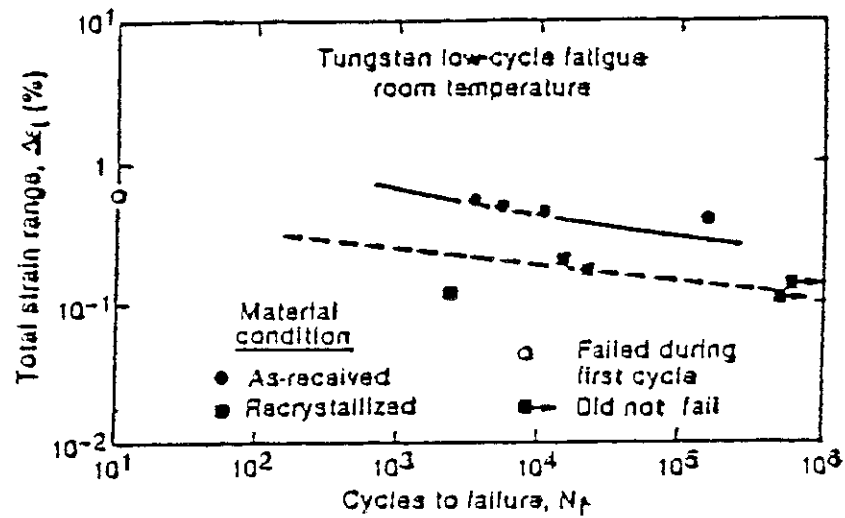


Fig. 4.11 Low cycle fatigue of cross rolled tungsten
R.E. Shmunk and G.E. Korth, "Tensile and
low-cycle fatigue measurements on cross-rolled
tungsten", J.Nucl.Mater. 103 & 104 (1981) 943

5. Fabrication

(1) Primary Fabrication

Process involved in transforming raw materials into consolidated forms doesn't leaves any special problems except for manufacture of heavy-section shell conductor material and neutron multiplier material. These are now designed to be made of 60 mm-thick beryllium plate which has no manufacture experience. Beryllium plate employed for shell conductor and neutron multiplier is required to be ductile from viewpoint of strain under operation.

Above-mentioned beryllium plate is feasible to be manufactured by the present hot pressing technique. However, it leaved some uncertainty and concern about its ductility.

It is supposed that such a heavy-section and ductile beryllium plate can be manufactured by Hot Isostatic Pressing technique which is considered one of new processes, and it should be confirmed by pilot production of such a plate.

(2) Secondary Fabrication

Transforming the products of primary fabrication into finished products consists of fabrication techniques such as plastic work, precise bending of breeder cooling tube, precise machining of blanket vessel and others.

Large machining center with adaptive control system, MD-NC system and CAD/CAM system, which have been recently applied in aircraft industry, is available to precise machining of large and thin-wall blanket vessel. The outline of these systems is explained as follows;

1) Adaptive Control System

Adaptive control system is very useful for machining of large thin-wall and complicated components, in which machining conditions is controlled by sensing.

2) MD-NC System

MD-NC system is available in case that machining is repeated for the works of same size and same dimension such as blanket vessel units. This system enables machining by numerical control using master dimensions.

3) CAD/CAM System

NC programming is so troublesome and annoying in numerically controlled machining of blanket vessel that many a manhour is needed for programming if done manually. CAD/CAM system is available in making programming tapes for numerical control from CAD drawing by computer.

(3) Bonding

Bonding of first wall, shell conductor, blanket vessel wall, breeder cooling tube and so on are respectively important technical points. And quality assurance of these bonded parts should be attached much importance to. New processes of these technical points are shown below.

1) Bonding of First Wall

It is required especially from stringent loading conditions to

consider both less deformation due to bonding and joining at low temperature. From this point of view, HIP method is potentially feasible enough to be applied to first wall bonding by large-size machine. This HIP method is grouped into "deformation welding" which is called "deformation diffusion welding". By this method, bonding is carried out at rather low temperature than by diffusion welding. It doesn't require precise machining for joint preparation. It should be considered that chromium oxide precipitation at the grain boundary is minimized.

2) Bonding of Blanket Vessel Wall

It is desired from viewpoint of less deformation resultant from welding that heat source of high energy density is applied to bonding of blanket vessel wall. And welding joint is not simple for blanket vessel wall bonding. From above-mentioned points of view, electron beam welding machine with multi-dimension path control system is considered to be one of effective element techniques.

3) Bonding and NDE of Breeder Cooling Tube Joint

Inner bore welding of butt joint between tube and tubesheet is most proper method to assure the integrity of welds. Pulse-TIG inner bore welding will be applied to this joint. NDE of the welds can be performed by small-size RI such as ^{170}Tm ($\phi 1\text{ mm}$) or micro-focus X-ray unit.

4) Bonding of divertor plates

Tungsten has been successfully joined to the copper heat sink by brazing, casting the copper onto the tungsten, and plasma spraying of tungsten. Nickel-based solder and silver-base solder have been used for the brazing. The brazing temperature is up to 950 C. The brazing process and the casting process require higher process temperatures which lead to the annealing of heat sink material.

The plasma spraying of tungsten on heat sink can keep at low temperature through the heat sink. This process will not cause the annealing of heat sink material. However, the strength of plasma sprayed tungsten appears to be critical.

The selection of reference bonding method is open, and R & D program is required.

6. Thermohydraulics and stress analysis

6.1 Divertor temperature and stress distribution

The parameters and materials used for temperature and stress calculations of the divertor plate are listed in Table 6.1. Two surface heat fluxes, 2 and 5 MW/m², and two tile thicknesses, 1 and 3 mm, and two different materials of heat sink, copper and copper alloy, have been considered in these calculations.

The thermo-mechanical analysis was also made for the case with the redeposited 316 stainless steel from the first wall. This case was considered because of the prediction that material eroded from the first wall by CX neutrals would be deposited on the divertor collector plates. The properties of the redeposited 316SS have been assumed to be the same one as the original 316SS, since there are no experimental data on the properties of redeposited material.

Three dimensional thermo-mechanical calculation were performed for the collector plate. The geometry used for the analysis is shown in Fig. 6.1.

Figure 6.2 and Fig. 6.3 show the maximum temperature and thermal stress variation with surface heat flux for the divertor plate with 1 mm thick tungsten tiles on copper heat sink. Figure 6.4 and Fig. 6.5 show the maximum temperature and thermal stress distribution with surface heat flux for the copper alloy heat sink.

Temperature and stress distributions in the divertor plate for the parameters listed in Table 6.1 are shown in Fig. 6.6 to Fig. 6.13. The maximum temperatures and stresses for two candidate heat sink materials are summarized in Table 6.2 to Table 6.5.

The brazing process of plasma side material on heat sink will cause the annealing of heat sink material. The allowable stresses of the annealed copper and copper alloy (Cu-0.6Be-2.5Co) are 120 and 180 MPa at 200 C, respectively. The calculated stresses exceed the ASME allowable stresses for the annealed copper and copper alloy. Therefore, the thermal stress will produce the plastic hysteresis in the brazed heat sink materials.

The plasma spraying of tungsten on heat sink can keep at low temperature through the heat sink. This process will not cause the annealing of heat sink materials. The copper and copper alloy have the high allowable stresses if these materials are not annealed. For the heat flux of 2 MW/m², the thermal stress of the heat sink does not exceed the allowable stress. The plasma spraying is preferred to the brazing from the standpoint of heat sink strength. However, the plasma sprayed tungsten is expected to exhibit the low tensile strength. The strength of tungsten appears to be critical for the plasma spraying.

The surface heat flux of 5 MW/m² causes the severe thermal stresses in the collector plate. The calculated stresses are not within acceptable limits for the brazing and plasma spraying designs. It is recommended that the high heat flux of 5 MW/m² is unacceptable because of the high thermal stress.

Temperature and stress distributions in the divertor plate for the case with redeposited stainless steel are shown in Fig. 6.14 to Fig. 6.15. Surface heat flux on plate is 2 MW/m² for all calculations. The maximum temperatures and stresses for the three plasma side materials are summarized in Table 6.6. The stresses in divertor plate are quite sensitive to the redeposition thicknesses of 316SS. The

stresses are increased as the redeposition thickness is increased. The redeposition of 2 mm of 316SS results in high stresses in the plasma side materials, and the redeposition of 4 mm of 316SS results in severe stresses in both plasma side materials and copper heat sink.

6.2 Limiter temperature and stress analysis

The parameters and materials used for temperature and stress calculations of the limiter plate are listed in Table 6.7. Thermo-mechanical analysis has been done for the top surface of the flat limiter. Two plasma side materials, beryllium and graphite, were considered in this analysis.

Three dimensional thermo-mechanical calculation were performed for the top surface of limiter plate. The geometry used for the analysis is shown in Fig. 6.16.

Temperature and stress distribution in the limiter plate for the two plasma side materials are shown in Fig. 6.17 to Fig. 6.20. The maximum temperatures and stresses for the two plasma side materials are summarized in Table 6.8 and Table 6.9. The maximum temperature in 20 mm thick beryllium tile is 651°C. The maximum temperature in 10 mm thick graphite tile is 609°C, and may be in the severe range of the chemical sputtering. The stress intensity in the copper heat sink is below the 3 Sm limit for all cases.

The sputtered first wall particles will deposit on the leading edge of the limiter plate. The redeposition from the 316SS first wall will cause the high stresses in the leading edge of the plate. The erosion/redeposition and the thermo-mechanical analysis for the leading edge should be made.

6.3 Alternative coolant for first wall, divertor and limiter

6.3.1 Thermal-hydraulic evaluation for helium-cooled first wall

Relatively low pressure and low temperature water has been chosen in the INTOR reference design as the coolant. This choice is considered to be reasonable, for temperature of the wall should be kept relatively low (<450°C), and no electricity will be generated in INTOR. Water has been used in many conventional plants and has good heat transport capacity. The choice of helium gas as coolant for first wall gives good neutronic performances, such as high tritium breeding ratio and high 14-MeV neutron transmission rate for testing. And detritiation from helium gas is relatively easier than from water coolant. Thermal-hydraulic performances of helium gas, however, are inferior to those of water. In this task, preliminary, thermal-hydraulic analysis has been carried out for helium-cooled first wall in INTOR, and the feasibility of helium-cooled first wall design in INTOR is discussed in this report.

(1) Conditions for analysis

First wall configuration discussed in this report is shown in Fig. 6.21. Material of the wall is type 316 stainless steel. Plasma side of the wall is the armor zone for erosion during the reactor life. Grooved armor was chosen to reduce thermal stress within the wall. Coolant in rectangular channels behind the armor zone flows in poloidal direction. Structurally, the first wall is separated from the blanket vessel from the view points of blanket vessel integrity and maintainability of the first wall when it would be damaged. The

wall is supported from the blanket vessel by hook-shaped support structures.

Model for the analysis is shown in Fig. 6.22. The thickness of the plasma side wall and the height of the coolant channel were represented by "t" and "h", respectively. In this analysis, the surface heat load and the heat deposited in the wall were assumed to be transported to the coolant through only the plasma side surface of the coolant channel.

The heat load conditions of the INTOR first wall are summarized in Table 6.10. Poloidal divertor option and pump limiter option are considered as impurity control systems in INTOR design. The poloidal divertor option was assumed to be chosen for the impurity control system in INTOR. This table shows that the heat flux through the coolant channel surface is about 29 W/cm^2 for both inboard and outboard first wall.

The density of gaseous coolants such as helium will remarkably change with pressure. Although helium has better thermal-hydraulic performances in high pressure, lower pressure is desirable from the structural view points of the first wall and reactor cooling systems. Coolant pressure was chosen as a parameter in this analysis, therefore, and changed from 1 MPa to 7 MPa. Low coolant inlet temperature is desirable to keep the wall temperature low and to get good heat transport performances. A value of 100°C was chosen as coolant inlet temperature considering the cooling systems design. Coolant temperature rise should be chosen as small as possible to keep the wall temperature low enough, otherwise large temperature rise is required to reduce coolant velocity and pressure losses. Therefore, outlet temperature was changed from 150°C to 300°C in this study.

Coolant flow area was also chosen as a parameter, and the height of coolant channel was changed from 3 mm to 15 mm. From the view points of structural integrity and the wall temperature limitation, small value of the channel height should be chosen, but large one is required to keep the pressure loss acceptably low.

A length of 5 m was assumed as the coolant channel length of first wall. A value of 0.03 was used as friction factor in this analysis in consideration of roughness on the coolant channel surface.

Table 6.11 shows the conditions used in this study. A parametric study for helium-cooled INTOR first wall has been carried out with these conditions.

(2) Results of study

1) Temperature rise within the first wall

Figure 6.23 shows the temperature rise within the first wall. This figure indicates that the temperature rise within outboard first wall is 136°C and that within inboard first wall is 151°C .

2) Maximum temperature of the first wall

Maximum temperature of the first wall can be estimated by adding this temperature rise within wall (151°C) to film temperature drop and coolant outlet temperature. Obtained results are shown in Figs. 6.24~6.27. It is required to keep the maximum temperature of the first wall lower than 450°C in INTOR. Problem about thermal stress does not occur, because the stress is relieved by grooving.

3) Coolant velocity

Excessive coolant velocity will cause a problem of vibration. In this study, it is assumed that the coolant velocity should be kept

less than 100 m/s. Results about coolant velocity are also shown in Figs. 6.24 ~ 6.27.

4) Pressure loss

Only friction loss in the coolant channel of the first wall is considered as pressure loss in this analysis. Figs. 6.24 ~ 6.27 show the results. Pressure losses in inlet and outlet headers etc. should be considered in detail, however, a value of 0.3 MPa is assumed as the limit of friction loss in the channel of the first wall in this study.

(3) Discussions and conclusions

Acceptable design ranges according to the results of preliminary analysis and the limits of thermal-hydraulic performance described above are shown in Figs. 6.28 ~ 6.31. These figures indicate that no acceptable ranges exist for coolant pressure less than 1 MPa. When coolant pressure is higher than 3 MPa, helium-cooled first wall can be designed, and the higher coolant pressure brings the larger acceptable design range. The effect of coolant velocity on coolant pressure is considerably large.

Low pressure and narrow coolant channel should be chosen for the structural integrity of the wall. It is considered, therefore, that the following conditions are appropriate.

- i) Coolant pressure ~3 MPa
- ii) Height of coolant channel ~8 mm
- iii) Coolant outlet temperature ~220 °C
- iv) Coolant inlet temperature ~100 °C

This analysis revealed that the design of first wall with helium gas as coolant can be practicable from the thermal-hydraulic view points. Detail investigation is required to adopt helium-cooled first wall for INTOR.

Heat load to the divertor (or limiter) plates is about ten times as large as that to the first wall. It is considered, therefore, that helium cooling for the divertor (or limiter) is difficult.

6.3.2 Comparison of the performances of water-cooled and helium-cooled first wall

The performances of helium-cooled first wall described in the previous section are compared with those of water-cooled first wall. Neutronic performances and effects on coolant detritiation systems are also discussed qualitatively. Results of this investigation are summarized in Table 6.12. The concept of water-cooled first wall discussed here is that suggested in Japanese contribution to INTOR Phase I.

Helium-cooled first wall is inferior to water-cooled first wall from the view point of structural integrity, since helium gas as coolant requires higher pressure and larger temperature rise than water. Therefore, countermeasures of stresses due to these causes should be required.

Thermal-hydraulic performances are expected to be satisfactory for both helium-cooled and water-cooled first wall. Helium-cooled first wall, however, is suffered severer conditions. The largest problems of helium-cooled first wall is large pumping power. In this investigation, the power needed to pumping helium gas is between 10 to 20 percents of thermal power of first wall.

Tritium breeding ratio and 14-MeV neutron transmission rate for material testing of helium-cooled first wall are higher than those of

water-cooled first wall.

Capital cost of detritiation systems for helium coolant is expected to be lower than that for water. More tritium release, however, may occur from helium coolant system due to more coolant leakage and higher temperature than water coolant system.

Further investigation is required to select the coolant for first wall, in consideration with total reactor design.

Table 6.1 Parameters and materials used for temperature and stress calculations of the divertor plate with tungsten tiles

Surface heat flux	2, 5 MW/m ²
Nuclear heating rate	
W	19 MW/m ³
Cu	10 MW/m ³
316SS	8 MW/m ³
Coolant temperature	
Inlet/Outlet	50/80°C
Coolant velocity	7 m/s
Heat transfer coefficient	3.2×10^4 W/m ² °C
Interface conductance	Infinite
Tile thickness (W)	1, 3 mm
Heat sink material	
Material	Cu, Cu-0.6Be-2.5Co
Thickness	20 mm
Support structure thickness (316SS)	20 mm

Table 6.2 Temperature and thermal stress of divertor plate with 1 mm thick tungsten tile (Heat flux = 2 MW/m²)

<u>Plasma side cladding</u>		
Material	W	
Allowable stress, 3Sm (MPa)	800 ⁽¹⁾	
<u>Heat sink</u>		
Material	OFCu	Cu-0.6Be-2.5Co
Allowable stress, 3Sm (MPa)		
As received	250	780
Annealed ⁽²⁾	120	180
<u>Maximum temperature</u>		
Plasma side cladding (°C)	194	228
Heat sink (°C)	178	214
<u>Maximum stress intensity</u>		
Plasma side cladding (MPa)	292	468
Heat sink (MPa)	227	381

(1) Value at 730°C

(2) Values at 200°C after annealing (850°C × 30 min)

Table 6.3 Temperature and thermal stress of divertor plate with 1 mm thick tungsten tile (Heat flux = 5 MW/m²)

<u>Plasma side cladding</u>		
Material	W	
Allowable stress, 3Sm (MPa)	800 ⁽¹⁾	
<u>Heat sink</u>		
Material	OFCu	Cu-0.6Be-2.5Co
Allowable stress, 3Sm (MPa)		
As received	250	780
Annealed ⁽²⁾	120	180
<u>Maximum temperature</u>		
Plasma side cladding (°C)	352	438
Heat sink (°C)	317	403
<u>Maximum stress intensity</u>		
Plasma side cladding (MPa)	695	981
Heat sink (MPa)	534	813

(1) Value at 730°C

(2) Values at 200°C after annealing (850°C × 30 min)

Table 6.4 Temperature and thermal stress of divertor plate with 3 mm thick tungsten tile (Heat flux = 2 MW/m²)

<u>Plasma side cladding</u>		
Material	W	
Allowable stress, 3Sm (MPa)	800 ⁽¹⁾	
<u>Heat sink</u>		
Material	OFCu	Cu-0.6Be-2.5Co
Allowable stress, 3Sm (MPa)		
As received	250	780
Annealed ⁽²⁾	120	180
<u>Maximum temperature</u>		
Plasma side cladding (°C)	223	258
Heat sink (°C)	181	216
<u>Maximum stress intensity</u>		
Plasma side cladding (MPa)	295	382
Heat sink (MPa)	300	426

(1) Value at 730°C

(2) Values at 200°C after annealing (850°C × 30 min)

Table 6.5 Temperature and thermal stress of divertor plate with 3 mm thick tungsten tile (Heat flux = 5 MW/m²)

<u>Plasma side cladding</u>			
Material		W	
Allowable stress, 3Sm (MPa)		800 ⁽¹⁾	
<u>Heat sink</u>			
Material		OFCU	Cu-0.6Be-2.5Co
Allowable stress, 3Sm (MPa)			
As received		250	780
Annealed ⁽²⁾		120	180
<u>Maximum temperature</u>			
Plasma side cladding	(°C)	424	509
Heat sink	(°C)	318	405
<u>Maximum stress intensity</u>			
Plasma side cladding	(MPa)	588	795
Heat sink	(MPa)	585	898

(1) Value at 730°C

(2) Values at 200°C after annealing (850°C × 30 min)

Table 6.6 Temperature and thermal stress of divertor plate with 1 mm thick tungsten tile on copper heat sink (Heat flux = 2 MW/m²)

		No erosion(1)	Redeposition of 316SS	
			2 mm(2)	4 mm(3)
<u>Plasma side cladding</u>				
Material			W	
Allowable stress, 3Sm	(MPa)		800(4)	
<u>Heat sink</u>				
Material			OFCu	
Allowable stress, 3Sm	(MPa)			
As received			250	
Annealed			120	
<u>Maximum temperature</u>				
Redeposited layer	(C°)	—	424	656
Plasma side claddeing	(C°)	194	195	195
Heat sink	(C°)	178	178	181
<u>Maximum stress intensity</u>				
Redeposited layer	(MPa)	—	665	555
Plasma side cladding	(MPa)	292	856	1460
Heat sink	(MPa)	227	255	639

(1) No net erosion of surface material

(2) Redeposition of 2 mm of 316SS from the first wall

(3) Redeposition of 4 mm of 316SS from the first wall

(4) Value at 730°C

Table 6.7 Parameters and materials used for temperature and stress calculations of the limiter plate

Surface heat flux	(MW/m ²)	3
Nuclear heating rate		
Plasma side cladding	(MW/m ³)	8
Heat sink (Cu)	(MW/m ³)	15
Support structure (SS)	(MW/m ³)	12
Coolant temperature		
Inlet/outlet	(°C)	50/80
Coolant velocity	(m/s)	7
Heat transfer coefficient	(W/m ² °C)	3.4×10^4
Plasma side cladding		
Material	Be	C
Thickness	(mm) 10,20	5,10
Heat sink thickness (Cu)	(mm)	10
Support structure thickness (SS)	(mm)	40

Note: Heat flux of top surface

Table 6.8 Temperature and thermal stress of limiter plate with beryllium tile on copper heat sink
(Heat flux = 3 MW/m²)

Plasma side cladding			
Material		Be	
Thickness	(mm)	10	20
Allowable stress, 3Sm	(MPa)	300	
Heat sink			
Material		OFCu	
Allowable stress, 3Sm	(MPa)	120	
Maximum temperature			
Plasma side cladding	(°C)	409	651
Heat sink	(°C)	176	179
Maximum stress intensity			
Plasma side cladding	(MPa)	200	215
Heat sink	(MPa)	97	106

Table 6.9 Temperature and thermal stress of limiter plate with graphite tile on copper heat sink
(Heat flux = 3 MW/m²)

Plasma side cladding			
Material		C	
Thickness	(mm)	5	10
Allowable stress, 3Sm	(MPa)	20	
Heat sink			
Material		OFCu	
Allowable stress, 3Sm	(MPa)	120	
Maximum temperature			
Plasma side cladding	(°C)	390	609
Heat sink	(°C)	175	176
Maximum stress intensity			
Plasma side cladding	(MPa)	20	20
Heat sink	(MPa)	60	60

Table 6.10 Heat Load Conditions of INTOR First Wall
- Divertor Option -

	OUTBOARD	INBOARD
Surface Heat	13.6 W/cm ²	11.6 W/cm ²
Volumetric Heat	13 W/cm ³	13 W/cm ³
Wall Thickness	11.7 mm	13.5 mm
Heat Flux to Coolant Channel	28.8 W/cm ²	29.2 W/cm ²

Table 6.11 Conditions for Parametric Survey
of Helium Cooling

Type of First Wall	Grooved Separated Wall (see Fig. 9.6.3-1) Infinite plate was assumed in this analysis. (see Fig. 9.6.3-2)
Material of First Wall	Type 316 Stainless Steel
Thermal conductivity	18.2 W/mK
Coolant	Helium Gas
Pressure	1 - 7 MPa
Inlet Temperature	100 °C
Outlet Temperature	150 - 300 °C
Coolant Channel Width	3.0 - 15.0 mm
Coolant Channel Length	5 m
Heat Flux to Coolant	2.9×10^5 W/m ²
Friction Factor	0.03

Table 6.12 Comparison of the Performances of Water-cooled and Helium-cooled First Wall

Coolant	water	helium
Pressure	1 MPa	3 MPa
Inlet/outlet Temperature	50/90 °C	100/220 °C
Structural Material	type 316 SS	type 316 SS
Maximum Temperature of First Wall	< 450°C (~360°C)	< 450°C
Coolant Velocity	≤ 6 m/s	≤ 100 m/s
Pressure Losses	~0.3 MPa	~0.2 MPa
Pumping Power	~0.2 MW	~16 MW
Tritium Breeding Ratio	relatively low	relatively high
14-MeV Neutron Transmission Rate	low	high
Coolant Detritiation Systems (Capital Cost)	high	low
Tritium Release from Coolant Systems	low(?)	high(?)

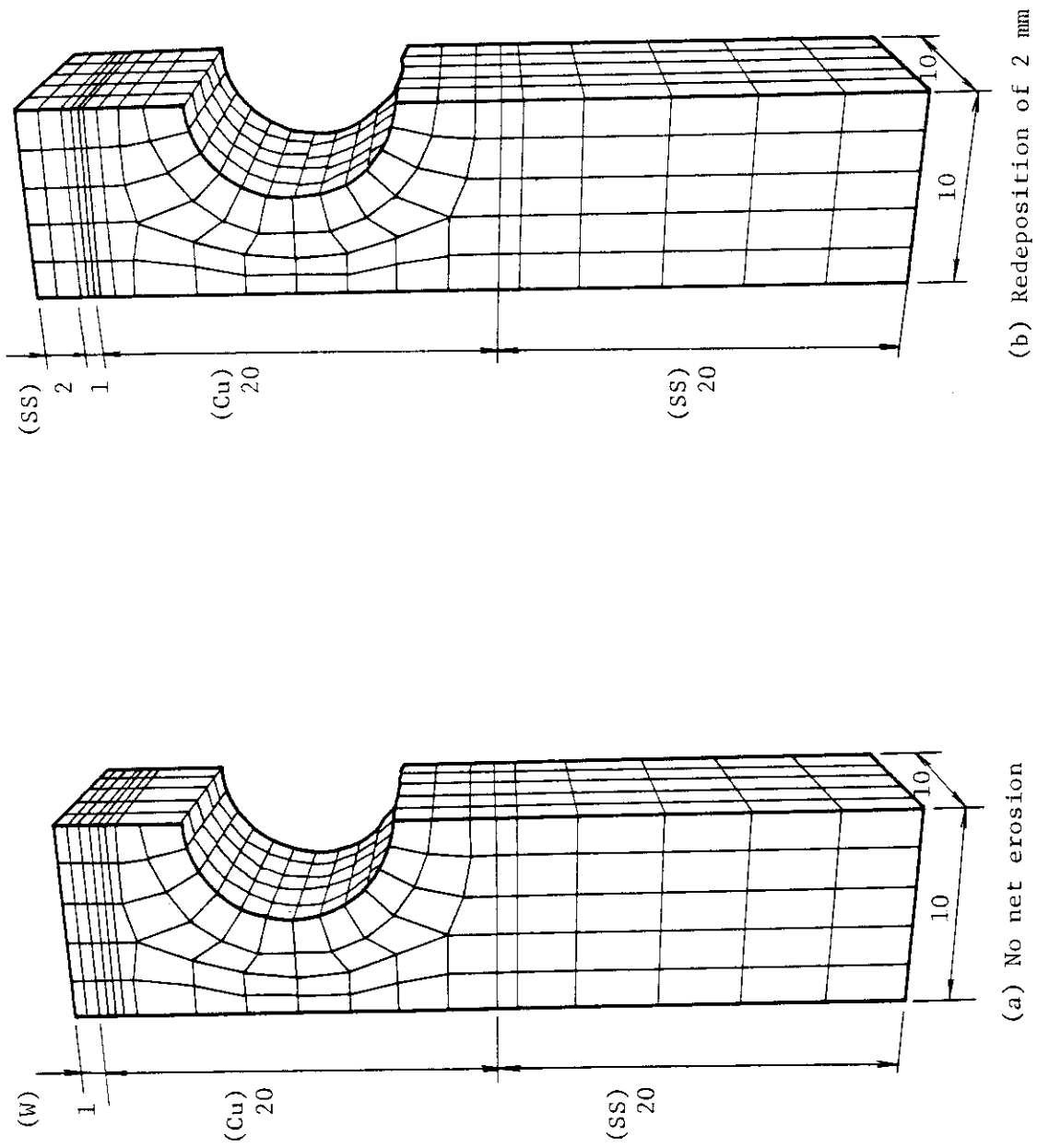


Fig. 6.1 Geometry used for thermal hydraulics and stress analysis
(Divertor plate with tungsten tile on copper heat sink)

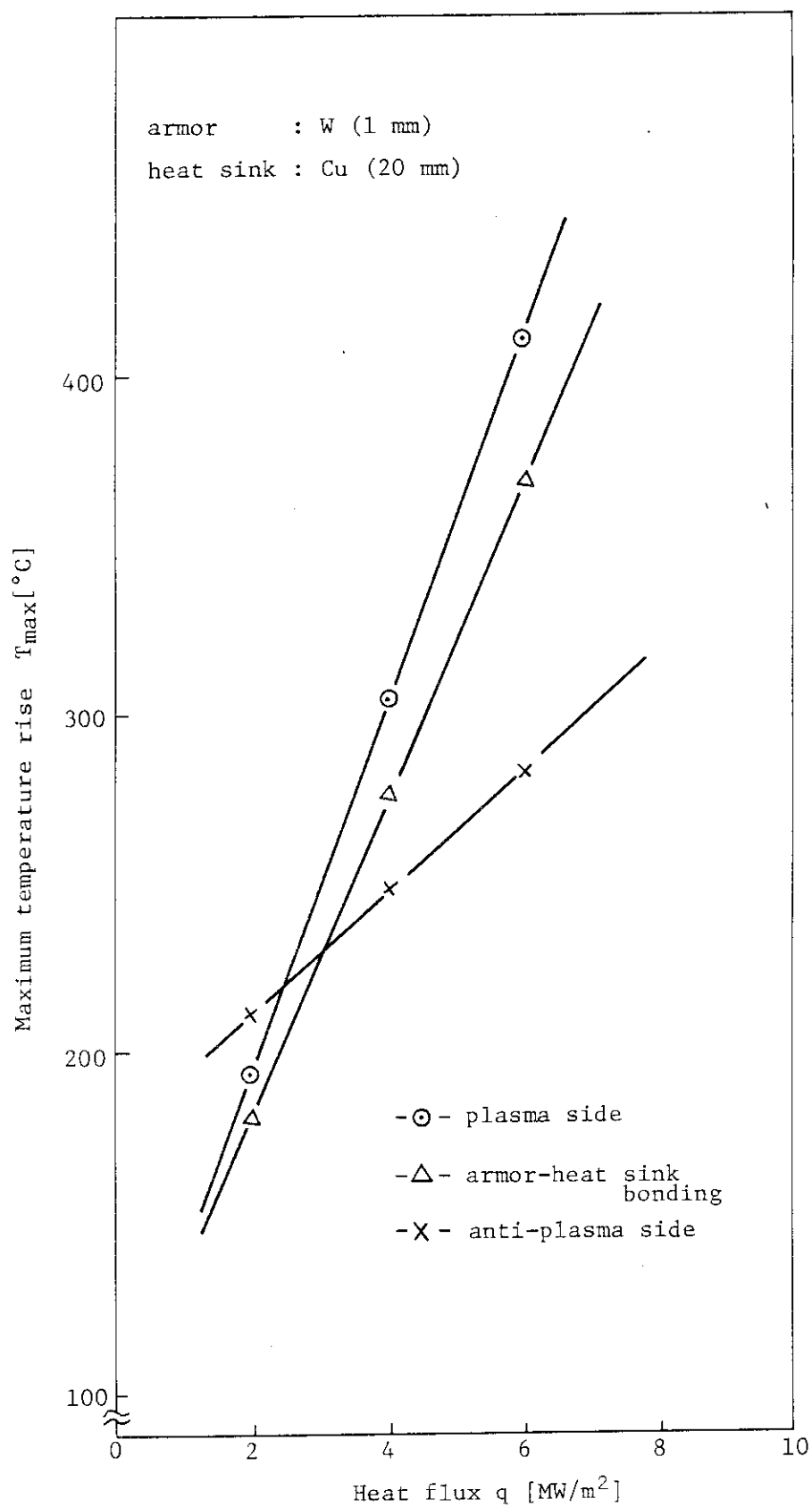


Fig. 6.2 Maximum temperature of divertor plate with copper heat sink

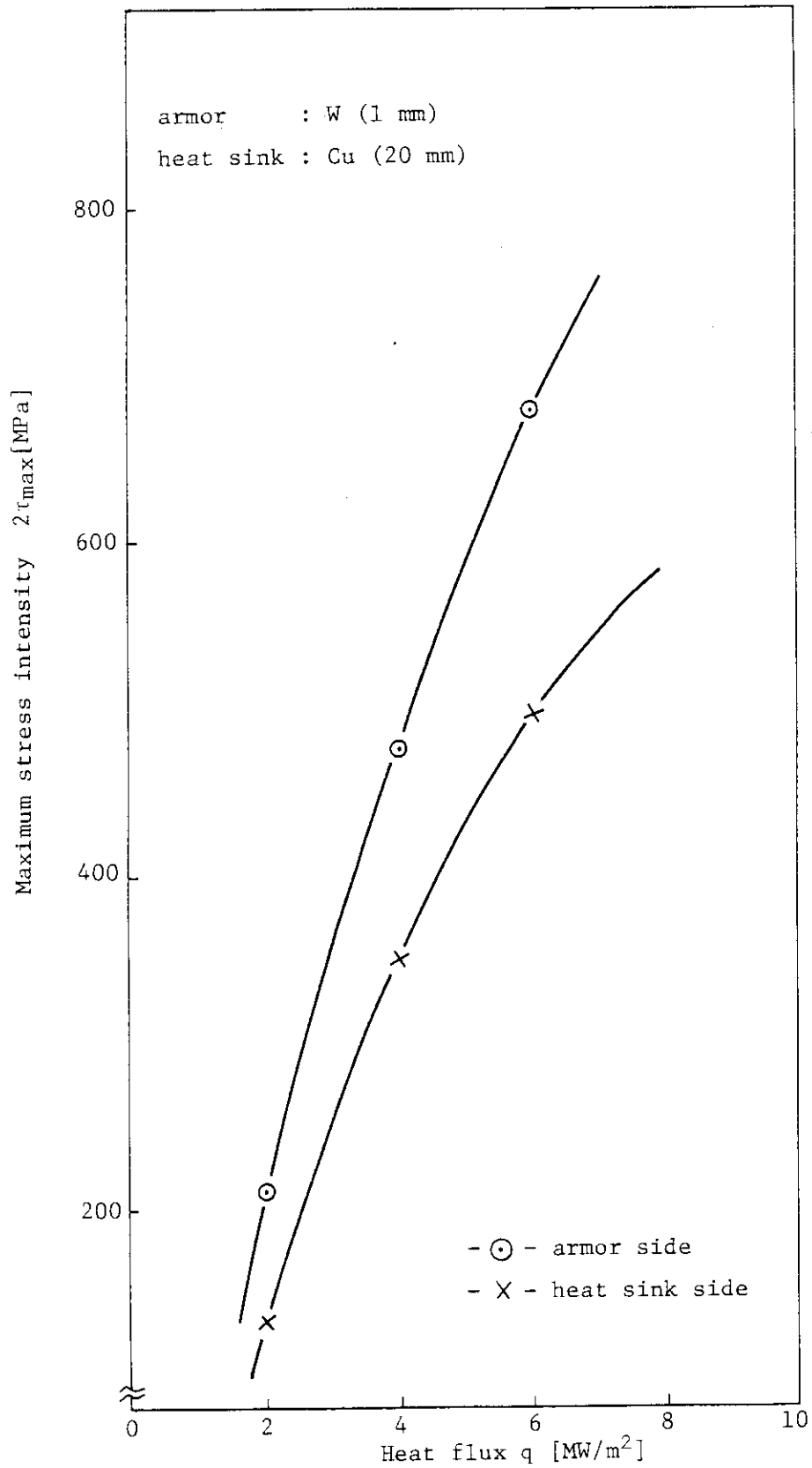


Fig. 6.3 Maximum thermal stress of divertor plate with copper heat sink

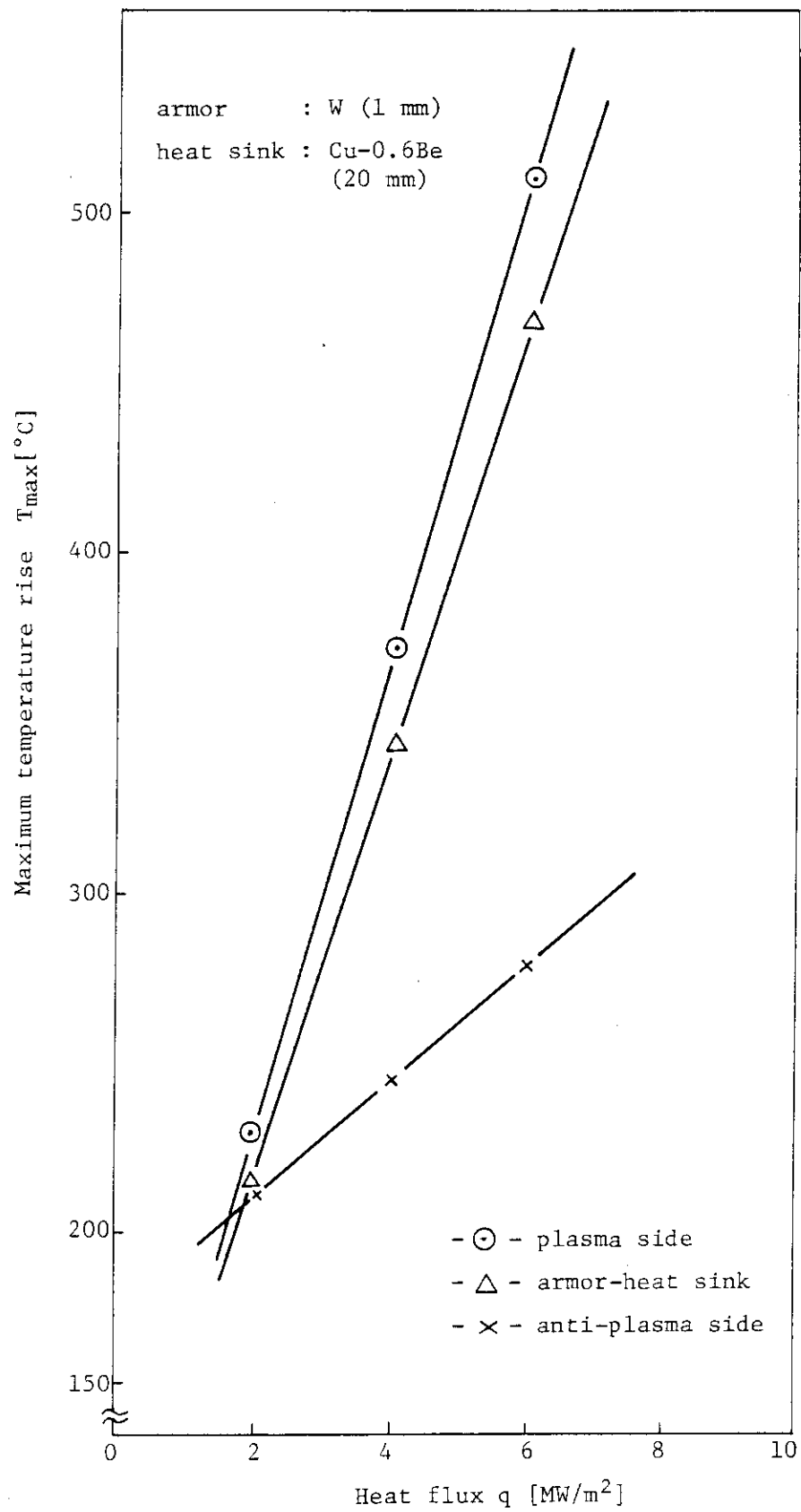


Fig. 6.4 Maximum temperature of divertor plate with copper alloy heat sink

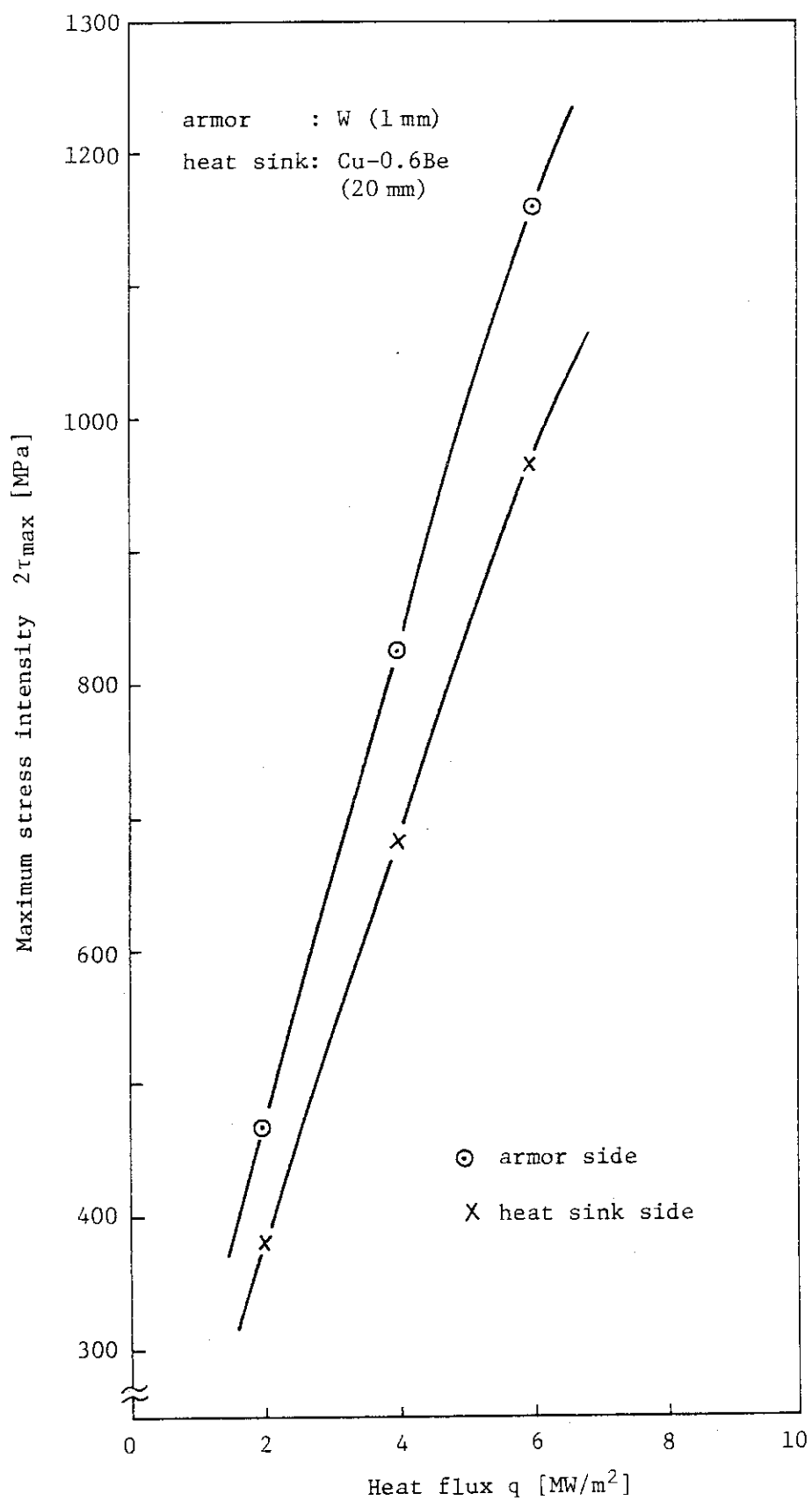
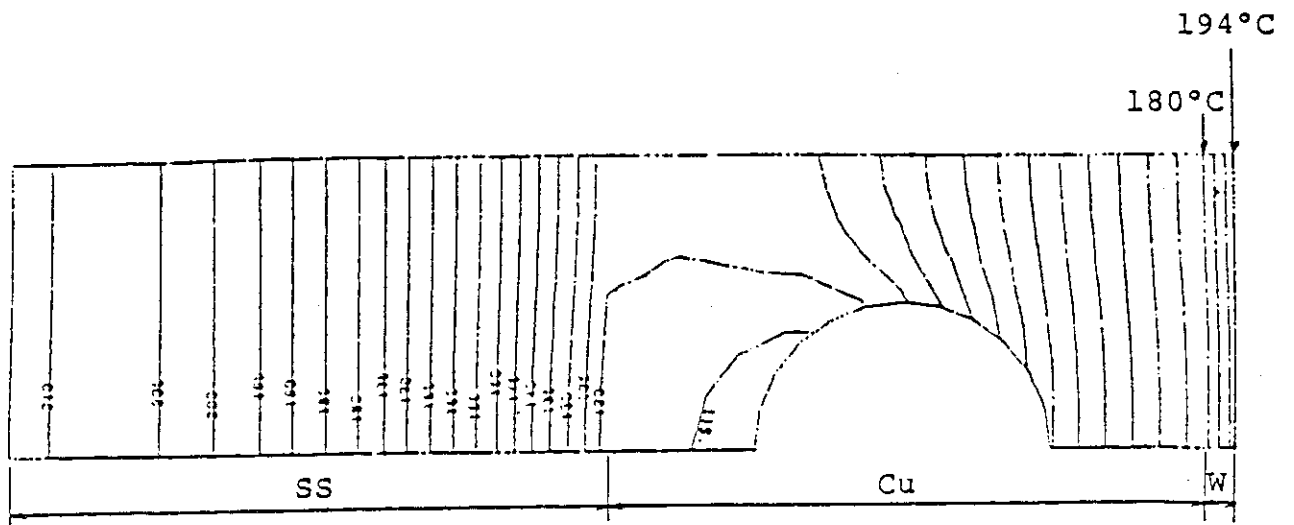
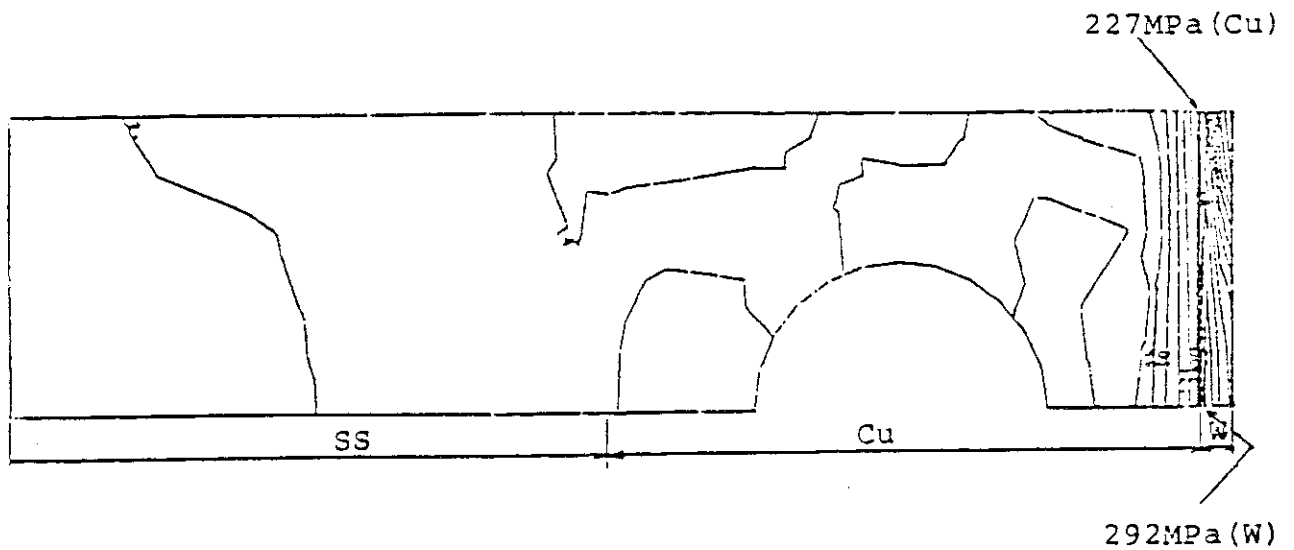


Fig. 6.5 Maximum thermal stress of divertor plate with Cu-0.6Be heat sink

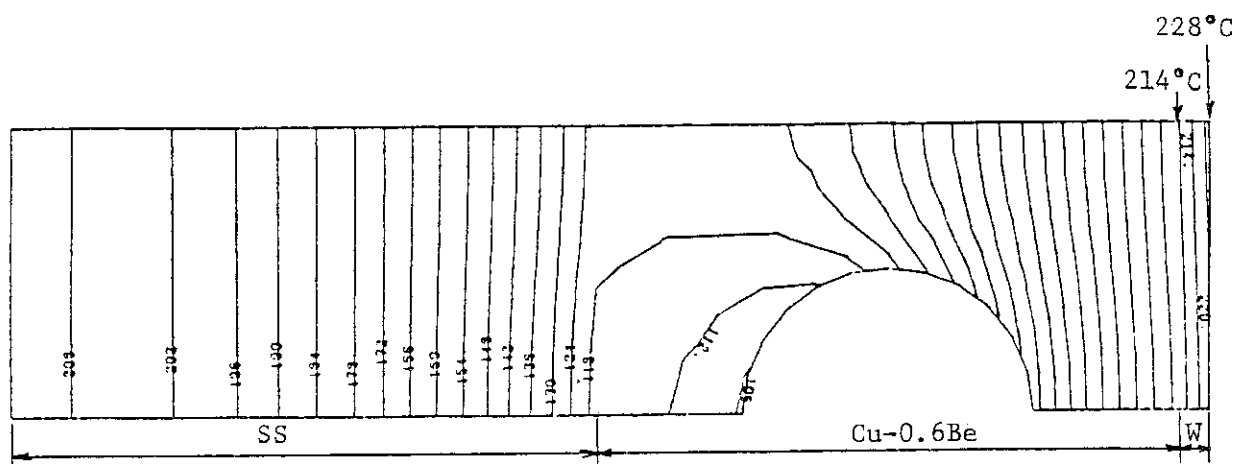


(a) Temperature distribution

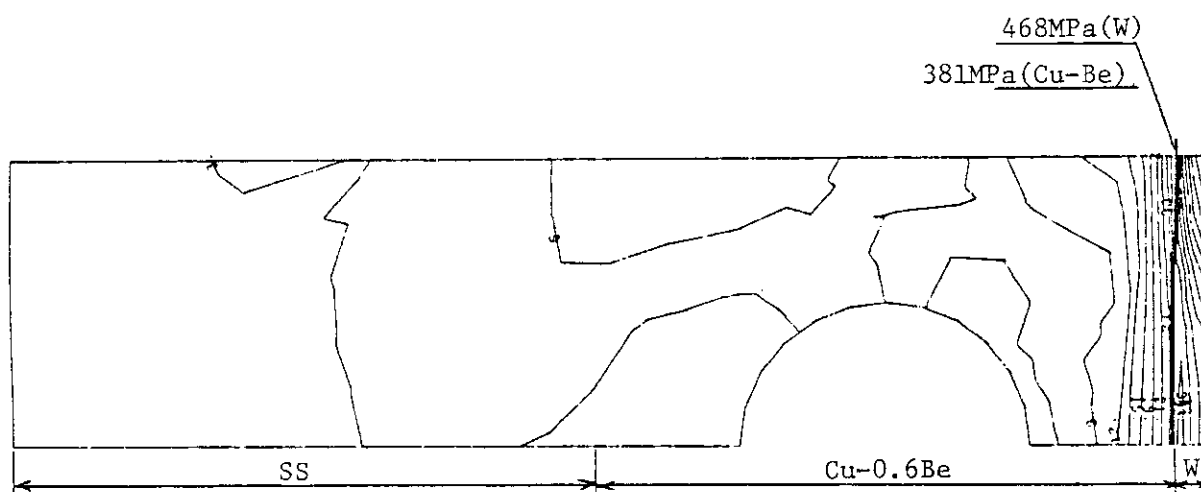


(b) Stress intensity (2τ) distribution

Fig. 6.6 Temperature and stress distribution of divertor plate with 1 mm thick tungsten tile on copper heat sink

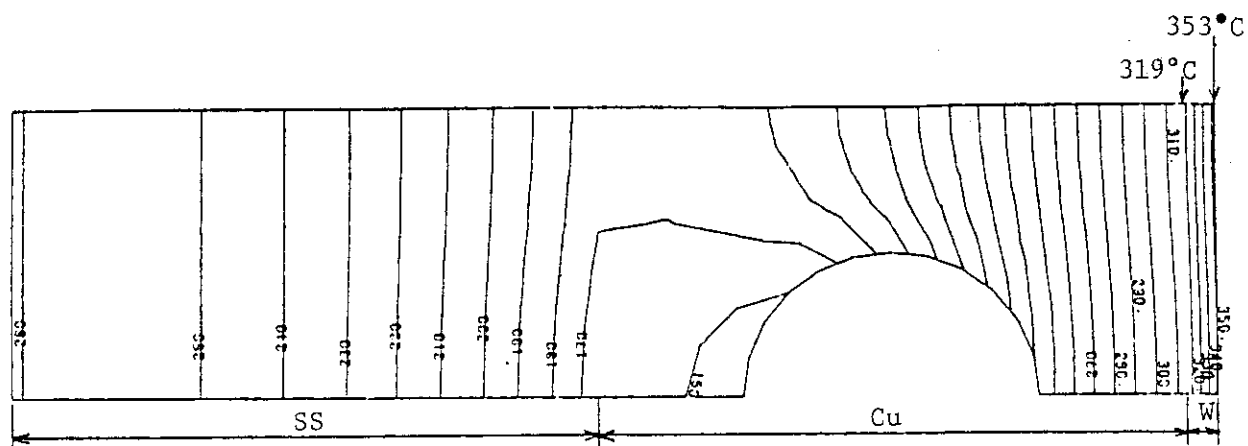


(a) Temperature distribution

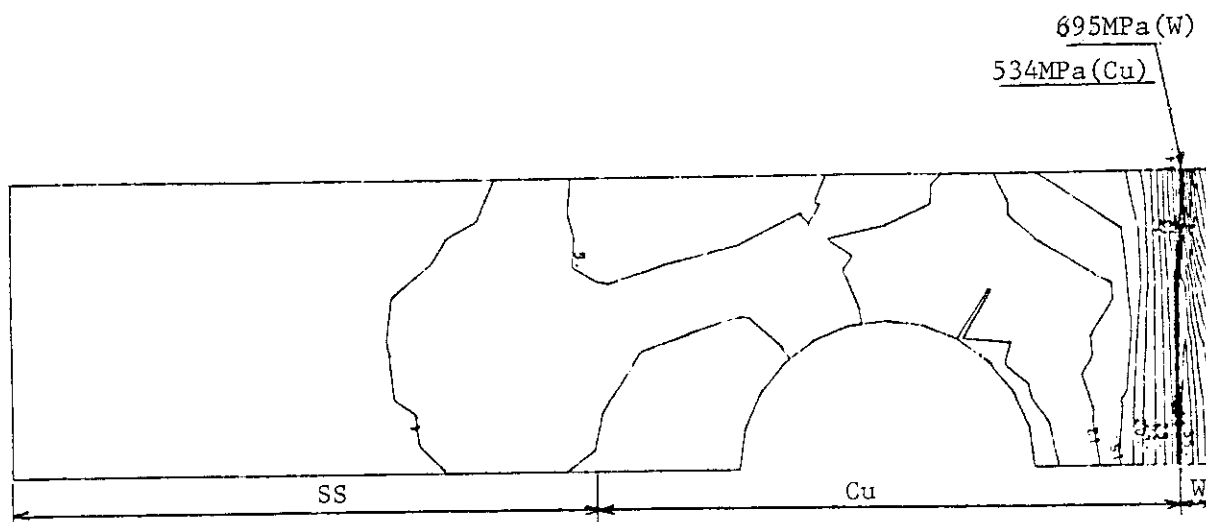


(b) Stress intensity (2τ) distribution

Fig. 6.7 Temperature and stress distribution of divertor plate with 1 mm thick tungsten tile on Cu-0.6Be heat sink (Heat flux = 2 MW/m^2)

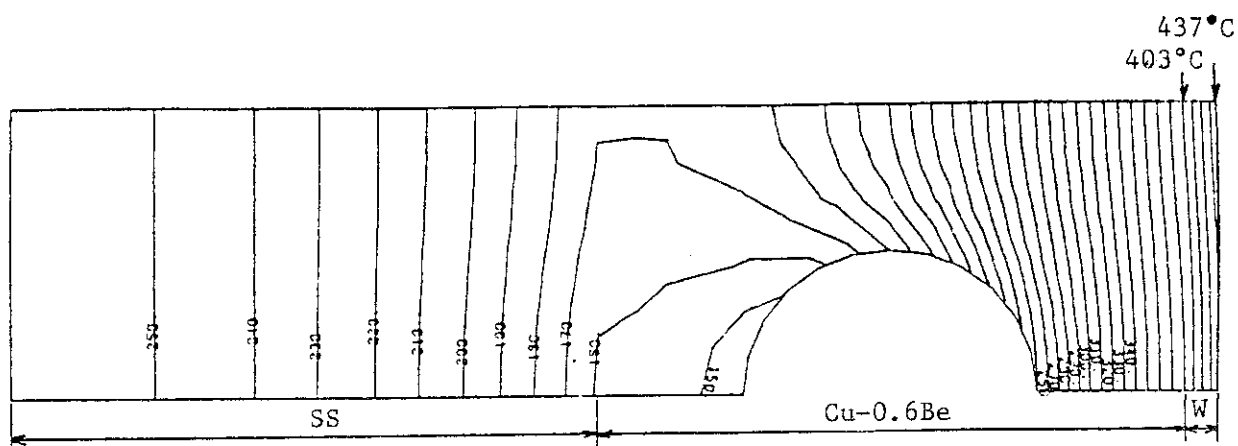


(a) Temperature distribution

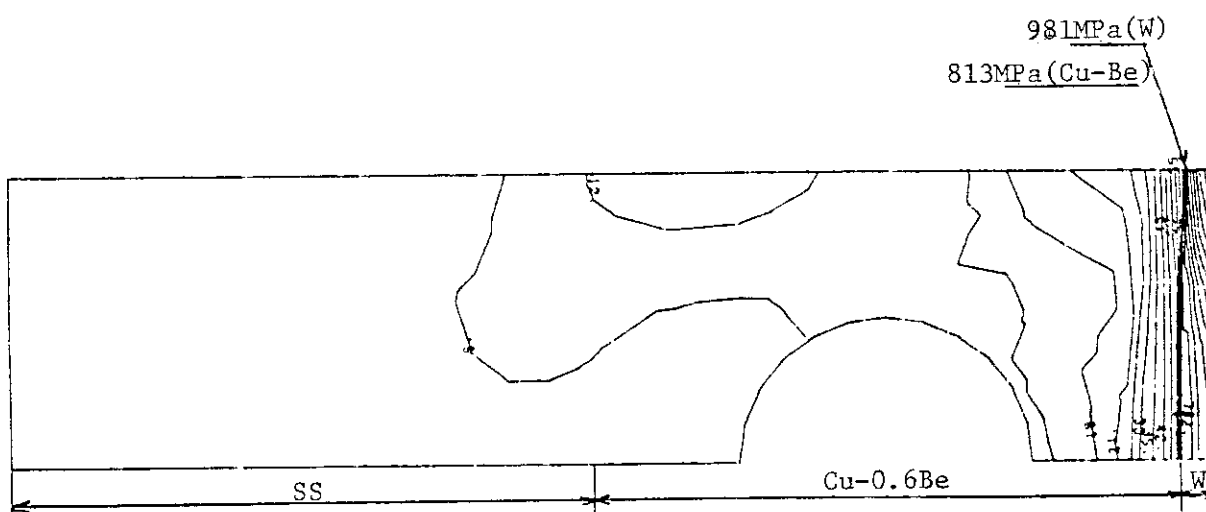


(b) Stress intensity (2τ) distribution

Fig. 6.8 Temperature and stress distribution of divertor plate with 1 mm thick tungsten tile on Cu heat sink (Heat flux = 5 MW/m^2)

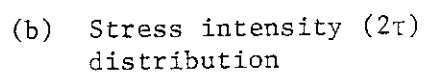
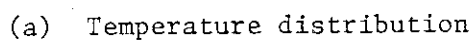


(a) Temperature distribution

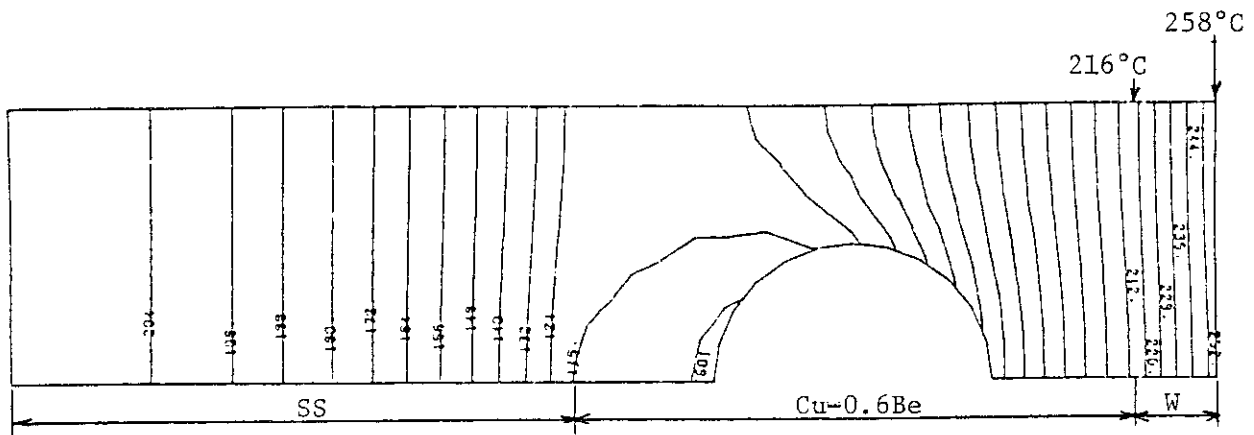


(b) Stress intensity (2τ) distribution

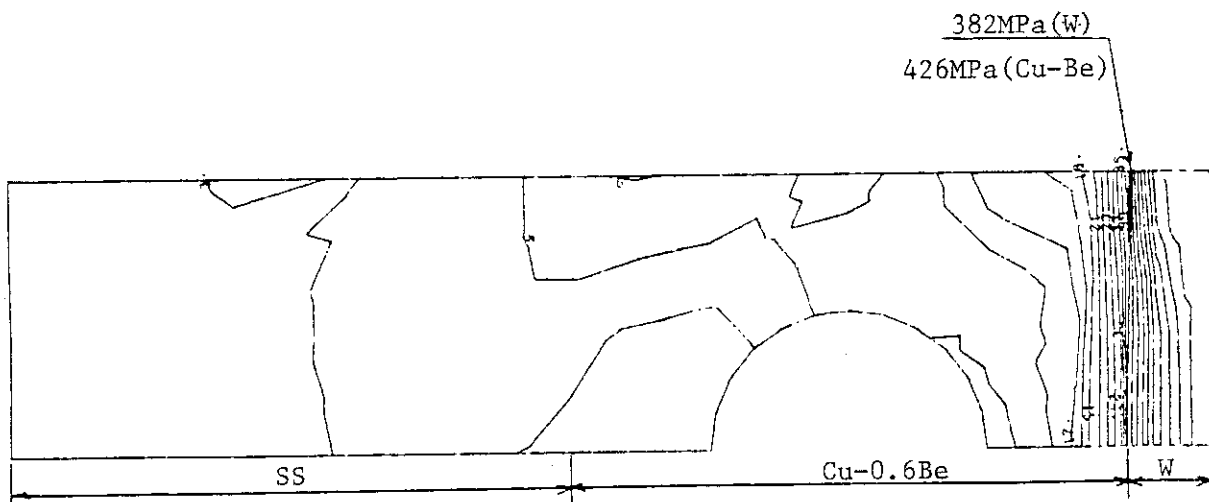
Fig. 6.9 Temperature and stress distribution of divertor plate with 1 mm thick tungsten tile on Cu-0.6Be heat sink (Heat flux = 5 MW/m^2)



(Heat flux = 2 MW/m^2)

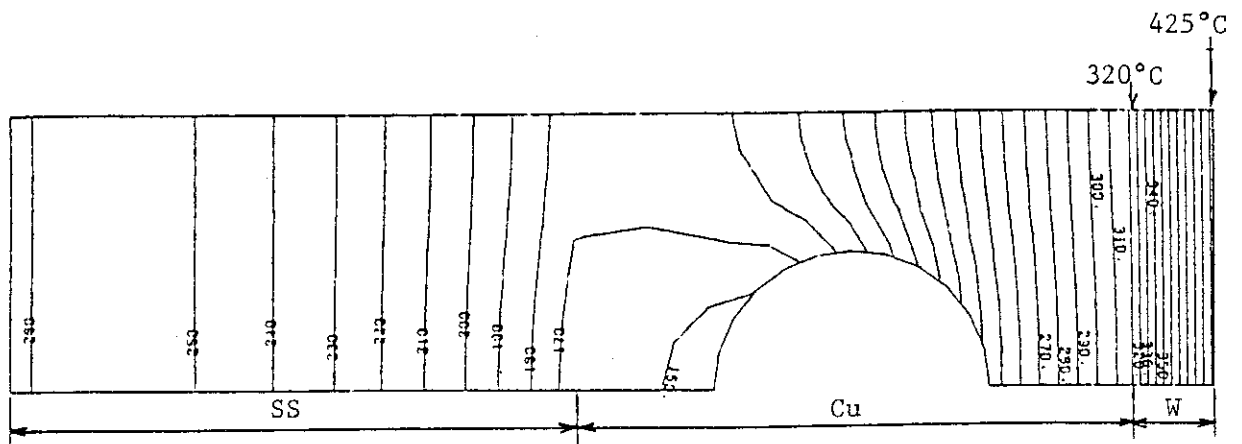


(a) Temperature distribution

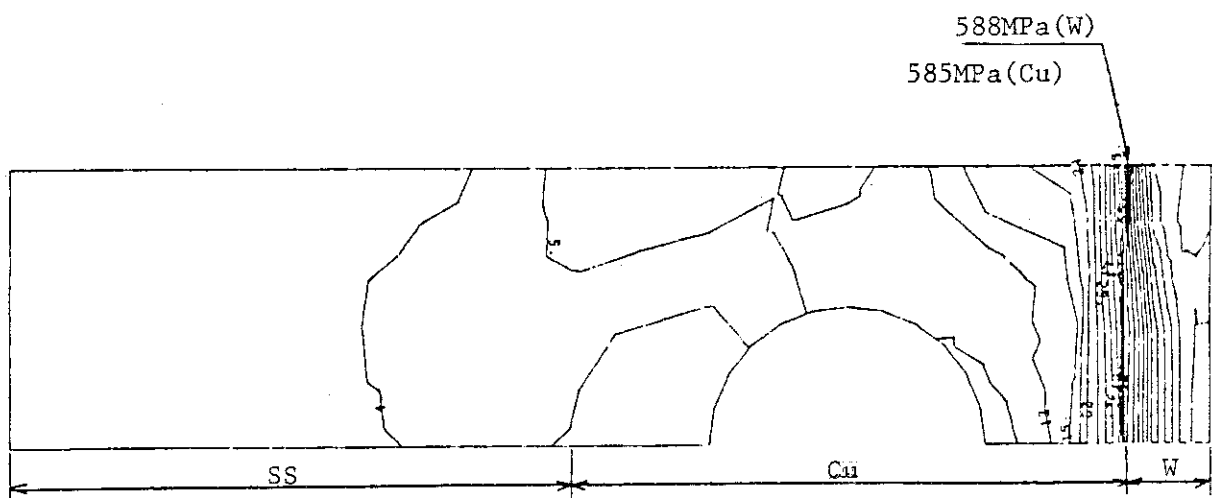


(b) Stress intensity (2τ) distribution

Fig. 6.11 Temperature and stress distribution of divertor plate with 3 mm thick tungsten tile on Cu-0.6Be heat sink (Heat flux = 2 MW/m^2)

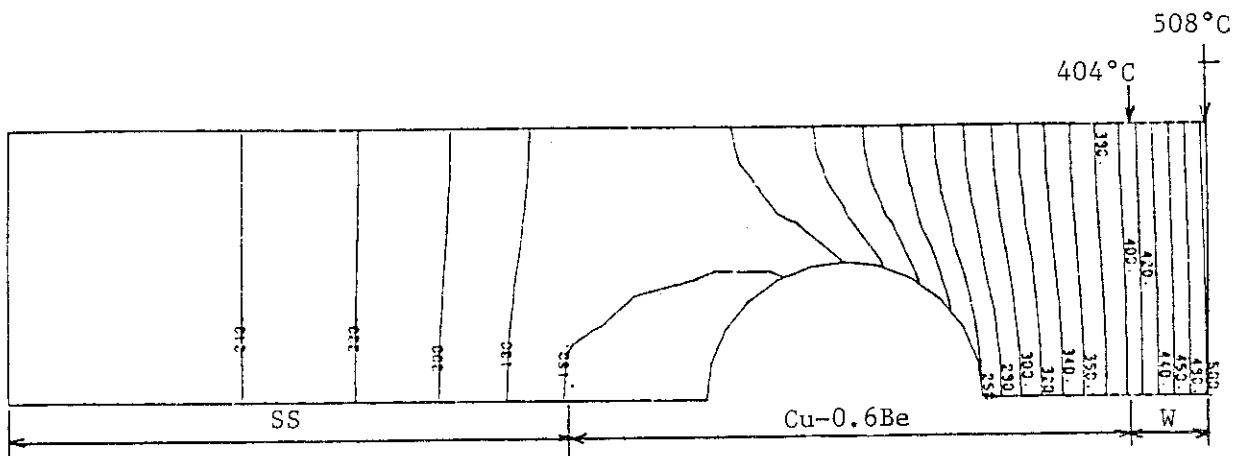


(a) Temperature distribution

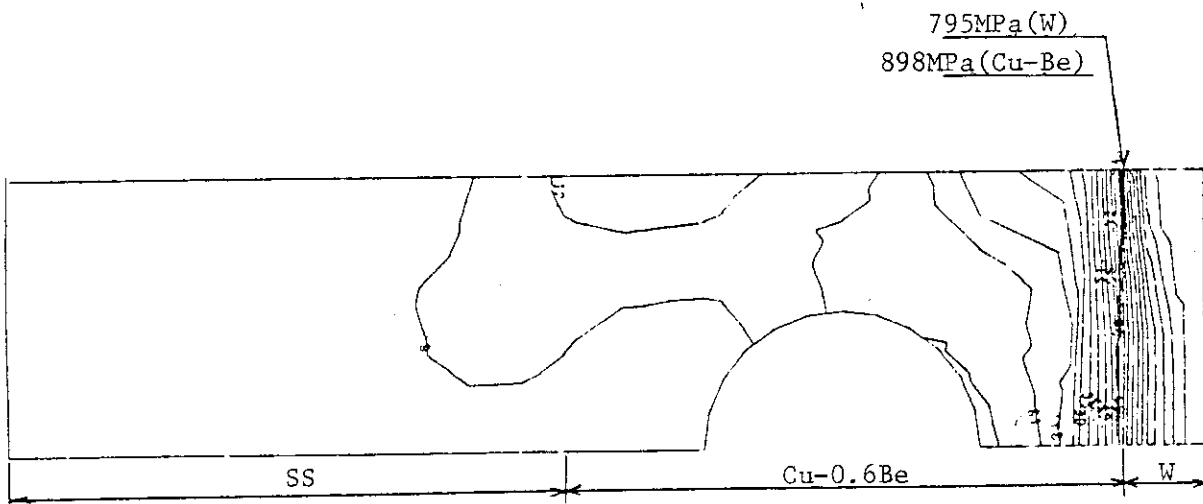


(b) Stress intensity (2τ) distribution

Fig. 6.12 Temperature and stress distribution of divertor plate with 3 mm thick tungsten tile on Cu heat sink (Heat flux = 5 MW/m^2)



(a) Temperature distribution



(b) Stress intensity (2τ) distribution

Fig. 6.13 Temperature and stress distribution of divertor plate with 3 mm thick tungsten tile on Cu-0.6Be heat sink (Heat flux = 5 MW/m²)

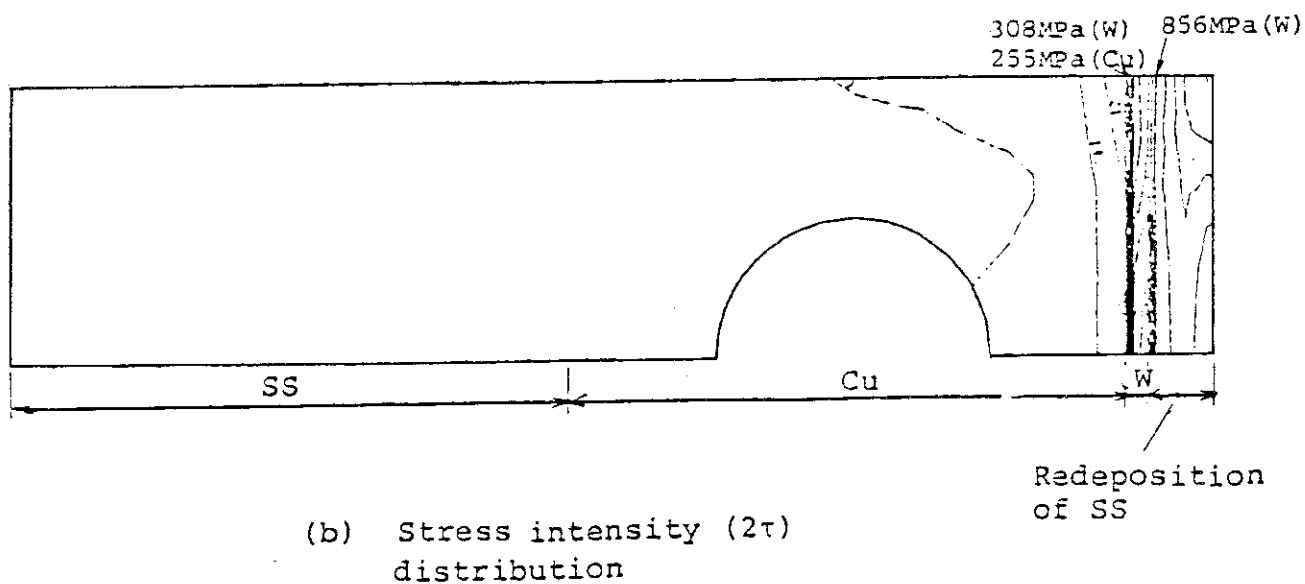
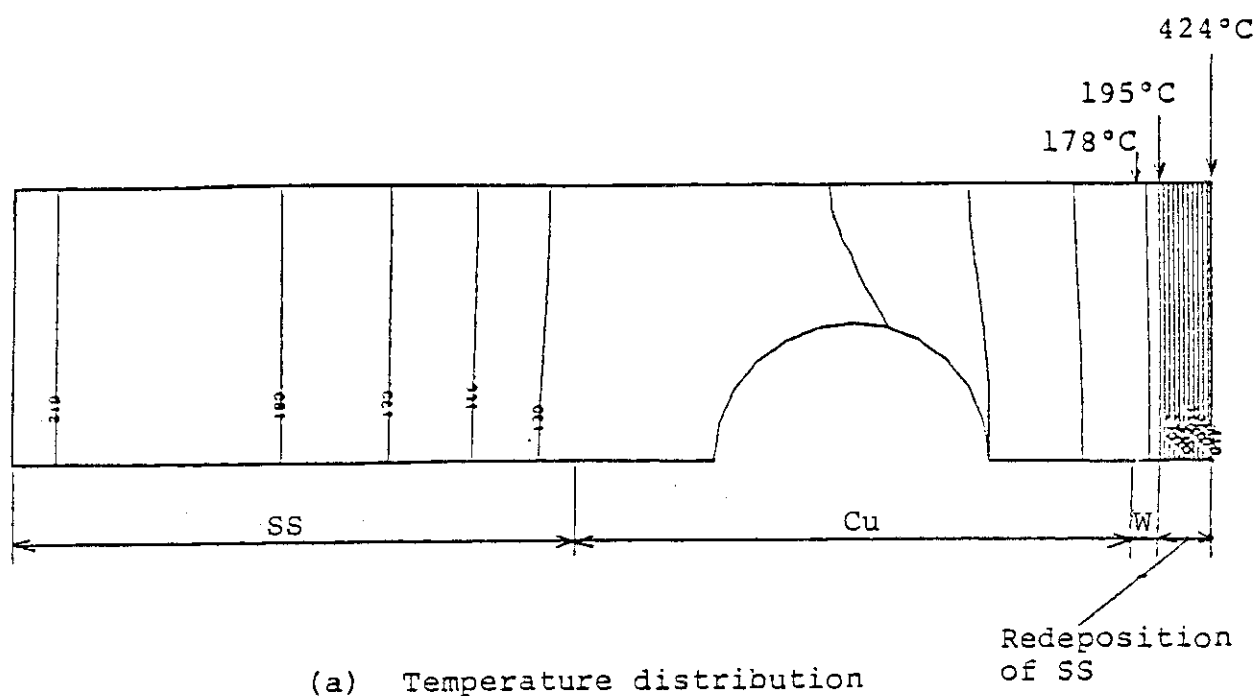
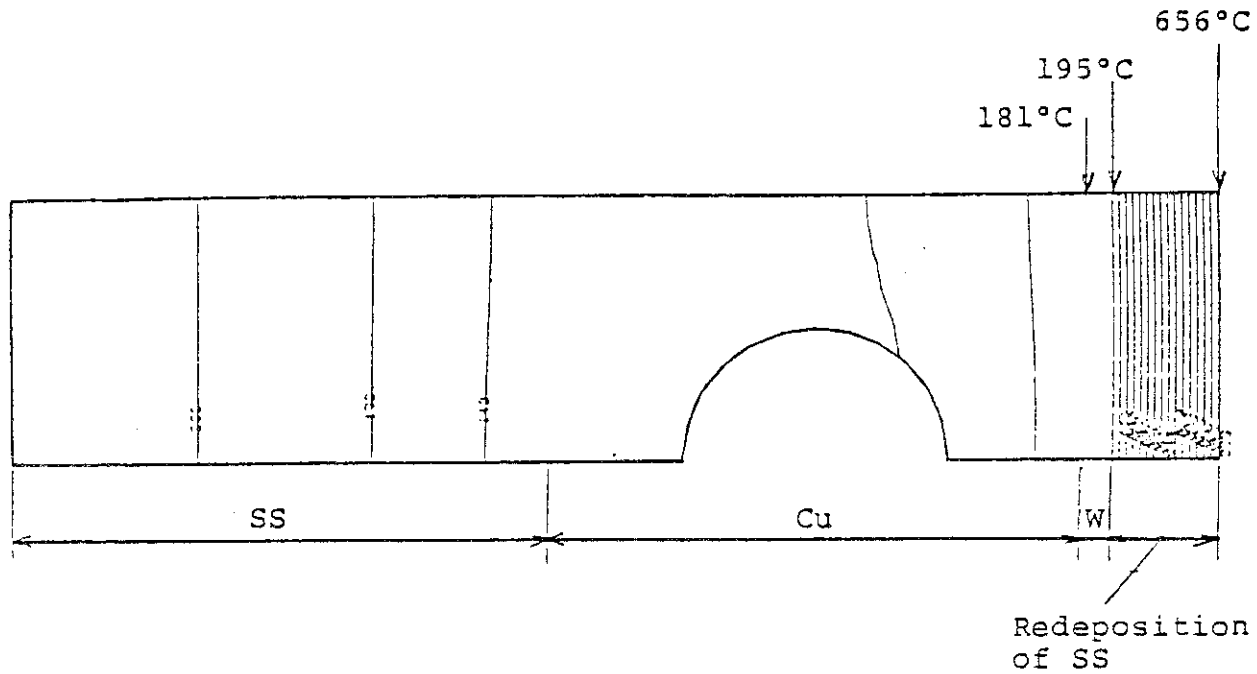


Fig. 6.14 Temperature and stress distribution of divertor plate with 1 mm thick tungsten tile on copper heat sink
(Heat flux = 2 MW/m^2 , thickness of redeposition (SS) = 2 mm)



(a) Temperature distribution

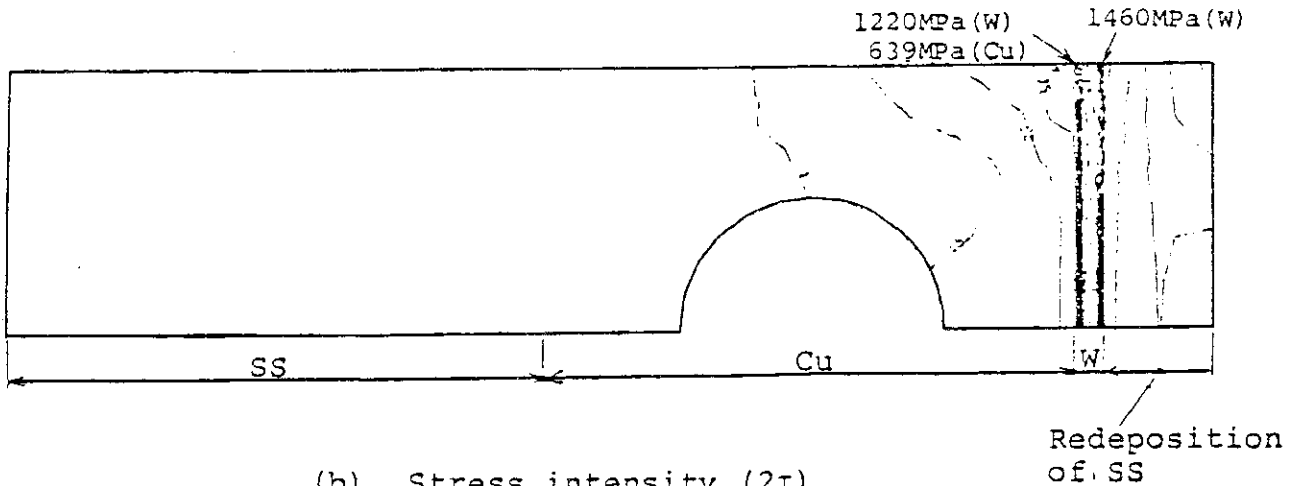
(b) Stress intensity (2τ) distribution

Fig. 6.15 Temperature and stress distribution of divertor plate with 1 mm thick tungsten tile on copper heat sink (Heat flux= $2\text{MW}/\text{m}^2$, thickness of redeposition (SS)=4mm)

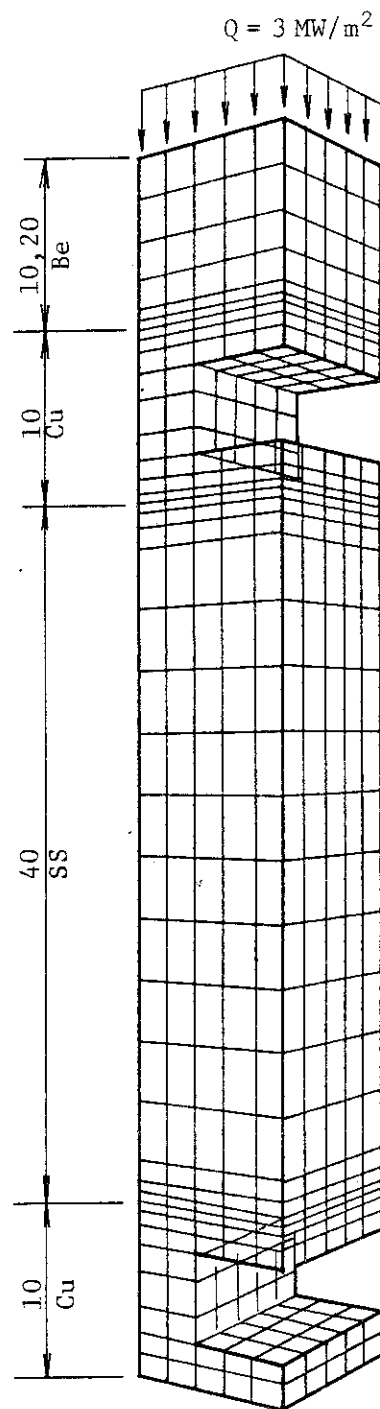
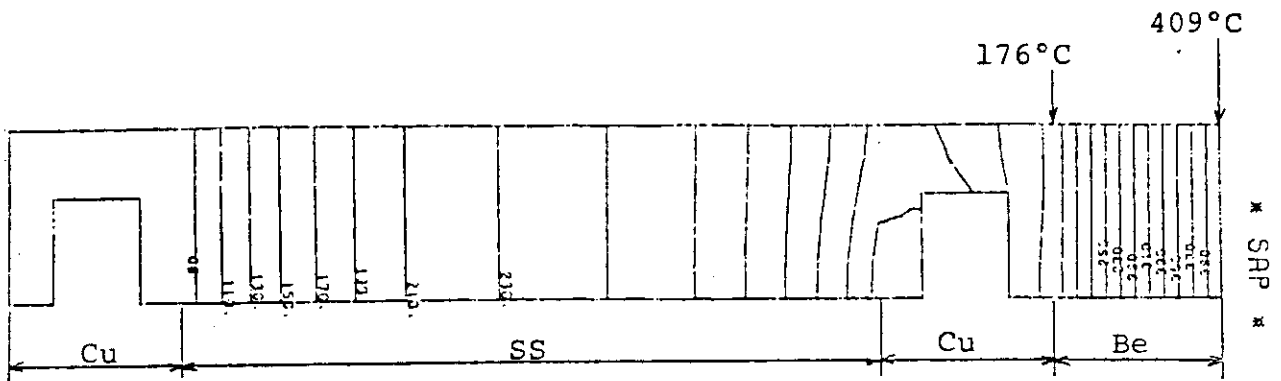


Fig. 6.16 Limiter plate geometry used for thermal hydraulics and stress analysis
(Medium edge temperature limiter)



(a) Temperature distribution

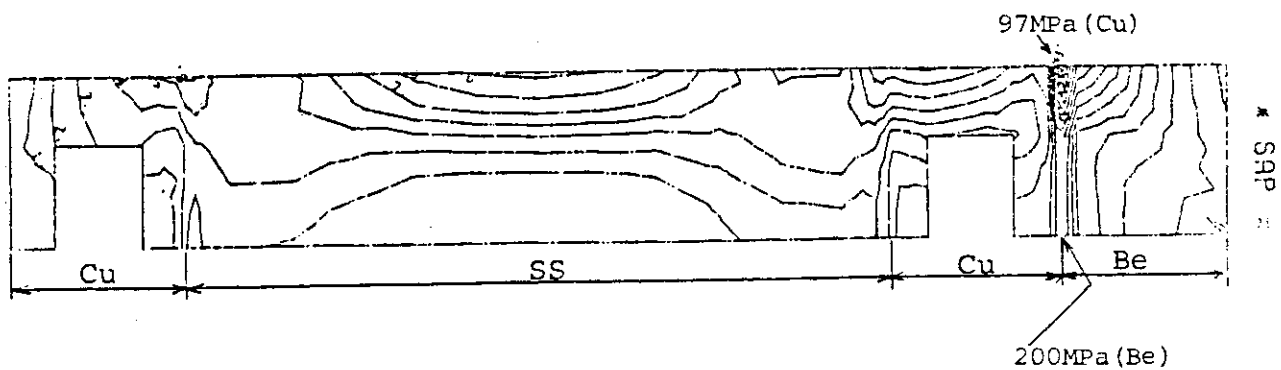
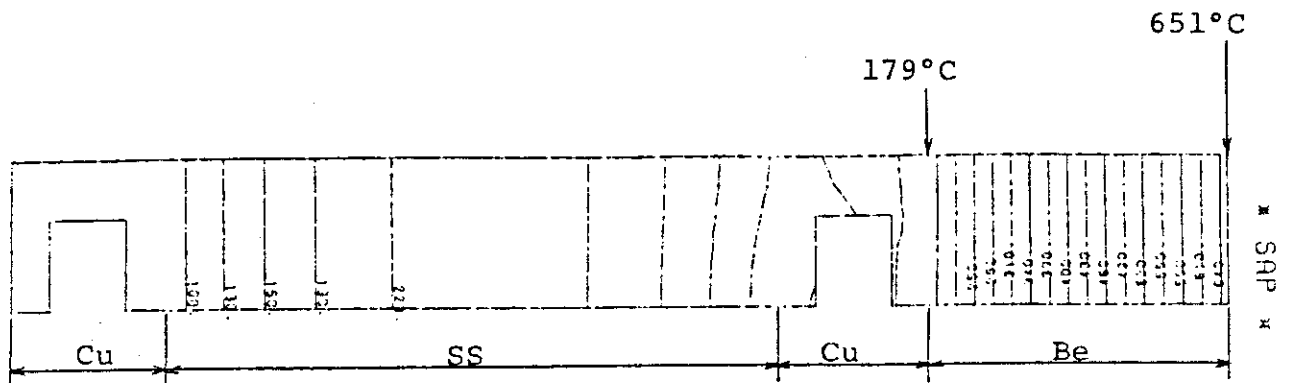
(b) Stress intensity (2τ) distribution

Fig.6.17 Temperature and stress distribution at the top surface of a medium edge temperature limiter with 10 mm thick beryllium tile on copper heat sink
(Heat flux = 3 MW/m^2)



(a) Temperature distribution

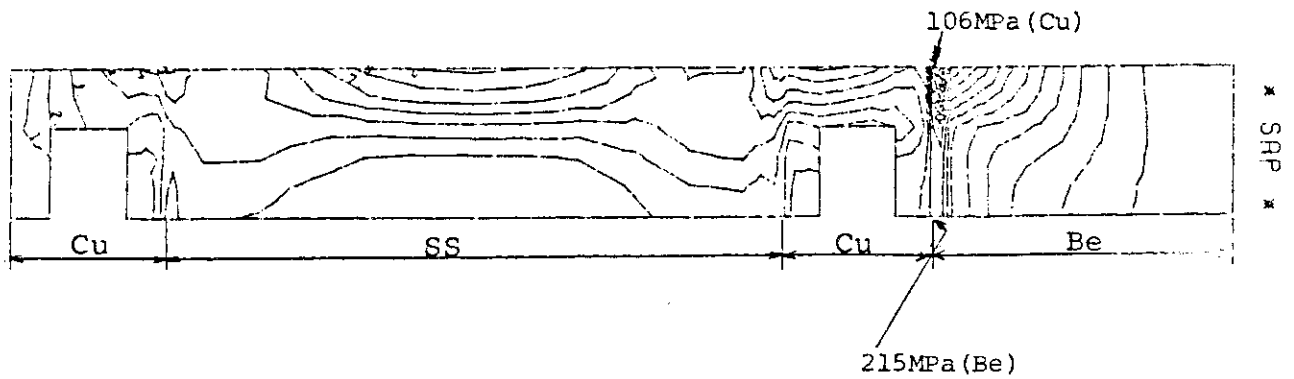
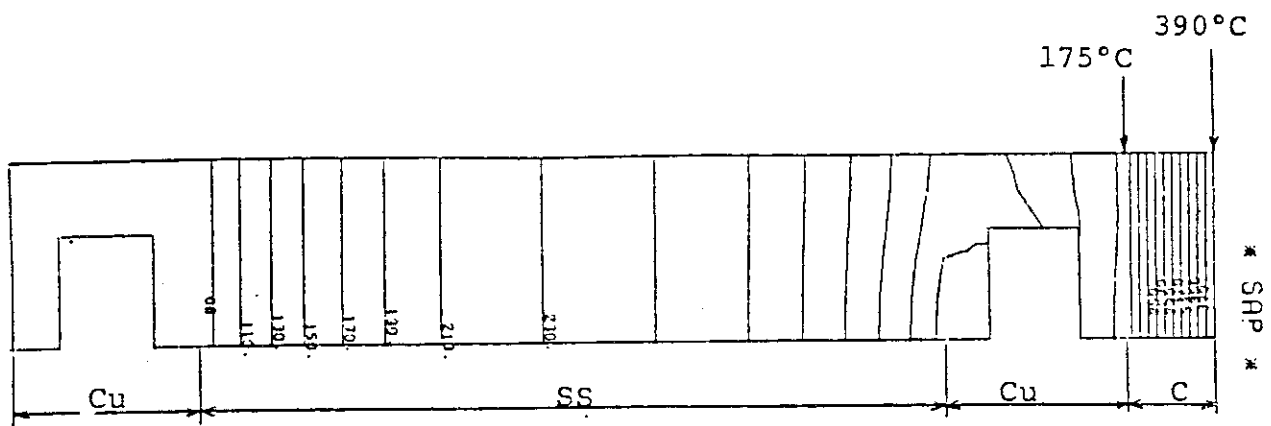
(b) Stress intensity (2τ) distribution

Fig.6.18 Temperature and stress distribution at the top surface of a medium edge temperature limiter with 20 mm thick beryllium tile on copper heat sink (Heat flux = 3 MW/m^2)



(a) Temperature distribution

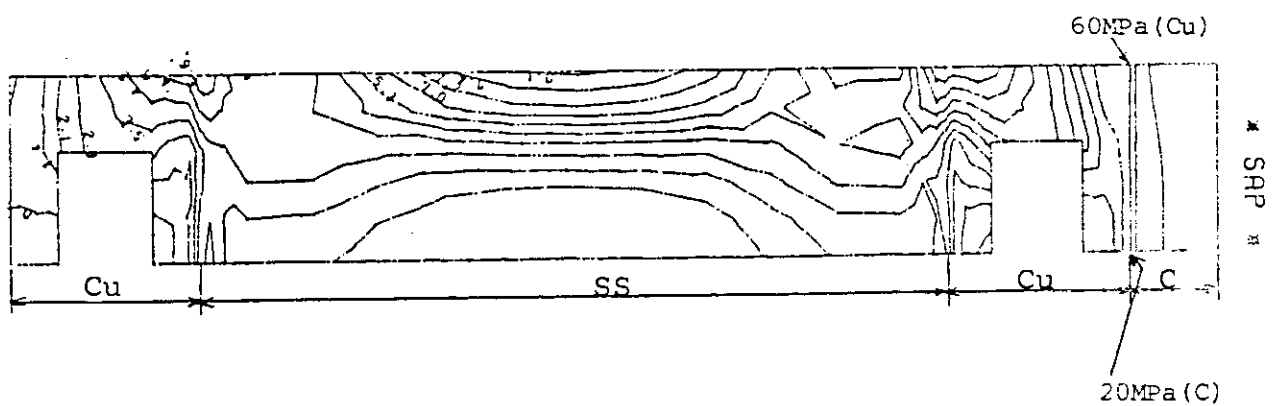
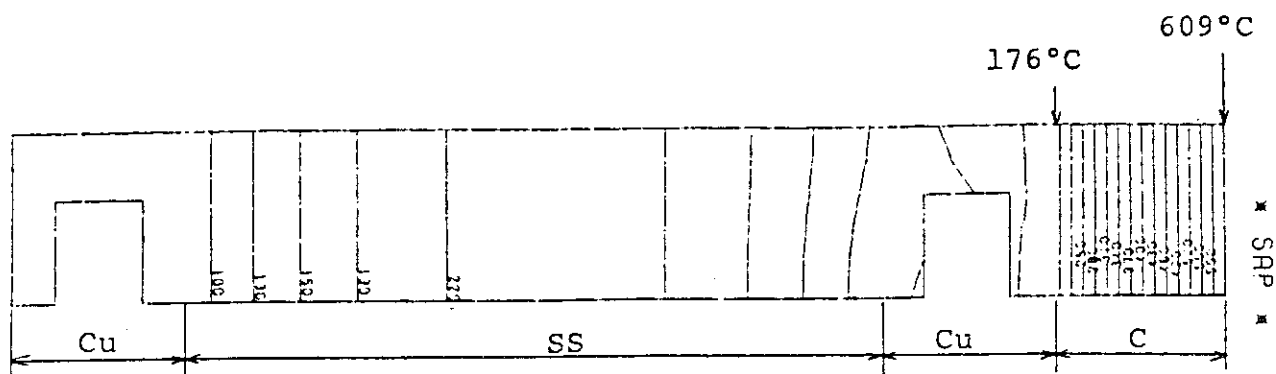
(b) Stress intensity (2τ) distribution

Fig.6.19 Temperature and stress distribution at the top surface of a medium edge temperature limiter with 5 mm thick graphite tile on copper heat sink (Heat flux = 3 MW/m^2)



(a) Temperature distribution

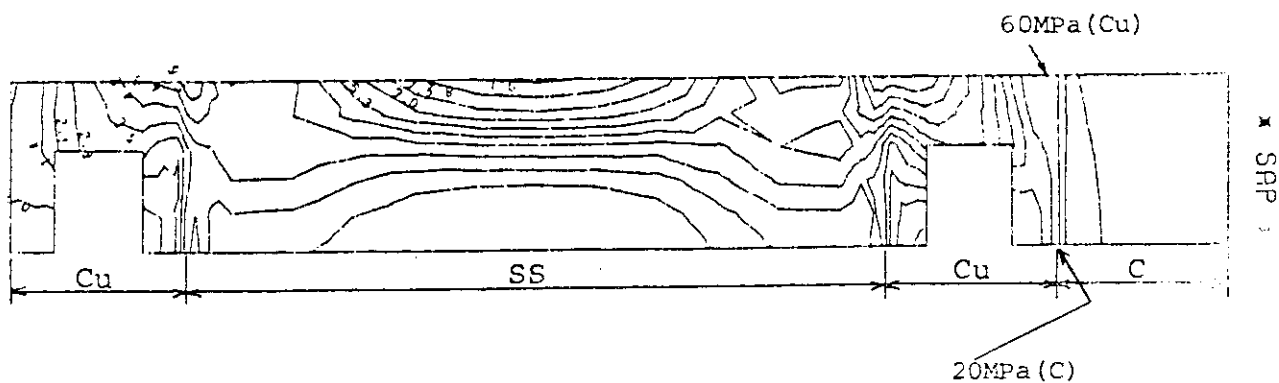
(b) Stress intensity (2τ) distribution

Fig. 6.20 Temperature and stress distribution at the top surface of a medium edge temperature limiter with 10 mm thick graphite tile on copper heat sink (Heat flux = 3 MW/m^2)

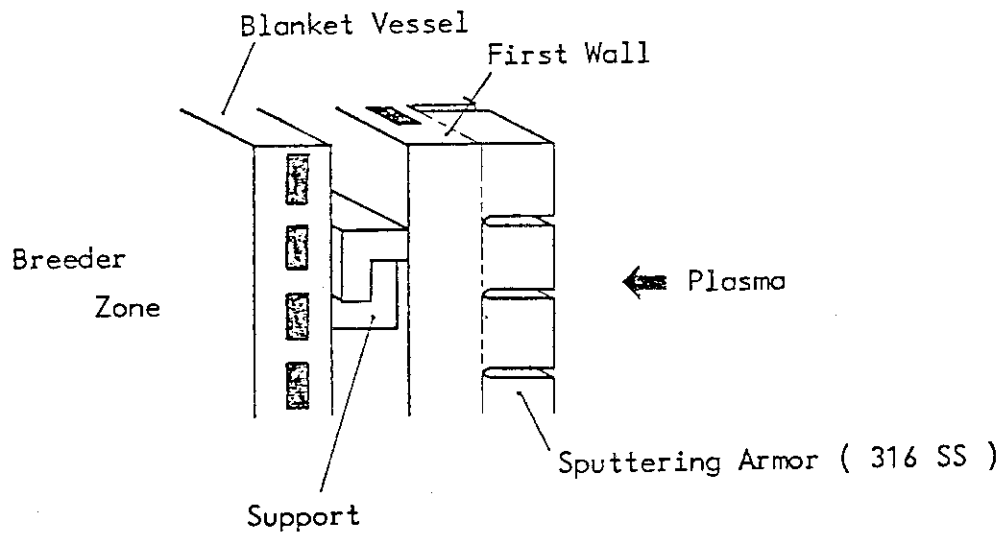


Fig. 6.21 First wall configuration

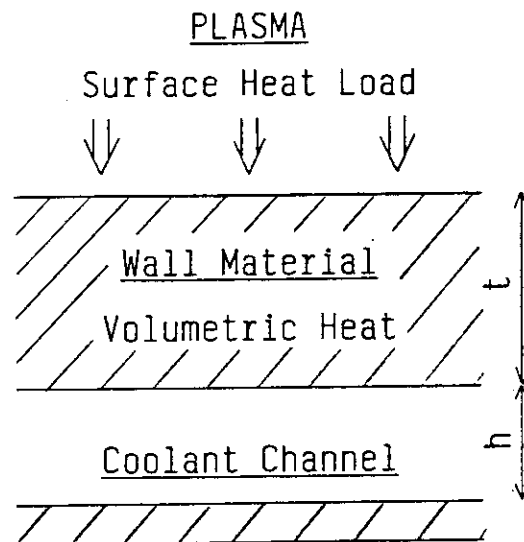


Fig. 6.22 Model for thermal-hydraulic analysis

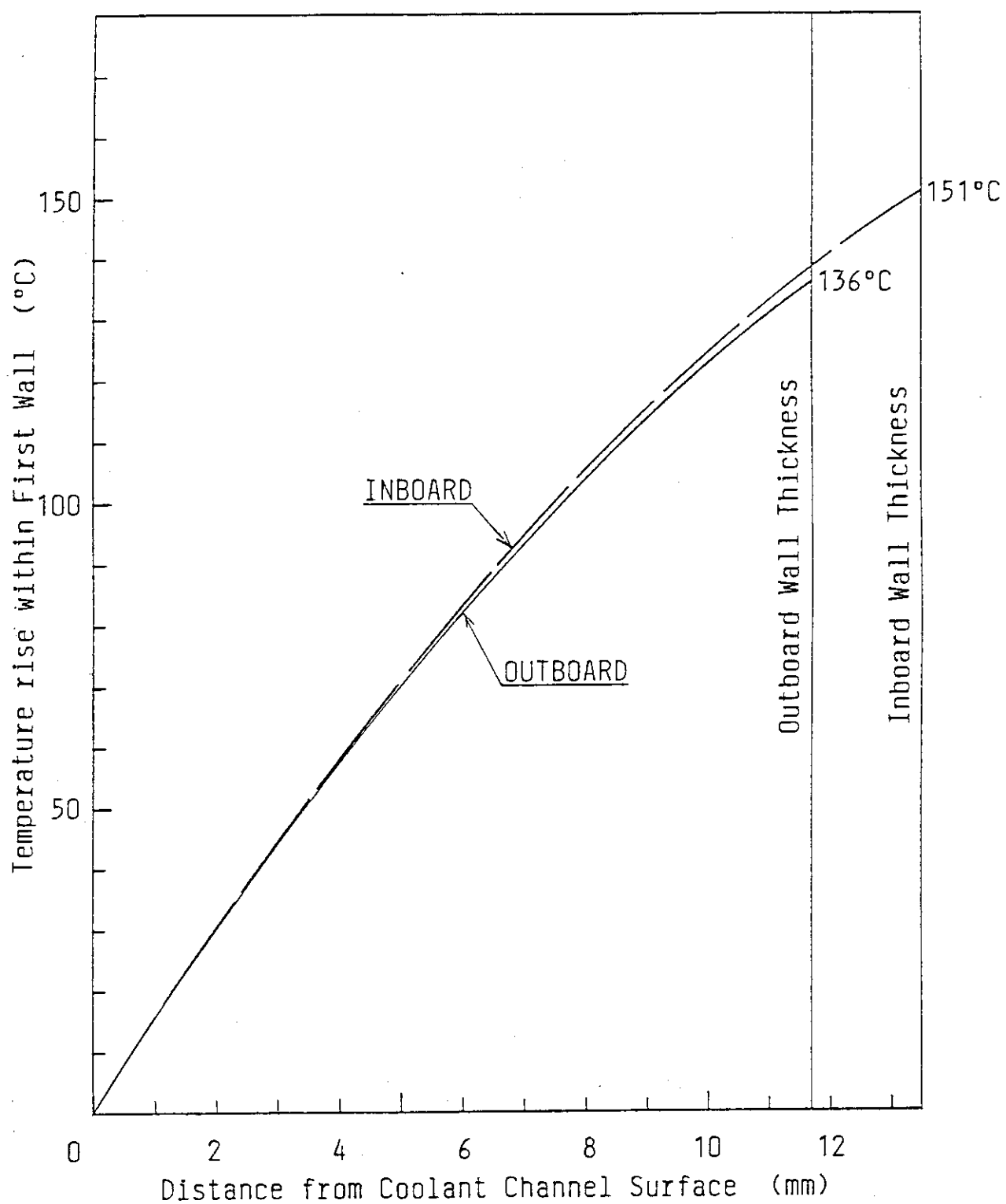


Fig. 6.23 Temperature rise within first wall

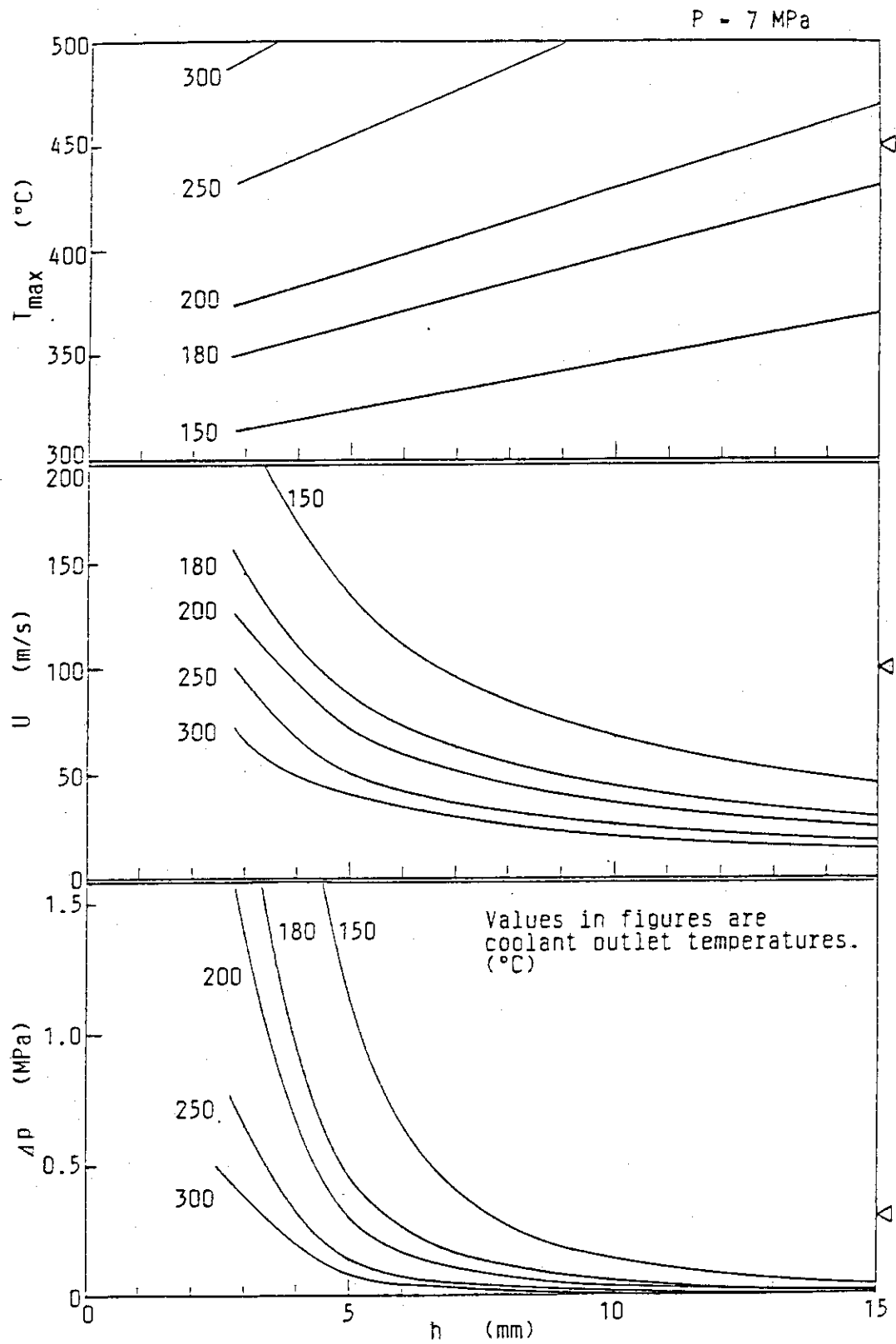


Fig. 6.24 Maximum wall temperatures, coolant velocities, and pressure losses (1) $P=7\text{MPa}$

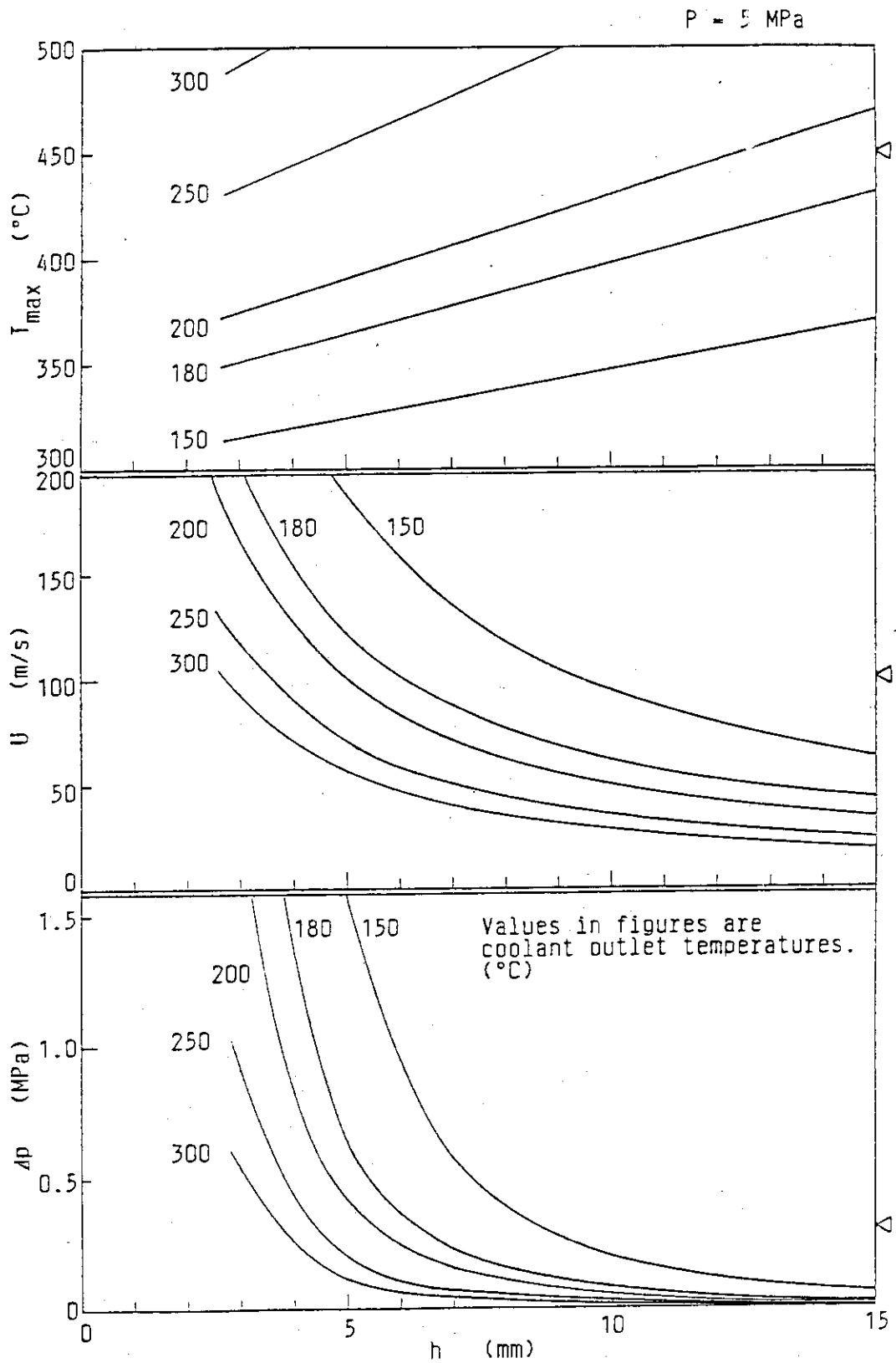


Fig. 6.25 Maximum wall temperatures, coolant velocities, and pressure losses (2) $P = 5 \text{ MPa}$

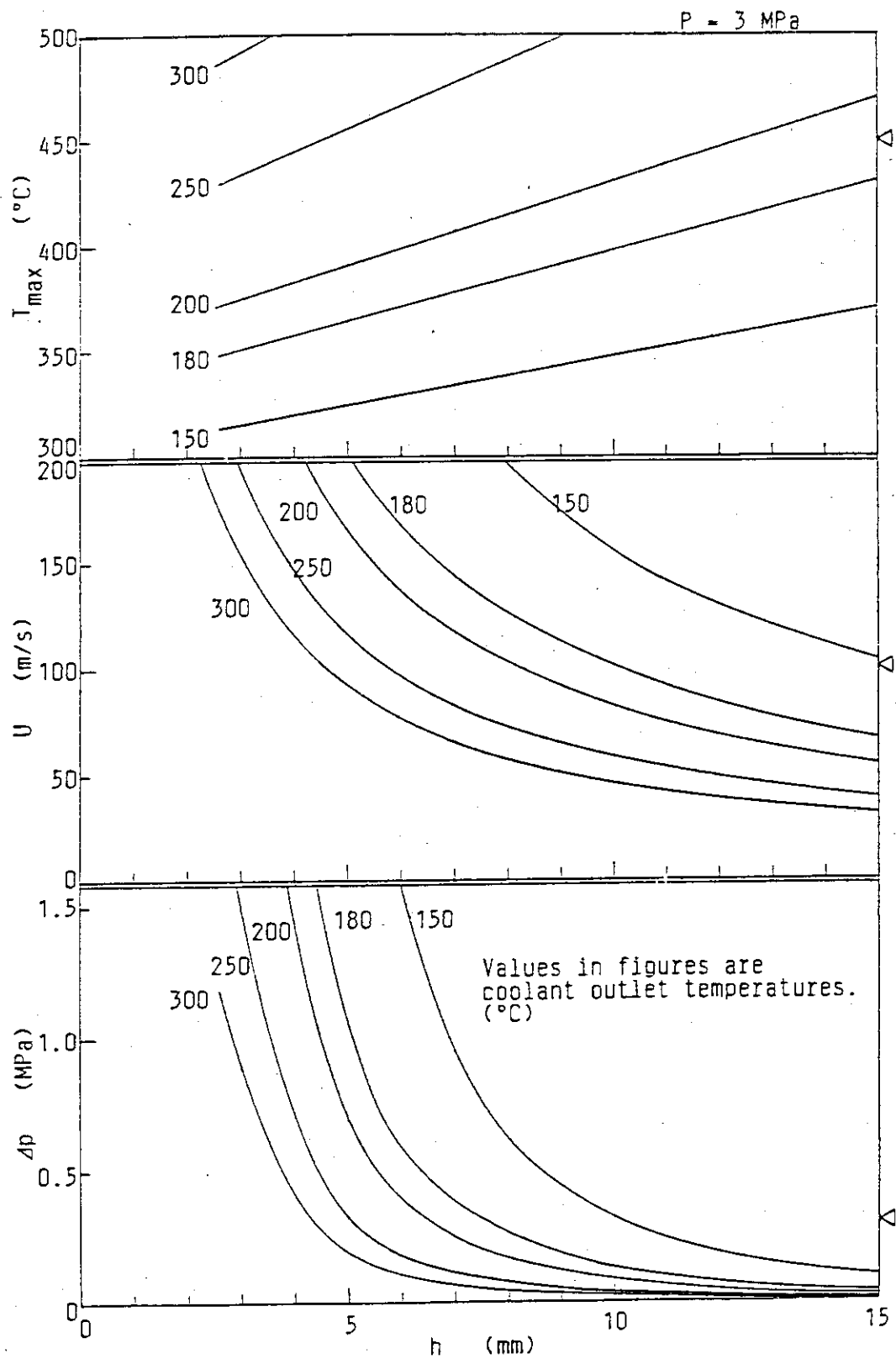


Fig. 6.26 Maximum wall temperatures, coolant velocities, and pressure losses (3) $P = 3 \text{ MPa}$

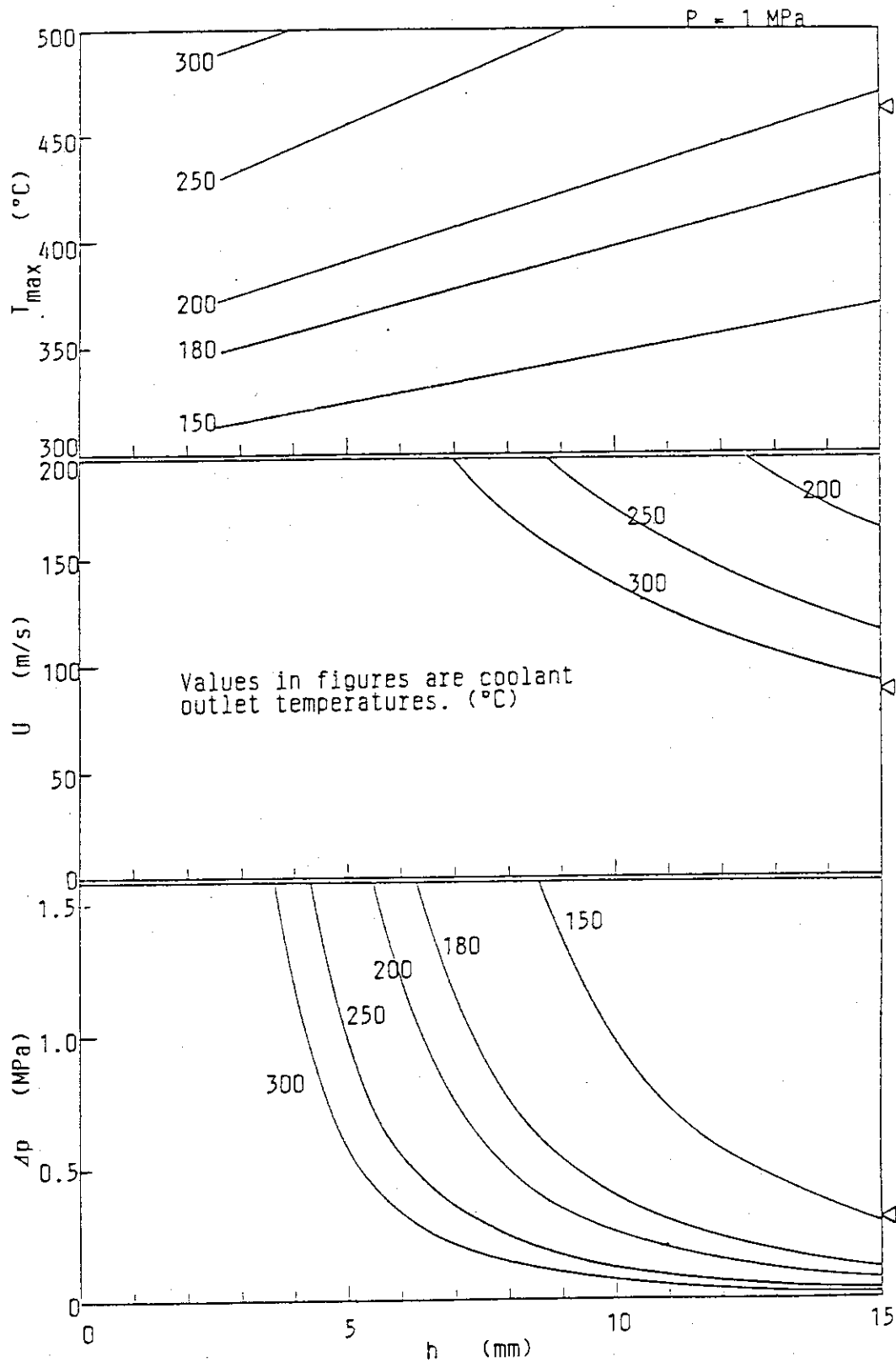


Fig. 6.27 Maximum wall temperatures, coolant velocities, and pressure losses (4) $P = 1 \text{ MPa}$

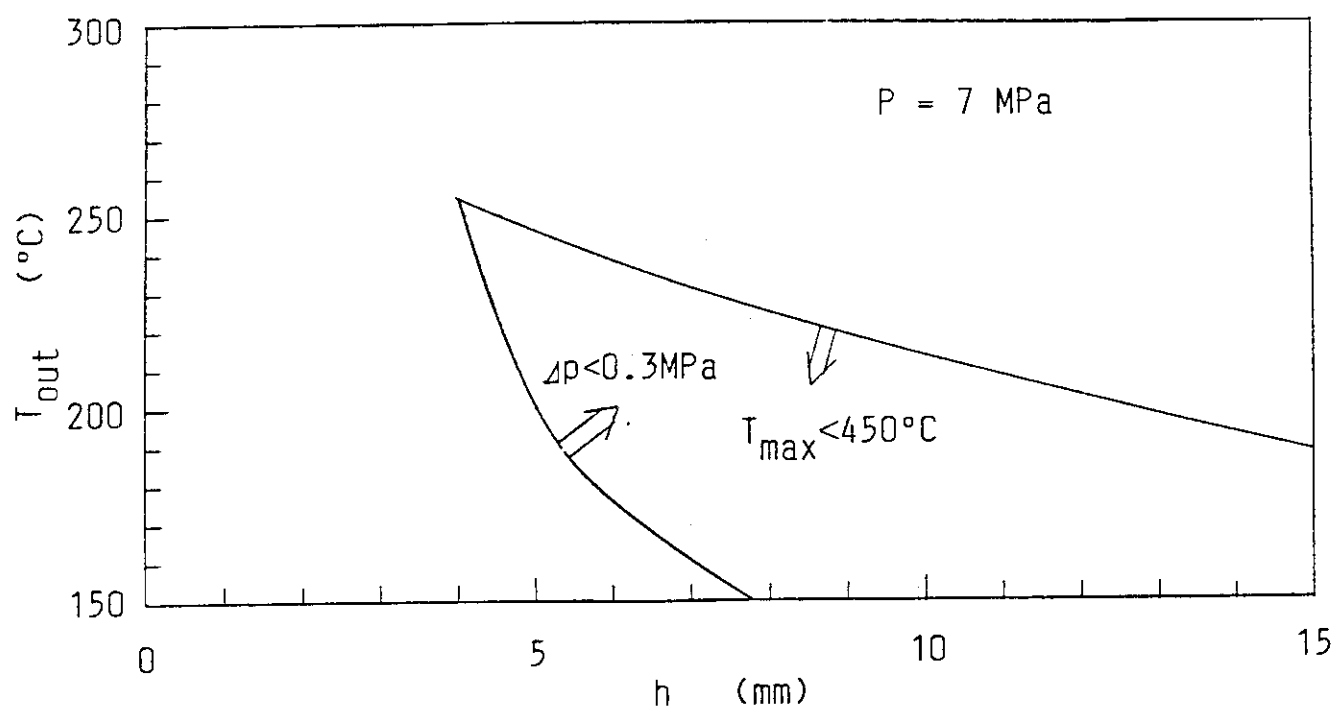


Fig. 6.28 Acceptable design range for helium-cooled first wall

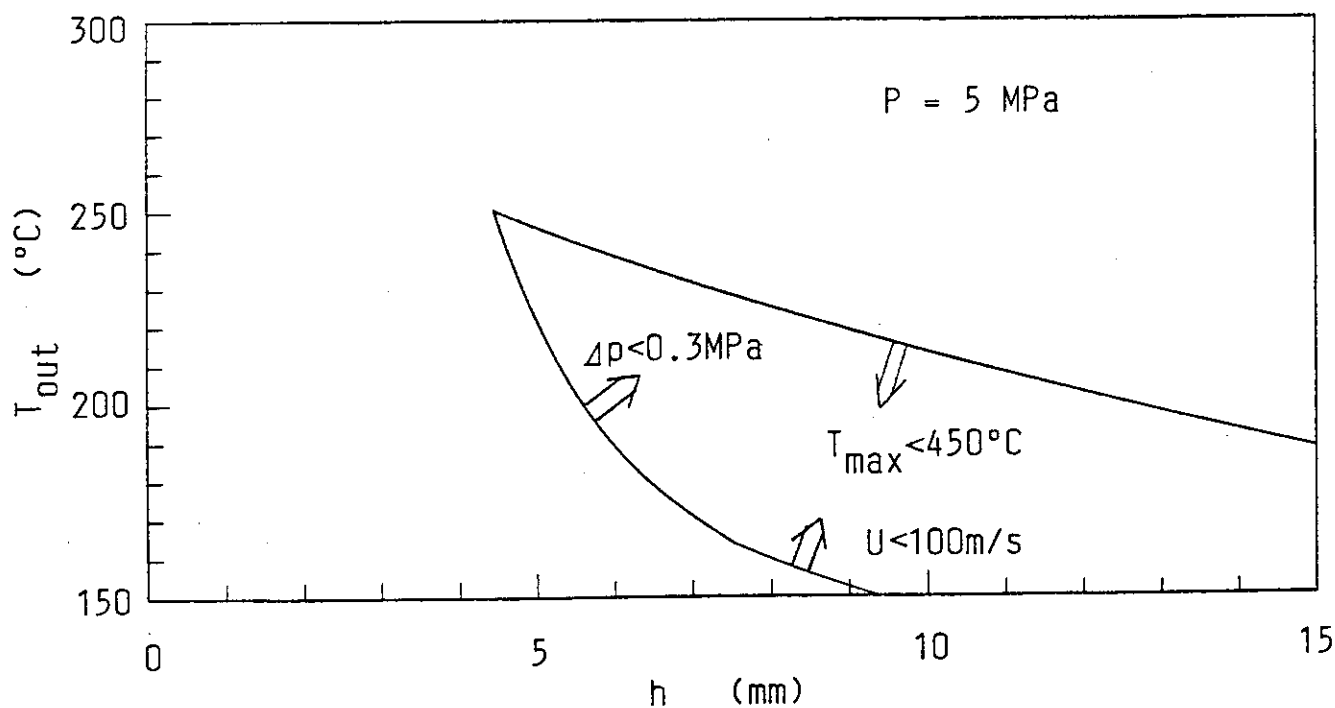
(1) $p = 7 \text{ MPa}$ 

Fig. 6.29 Acceptable design range for helium-cooled first wall

(2) $P = 5 \text{ MPa}$

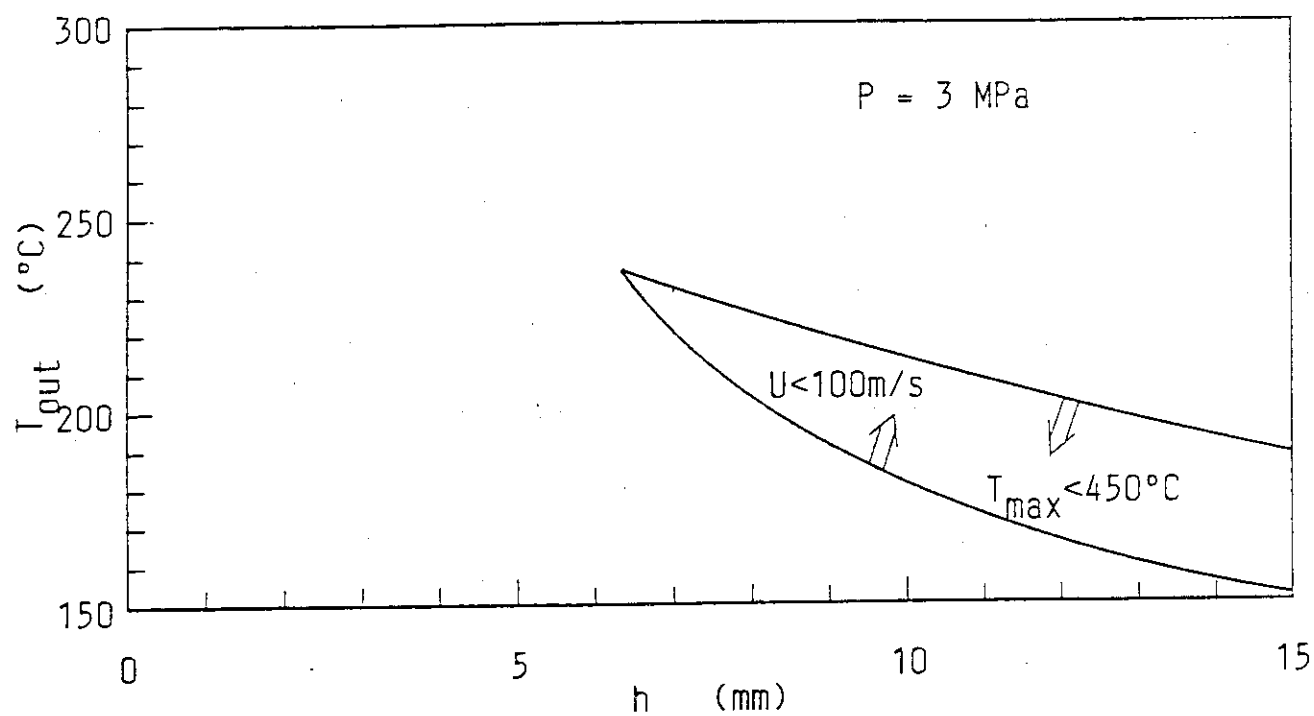


Fig. 6.30 Acceptable design range for He-cooled first wall
(3) $P = 3 \text{ MPa}$

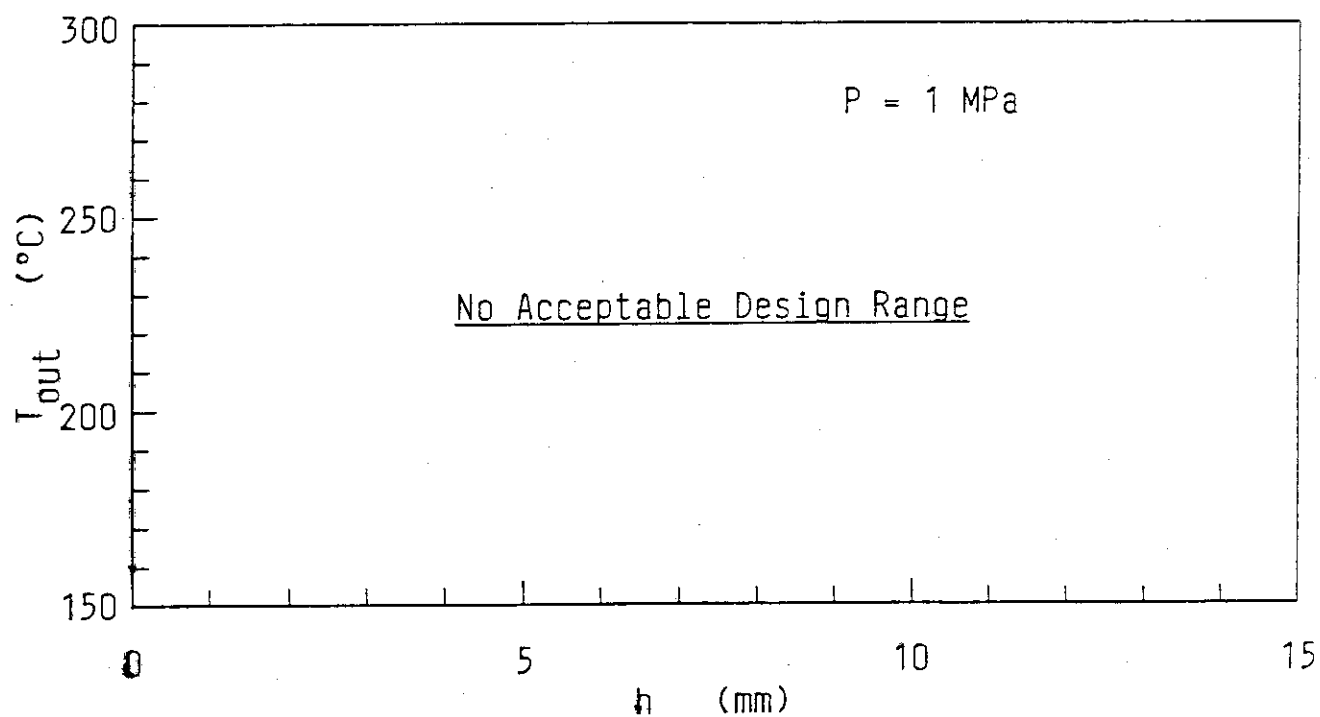


Fig. 6.31 Acceptable design range for He-cooled first wall
(4) $P = 1 \text{ MPa}$

7. Electromagnetics

Japanese effort on electromagnetics was concentrated on "Transient Electromagnetics", Group C.
No work has been performed for Group A.

8. Disruption

Plasma disruption gives rise to a intense surface heating on the first wall and limiter/divertor. Several computer codes capable of accommodating the effects of melting and vaporization have been developed and applied to predict melt and vaporized layer thickness for the INTOR disruption conditions. In the Phase IIA Part 1 report, calculated results for various materials have been well summerized.

The reference disruption conditions are as follows.

- o Peak energy flux
 - divertor plate : 230 J/cm²
 - first wall : 170 J/cm²
- o Time for energy deposition : 20 ms, 5 ms (alternative)

8.1 Thermal response

In this report thermal response of the divertor wall covered with thin stainless steel layer 1 μ m and 1 mm thick are presented. This situation simulates the case that sputtered stainless steel of the first wall uniformly deposits on a tungsten armor of the divertor plate.

Calculations were made for the following conditions.

- o Energy flux : 230 J/cm²
- o Disruption period : 5 ms and 20 ms
- o Thickness of 316 SS : 1 μ m and 1 mm
- o Initial temperature : 200°C

Calculated results are summerized in Tab. 8.1. Temperature traces as a function of time are plotted in Fig. 8.1 - 8.2. Melt layer thickness is plotted as a function of time in Figs. 8.3 - 8.4. Figs. 8.5 - 8.6 show vaporized thickness.

Following conclusions are obtained.

1. Tungsten does not melt for either of the conditions.
2. Melt layer and vaporized thicknesses increase with increasing thickness of the stainless steel.
3. In the case of 1 μ m deposition layer, the SS layer completely melts for 5 ms disruption. Thus if all the melt layer is lost, stainless steel cannot accumulate on the tungsten surface thicker than 1 μ m.
4. Judging from these results, a certain deposited thickness exists which melts completely for 20 ms disruption.

8.2 Liquid metal kinetics

8.2.1 Tollmien-Schlichting and Marangoni Instabilities

1. Introduction

It is difficult to solve a stability problem of melt layer following a plasma disruption. The difficulty includes:

1) Melt layer appears suddenly and changes its thickness rapidly with time in the course of the plasma disruption. The melt layer exists only in a short period. So, we should treat a full unsteady problem although hydrodynamic stability theory has not yet been established for each an essentially unsteady flow.

2) Once the melt layer forms, the liquid free surface may become wavy due to the instability of the melt layer. As a result, the

resolidified surface will not be flat. This means that the liquid-solid interface between melt and solid layer is believed to be flat only for the first disruption, and the interface will be wavy for the following disruptions. Thus the stability analysis becomes more complex even if we treat only a quasi-steady layer.

3) Even if we consider the quasi-steady melt layer and the flat interface, we cannot treat analytically nonlinear evolution of waves on the free surface of the liquid with arbitrary amplitude.

Because of these reasons, only one way to estimate the stability of the melt layer is full numerical treatment. Before we resort to numerical calculations, it is helpful to understand the outline of characteristics of these phenomena qualitatively. In this report, we investigate the linear stability of the melt layer in a idealized fashion.

There is only one investigation on this stability problem. Wolfer and Hassanein (1982) has dealt with this problem following Feldman's analysis (1959). Feldman considered the stability of the melt surface on an ablating body on re-entry into the atmosphere. In his analysis (and also in Wolfer and Hassanein's analysis), next five assumptions have been made.

- i) There is no basic flow; that is an undisturbed state is at rest.
- ii) Body forces act on the liquid layer in the vertical direction.
- iii) An undisturbed state is steady.
- iv) Temperature is constant across the liquid layer.
- v) Deformation of free surface is neglected.

Under these circumstances, the stability problem to be solved is reduced to the Rayleigh-Taylor (RT) instability problem. Consider the case that the liquid layer is above the solid layer. If a body force acts in the downward direction, the liquid layer is stable and this liquid-air configuration is called the stable stratification. On the other hand, if a body force acts in the upward direction, the liquid layer is unstable and is called unstable stratification. Based on the RT instability analysis, we can have only the above information. These results are in the sense of the asymptotic stability criteria.

Wolfter and Hassanein considered the practical stability criteria; i.e., they regarded that asymptotically unstable configuration could be maintained if the final deformation of the free surface is small compared with the thickness of the first wall. And they considered that the RT instability is dominant in comparison with the Tollmien-Schlichting (TS) instability; namely, the travelling wave instability.

For the real melting phenomena, above five assumptions do not always hold. Let us reconsider the significance of these five assumptions. First, the depth of the liquid layer changes very rapidly. A quasi-steady approach is invalid when the time scale of the evolution of the liquid layer is comparable with that of the growth of disturbance. Second, by considering the temperature gradient across the liquid layer and the deformation of the free surface, we can have stable stratification even if the body force acts in the upward direction. This indicates that the assumptions iv) and v) should not be made. Finally, in these stable stratified state, the TS instability plays an essential role. Therefore, the above five assumptions are not necessarily placed.

In this paper, we remove the four assumptions i), ii), iv), and v). The third assumption still remains because hydrodynamic stability

of an unsteady flow is a difficult problem and cannot be treated satisfactory today.

As we show in the following sections, the RT problems will be changed into the TS and the Marangoni instability problems because the temperature dependency of the surface tension plays an essential role in our analysis.

2. Mathematical Formulations

2.1 Physical Configuration

As is shown in Fig. 8.7, we consider that the liquid layer is above the solid layer.

The body force \mathbf{g} , which is the vectorial sum of the gravity and electromagnetic forces, acts in the inclined direction with an angle of γ with respect to the vertical direction. Coordinate x is the horizontal direction along the solid surface, y is the vertical direction and z is perpendicular to them. The direction of the coordinate system is taken such that the components of the body force are $(g \sin \gamma, -g \cos \gamma, 0)$.

Because of non-zero x -component of $g \sin \gamma$, basic flow $U(y)$ exists in the x direction at an undisturbed state.

We denote t the time, ν the kinematic viscosity, ρ the density, p the pressure, T the temperature, d the height of the liquid layer, the deformation of the free surface, T_a the temperature in the air, and T_s the temperature at the solid surface.

2.2 Basic Flow

In this paper, we neglect the buoyancy effect in the liquid layer because it is very thin. Let Newton's law

$$-k \frac{\partial T}{\partial y} = k(T - T_a) \quad , \quad (2.1)$$

be satisfied at the liquid-air interface (free surface), where k is the thermal conductivity of the liquid, h the heat transfer coefficient at the free surface.

Governing equations for velocity (\mathbf{v}) and temperature field are

$$\text{div } \mathbf{v} = 0 \quad (2.2)$$

$$\frac{\partial \mathbf{v}}{\partial t} + (\mathbf{v} \cdot \text{grad}) \mathbf{v} = -\frac{1}{\rho} \text{grad } p + \nu \Delta \mathbf{v} + \mathbf{g} \quad (2.3)$$

$$\frac{\partial T}{\partial t} + (\mathbf{v} \cdot \text{grad}) T = \kappa \Delta T \quad (2.4)$$

where $\Delta \equiv \frac{\partial^2}{\partial x^2} + \frac{\partial^2}{\partial y^2} + \frac{\partial^2}{\partial z^2}$, κ is the thermal diffusivity.

By considering that $u = U(y)$, $v = w = 0$ and $T = T(y)$, we obtain the basic flow as follows.

$$\bar{u} = \nu^{-1} d^2 \sin \gamma \left[\frac{y}{d} - \frac{1}{2} \left(\frac{y}{d} \right)^2 \right], \quad \bar{v} = \bar{w} = 0 \quad (2.5)$$

$$\bar{p} = P_a + \rho g(d - y) \cos \gamma; \quad \bar{p} = P_a \quad \text{at } y = d,$$

$$\bar{T} = T_s - \beta y, \quad \beta = \frac{h(T_s - T_a)}{(k - hd)}$$

We will take $\frac{1}{2} v^{-1} d^2 g \sin \gamma$ as the characteristic velocity and d as the characteristic length.

2.3 Disturbance Equations

By substituting $(v, p, T)^T = (\bar{v}, \bar{p}, \bar{T})^T + (\hat{v}, \hat{p}, \hat{T})^T$ into eqs. (2.2)-(2.4) and by linearizing we obtain the disturbance equations for \hat{v}, \hat{p} and \hat{T} . By eliminating \hat{u}, \hat{w} and \hat{p} , we have two disturbance equations.

$$\frac{\partial}{\partial t} \Delta \hat{v} + U \frac{\partial}{\partial x} \Delta \hat{v} - U'' \frac{\partial v}{\partial x} - v \Delta^2 \hat{v} = 0,$$

$$\frac{\partial \hat{T}}{\partial t} + U \frac{\partial \hat{T}}{\partial x} - \beta \hat{v} = \kappa \Delta \hat{T},$$

where primes indicate differentiation with respect to y .

2.4 Boundary Conditions (BCs)

At free surface $y = d + \xi$, surface tension S should be balanced with the stress tensor s_{ij} .

From balance equations, we have four BCs at $y = d$.

$$-\rho v (\Delta_2 - \frac{\partial^2}{\partial y^2}) \hat{v} + \sigma \beta \Delta_2 \xi - \sigma \Delta_2 \hat{T}_f = 0,$$

$$\rho \left[\frac{\partial}{\partial t} + U \frac{\partial}{\partial x} - 3\rho v \Delta_2 - \rho v \frac{\partial^2}{\partial y^2} \right] \frac{\partial \hat{v}}{\partial y} - \rho U' \frac{\partial \hat{v}}{\partial y} + \rho \left[v U' \frac{\partial}{\partial x} - g \cos \gamma \right] \Delta_2 \xi + S_s \Delta_2^2 \xi = 0,$$

$$k \frac{\partial \hat{T}}{\partial y} + h \hat{T} - h \beta \xi = 0,$$

$$v = \frac{\partial \xi}{\partial t} + U \frac{\partial \xi}{\partial x},$$

and at $y = 0$, we have

$$\hat{v} = \partial \hat{v} / \partial y = \hat{T} = 0$$

where $\Delta_2 \equiv \frac{\partial^2}{\partial x^2} + \frac{\partial^2}{\partial z^2}$, $\sigma = -(\frac{\partial s}{\partial T})_T = \bar{T}_f$, $S_s = S(\bar{T}_f)$, T_f the temperature of the liquid layer at the free surface, $\bar{T}_f = T_s - \beta d$, $T_f = \bar{T}_f - \beta \xi + \hat{T}_f$, S the surface tension as a function of T .

2.5 Non-dimensionalization

For non-dimensionalization, $(dx^*, dy^*, dz^*) = (x, y, z)$, $dt^*/U = t$, $U_0 v^* = \hat{v}$, $U_0 U^* = U$, $\theta^* \beta d = T$, $\eta^* d = \xi$, where $U_0 = \frac{1}{2} v^{-1} d^2 g \sin \gamma$ where used. Quantities with an asterisk are non-dimensional numbers.

Then the following six non-dimensional parameters appear; namely, $R = U_0 d / \nu$, the Reynolds number; $P = \nu / \kappa$, the Prandtl number; $M = \frac{\sigma \beta d^2}{\rho \nu \kappa}$, the Marangoni number; $N_C = \frac{\rho \nu \kappa}{S_{sd}}$, crispatation number; $N_G = \frac{\rho g d^2}{S_s}$, the Weber number; and $B = h d / k$, the Biot number.

2.6 Normal Mode Analysis

Now we introduce two-dimensional Fourier decomposition. This mode corresponds to a transverse roll:

$$(v^*, \theta^*, \eta^*)^T = (\phi, \mathbb{H}, H)^T \exp(\omega t^* + i \alpha x^*). \quad (2.16)$$

we obtain the following set of ODEs:

$$[\omega(D^2 - \alpha^2) + i \alpha U(D^2 - \alpha^2) - i \alpha U'' - R^{-1}(D^2 - \alpha^2)^2] \phi = 0, \quad (2.17)$$

$$[\omega + i \alpha U - (PR)^{-1}(D^2 - \alpha^2)] \mathbb{H} = \phi, \quad (2.18)$$

with BCs:

$$\text{at } y = 1, \quad (D^2 + \alpha^2) \phi + M(PR)^{-1} \alpha^2 (\mathbb{H} - H) = 0, \quad (2.19)$$

$$\begin{aligned} & [\omega + i \alpha U + 3 \alpha^2 R^{-1} - R^{-1} D^2] D \phi - i \alpha U' \phi \\ & - [i \alpha U' R^{-1} - N_G N_C^{-1} P^{-1} R^{-2} \cos \gamma] \alpha^2 H + N^{-1} P^{-1} R^{-2} \alpha^4 H = 0, \end{aligned} \quad (2.20)$$

$$(D + B) \mathbb{H} - BH = 0, \quad (2.21)$$

$$(\omega + i \alpha U) H = \phi, \quad (2.22)$$

and at $y=0$,

$$\phi = D \phi = \mathbb{H} = 0 \quad (2.23)$$

where $D = d/dy$.

Equations (2.17)-(2.23) consists eigenvalue problems. For given T_s , T_a , and γ , the quantities R , P , M , N_G , N_C , and B are uniquely determined. And for given real α , ω is obtained as discrete eigenvalues. The maximum value of the real part of ω gives the linear growth rate. Basic flow is stable for $\omega_r < 0$, unstable for $\omega_r > 0$, and marginally stable for $\omega_r = 0$, where $\omega_r = \text{Re} \omega$.

3. Numerical procedure

Because the main flow velocity $U(y)$ is involved in the equations (2.17)-(2.23), it is impossible to analytically solve the eigenvalue problem. Here we solve the equations (2.17)-(2.23) by using the Collocation method (Pseudo-spectral method) to obtain ω in the following form as an eigenvalue for a given set of parameters $(\alpha, R, P, M, N_G, N_C, B)$:

$$(\phi, \mathbb{H})^T = \sum_{n=0}^N (\phi_n, \mathbb{H}_n)^T T_n(y), \quad T_n(y) = \cos(n \cos^{-1} y); \quad N \gg 1. \quad (3.1)$$

Here $T_n(y)$ is the Chebyshev polynomials.

By substituting Eq.(3.1) into Eqs.(2.17) and (2.18) at each Collocation point and by applying the BCs (2.19)-(2.23) using the Lanczos' tau method, we can write the eigenvalue problem in the next form.

$$A\Phi = \omega B\Phi. \quad (3.2)$$

Eigenvalue ω can be solved by the QR method for complex coefficients.

Here $n=0, 1, 2, 3, \dots, N$, because $(\phi, \mathbb{H})^T$ is asymmetric. We truncated the terms at $N=24$.

We checked some typical results with the ones obtained by Shooting method.

4. Numerical results

For probable disruption conditions, the values of the six non-dimensional parameters are $R=14.466$, $\sin \frac{\pi\gamma}{180}$, $P=1.6 \times 10^{-1}$, $B=10^{-4}$, $N_G=3.5 \times 10^{-4}$, $N_C=7.48 \times 10^{-5}$, where $\gamma = \frac{\pi Y}{180}$.

A combination of these values gives ill-posed boundary conditions; that is, one term in each of the BGs (2.17)-(2.23) becomes extremely large compared with the rest of the terms, which leads to large numerical errors. The difficulty was alleviated so much by changing the value of B to 10^{-3} . And the value of B was found to affect the linear amplification factor only slightly. The factors for $B=10^{-4}$ and $B=10^{-3}$ agreed to the third figures. Thus we used the value of 10^{-3} for the Biot number.

A dimensional number of $\tilde{\omega}_r \equiv \omega_r' U_0/d = \frac{1}{2} v^{-1} \text{dg}(\sin \frac{\gamma' \pi}{180}) \cdot \omega_r'$ is plotted against γ' in Fig. 8.8, where γ' the maximum amplification factor. Hereafter dimensional numbers are used for practical convenience.

The value of $\tilde{\omega}_r$ decreases monotonically with γ decreasing from 90° , and seems to asymptotically approach to a constant value with $\gamma \rightarrow 0$. It should be emphasized that travelling waves on a surface of a liquid layer following downward along a vertical wall are found to be most unstable in the present results. This contrasts striking with the results of Wolfer and Hassanein. They predicted that these waves were more stable than the other waves.

An amplification factor is of the order of 10^2 and γ' -dependence is relatively low.

From the present results, we can plot $e^{\tilde{\omega}_r \Delta \tau}$ against γ' in Fig. 8.7 which $\Delta \tau = (t_{\text{res}} - t)$ as a parameter, where T_{res} is the time elapsed between the beginning of melting and the end of

resolidification.

We employ 5 ms and 2 ms for .

For $\tau = 2$ ms, initial unevenness of the solid surface would be amplified by 1.3 times for one disruption. This means that thousands times of disruption could make the unevenness enormously large.

Of course we cannot apply the linear stability theory to such large amplitude disturbance, but the present analysis suggests that it is doubtful for the first wall to be kept sound when exposed to many times of disruption. It is required from the safety point of view that the amplification factor be negative. And to lower the amplification factor, it is necessary to make the absolute value of the Marangoni number small.

In the above discussion, no consideration is made on unsteadiness and nonlinearity of the phenomena. Changing thickness of the melt layer with time would promote instability. Instead of stability for parallel flow which is treated here, stability for vertical flow, such as the stability of a free surface of fluid layer on a porous wall subject to emission or suction might be taken into account.

For a practical application, soundness of the first wall against different kinds of instabilities including liquid-solid and liquid-vapor interfacial instabilities under evaporation, condensation, melting, and resolidifying should be studied both theoretically and experimentally.

Table 8.1 Behavior of Divertor Surface during Major Plasma Disruption

Divertor armor	Tungsten			
Redeposited Material	type 316 Stainless Steel			
Redeposited Thickness	1 μm		1 mm	
Exposed Energy Flux	2.3 MJ/m ²			
Disruption Time	5 msec	20 msec	5 msec	20 msec
Maximum Surface Temperature	2530 K	1680 K	2950 K	2080 K
Maximum Melt Layer Thickness	1.0 μm	NM [*]	110 μm	65 μm
Vaporized Thickness	0.2 μm	–	7.2 μm	0.02 μm
Melting Duration	4.9 ms	–	11.0 ms	12.3 ms

* No melting occurs.

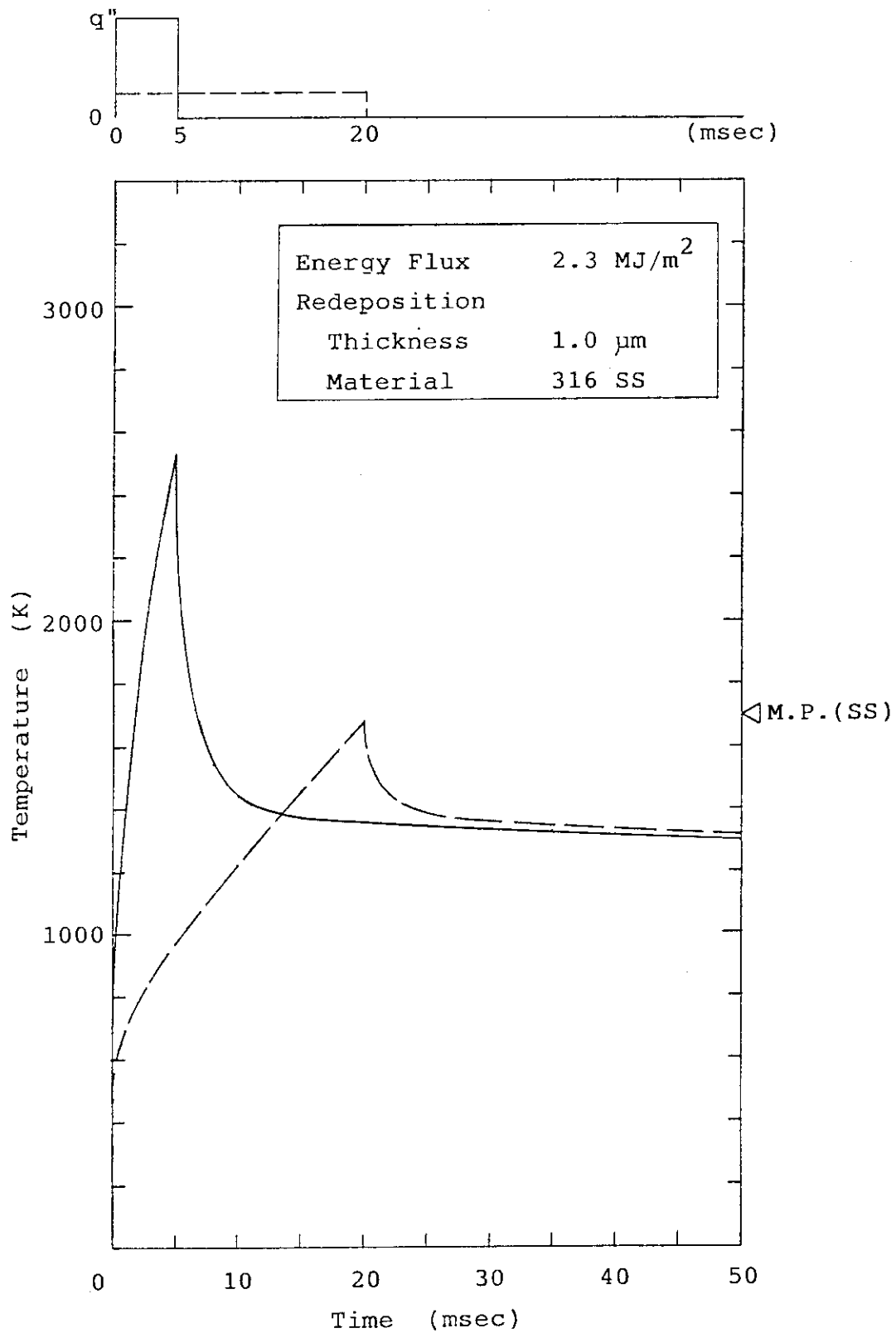


Fig.8.1 Divertor Surface Temperature Responses during Major Plasma Disruption

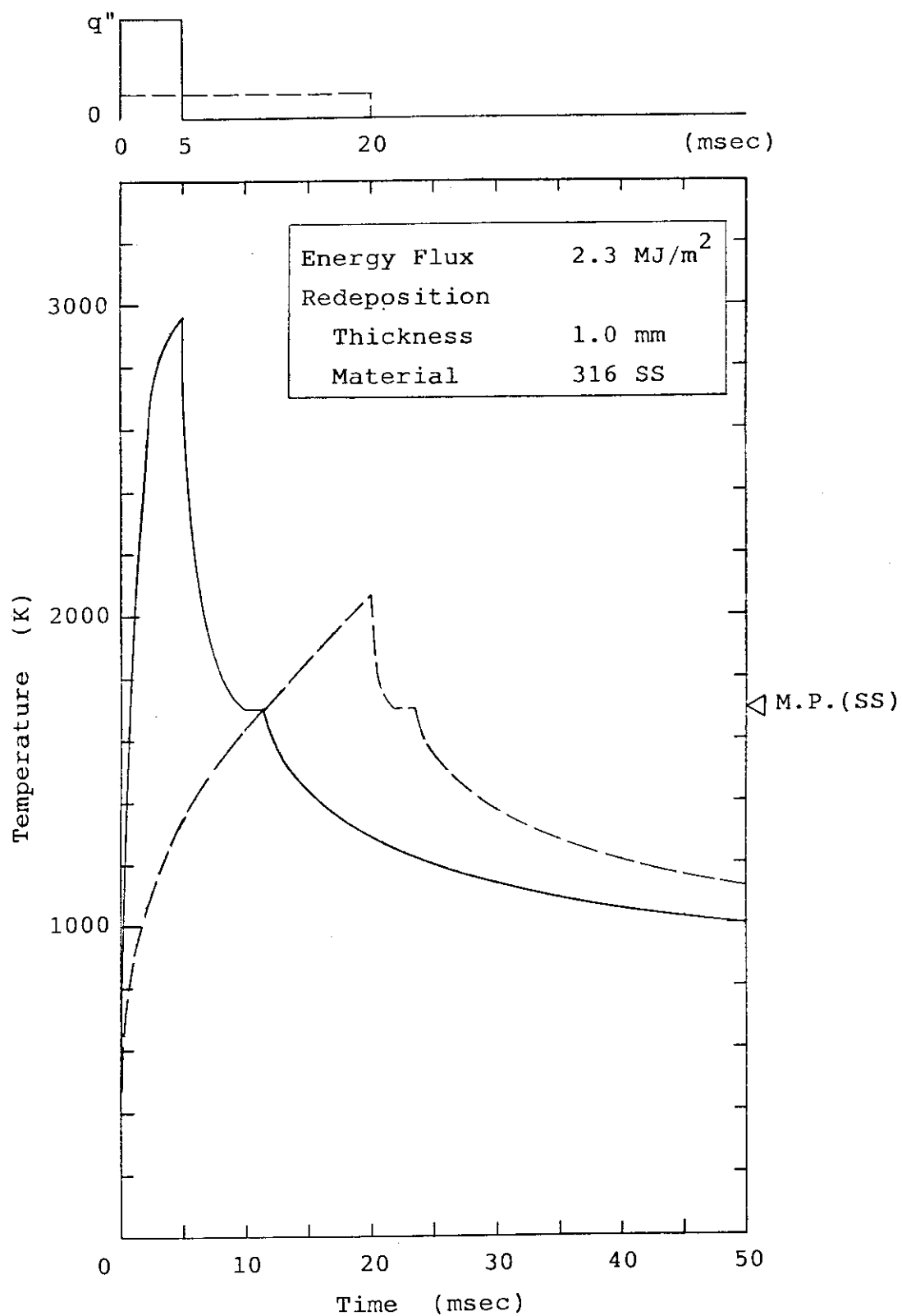


Fig. 8.2 Divertor Surface Temperature Responses during Major Plasma Disruption

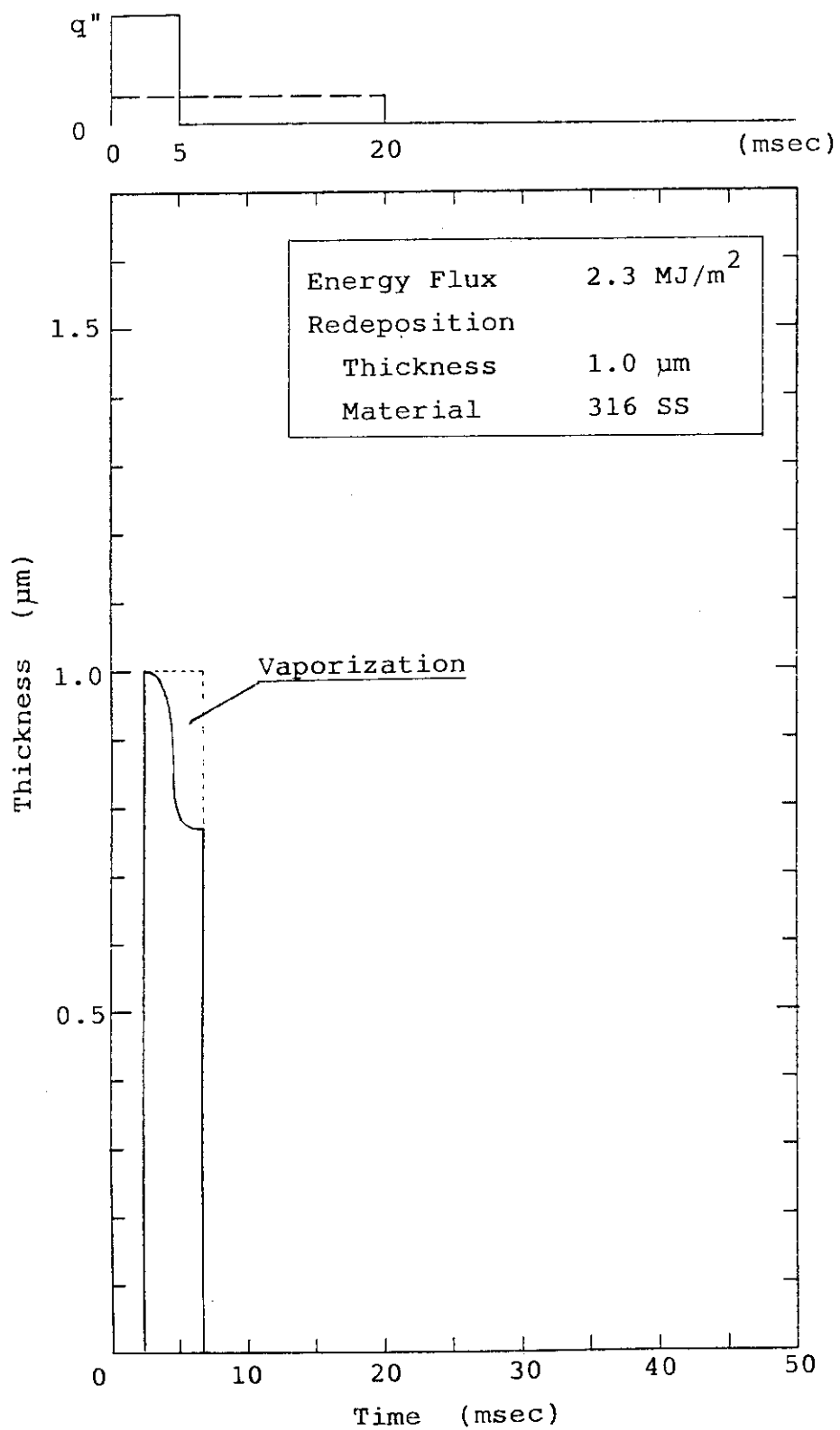


Fig.8.3 Melt Layer Thickness during Major Plasma Disruption

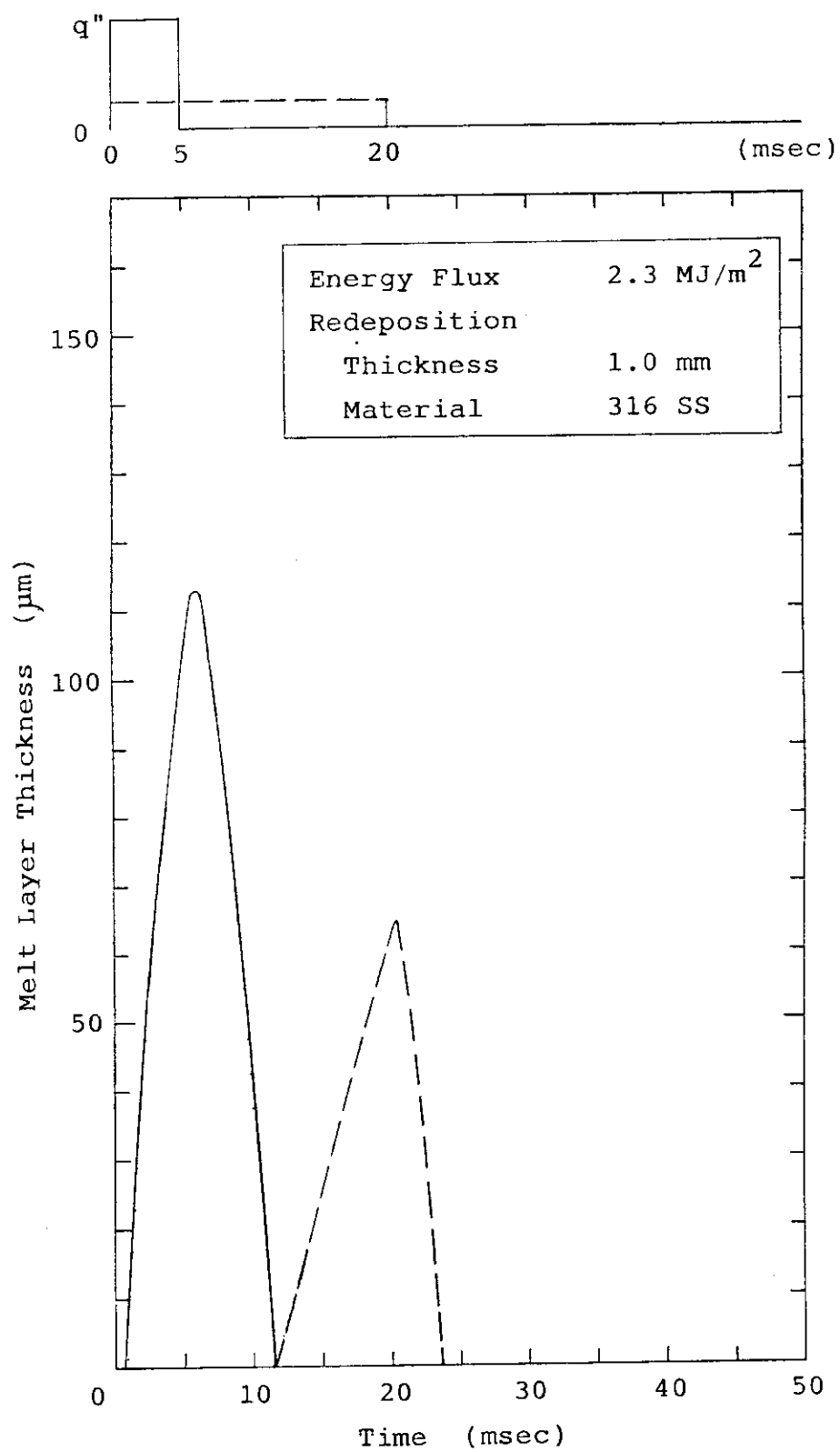


Fig. 8.4 Melt Layer Thickness during Major Plasma Disruption

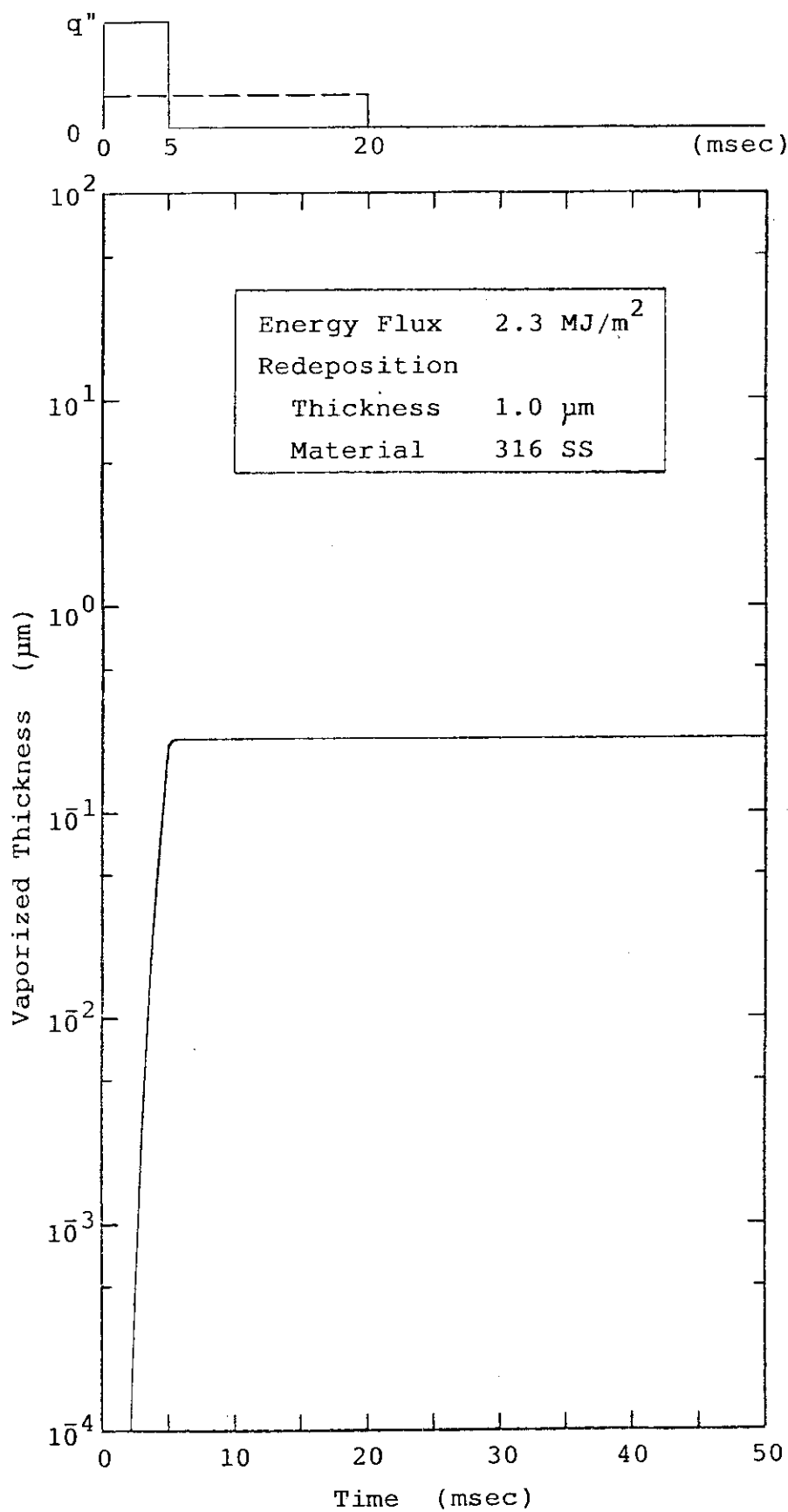


Fig. 8.5 Vaporized Thickness during Major Plasma Disruption

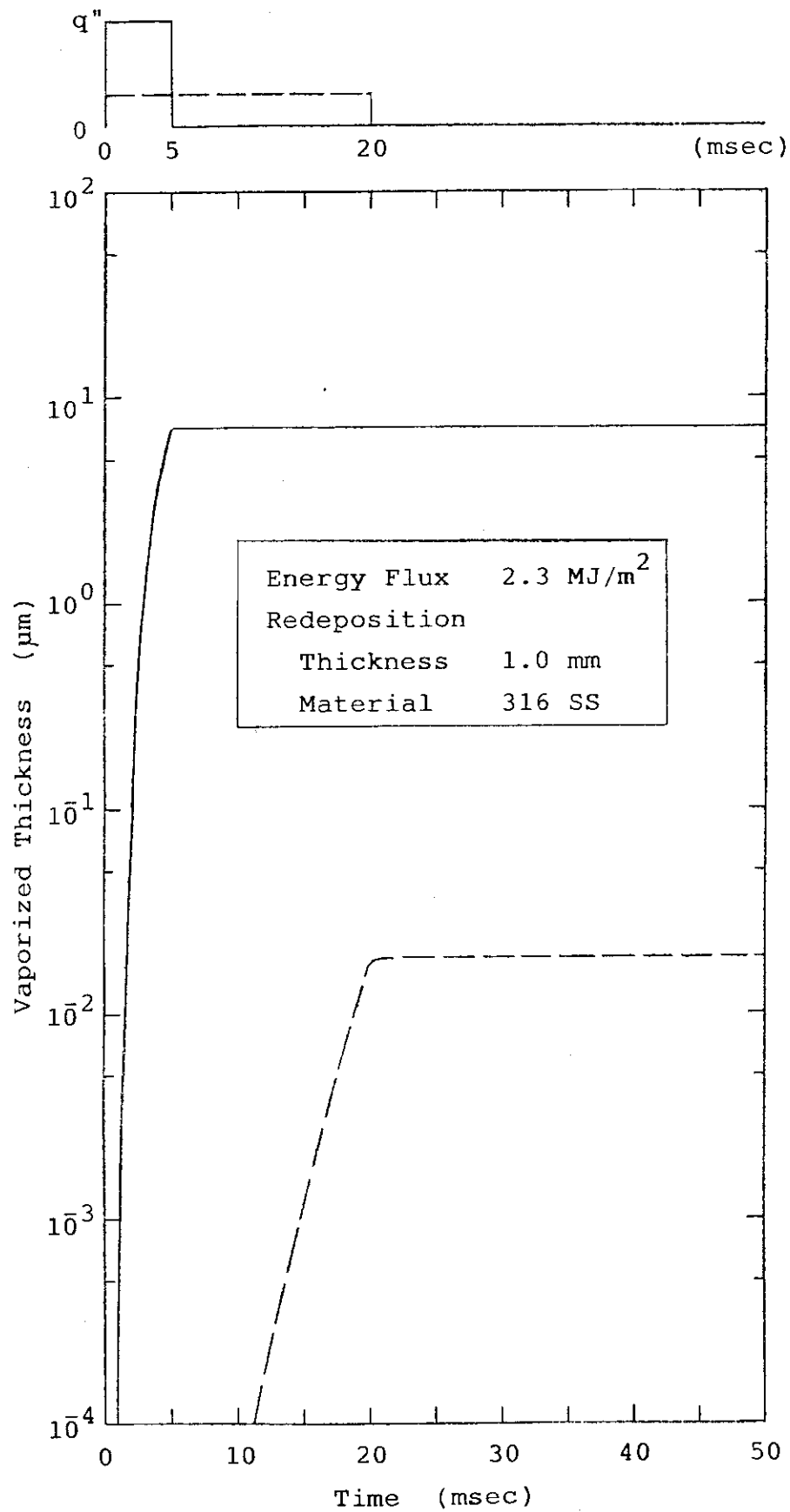


Fig. 8.6 Vaporized Thickness during Major Plasma Disruption

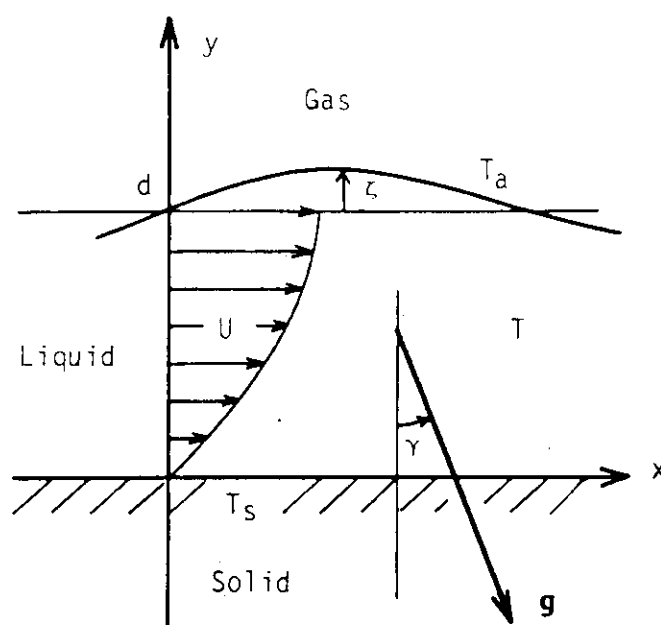


Fig. 8.7 Physical Configuration

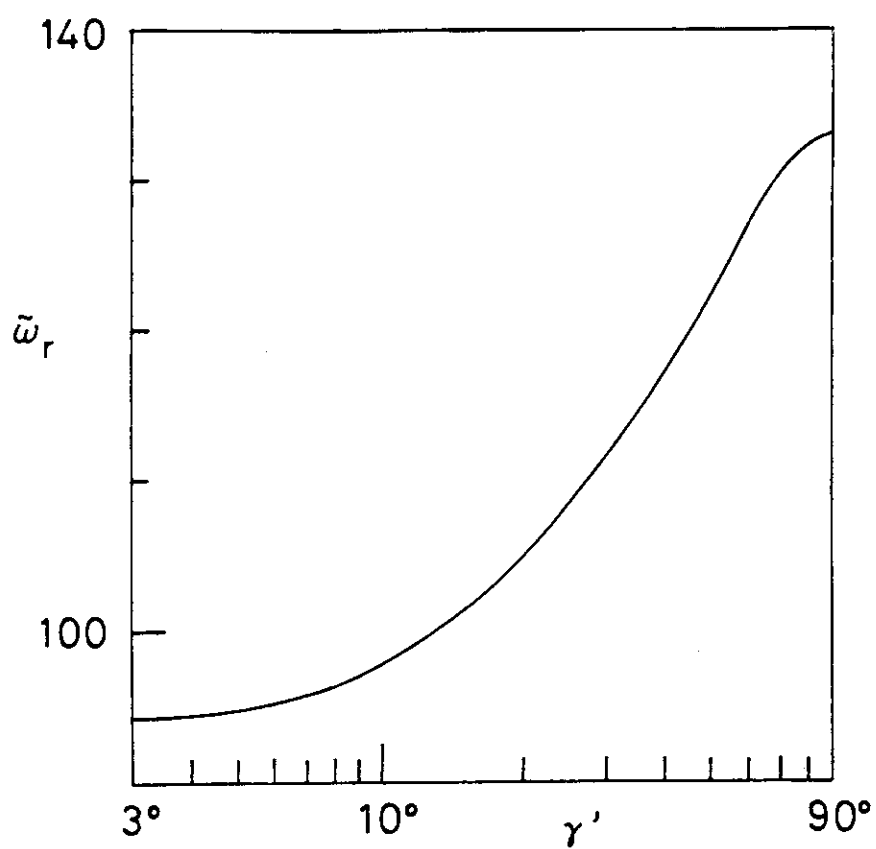


Fig. 8.8 Linear amplification factor vs. inclination

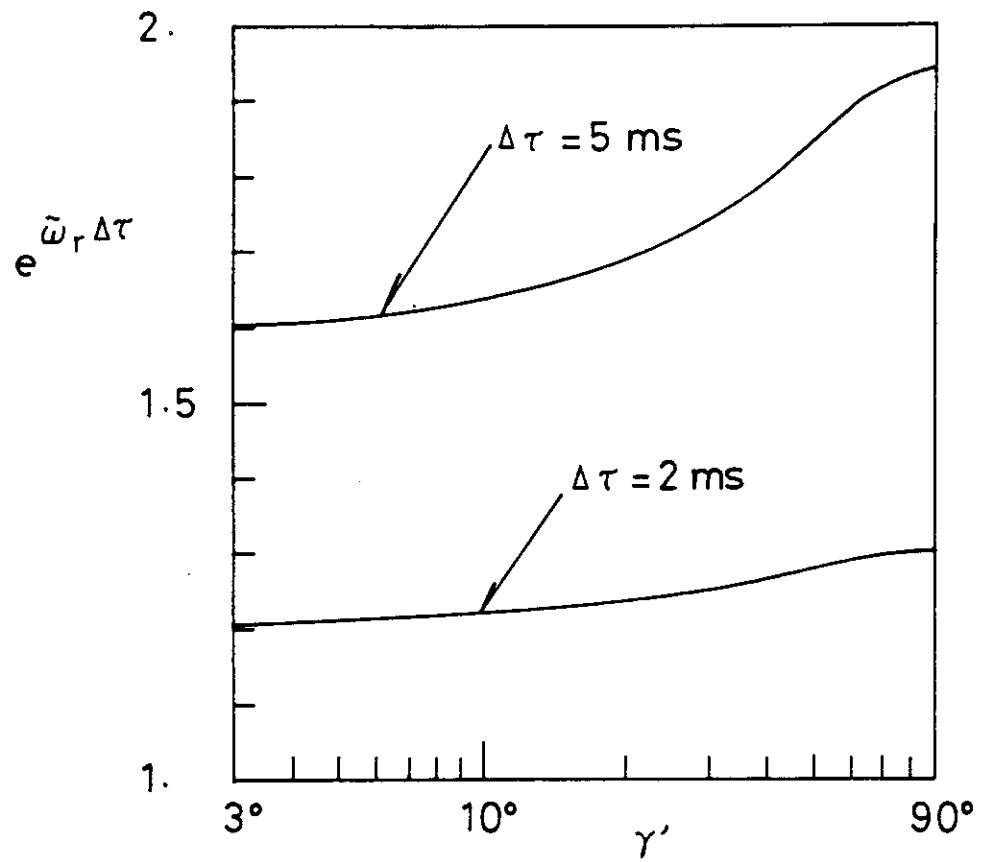


Fig. 8.9 Net amplification vs. inclination

9. Sputtering erosion/Redeposition

A code for calculation of sputtering and redeposition is now being developed at JAERI. Results will be available in the next Phase.

10. Lifetime analysis

The plasma performance, reactor operating scenario, disruption conditions are given in Table 10.1 and Table 10.2. The lifetime of the plate has been estimated by the erosion of plasma side material and the fatigue life.

10.1 Divertor

The divertor collector plates have been assumed to be set at an angle with respect to the magnetic field lines to limit the peak heat flux to 2 MW/m^2 and 5 MW/m^2 . In the case of the heat flux of 2 MW/m^2 , the angle between plate and separatrix is 8° for the inner plate and 6° for the outer one. In the case of heat flux of 5 MW/m^2 , the angle between plate and separatrix is 20° for the inner plate and 14.5° for the outer one.

The plate is composed of a protective material of 1 mm of 3 mm thick tungsten, heat sink of copper and copper alloy, and supporting structure of 316SS.

Table 10.3 shows the erosion rate of divertor plate. The estimated erosion rate does not include the effect of the redeposition of the sputtered impurity ions.

The estimated lifetimes of plates with the copper and copper alloy heat sink are shown in Table 10.4 and 10.5, respectively. The design fatigue curve with the safety factor of 2 on strain range or 20 on life is employed. The stress range used for evaluating the lifetime is the result from elastic analysis. There are many cases that the stress range exceeds the $3S_m$ limit. The real fatigue lives for these cases are shorter than the estimated life shown in Table 10.4 and Table 10.5, and will be evaluated exactly if plastic analysis is used.

As shown in Table 10.4, the fatigue life of the copper heat sink with tungsten tiles is very short. The peak heat flux is needed to be reduced to increase the fatigue life. The lifetime due to erosion is long for the tungsten tiles.

Table 10.5 shows that the copper alloy heat sink has the long fatigue life for the heat flux of 2 MW/m^2 . Fatigue life estimates have been made for the copper alloy with non-annealed material conditions. The plasma spraying may satisfy this condition. However, the plasma sprayed tungsten will provide the quite short fatigue life if tungsten is in the recrystallized condition. The lifetime is reduced to about 0.02 year (10^3 cycles) for a 1 mm recrystallized tungsten under the heat flux of 2 MW/m^2 . Further studies are needed to estimate the accurate lifetime for the plasma sprayed collector plate.

The collector plate lifetime appears to be short for the heat flux of 5 MW/m^2 . The peak heat flux of 5 MW/m^2 may be unacceptable from this standpoint.

10.2 Limiter

Table 10.6 shows the erosion rate of limiter plate at the top surface. The estimated erosion rate does not include the effect of the redeposition of the sputtered impurity ions. The sputtered first wall particles will not deposit on the top surface of the limiter

plate, because the 316SS exceed unity at incident particle energy of 400 eV. However, the sputtered first wall particles will deposit on the leading edge of the plate.

The lifetime of the limiter plate has been estimated by the erosion of plasma side material and the fatigue life of copper heat sink. The estimated lifetime are shown in Table 10.7.

The limiter plate of copper heat sink has the long fatigue life for all cases. However, the lifetime due to erosion is unacceptably short if the effect of redeposition of the sputtered impurity ions is not considered.

10.3 First wall

Table 10.8 shows the first wall operating conditions. The surface heat flux is 10 W/cm^2 and the nuclear heating is 13 W/cm^3 . The first wall is composed of Type 316 stainless steel.

Erosion of the first wall could occur by physical sputtering and disruption. Table 10.9 shows the physical sputtering yields for stainless steel at 100 eV. Table 10.10 shows the wall thickness required to last for the full reactor lifetime under the reactor operating conditions. For the disruption, it has been assumed that the entire melt layer is lost. If the melt layer is stable, no erosion occurs during the disruption, and the thickness necessary for the first wall is only 6.9 mm to last for the full reactor lifetime.

Temperature distribution in the first wall is shown in Fig. 10.1, and thermal stress in the wall is shown in Fig. 10.2. The fatigue lifetime of the first wall has been estimated by using the design fatigue strain range for 316SS, as shown in Fig. 10.3. Figure 10.4 shows the allowable first wall thickness as a function of fatigue life. As the plate erodes, the peak stress levels are reduced. However, the effect of the reduced stress is not included in this analysis because of the uncertainty of the erosion rate.

As shown in Fig. 10.4, the wall thickness required for the full reactor lifetime exceeds the allowable thickness. On the other hand, the wall thicknesses required for Stage (I and II) or Stage III operation does not exceed the allowable thickness. Therefore, it would be necessary to exchange the first wall at least once.

10.4 Benefits of long pulse operation

The purpose of the task is to determine quantitatively the advantages of long pulse operation to the first wall and divertor. The reactor operating parameters and disruption condition are presented in Table 10.11. All other operating parameters has been taken to be the reference parameters from Phase IIA.

10.4.1 Divertor

Table 10.12 shows the divertor operating conditions used for comparison of the reference operation and the long pulse operation. The peak heat flux has been taken to be 2 MW/m^2 . The divertor plate has been assumed to be composed to a protective material of 1 mm thick tungsten, heat sink of OFCu copper, and supporting structure of 316SS.

The lifetime of the divertor plate has been estimated by the erosion of plasma side material and fatigue life of copper heat sink. Table 10.13 shows the estimated lifetime of plate. The estimated

erosion rate by sputtering does not include the effect of the redeposition on the plate of the sputtered impurity ions.

The burn time per year in the long pulse operation is the same as in the reference operation, as shown in Table 10.11. Therefore, the lifetime due to erosion remains the same as in the reference operation. In the Case 2, the lifetime due to erosion is 0.7 year for the plate with 1 mm thick tungsten tiles. The effect of the redeposition will extend the lifetime of plate.

The long pulse operation has the advantage of much fatigue life compared with the fatigue life in the reference operation. For the long pulse operation, the fatigue life of heat sink is 3.3 year in the Case 1, and 1.6 year in the Case 2.

10.4.2 First wall

The first wall operating parameters for the long pulse operation remain unchanged from the reference values shown in Table 10.8. Table 10.14 shows the wall thickness required to last for the full reactor lifetime under the reactor operating conditions. For the disruption, it has been assumed that the entire melt layer is lost.

Temperature distribution in the first wall is shown in Fig. 10.5. Figure 10.6 shows the allowable first wall thickness as a function of fatigue life. As the plate erodes, the peak stress levels are reduced. However, the effect of the reduced stress is not included in this analysis because of the uncertainty of the erosion rate.

As shown in Fig. 10.6, the wall thickness required in Case 2 of the reference operation exceeds the allowable thickness. Therefore, it would be necessary to exchange the first wall at least once. On the other hand, the wall thickness required in the long pulse operation does not exceed the allowable thickness. For the long pulse operation, the lifetime of the first wall is expected to be more than the full reactor lifetime.

10.5 Conclusions

The lifetime has been analysed for the divertor plate, the limiter plate and first wall. The lifetime in the reference operation are:

- (a) The divertor plate will have the unacceptable lifetime under the heat flux of 5 MW/m^2 . The peak heat flux should be reduced to increase the fatigue life. Further studies are needed for the accurate lifetime estimation and the election of reference bonding method.
- (b) The limiter plate of copper heat sink has the adequately long fatigue life for the beryllium and graphite tiles. The lifetime due to erosion is unacceptably short if the effect of redeposition is not considered.
- (c) The first wall is composed of Type 316 stainless steel. If the melt layer is stable, the thickness with an allowance for erosion of first wall is only 6.9 mm, and the first wall is expected to survive the reactor lifetime in terms of fatigue damage accumulation. Using the assumption that the entire melt layer is lost, the first wall has to be replaced at least once.

The lifetime of the divertor plate and the first wall has been analysed for the long pulse operation, and has been compared with that in the reference operation. The advantages of the long pulse operation are:

- (a) The fatigue life of the divertor plate is 5 times longer than that in the reference operation. For the long pulse operation, the fatigue life of heat sink is 3.3 year in the Case 1, and 1.6 year in the Case 2.
- (b) The lifetime of the first wall is expected to be more than the full reactor lifetime. On the other hand, it would be necessary to exchange the first wall at least once for the reference operation of Case 2.

Table 10.1 Common operating parameters

Stage	I	II	III
Plasma			
Thermonuclear power (MW)	620	620	620
α -power (MW)	124	124	124
Neutron power (MW)	496	496	496
Neutron wall loading (MW.m ⁻²)	1.3	1.3	1.3
Operating scenario			
Years of operation	3	4	8
Availability (%)	13.3	25	50
Cycle time (s)	146	246	246
Burn time (s)	100	200	200
Total burn time (s)	8.7×10^6	25.6×10^6	103×10^6
Total cycles	8.7×10^4	12.8×10^4	51.5×10^4
Total neutron fluence	1.5×10^{28}	5.5×10^{28}	22.1×10^{28}
Integral wall loading (MW.a.m ⁻²)	0.3	1	4.2
Disruptions			
(Major disruptions)			
Frequency	5×10^{-3}	10^{-3}	10^{-3}
Disruptions/year	165	31	62
Total disruptions	495	124	496
Total energy (MJ)	290	290	290
Thermal plasma energy (MJ)	230	230	230
Field energy (MJ)	60	60	60
Disruption time			
Poloidal field (ms)	20	20	20
Plasma current (ms)	20	20	20
Thermal energy (ms)			
Reference	20	20	20
Alternate	5	5	5
(Minor disruptions)			
Frequency	10^{-2}	5×10^{-3}	5×10^{-3}
Disruptions/year	330	155	310
Total disruptions	990	620	2480
Total energy to limiter/divertor (MJ)	50	50	50
Disruption time			
Thermal energy (ms)			
Reference	20	20	20
Alternate	5	5	5

Table 10.2 Divertor/limiter disruption characteristics

	Peak energy density ($\text{J}\cdot\text{cm}^{-2}$) *
MAJOR DISRUPTIONS	
Case 1: divertor case	
First wall	170
Divertor plate	230
Case 2: high load to limiter	
First wall	35
Limiter	535
Case 3: reasonable load to limiter	
First wall	170
Limiter	270
MINOR DISRUPTIONS	
Case 1: divertor	
Divertor plate	170
Case 2: limiter	
Limiter	170

* The area of the limiter blade or divertor collector plates
is about 50 m^2 .

Table 10.3 Erosion rate of divertor plate

Stage		I	II	III
<u>Operating conditions</u>				
Particle flux on plate	($\text{m}^{-2}\text{s}^{-1}$)			
Case 1 ⁽¹⁾			1.0×10^{23}	
Case 2			2.4×10^{23}	
Electron temperature on plate	(eV)		35	
Duty cycle	(%)	69	82	82
Availability	(%)	13.3	25	50
<u>Erosion rate of tungsten⁽²⁾</u>				
Case 1		0.3	0.7	1.4
Case 2		0.8	1.7	3.5

(1) Inclination of divertor plate to separatrix

Case 1: 6° (outboard), 8° (inboard)

Case 2: 14.5° (outboard), 20° (inboard)

(2) Self sputtering and redeposition is not included.

Table 10.4 Lifetime of divertor plate with copper heat sink for stage III operation

		<u>1 mm thick tungsten tiles</u>		<u>3 mm thick tungsten tiles</u>	
		Case 1 ⁽¹⁾	Case 2 ⁽¹⁾	Case 1	Case 2
<u>Life due to erosion</u>					
Erosion by sputtering	(mm/y)	1.4	3.5	1.4	3.5
Life	(y)	0.7	0.3	2.1	0.9
<u>Fatigue life of heat sink</u>					
Heat flux	(MW/m ²)	2	5	2	5
Stress range	(MPa)	227	534	300	585
Life	(y)	0.35	0.02	0.11	0.02

(1) Inclination of divertor plate to separatrix

Case 1: 6° (outboard), 8° (inboard)

Case 2: 14.5° (outboard), 20° (inboard)

Table 10.5 Lifetime of divertor plate with Cu-0.6Be-2.5Co heat sink for stage III operation

		1 mm thick tungsten tiles		3 mm thick tungsten tiles	
		Case 1 ⁽¹⁾	Case 2 ⁽²⁾	Case 1	Case 2
<u>Life due to erosion</u>					
Erosion by sputtering	(mm/y)	1.4	3.5	1.4	3.5
Life	(y)	0.7	0.3	2.1	0.9
<u>Fatigue life of heat sink</u>					
Heat flux	(MW/m ²)	2	5	2	5
Stress range	(MPa)	381	813	426	898
Life ⁽²⁾	(y)	3.2	$\sim 0.2^{(3)}$	1.6	$\sim 0.2^{(3)}$

(1) Inclination of divertor plate to separatrix

Case 1: 6° (outboard), 8° (inboard)

Case 2: 14.5° (outboard), 20° (inboard)

(2) Using the fatigue curve under stress control condition for the as-received material (not annealed)

(3) Assuming that number of allowable cycles under 0.6% strain range is 10^4 cycles.

Table 10.6 Erosion rate of limiter plate at the top surface under a medium edge temperature condition

Stage		I	II	III
Operating conditions				
Particle flux on plate	(m ⁻² s ⁻¹)		4.8×10 ²²	
Electron temperature on plate	(eV)		80	
Duty cycle	(%)	69	82	82
Availability	(%)	13.3	25	50
Erosion rate (1)				
Be	(mm/y)	43	95	190
C	(mm/y)	43	95	190

(1) In case of no redeposition

Table 10.7 Lifetime of limiter plate

Material Thickness	Be		C	
	10 mm	20 mm	5 mm	10 mm
<u>Life due to erosion⁽¹⁾</u>				
Erosion by sputtering(mm/yr)		190		190
Life (yr)	0.05	0.11	0.03	0.05
<u>Fatigue life of heat sink(Cu)⁽¹⁾</u>				
Stress range (MPa)	97	106	60	60
Life (yr)	>Reactor life	>Reactor life	>Reactor life	>Reactor life

(1) Life for Stage III operation in case of no redeposition

Table 10.8 First wall operating conditions

Total energy to first wall	37 MW
Surface heat flux	10 W/cm ²
Nuclear heating	13 W/cm ³
Coolant temperature	
Inlet/Outlet	50°C/100°C
Coolant velocity	4 m/s
Heat transfer coefficient	2.5×10^4 W/m ² °C

Table 10.9 Sputtering yield values for stainless steel

Particle energy (eV)	Incident particle	Yield (atmos/particle)	Fraction of flux (%)	Effective yield (atoms/particle)	Fraction of yield (%)
100	D	0.004	50	0.002	33
100	T	0.008	50	0.004	67
100	D+T	-	-	0.006 ⁽¹⁾	100

(1) Corresponds to 2.7×10^{-8} mm/s

Table 10.10 Wall thickness requirement for the first wall

	Stage I (mm)	Stage II (mm)	Stage III (mm)	Over reactor life (mm)
Physical sputtering erosion ⁽¹⁾	0.2	0.9	2.8	3.9
Erosion during disruption ⁽²⁾	6.9	1.7	6.9	15.5
Remaing wall thickness	3	3	3	3
Wall thickness required	10.1	5.6	12.7	22.4

(1) Erosion rate = 2.7×10^{-8} mm/s

(2) Assuming that the entire melt layer is lost

Table 10.11 Parameters for the long pulse operation

		Case 1	Case 2
Reference burn pulse	-	200 S	200 S
Long burn pulse	-	1000 S	1000 S
Availability	-	25%	50%
Total fluence	-	3 MW-a/m ²	6 MW-a/m ²
Reference # of cycles	-	3.3×10 ⁴ /a	7×10 ⁴ /a
	-	3.3×10 ⁵ total	7×10 ⁵
Long pulse # of cycles	-	6.6×10 ³ /a	1.4×10 ⁴ /a
		6.6×10 ⁴ -total	1.4×10 ⁵
Disruptions per pulse	-	10 ⁻³	10 ⁻³

Table 10.12 Divertor operating conditions used for comparison of the reference operation and the long pulse operation

Total power to plate		35.3 MW
Peak heat flux normal to plate ⁽¹⁾		2 MW/m ²
Nuclear heating	W	19 MW/m ³
	Cu	10 MW/m ³
	SS	8 MW/m ³
Coolant temperature		
Inlet/Outlet		50°C/80°C
Coolant velocity		7 m/s
Heat transfer coefficient		3.2×10 ⁴ W/m ² °C

(1) Collector plates are placed at 6° and 8° to magnetic field lines at outboard and inboard locations, respectively.

Table 10.13 Lifetime of divertor plate with 1 mm thick tungsten tiles

	Reference		Long pulse	
	Case 1	Case 2	Case 1	Case 2
<u>Life due to erosion</u>				
Erosion by sputtering (mm/y)	0.7	1.5	0.7	1.5
Life (y)	1.4	0.7	1.4	0.7
<u>Fatigue life of heat sink (Cu)</u>				
Stress range (MPa)	227	227	227	227
Life (y)	0.7	0.31	3.3	1.6

Table 10.14 Wall thickness requirement for the first wall

	Reference		Long pulse	
	Case 1 (mm)	Case 2 (mm)	Case 1 (mm)	Case 2 (mm)
Physical sputtering erosion ⁽¹⁾	1.8	3.8	1.8	3.8
Erosion during disruption ⁽²⁾	4.6	9.8	0.9	2.0
Remaining wall thickness	3.0	3.0	3.0	3.0
Wall thickness required	9.4	16.6	5.7	8.8

(1) Erosion rate = 2.7×10^{-8} mm/s

(2) Assuming that the entire melt layer is lost

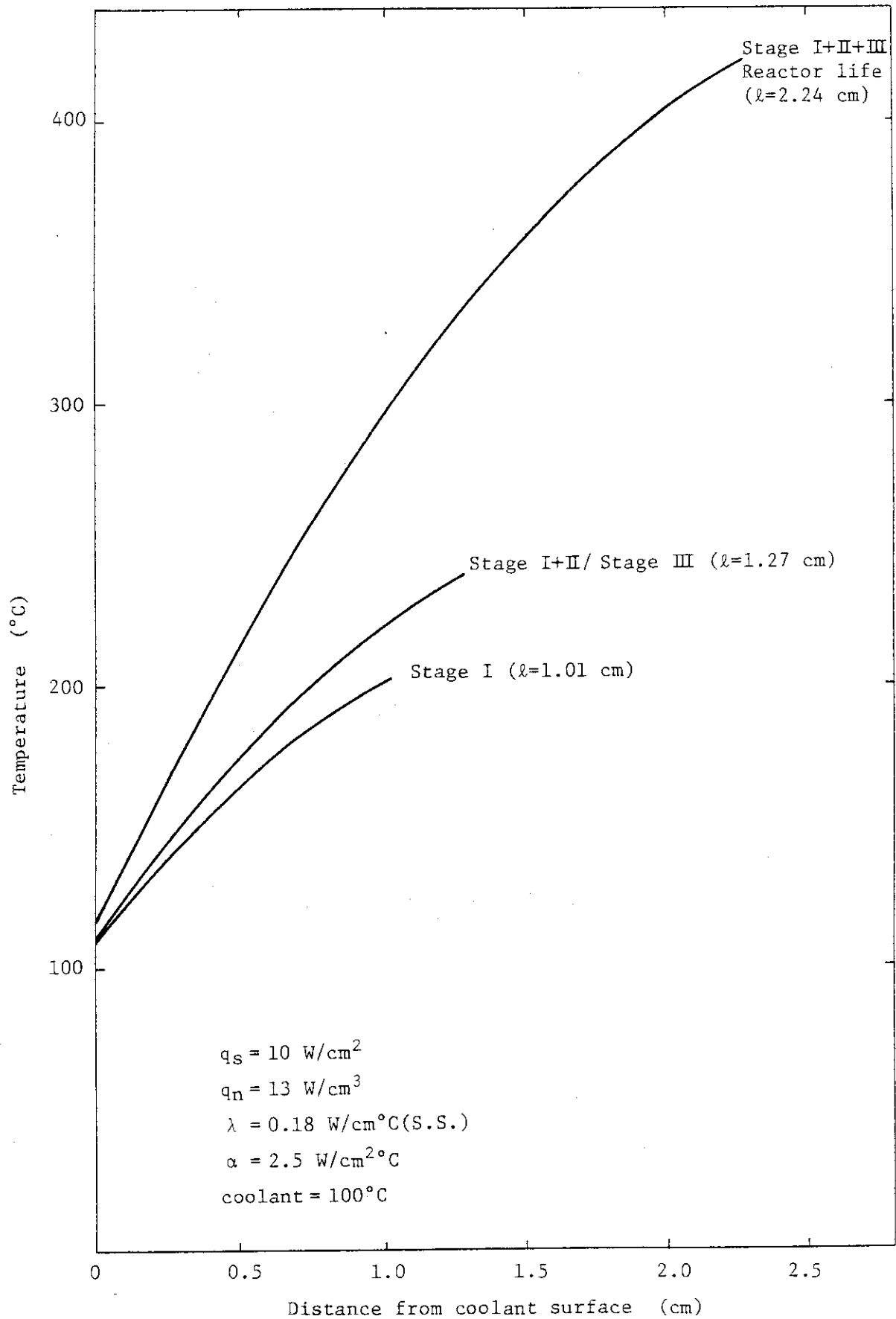


Fig. 10.1 Temperature distribution in first wall

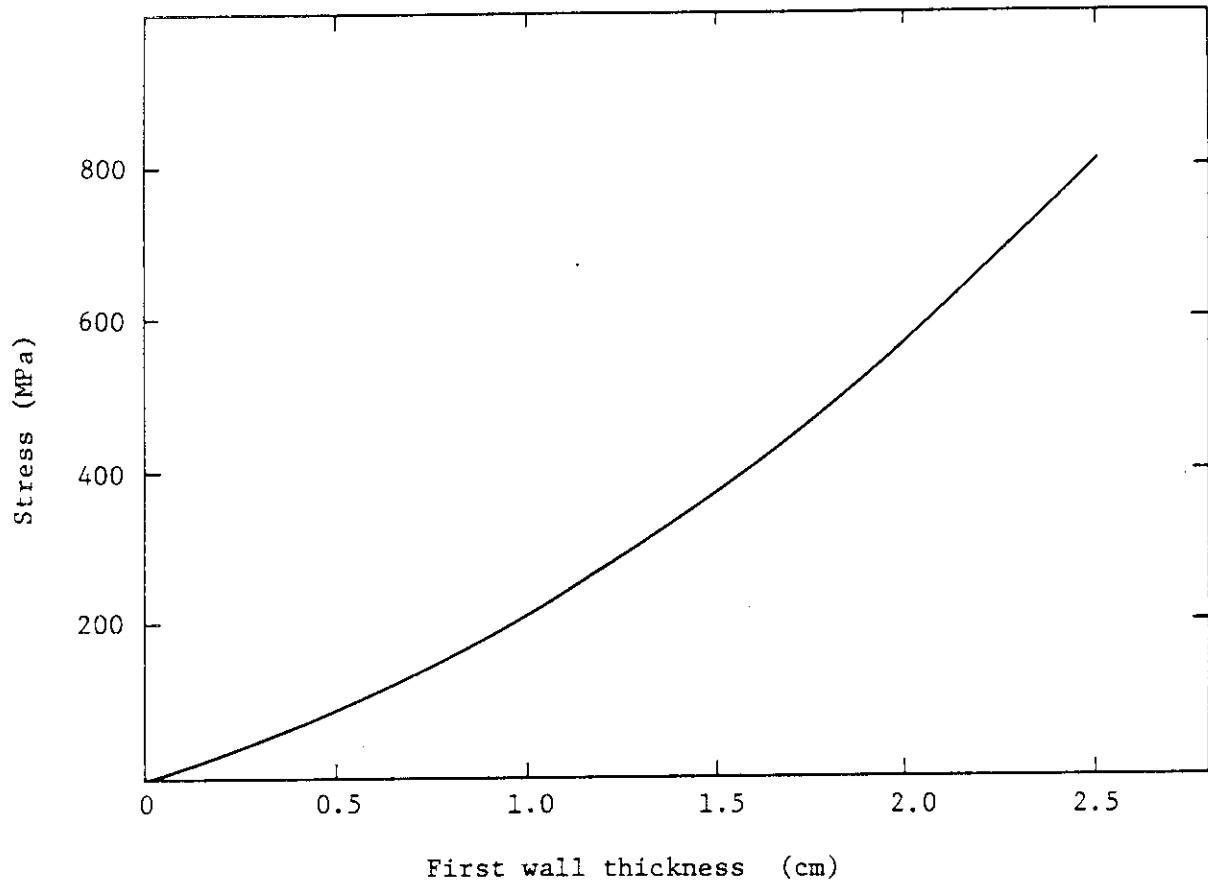
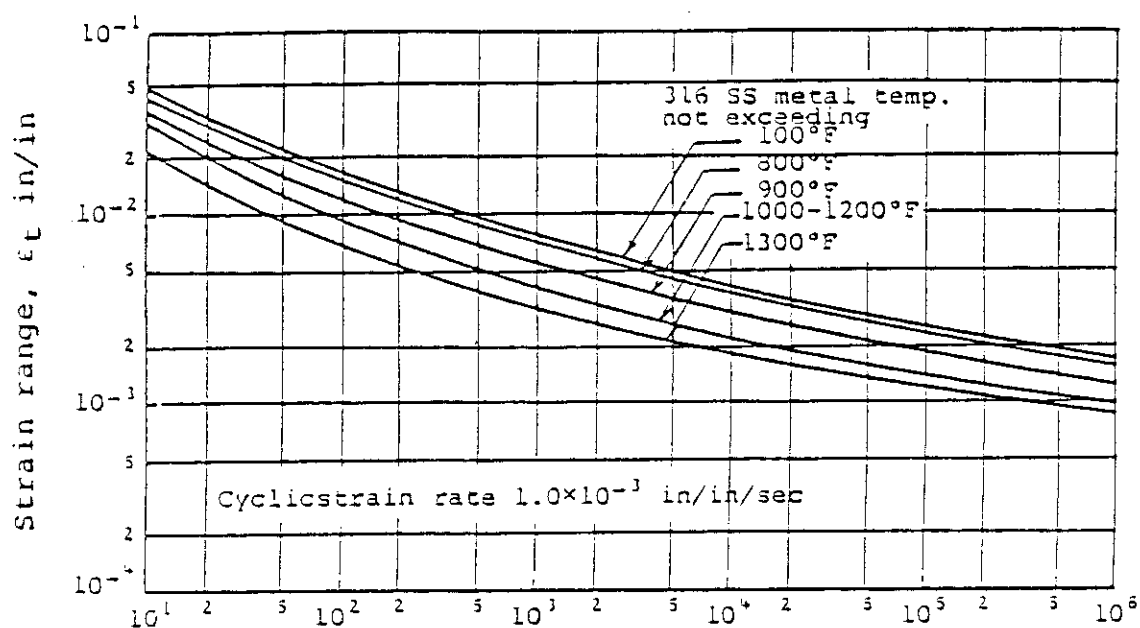


Fig. 10.2 Thermal stress in first wall

Cases of ASME boiler and pressure vessel code

Number of allowable cycles, N_d

N_d Number of Cycles	ϵ_t , Strain range (in/in) at temperature				
	100F	300F	900F	1000-1200F	1300F
10^1	.0507	.0438	.0378	.0318	.0214
2×10^1	.0357	.0318	.0251	.0208	.0149
4×10^1	.026	.0233	.0181	.0148	.0105
10^2	.0177	.0159	.0123	.00974	.00711
2×10^2	.0139	.0125	.00961	.00744	.00551
4×10^2	.0110	.00956	.00761	.00574	.00431
10^3	.00818	.00716	.00571	.00424	.00328
2×10^3	.00643	.00581	.00466	.00339	.00268
4×10^3	.00518	.00476	.00381	.00279	.00226
10^4	.00403	.00376	.00301	.00221	.00186
2×10^4	.00343	.00316	.00256	.00186	.00162
4×10^4	.00293	.00273	.00221	.00161	.00144
10^5	.00245	.00226	.00182	.00136	.00121
2×10^5	.00213	.00196	.00159	.00121	.00108
4×10^5	.00188	.00173	.00139	.00109	.000954
10^6	.00163	.00151	.00118	.000963	.000834

Cyclic strain rate : 1×10^{-3} in/in/secFig. 10.3 Design fatigue strain range, ϵ_t , for SS 316

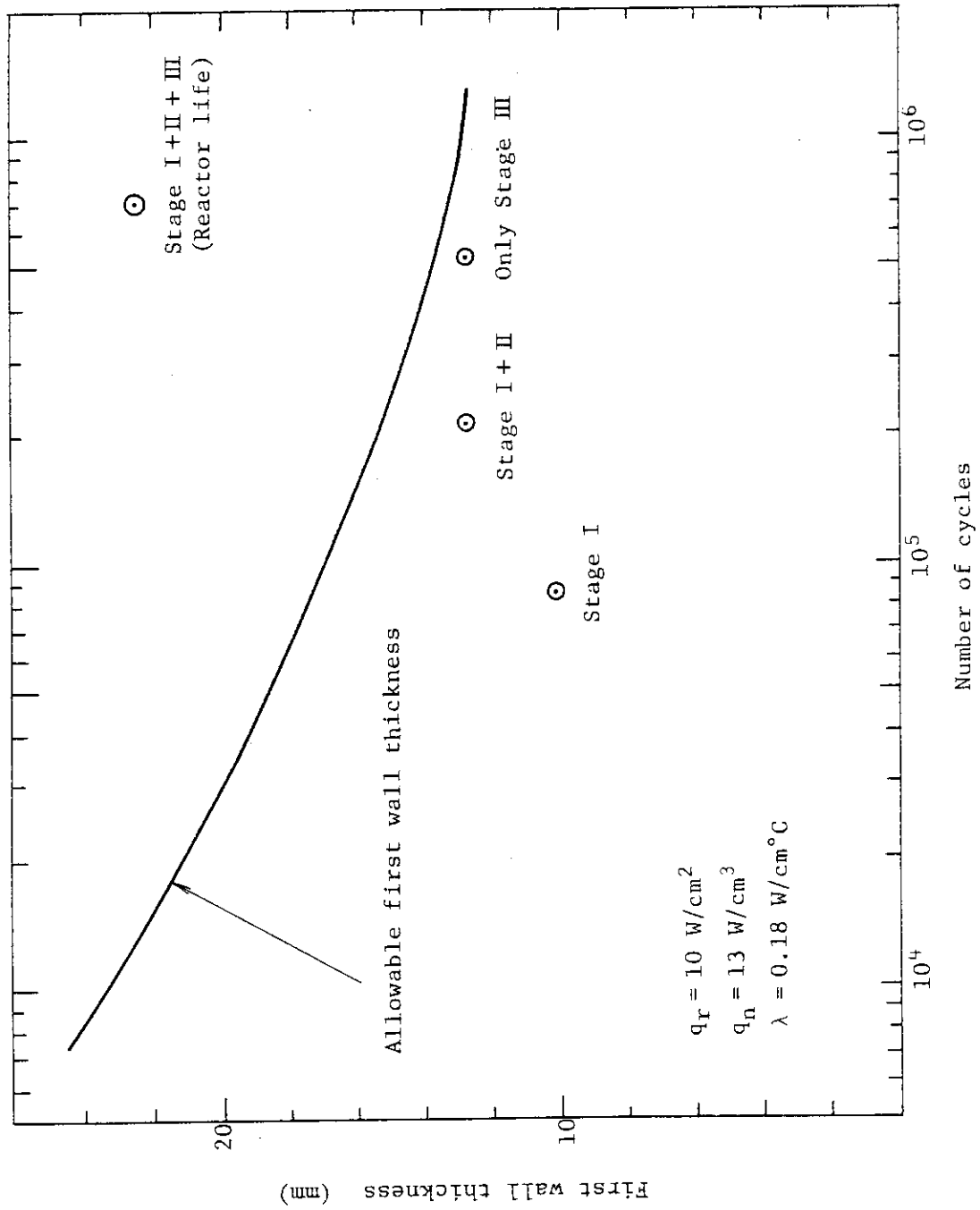


Fig. 10.4 Allowable first wall thickness as a function of fatigue life

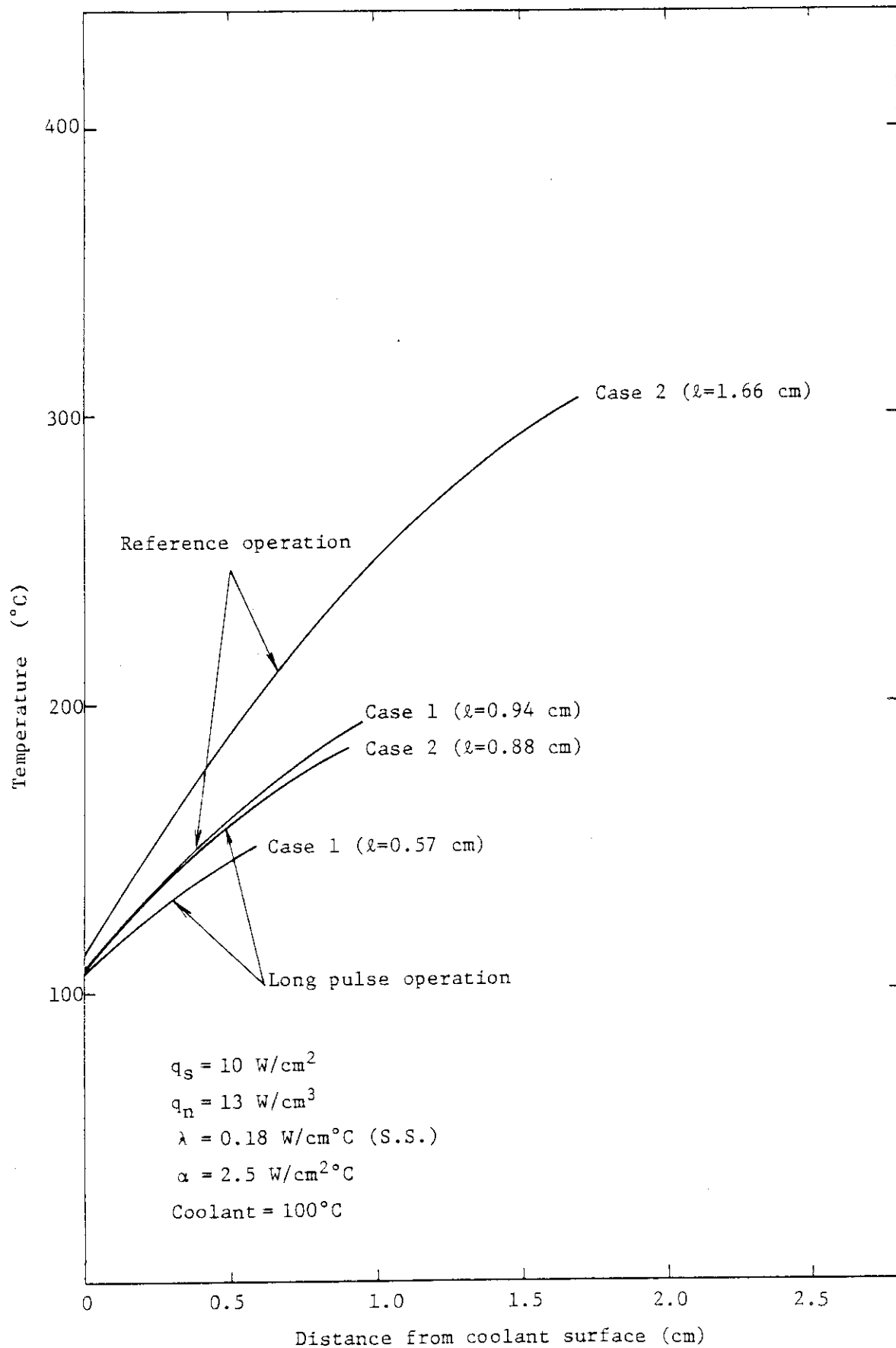


Fig. 10.5 Temperature distribution in first wall

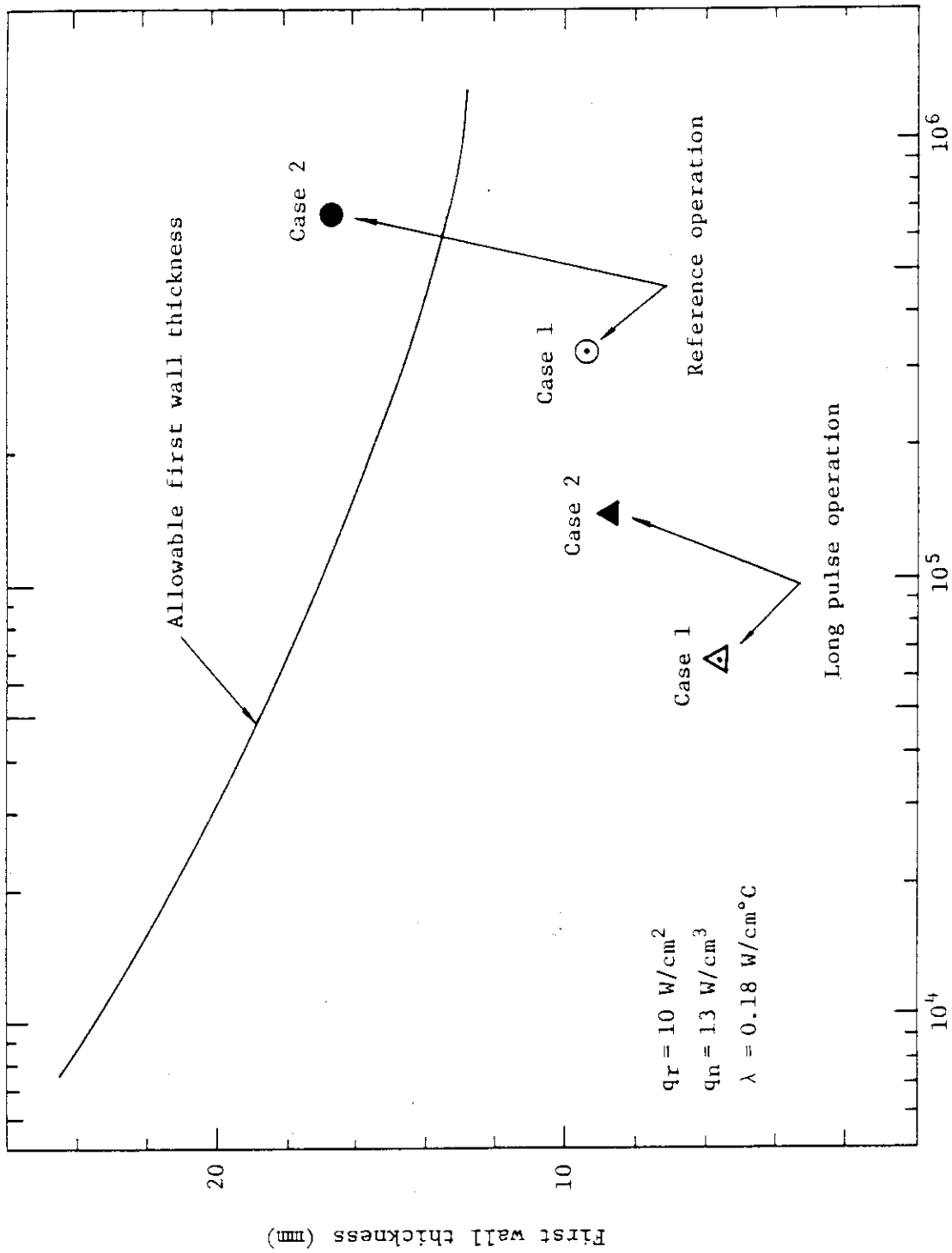


Fig. 10.6 Allowable first wall thickness as a function of fatigue life

11. Tritium permeation through divertor/limiter and first wall

11.1 Tritium permeation into the primary water coolant

One of the potential source of tritium contamination during the maintenance period is the spilled tritiated water when the blanket or limiter modules are disassembled. Tritium concentration level in the primary coolant strongly affects the size of detritiation system. Hence the tritium permeation rate is the key parameter to evaluate a feasible tritium separation method.

The best estimated permeation rate up to the present time is the steady-state rate of about 250 Ci/day most of which permeates through the first wall. The amount of permeation through the graphite limiter is negligible, since the active diffusion in the cooled limiter plate is unlikely due to the large activation energy for hydrogen migration. However, the time to reach the steady-state permeation rate will be beyond the INTOR mission period, it will be more longer if one takes the neutron damage traps into account. It is more appropriate to evaluate the transient-state permeation rate during the plant life time.

We analyzed the transient-state hydrogen isotopes migrations using the numerical code, TRIP (Tritium Reemission, Inventory and Permeation) based on Fickian diffusion equation¹⁻³. TRIP allows us to deal with three hydrogen isotopes simultaneously, tritium decay and an arbitrary running mode like a pulsed operation under the following conditions:

- (a) Molecular recombination release and Sievert's law adsorption,
- (b) Fickian and thermal (Soret effect) diffusion in bulk materials, and
- (c) Interaction with material defect by Willson-Baskes' trapping-detrapping detrapping model.

For the calculation presented here, we used two sets of data base and a set of nominal INTOR conditions shown in Table 11.1-11.4. Though there are still large uncertainties among the experimental data, data base #1 of the stainless steel first wall is adapted as a reference because the tritium diffusion coefficients were directly measured. Graphite as the limiter material has two contradistinctive data sets, one for mobile tritium atoms and the other for almost stucked tritium atoms to the implanted site. Therefore the analytical results based on these data should be carefully applied to the detritiation system.

Transient-state permeation as a function of continuous operation time are shown in Fig. 11.1-11.4. In comparison with a pulsed mode operation, tritium migration during the dwell time is found to be negligibly slow and a 4.1 years continuous operation corresponds to whole INTOR mission period. The results are summarized as follows:

- (1) The permeation through the outboard first wall is no greater than 1 Ci/day at the end of INTOR mission even if the thinner wall corresponding to the end of life is used, as shown in Fig. 11.1.
- (2) The inboard first wall gives same order of permeation rate to the outboard first wall.
- (3) The data sets of hydrogen diffusivities and solubilities for stainless steel make difference of permeation rate by factor 4 as shown in Fig. 11.2. Fig. 11.3 shows that the permeation will

reduce by one order of magnitude if one uses the molecular sticking coefficient of ≈ 0.5 as insisted in ref. 11. The molecular sticking coefficient is the most critical parameter which has strong effects on the magnitude of tritium permeation.

- (4) There is no permeation through the graphite limiter if one uses the data set #1. Conversely, for the set #2 there is a rapid increase of permeation to the order of 10^3 Ci/day after 4 years continuous operation as shown Fig. 11.4. However, the above break-through may not be achieved if the graphite surface is more quickly eroded by bombarding hydrogen atoms than implanted with these atoms. Based on extremely limited data base, it is difficult to obtain more detailed conclusion.
- (5) When tritium permeation into the primary coolant during INTOR mission is under the transient-state, its rate is much less than that of steady-state level even though there is highly uncertainty in the graphite limiter.

11.2 Tritium re-emission from the first wall and limiter surface

Another tritium source during the maintenance period is the reemission of tritium gas which flows into the reactor hall after the reactor vessel is opened to air.

We used the TRIP code with the same data base shown in Table 11.1-11.4 to evaluate the tritium release rate from the stainless steel first wall and graphite limiter. It is assumed that the reactor runs for two year with duty factor 80% and availability 50%, then it is shut down for the repair or maintenance. In some cases one to several days baking at 150 C is considered before air is introduced into the vessel. Results are shown in Fig. 11.5-11.6 and summarized as follows:

- (1) Without baking after the shut down, tritium is released from the first wall at a rate of 500 Ci/day. When the first wall is baked at 150 C for 24 hours, the release rate reduces to 10 Ci/day. It is necessary to bake for more than one week to decrease this value less than 1 Ci/day.
- (2) There is no tritium release from the graphite limiter surface if one uses the data set #1 at a 150°C baking condition. Conversely, for the set of #2 the graphite limiter releases more tritium than the first wall dose. Its release rate exceeds 1500 Ci/day even after 30 days continuous baking as shown in Fig. 11.6.
- (3) If the tritium release from the graphite limiter is negligible, one can expect the tritium release of 10 Ci into the reactor hall of 10^5 m³ per day, in which case room concentration of 10^{-5} Ci/m³ may be obtainable by less expensive tritium control or ventilation system.

References

- 1) Baskes M.I. : SAND80-8201, Sandia National Lab, (1980)
- 2) Wilson K.L. and Baskes M.I. : J. Nucl. Mater., 76&77(1978)291
- 3) Baskes M.I. : ibid., 92(1980)318
- 4) Chaney K.F. and Powell G.W. : Metall. Trans., 1(1970) 2356
- 5) JAERI Group : "Tritium Group Rep-3, Tritium Permeation into Coolant", Rep. for INTOR Workshop, Phase IIA, Section III, (1981)9

- 6) Baskes M.I., Bauer W. and Wilson K.L. : J. Nucl. Mater., 111&112, (1982)663
- 7) Causey R.A., Elleman T.S. and Verghese K. : Carbon, 17(1979)323
- 8) Wilson K.L. : FED-INTOR/TRIT/82-5(USA) Appendix A, Sec. 1.1.3.
- 9) Haggmark L.G. and Biersack J.P. : J. Nucl. Mater., 85&86(1979)1031
- 10) Look G.W. and Baskes M.I. : J. Nucl. Mater., 85&86(1979)995
- 11) Causey R.A., Holland D.F. and Sattler M.L. : Nucl. Technol/Fusion, 4(1983)64.

Table 11.1 Hydrogen diffusivities and solubilities data base
for the materials of this analysis

Material	Data Ba	D^0 ^(a) (cm /sec)	E (eV)	S_0 (atom/cm ³ .atm ^{1/2})	E_s (eV)	Ref
SS	①	2.15×10^{-2}	0.59	1.01×10^{20}	0.094	4), 5)
	②	1.20×10^{-1}	0.61	7.65×10^{19}	0.091	6)
C	①	5.75×10^2	4.27	4.85×10^{15}	-1.44	7)
	②	9.90×10^{-3}	0.5	7.9×10^{20}	0.05	8)

Table 11.2 Hydrogen total detrapping energies data base for the
radiation damage material defect of this analysis ^(a)

	SS	C
ET (eV)	0.85	2.5

(a) from Ref. 8.

Table 11.3 First wall reference Parameters

Parameter	Reference value		
	Out board(BOL)	Out board(EOL)	Inboard(BOL)
Wall thickness(cm)	1.2	0.33	1.4
Wall area(m ²)	266	266	114
Wall temperature(K)			
Plasma side surface	606	438	652
Coolant side surface	394	387	397
Implantation flux (atom/cm ² ·s)	1.7×10^{16} -T, 1.7×10^{16} -D ^(e)		
Implantation energy(eV)	200		
Depth profile	Calculated profile for Maxwellian energy distribution and cosine angular distribution for 200 eV D-T/SS ^(a)		
Reflection coefficient	0.62 ^(a)		
Surface boundary condition	Recombination for both sides		
Molecular sticking coefficient	Plasma side: $\alpha_1=5 \times 10^{-3}$, coolant side: $\alpha_2=0.5$		
Diffusivity, Solubility	Data Base ① ⁽⁶⁾		
Heat of Transport(eV)	-0.065 ^(c)		
Trap	Present: Er = 0.85 eV ^(d)		
Trap concentration	0.01 atom. fraction (uniform and constant)		
Tritium decay	Included		

(a) from Ref. 10

(b) See Table 11.1

(c) from Ref. 6

(d) from Ref. 8

(e) duty cycle = continuous.

Table 11.4 Limiter/Divertor Parameters

Parameter	C/Cu Brazed Limiter		C Armor on Cu Mechanically Attached Limiter	W/Cu Divertor
	Beginning-of-Life	End-of-Life		
Thickness (cm)	1.0/0.2	0.3/0.2	2.0	2.0/0.5
Area (m ²)	32	32	32	10
Plasma side surface	473	443	1650	730
Material interface	425	418	910	430
Coolant side surface	403	403	-	-
Flux (atom/cm ² ·sec)	3.9 × 10 ¹⁸ D-T (a)			3.35 × 10 ¹⁸ -T, 3.35 × 10 ¹⁸ -D
Implantation Energy (eV)	97.5			135
Depth profile	it is assumed to be same as first wall case			
Reflection coefficient	0 (b)			0.7 (b)
Surface molecular sticking coefficient	$\alpha = 0.5$ for the both sides.			
Material data base	See Table 11.1 and 11.2			

(a) In these case, it is assumed that deuterium has same material properties as tritium, except for no β -decay.

(b) from Ref. 9

(c) duty cycle = continuous

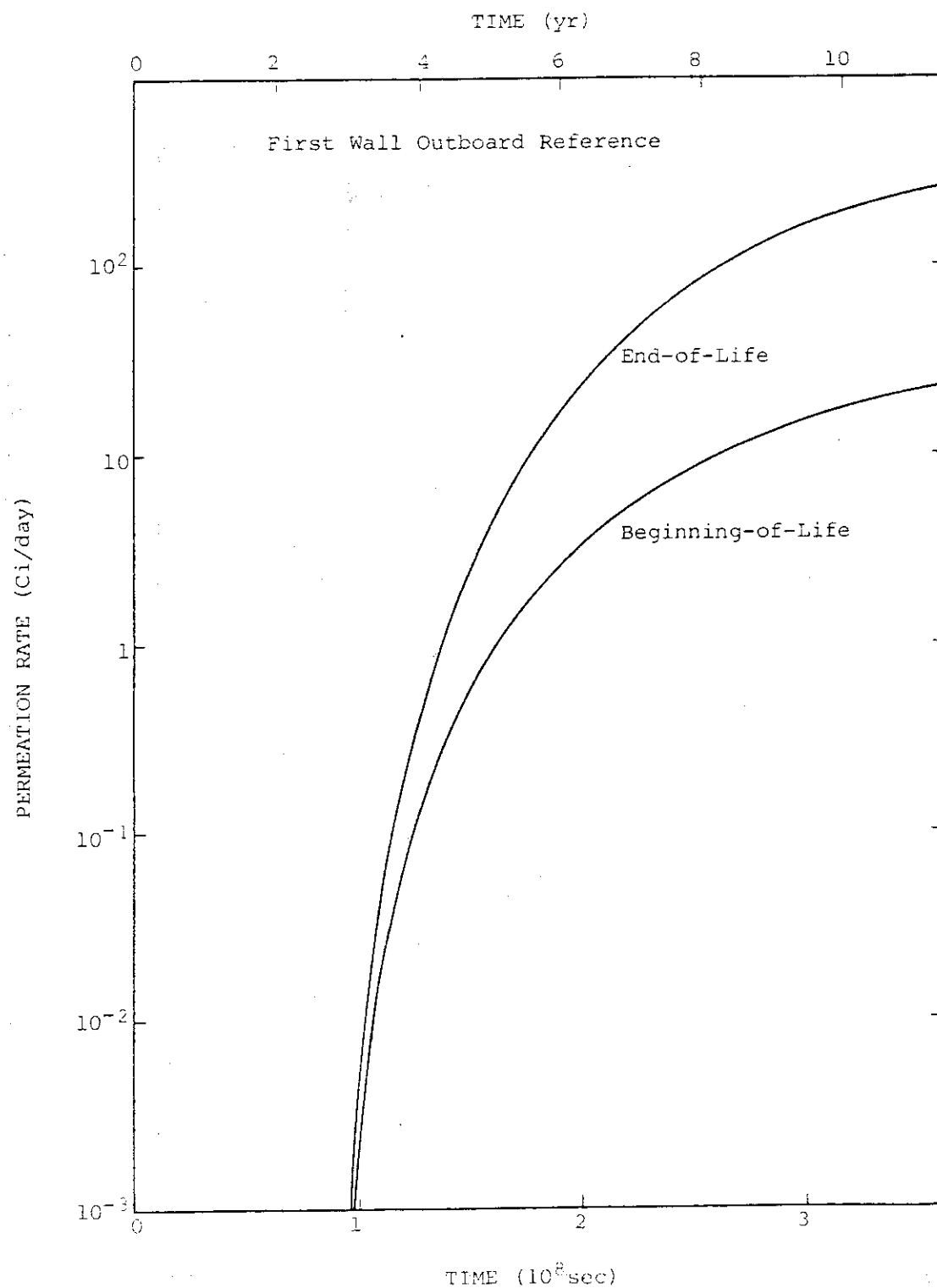


Fig. 11.1 Transient permeation rate as a function of continuous operation time (1)

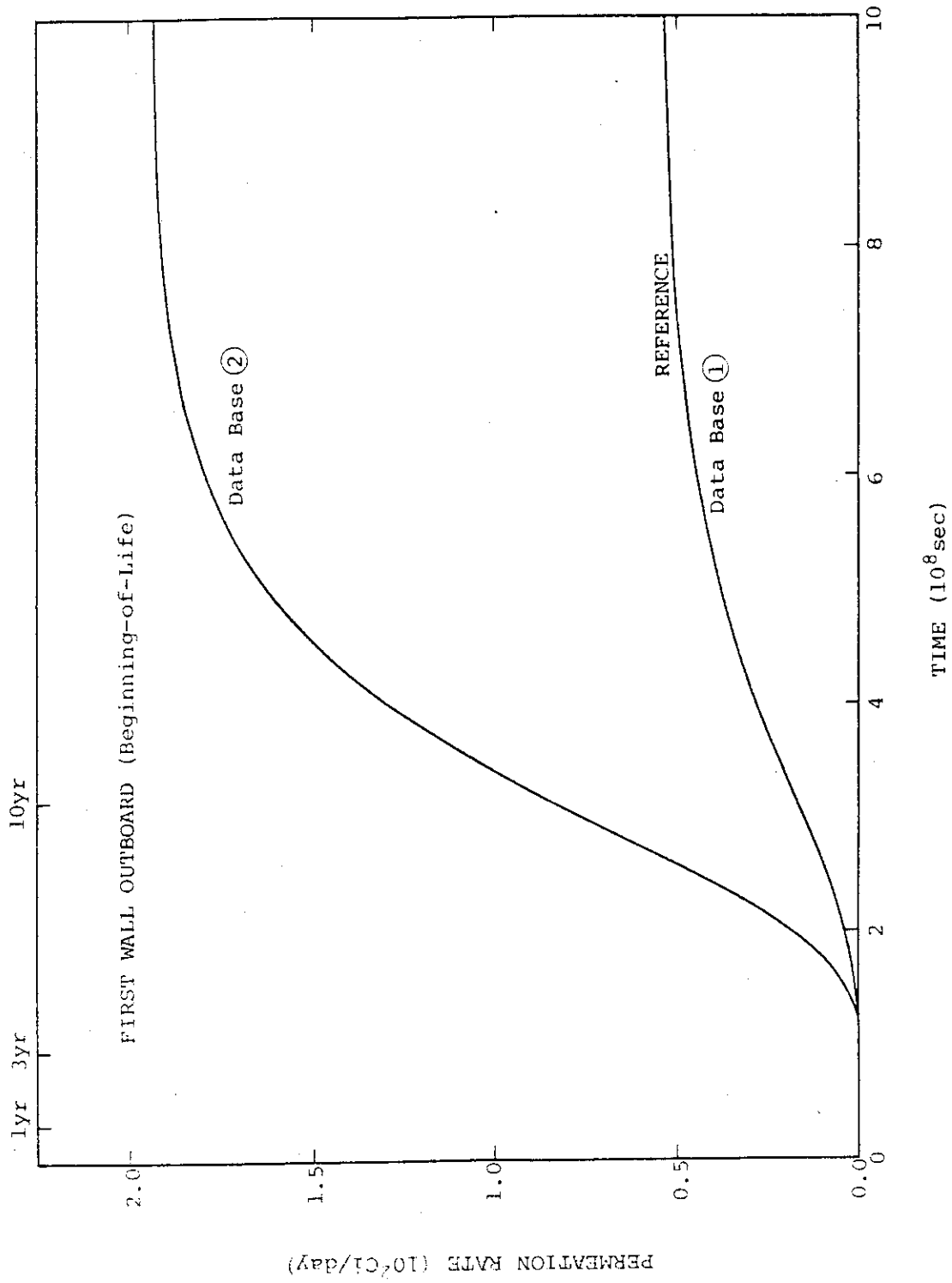


Fig. 11.2 Transient permeation rate as a function of continuous operation time (2)

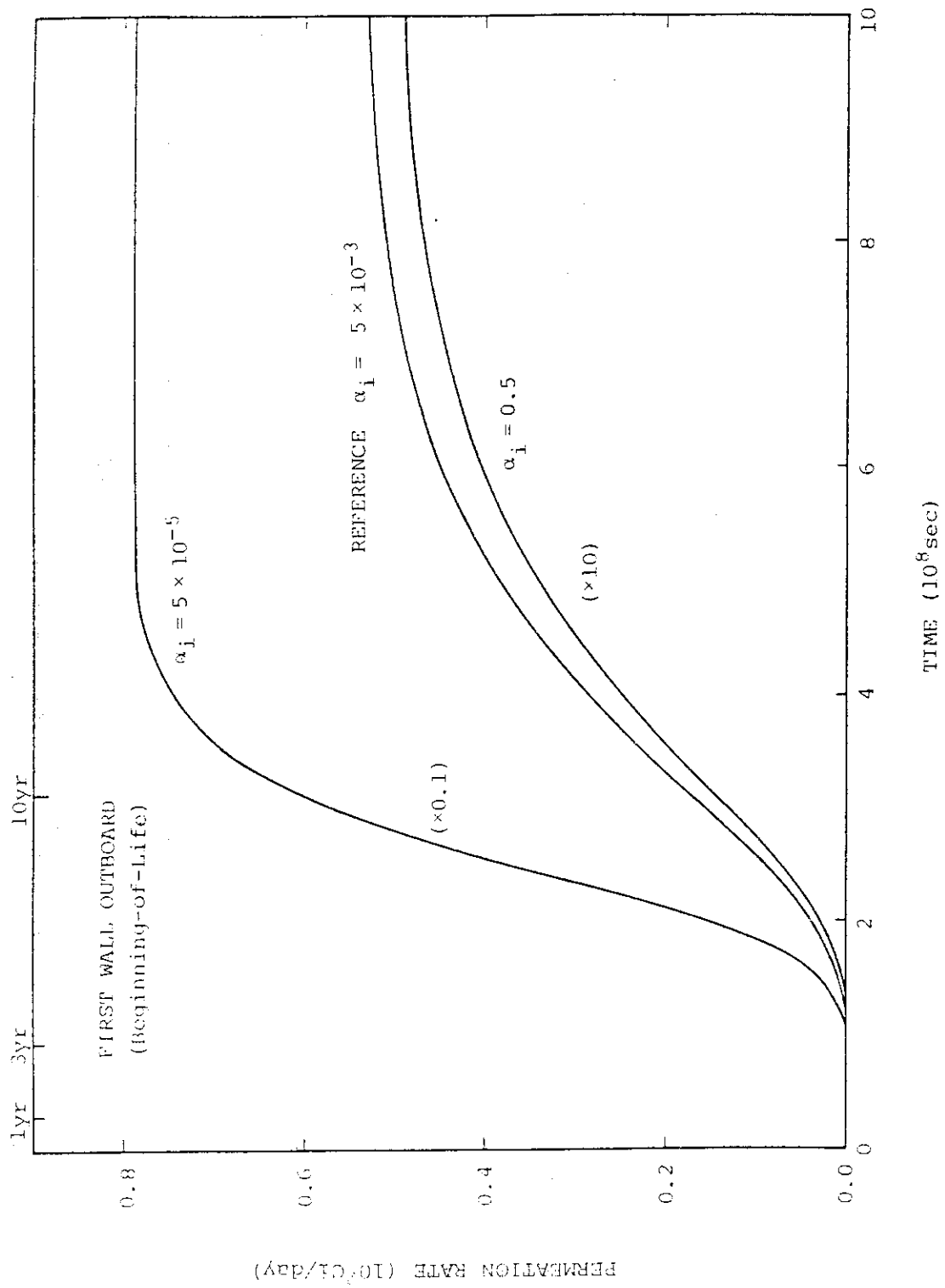


Fig. 11.3 Transient permeation rate as a function of continuous operation time (3)

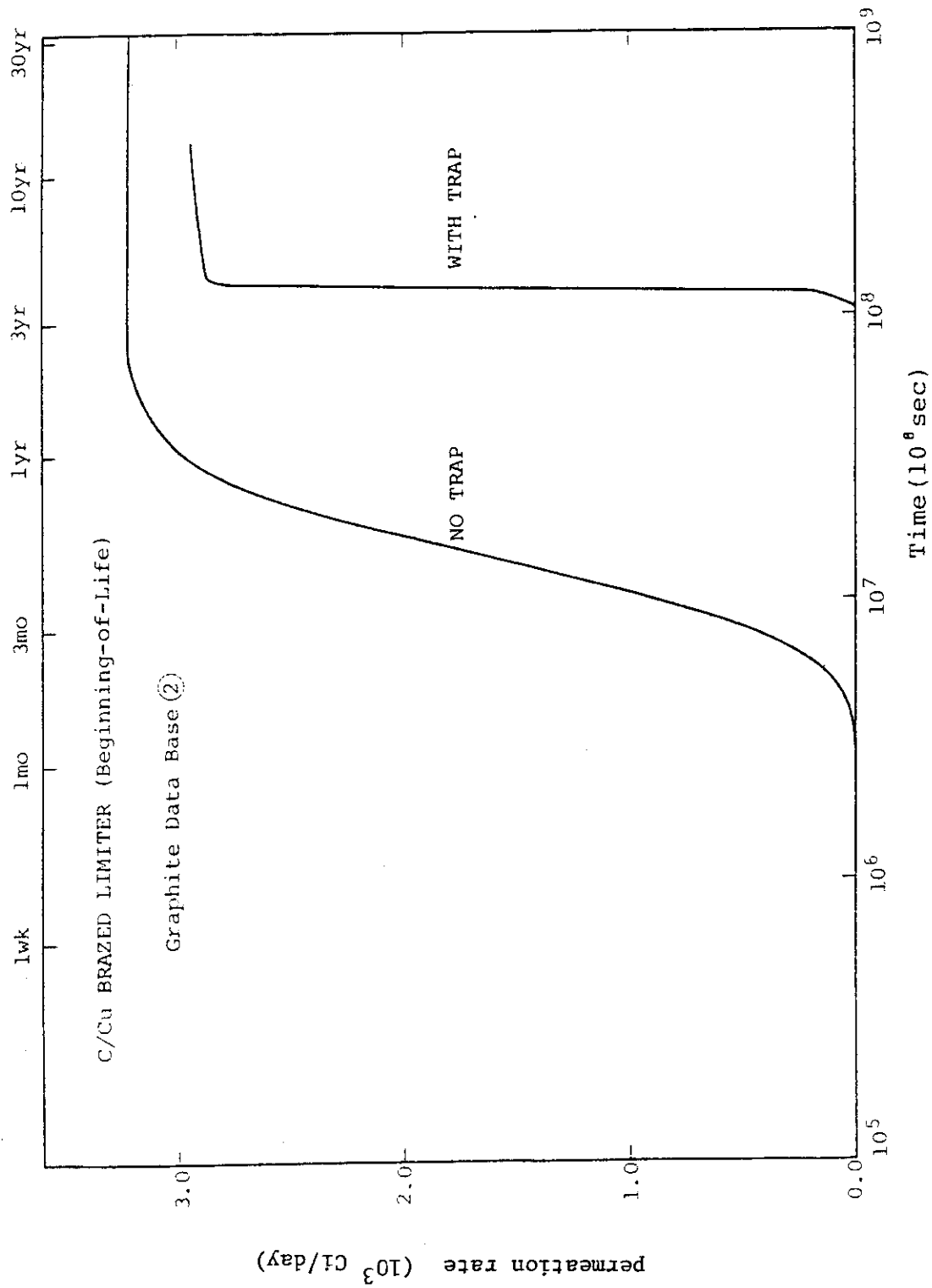


Fig. 11.4 Transient permeation rate as a function of continuous operation time (4)

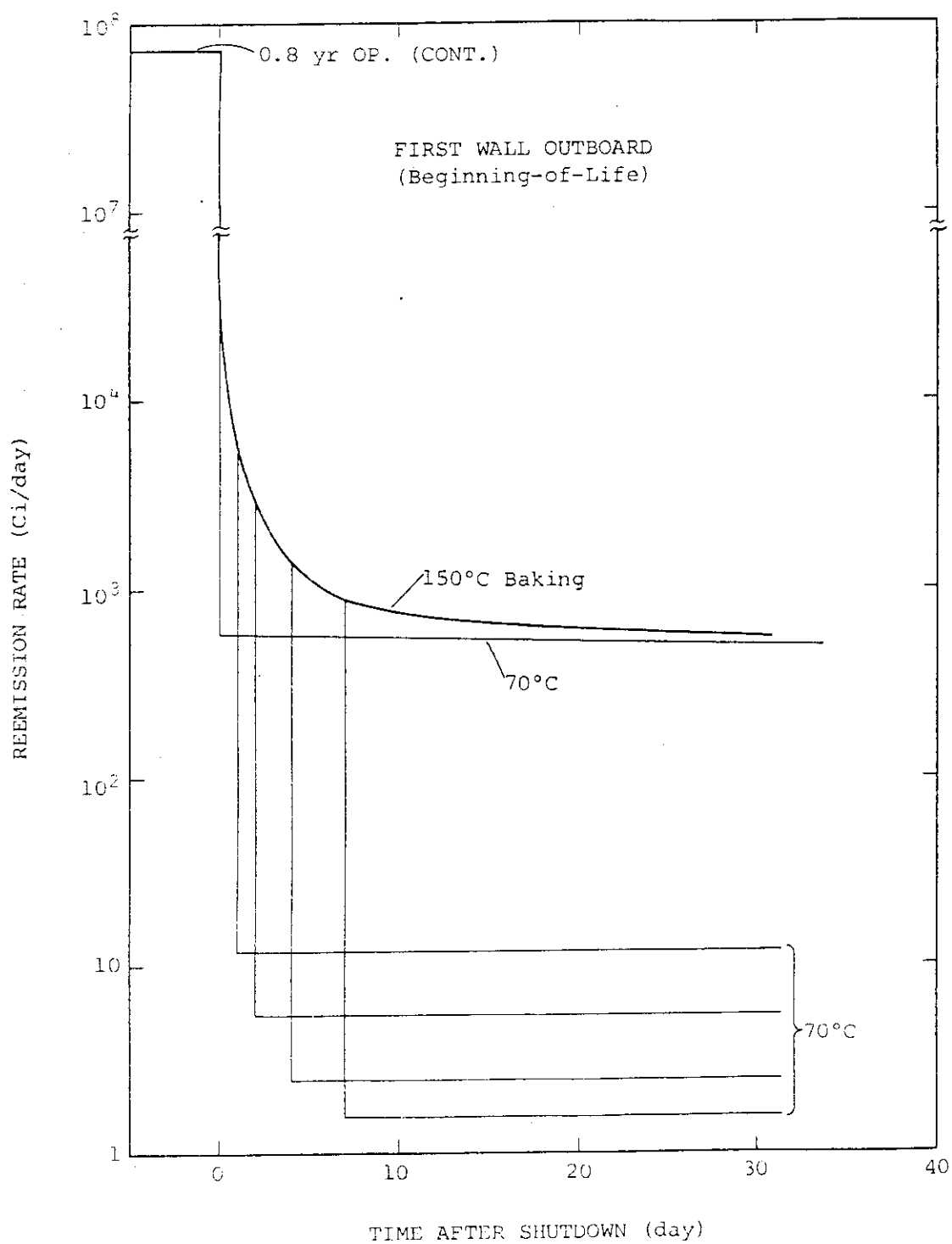


Fig. 11.5 Reemission rate vs time after shut down (1)

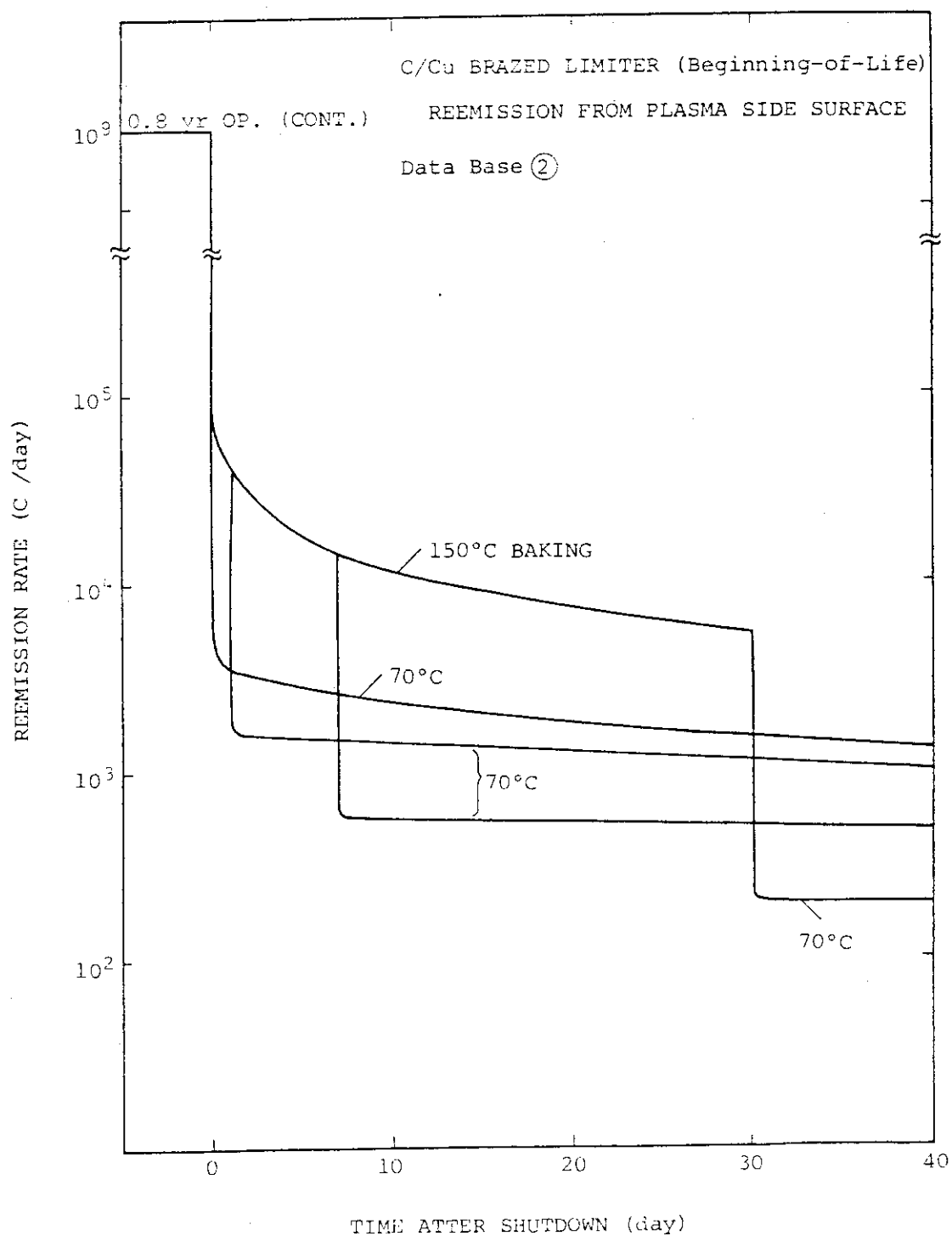


Fig. 11.6 Reemission rate vs time after shutdown (2)

12. Vacuum
No further work has been done in the present phase.
13. Innovative concepts
No work has been done in this area.

12. Vacuum
No further work has been done in the present phase.
13. Innovative concepts
No work has been done in this area.

14. Data Base Assessment

14.1 Impurity control and first wall design requirements

The components include the first wall, pumped limiter, and divertor. These components are subject to high particle and heat fluxes during normal operation, and they are also exposed to intense surface heating during disruption.

The reference operating conditions are listed in Table 2.1-2.3

14.2 Data base assessment

14.2.1 Review of Phase 0, 1, 2A Assessment

A materials data base assessment has been made in previous INTOR reports.

Materials assessed were as follows:

- Plasma-side materials
 - Low-Z : C, Be, B, TiC, SiC, B₄C, BeO
 - Med-Z : Stainless Steel, V
 - High-Z : W, Ta, Nb, Mo
- Heat sink materials
 - Copper alloy
 - Zirconium alloy
 - Niobium alloy
 - Stainless steel

Properties assessed were as follows:

- Plasma side materials
 - Physical sputtering :
 - energy-dependent sputtering yields
 - experimental data on light-ion sputtering for normal incidence
 - Chemical sputtering :
 - hydrogen effects on graphite
 - oxygen effects on tungsten

- Arcing
- H/He retention/release
- Blistering erosion
 - o hydrogen blistering
- Bulk properties :
 - o Thermophysical properties
 - o Tensile properties
 - o Fatigue
 - o Swelling
 - o Low-Z materials
 - o High-Z materials
 - o Redeposited materials
- Heat sink materials
 - Bulk properties
 - Radiation effects
 - o Swelling
 - o Effects on yield stress, ultimate tensile stress, and ductility
 - o Effect on thermal conductivity
 - Corrosion/compatibility
 - Fabrication

14.2.2 Recent Data Base Development

14.2.2.1 Structural materials

14.2.2.1.1 Physical and mechanical properties

Type 316 Stainless Steel, Copper

Pure copper and a copper alloy (Cu-0.6Be-2.5Co) were considered as the heat sink. Type 316 stainless steel was considered for the support structure.

Physical and mechanical properties are given in Table 14.1. The tensile and fatigue properties of OFHC copper and Cu-0.6Be-2.5Co are presented in Table 14.2 to Table 14.5. The strengths in the as-received and the annealed conditions are compared in these tables. Copper and the copper alloy lose the strengths due to annealing.

The room temperature fatigue curve of pure copper under the strain control condition is shown in Fig. 14.1. Figure 14.2 shows the fatigue behavior of OFHC copper at 300°C in high vacuum.

Ferritic Stainless Steels

The alloy development for irradiation performance (ADIP) task has been studying the 9-12 Cr dose of ferritic steels to establish the feasibility of using them in first wall/breeding blanket applications. The advantages of ferritic steels include superior swelling resistance, low thermal stresses compared to austenitic stainless steels, attractive mechanical properties up to 600°C and a service history to > 100,000 hr. The perceived issues are the increase in the ductile-brittle transition temperature (DBTT) with neutron damage, the compatibility with liquid metals and solid breeding materials, and their weldability.

14.2.1.2 Irradiation properties

Type 316 Stainless Steel, Copper

(1) Neutron irradiation data in mechanical properties of copper

Fig. 14.2.2.3 shows the effect of irradiation on mechanical properties of copper, indicating that sharp increase of tensile and yield strength and decrease of elongation in high neutron fluences.

Under the fusion reactor operation at 620 MW, the first wall components are exposed to fast neutron flux of 6×10^{18} n/m². sec, and 9×10^{25} n/m² in 6 months. Copper-made components may suffer severe mechanical property degradation in such high fluence regime. However, high fluence data are not available at this time. It is to be investigated whether high fluence elongation can be extrapolated from the present 10^{24} n/m² data, as shown by the curve in Fig. 14.3.

(2) Swelling

Swelling appears at temperatures between $0.35 T_m$ ($= 202^\circ\text{C}$ for Cu) and $0.55 T_m$ ($= 473^\circ\text{C}$), and maximum value of $\Delta V/V$ is 0.3-0.5% at $0.45 T_m$ ($= 337^\circ\text{C}$) at 5×10^{20} n/cm², as shown in Fig. 14.4.

Swelling is represented as a function of fluence up to 10^{20} n/cm². At swelling peak temperature, 335°C , swelling may reach as high as 10% at the irradiation up to 10^{22} n/cm² if void swelling is assumed to be proportional to (fluence)^{0.75}. However, if the temperature is maintained below 250°C , swelling is suppressed lower than 1.9% even at 10^{22} n/cm² irradiation.

Copper swelling could be ignored by following reasons:

- (i) The maximum temperature of the cooling plate is about 200°C .
- (ii) The limiter plate has a loose structure to permit a thermal deformation. This structure will compensate the volume change by the swelling.

Ferritic Stainless Steel

These steels show the increase in the ductile-brittle transition temperature (DBTT) with neutron damage, and have excellent resistance to total swelling to greater than 110 dpa. During irradiation, the tensile strength of 12 Cr-1 Mo WV and 9 Cr-1 Mo W Nb increase as does the DBTT. At irradiation temperatures of less than 400°C , the DBTT increases more than that of higher irradiation temperatures. After irradiation at $450-500^\circ\text{C}$ in EBR-II to 13 dpa, the DBTT of 9 Cr-1 Mo W Nb does not change significantly, although after 550°C irradiation in HFIR to 5 dpa, the DBTT was 90°C . In 12 Cr-1 Mo WV, the DBTT after 13 dpa at 400°C was 125°C . Based on pressure vessel steel data, the DBTT shift will saturate during irradiation in the 9-12 Cr steels as the increase in hardness slows.

14.2.2.1.3 Coolant compatibility

(Copper)

The corrosion of the copper heat sink was assumed in the Phase IIA Part 1. The major conclusions are:

- (a) The corrosion rates depend on the conductivity and oxygen content in the water, and the temperature and velocity of water.
- (b) The data of the water cooled generator indicate that the

corrosion of copper should not be excessive if the water condition is controlled at reasonable levels.

- (c) The corrosion rate of copper may be approximately 0.06 mm/y at 90°C and 5 m/s of water in the conductivity less than 5 μ S/cm and the oxygen content of 2 ppm.

Ferritic Stainless Steels

The compatibility of 12 Cr - 1M WV with Li and $\text{Li}_{17}\text{Pb}_{83}$ is excellent and is about 10 times less in flowing Li than for the Al81 316. Recent designs in the blanket comparison and selection study (BCSS) have shown that the upper temperature limits placed on the structural materials are primarily driven by corrosion with coolants and with liquid metal corrosion or elevated temperature helium embrittlement (>600°C).

14.2.2.2 Plasma side materials

14.2.2.2.1 Physical and mechanical properties

Tungsten was considered as plasma side material of the divertor plate. Physical and mechanical properties are given in Table 14.1. The elevated temperature properties extracted from PLANSEE bulletin are shown in Fig. 14.5 to Fig. 14.10.

Low-cycle fatigue of cross rolled tungsten is shown in Fig. 14.11 for the as-received and recrystallized material conditions. Tungsten in the recrystallized form exhibits the low tensile strength and short fatigue life.

Zirconium, Beryllium, SiC

No significant new information has become available for this material.

14.2.2.2.2 Irradiation effects

Tungsten

Little is known about the irradiation effects on tungsten. Here, we only show the relative damage rates and the damage efficiencies which are obtained at RTNS-II by measuring electrical resistivity at low temperature.⁽¹⁾

	Damage Rate	Damage Efficiency
V	18.01	0.147
Mo	9.47	0.162
W	11.55	0.345
Al	4.18	0.187
Cu	2.48	0.163

Tungsten seems to be unusual, however further work is required to determine the irradiation effects.

SiC

The thermal and electrical conductivities, fracture strength, and swelling of sintered alpha-phase SiC and siliconized reaction-bonded SiC materials were studied before and after irradiation with reactor neutrons.⁽²⁾ According to the comparison of two kinds of SiC, the

deterioration rate of strength of sintered-SiC is shown to be larger relative to siliconized SiC, under the conditions of $8 \times 10^{20} \text{ n/cm}^2$ and 1000K. This effect is most likely due to the presence of boron in sintered-SiC, which will result in the buildup of the gas. The measurements on swelling $\Delta V/V_0$ of these SiC indicate that the value of $\Delta V/V_0$ is about 1.5% for siliconized SiC and about 2.5% sintered-SiC. Thermal diffusivity dependent on temperature for these SiC shows to decrease largely by neutron irradiation ($7.6 \times 10^{20} \text{ n/cm}^2$), as well known. But, the thermal cycling has little or no effect on fracture strength in these SiC.

14.2.2.2.3 Hydrogen permeation and embrittlement

Solution and diffusion of hydrogen in Tungsten are discussed in Ref. 3. Solubility and diffusion constants are derived from degassing rates. Comparison to theory indicates that the solubility and diffusion constants are characteristic of interstitially dissolved hydrogen. Results are shown in Figs. 14.12 14.19. Transient analysis of tritium migration using these values are seen elsewhere ⁽⁴⁾

14.2.2.3 Bonds

14.2.2.3.1 Physical and mechanical properties

Austenitic Stainless Steels

Austenitic stainless steels have been applied as first wall and blanket structural materials for the INTOR. For the bonding methods of these structural materials, electron beam welding (EBW) and diffusion bonding including hot isostatic pressing (HIP) are expected to be available. The comparison of these bonding techniques is shown in Table 14.6. Especially, diffusion-bonded joints have a potential advantage of mechanical integrity approaching to that of the base metal. However, there has been surprisingly little study on these physical and mechanical properties of bonds.

In this section, recent studies of physical and mechanical properties of bonds for austenitic stainless steels are summarized.

(1) Tensile strength

In the case of fusion welds, tensile strengths of austenitic stainless steel between room temperature and 600°C are slightly lower than those of base metal as shown in Fig. 14.20. It is also clear from this figure that electron beam welds are superior to other fusion welds.

In the case of diffusion bonding, tensile strength depends on the bonding temperature as shown in Fig. 14.21. Tensile strength is reduced drastically as the bonding temperature goes below 1,000°C. Whereas, the bonding temperature above 1,000°C enables tensile strength of bonds to be equal to or higher than that of base metal. At high bonding temperature beyond 1,000°C, however, bonds and base metal may suffer reduction in properties caused by excessive grain growth. So that, the optimum bonding temperature should be established taking the effects of grain growth into consideration.

(2) Creep rupture strength

Creep rupture strength of austenitic stainless steel fusion welds between 500 °C and 600 °C are lower than that of base metal as shown

in Fig. 14.2.2.3-3. Creep rupture strength of electron beam welds, which is superior to that of other fusion welds, tends to approach gradually to that of base metal with increasing the rupture time. Creep rupture data of diffusion bonds for austenitic stainless steel have apparently not been published to date. However, creep rupture strengths of bonds by HIP and press rod type are expected to equal to or higher than that base metal, if bonding temperature is above 1,000 °C.

Tungsten Copper joints

Tungsten has been successfully joined to the copper heat sink by brazing, casting the copper onto the tungsten, and plasma spraying of tungsten.

The data base is inadequate for the bond properties. Development is needed to establish the data base for the bond properties and the reference bonding method. Additional development is required for experimental confirmation of component performance under the repetition of high heat flux.

14.2.2.3.2 Irradiation effects

Reports on irradiation effects on mechanical properties of electron beam welds and diffusion bonds for austenitic stainless steel have apparently not been published to date although those for such fusion welds as shield metal arc welding have been published.

Table 14.7⁽⁵⁾ and 14.8⁽⁵⁾ show irradiation effects on tensile properties of stainless steel fusion welds. There is no significant difference in tensile properties at RT between unirradiated and irradiated specimens of welds. At 400°C, however, the irradiated specimen of welds exhibits high tensile strength compared with the unirradiated one. Decreasing of toughness by irradiation, which is observed in base metal, is also seen in the welds as shown in Fig. 14.23⁽⁵⁾. As for the creep rupture life, no consistent irradiation effect is detectable as shown in Fig. 14.24⁽⁵⁾.

Irradiation effects on mechanical properties of diffusion bonds are expected to be same as base material because of no structure change in bonded zone. At any rate, it is hoped to investigate the irradiation effects on mechanical properties of electron beam welds and diffusion bonds.

14.2.2.5 Fabrication Development

14.2.2.5.1 Primary Fabrication

Process involved in transforming raw materials into consolidated forms doesn't leaves any special problems except for manufacture of heavy-section shell conductor material and neutron multiplier material. These are now designed to be made of 60 mm-thick beryllium plate which has no manufacture experience. Beryllium plate employed for shell conductor and neutron multiplier is required to be ductile from viewpoint of strain under operation.

Above-mentioned beryllium plate is feasible to be manufactured by the present hot pressing technique. However, it leaved some uncertainty and concern about its ductility.

It is supposed that such a heav-section and ductile beryllium plate can be manufactured by Hot Isostatic Pressing technique which is considered one of new processes, and it should be confirmed by pilot production of such a plate.

14.2.2.5.2 Secondary Fabrication

Transforming the products of primary fabrication into finished products consists of fabrication techniques such as plastic work, precise bending of breeder cooling tube, precise machining of blanket vessel and others.

Large machining center with adaptive control system, MD-NC system and CAD/CAM system, which have been recently applied in aircraft industry, is available to precise machining of large and thin-wall blanket vessel. The outline of these systems is explained as follows;

1) Adaptive Control Systems

Adaptive control system is very useful for machining of large, thin-wall and complicated components, in which machining conditions is controlled by sensing.

2) MD-NC System

MD-NC System is available in case that machining is repeated for the works of same size and same dimension such as blanket vessel units. This system enables machining by numerical control, using master dimensions.

3) CAD/CAM System

NC programming is so troublesome and annoying in numerically controlled machining of blanket vessel that many a manhour is needed for programming if done manually. CAD/CAM system is available in making programming tapes for numerical control from CAD drawing by computer.

14.2.2.5.3 Bonding

Bonding of first wall, shell conductor, blanekt vessel wall, breeder cooling tube and so on are respectively important technical points. And quality assurance of these bonded parts should be attached much importance to. New processes of these technical points are shown blow.

1) Bonding of First Wall

It is required especially from stringent loading conditions to consider both less deformation due to bonding and joining at low temperature. From this point of view, HIP method is potentially feasible enough to be applied to first wall bonding by large-size machine. This HIP method is grouped into "deformation welding" which is called "deformation diffusion welding". By this method, bonding is carried out at rather low temperature than by diffusion welding. It doesn't require precise machining for joint preparation. It should be considered that chromium oxide precipitation at the grain boundary is minimized.

2) Bonding of Blanket Vessel Wall

It is desired from viewpoint of less deformation resultant from welding that heat source of high energy density is applied to bonding of blanket vessel wall. And welding joint is not simple for blanket vessel wall bonding. From above-mentioned points of view, electron beam welding machine with multi-dimension path control system is considered to be one of effective element techniques.

3) Bonding and NDE of Breeder Cooling Tube Joint

Inner bore welding of butt joint between tube and tubesheet is most proper method to assure the integrity of welds. Pulse-TIG inner bore welding will be applied to this joint. NDE of the welds can be performed by small-size RI such as $^{170}\text{Tm}(\phi 1 \text{ mm})$ or micro-focus X-ray unit.

4) New Bonding Technology of SiC Ceramics and Metals

Newly developed high grade SiC ceramics (a surprisingly high thermal conductivity with high electric resistance SiC, and a high thermal conductivity with a good electric conductivity SiC) and eutectic bonding [EB] method applicable to them have been developed.

The EB technology is used successfully for bonding metals to the SiC ceramics interposing a complicant metal layer made of copper-carbon fiber composite (medium thermal expansion coefficient) between them. The structure of the bonded material is shown in Fig. 14.25.

Bonding Conditions

Atmosphere : Air
 Heating Temp.: 880 °C
 (RF Ind. Heating)
 Bonding Pressure : 5 kgf/cm²
 Press. Loading Time : 1 sec

Results

High Bonding Strength : > 200 kgf/cm²
 Applicability to Wide Bonding Area : Up to 2 inches sq.
 Low Residual Stress at the Bonding Interface :
 Use of Compliant layer (Cu-C Fiber Composite)
 Durability under the High Heat Flux: Up to 800 W/cm² (under the
 water cooling of metal side)

5) Low Pressure Plasma Sprayed Titanium Coatings⁽⁹⁾

Plasma spray process which can produce metal and ceramic coatings have extensively been employed in a variety of engineering applications where surface hardness and corrosion resistant property are important. But, when plasma spray coating is carried out in the air the plasma jet is mixed with a considerable amount of the air. As a result the surface of the molten metal particles in the plasma jet is oxidized by oxygen in the air, and the metal oxide film is formed. The metal oxide causes the coatings to be porous having the defects such as the microvoid or microcrack, and lowers the density of the coatings down to 70% - 80% of the theoretical value.

However, conventional plasma sprays utilize only the high thermal energy and the high velocity of the plasma jet.

It is worth while to note that the gas in the plasma state is in excited state where chemical reactions easily take place. Therefore, it is considered that with the plasma spray process, it may be possible to utilize the excited state N_2 gas of the plasma jet to nitride metal powders which are sprayed. For this type of application it is necessary to prevent oxidization of powders as well as to control the reaction between N_2 and the metal powders. LPC process which can satisfy the above two requirements is considered to be suitable for this application and Ti powder has been sprayed which easily reacts in N_2 with LPC process using N_2 as a plasma gas. LPC sprayed Ti coatings by N_2 - H_2 mixed plasma gas are shown to be very dense and less porous. The hardness of these coatings is Hv 800 and by controlling the ratio of Ti nitride content, very hard and dense coating is constant at Hv 800 to 450 C.

6) TiC coating

The development of titanium carbide (20 μ m thickness) coated first wall of which substrates are molybdenum and Inconel 625 has been carried out. TiC coating onto Molybdenum and Inconel 625 requires the deposition temperature below 950 °C and 600 °C respectively, because the recrystallization of Molybdenum and the age hardening of Inconel 625 occur above the respective temperatures. A new coating method named TP-CVD of which deposition temperature is below 900 °C is successfully developed for Molybdenum substrate, and another new coating method named HCD-ARE of which deposition temperature is below 500 °C is also developed for Inconel 625.

It has been confirmed that the characteristics of these TiC coated walls satisfy the necessary requirement from JT-60 operation conditions. The data base is shown in Fig. 14.26-14.35 and in Table 14.8-14.13.

Reference

- (1) M.W. Guinan and J.H. Kinney, J. Nucl. Mater. 108 & 109 (1982) 95
- (2) J.C. CORELLI, J. HOOLE, et al., "Mechanical, Thermal, and Microstructural Properties of Neutron-Irradiated SiC", Journal of the American Ceramic Society, Vol. 66. No.7 529-537 (1983).
- (3) R. Frauenfelder, J. Vac. Sci. Technol. 6 (1969) 388.
- (4) K. Ashibe and K. Ebisawa, to be submitted at 6th Int. Conf. Plasma Wall Interaction, Nagoya, 14-18 May 1984.
- (5) E. MORI, "A Study on Application of Electron Beam Welding for Austenitic Stainless Steel Piping of Nuclear Plant", 1983,

- Austenitic Stainless Steel Piping of Nuclear Plant", 1983, Doctoral Thesis, Nagoya Univ., in Japanese
- (6) I. MASUMOTO and H. HIRA, "Effect of the Prior Microstructure on Diffusion Weldability of SUS304 Stainless Steel", Jour. of the Japan Welding Society, Vol. 50, (1981), No. 3, 284-290
 - (7) J. DUFRESNT, B. HENRY and H. LARSSON, "Fracture Toughness of Irradiated AISI 304 and 316L Stainless Steel", ASTM Spec. Tech. Publ., (1979) No.683, 511-528
 - (8) A.L. WARD, "Irradiation Effects on Mechanical Properties of an SMAW Deposited Type 308 Stainless Steel", Welding Jour. Vol. 54, (1975), No.8, 259S-264S
 - (9) N. Asahi and Y. Konima, Proc. 7th ICVM, (6-4), 1982, Tokyo, Japan

Table 14.1 Properties of divertor plate materials

Property	Temp. [°C]	Tungsten	Copper	Cu-0.6Be-2.5Co	316SS
Thermal Cond. [W/m°C]	20	156	366	209	17.5
	725	110			
Thermal Exp. [$\times 10^{-6}$ /°C]	20	5.0	16.5	17.6	18.6
	300				18.6
	500				20.3
Density [g/cm ³]	20	1.93	8.9	8.75	7.9
Elastic Modulus [GPa]	20	411	129	124	193
	100	408	126		188
	300	400	116		177
	500	392	99.1		159
Tensile Strength [MPa]	20	1500	210	860	590
Poisson's Coef.	20	0.31	0.3	0.3	0.3
Specific Heat [J/kg°C]	20	132	385	377	494
Melting Temp. [°C]		3410	1083	1030~1070	1300

Table 14.2 Tensile properties of OFHC

	Test temp.	UTS (MPa)	0.2% YS (MPa)	Elongation (%)
<u>As received</u>	20°C	310	300	18
	100°C	280	260	12
	200°C	250	230	7
<u>850°C×30 min annealed</u>	20°C	220	59	38
	100°C	200	59	36
	200°C	170	59	36

Data presented by Furukawa Metals Co., Ltd. in 1976

Table 14.3 Fatigue of OFHC under stress control condition

	Test temp.	Amplitude of stress (MPa)	
		N = 10 ⁴	N = 10 ⁵
<u>As received</u>	20°C	200	190
	100°C	190	170
	200°C	160	140
<u>850°C×30 min annealed</u>	20°C	170	120
	100°C	150	110 (1)
	200°C	130	98 (1)

(1) Data at 400°C × 30 min annealed condition

Data presented by Furukawa Metals Co., Ltd. in 1976

Table 14.4 Tensile properties of Cu-0.6Be-2.5Co

	Test temp.	UTS (MPa)	0.2% YS (MPa)	Elongation (%)
<u>As received</u>	20°C	860	780	11
	100°C	820	760	11
	200°C	780	720	9
<u>850°C×30 min annealed</u>	20°C	240	130	11
	100°C	210	120	11
	200°C	180	120	9

Data presented by Furukawa Metals Co., Ltd. in 1976

Table 14.5 Fatigue of Cu-0.6Be-2.5Co under stress control condition

	Test temp.	Amplitude of stress (MPa)	
		N = 10 ⁴	N = 10 ⁵
<u>As received</u>	20°C	520	410
	100°C	510	400
	200°C	490	390
<u>850°C×30 min annealed</u>	20°C	200	180
	100°C	200	170
	200°C	180	120

Data presented by Furukawa Metals Co., Ltd. in 1976

Table 14.6 Comparison of EBW and diffusion bonding

	Principle	Notable feature	Problem to application
EBW	Fusion welding in vacuum using accelerated electron beam	<ul style="list-style-type: none"> ◦ Small distortion of welds ◦ Well controlled quality of weldments ◦ High rate of joint production 	<ul style="list-style-type: none"> ◦ Scale up of vacuum chamber ◦ Localization of vacuum chamber
Diffusion bonding	Press rod type	<ul style="list-style-type: none"> ◦ No change of structure in bonded zone ◦ Same physical and mechanical properties as base metal 	<ul style="list-style-type: none"> ◦ Scale up of equipment
	Gas pressurizing type (HIP)	<ul style="list-style-type: none"> ◦ No change of structure in bonded zone ◦ Same physical and mechanical properties as base metal ◦ Independent of material thickness for bonding ◦ Bonding of multi-joints ◦ Bonding of any curved surface 	<ul style="list-style-type: none"> ◦ Scale up of working chamber <p>Up-to-date Max. is</p> <p>Diameter : 1,500 mm</p> <p>Height : 4,500 mm</p>

Table 14.7 Tensile properties at 20°C

Material		σ_u , MN/m ²		σ_y , MN/m ²		ϵ_r , %		Fluence	
								dpa	n/m ² (total)
AISI304	base	602		264		68			
		627	614	262	263	73	71		
		614		264		71			
	welded	700		472		41			
		665	680	462	462	31	35		
		675		473		32			
	base	582		239		68			nonirradiated
		578	579	247	239	63	64		
		577		230		65			
	welded	689		505		36			
		665	680	432	478	31	34		
		685		497		34			
AISI304	base	662	668	372	383	62	62	2.39	8.22×10 ²⁵
		675		394		62			
	welded	674	679	487	492	30	31	2.34	8.05
		684		498		33			
AISI316L	base	624	632	324	333	65	61	2.01	7.35
		641		342		57			
	welded	693	688	514	498	30	30	2.15	7.72
		683		482		30			

Table 14.8 Tensile properties at 400°C

Material		σ_u , MN/m ²		σ_y , MN/m ²		ϵ_r , %		Fluence	
								dpa	n/m ² (total)
AISI304	base	467		136		45			
		468	466	159	145	45	45		
		462		140		46			
	welded	439		306		14			
		466		310		18	17		
		456		296		18			nonirradiated
AISI316L	base	426		106		40			
		432	328	110	117	41	39		
		427		134		36			
	welded	476		345		17			
		480	465	339	330	19	17		
		439		307		15			
AISI304	base	508	508	292	294	33	33	2.39	8.22×10 ²⁵
		508		295		33			
	welded	509	505	386	386	16	16	2.34	8.05
		500							
AISI316L	base	465	467	229	227	33	33	2.01	7.35
		470		225		34			
	welded	520	523	381	397	17	17	2.15	7.72
		526		413		16			

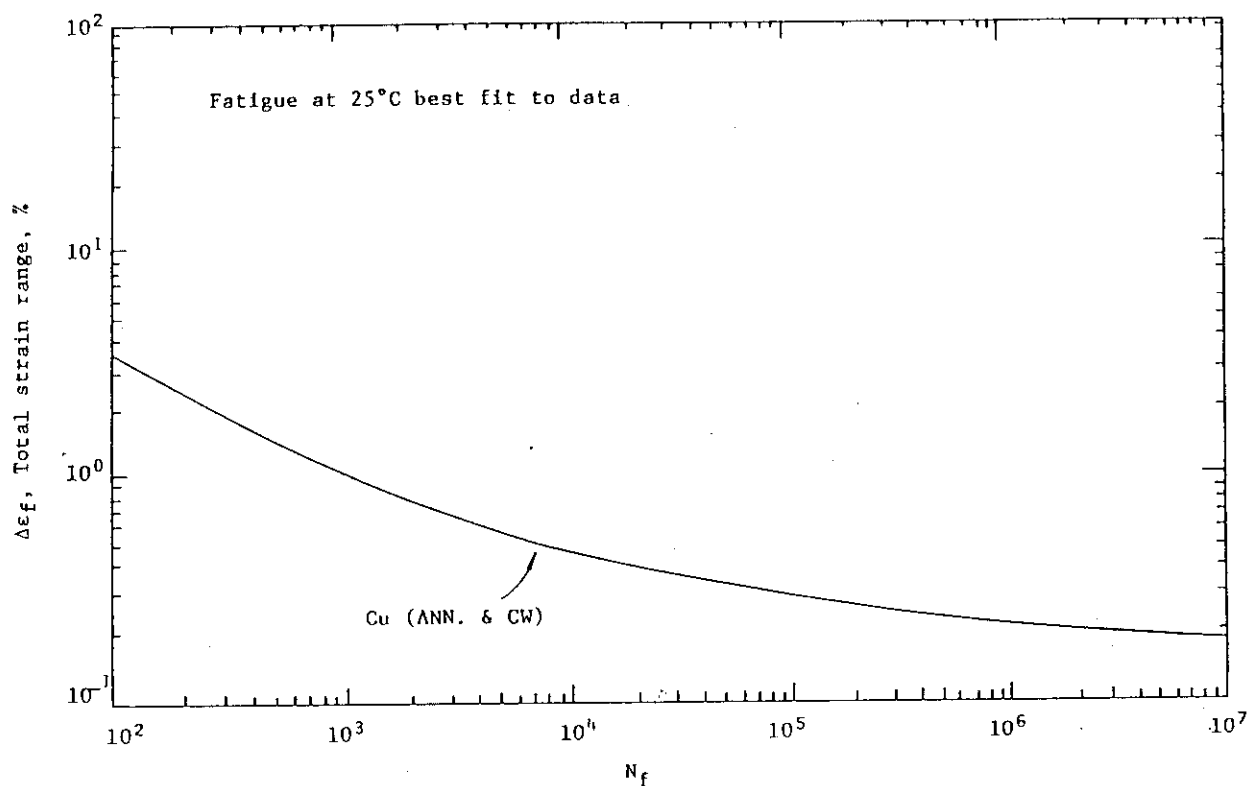


Fig. 14.1 Fatigue data for copper at room temperature

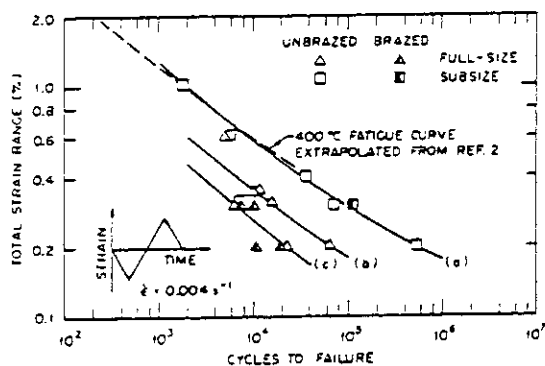


Fig. 14.2 Total strain range ($\Delta\epsilon_t$) as a function of cycles to failure (N_f) for OFHC copper tested at 300°C in vacuum

K.C. Liu and C.M. Loring, Jr. "Low-cycle fatigue Behavior of oxygen-free high-conductivity copper at 300°C in high vacuum", J. Nucl. Mater. 122 & 123 (1984) 783.

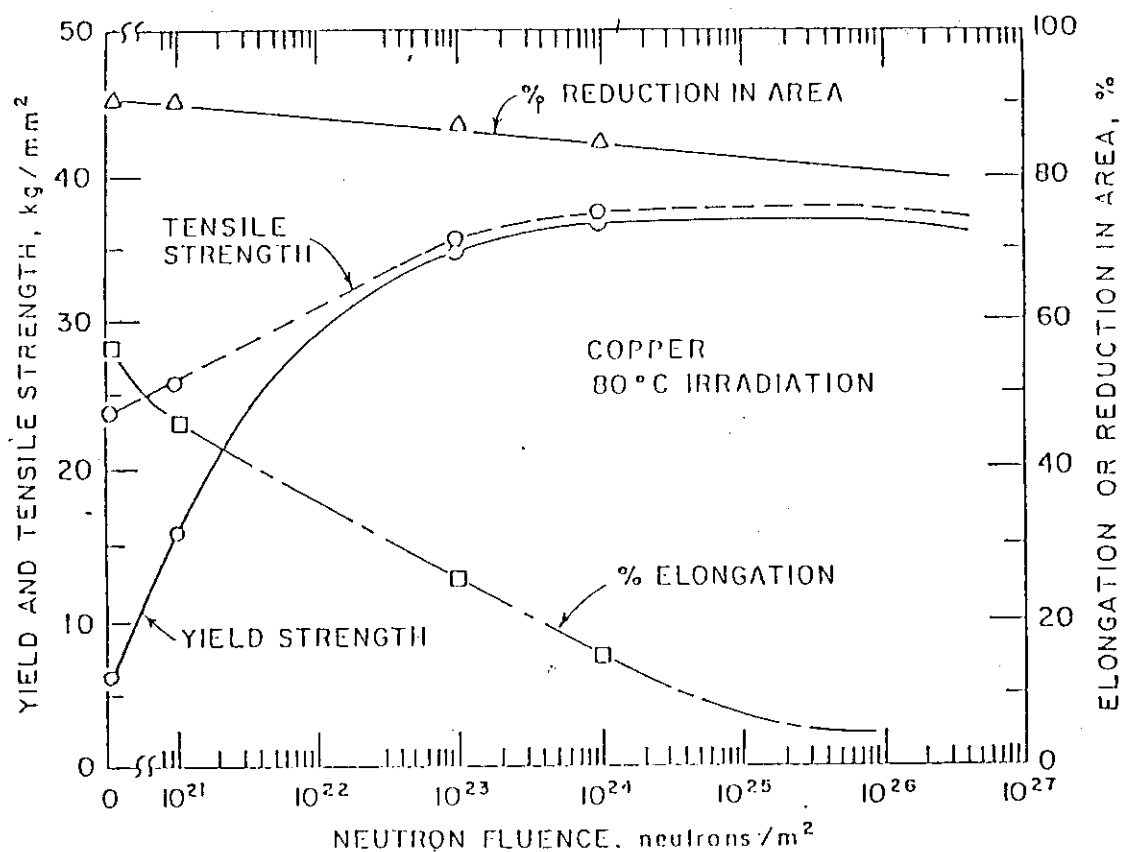


Fig. 14.3 Effect of irradiation at 80°C on room-temperature tensile properties of copper

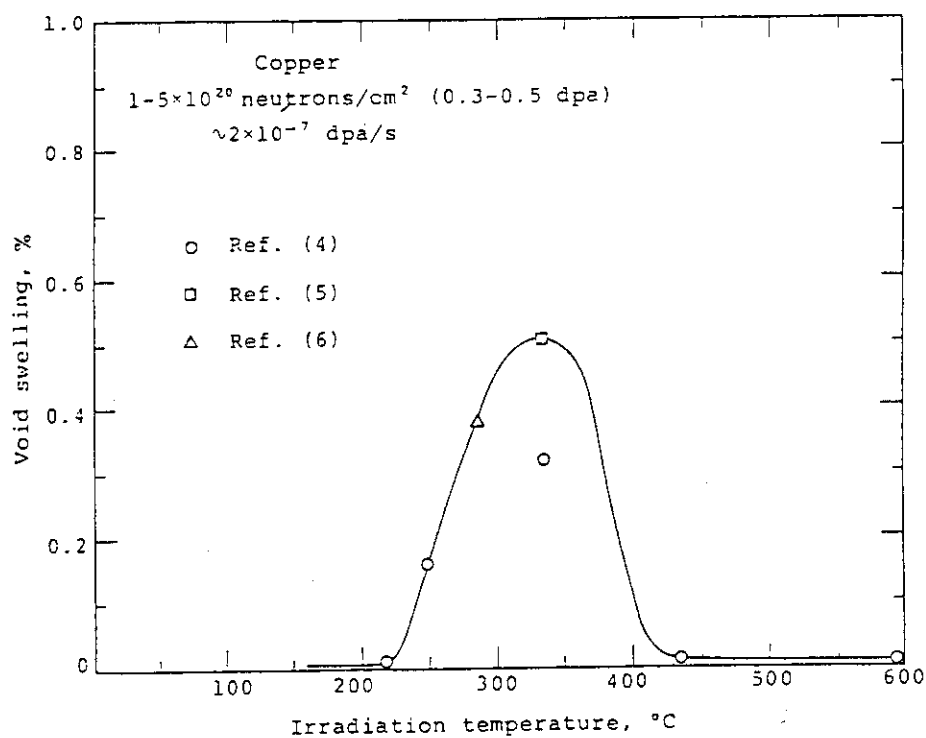


Fig. 14.4 Dependence of void swelling of neutron-irradiated copper on temperature

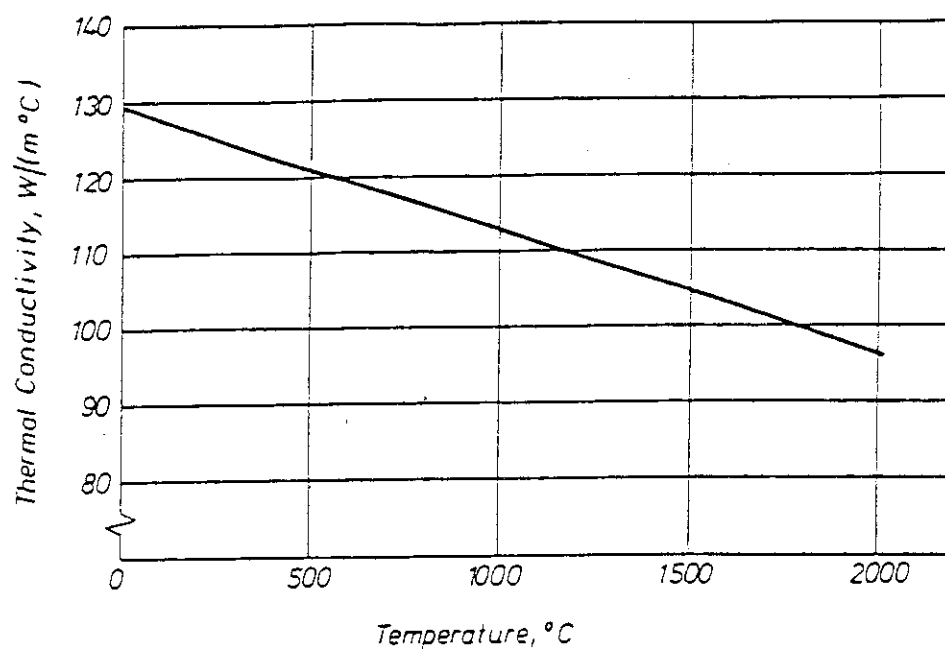


Fig. 14.5 : Thermal conductivity of tungsten versus temperature.

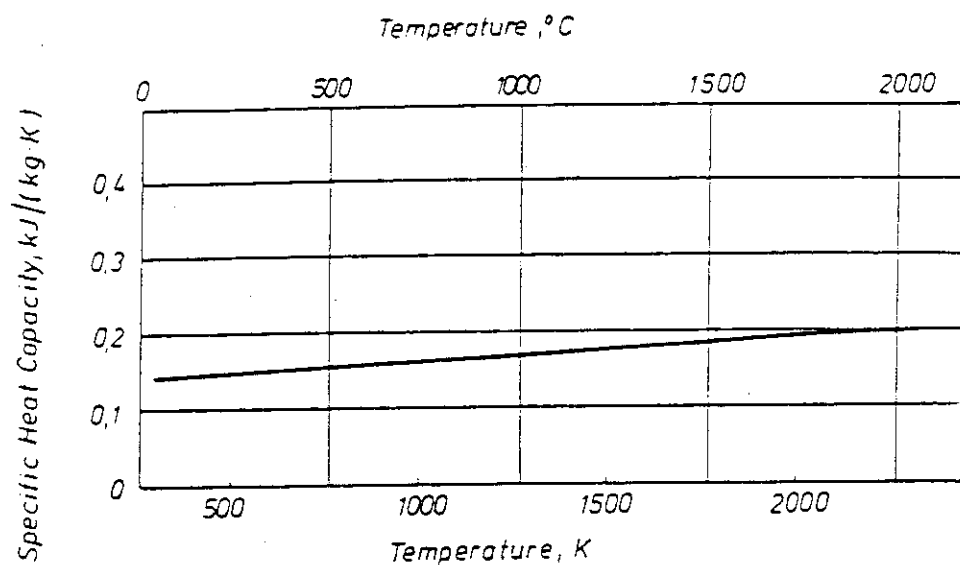


Fig. 14.6 : Specific heat capacity of tungsten versus temperature.

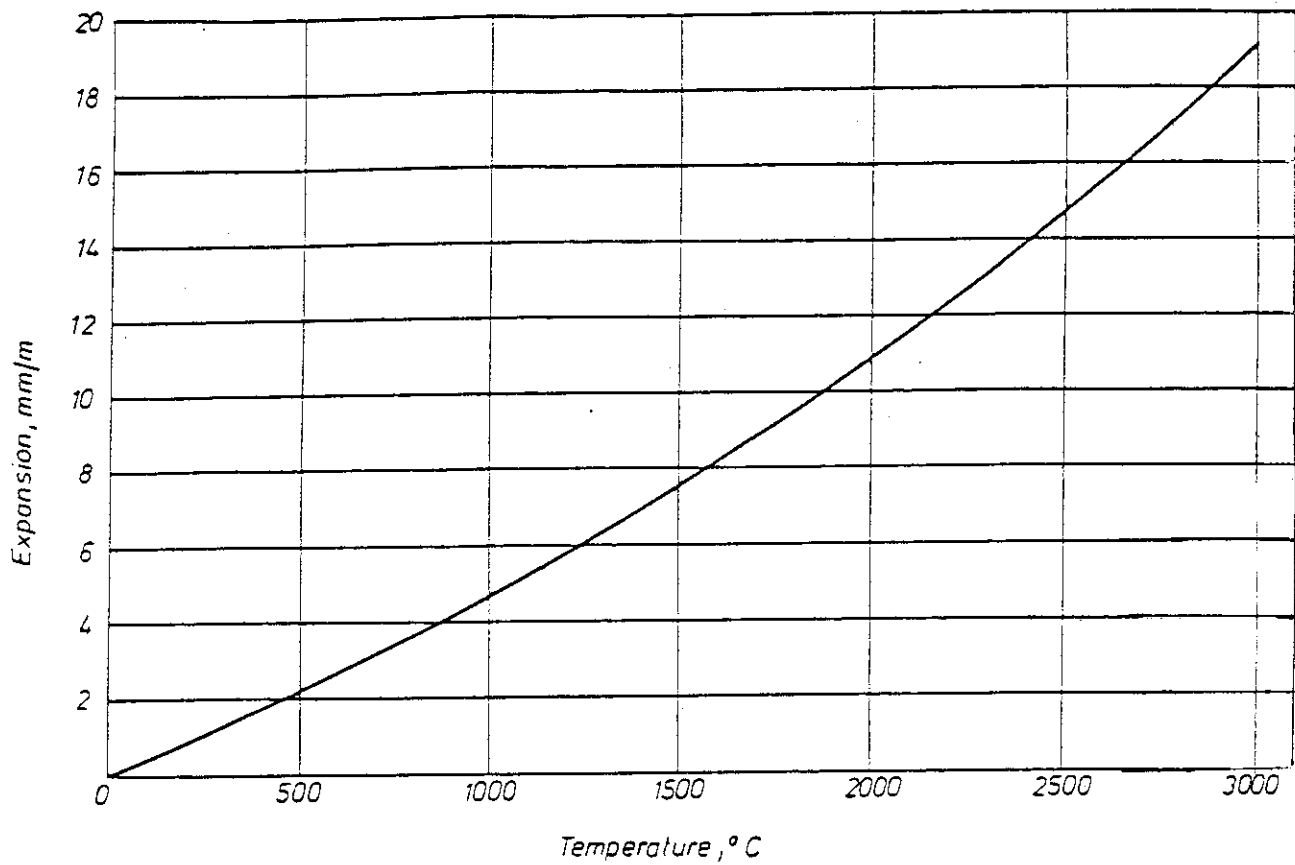


Fig. 14.7 : Thermal expansion of tungsten versus temperature.

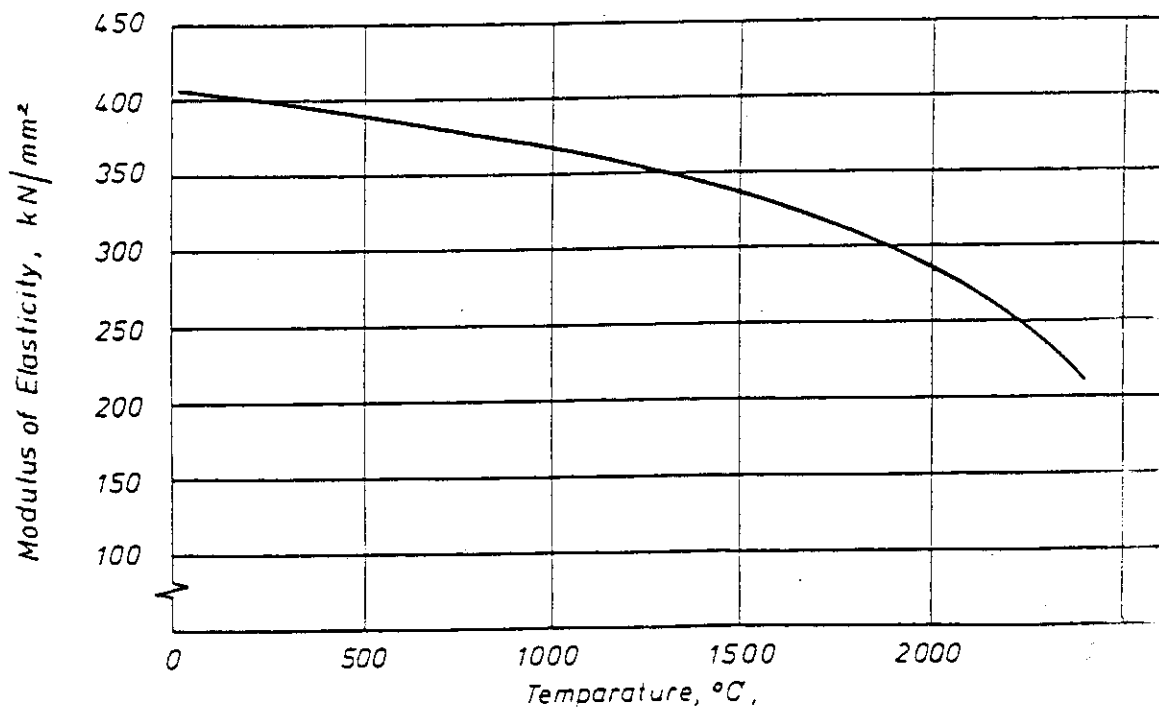


Fig. 14.8 : Modulus of elasticity versus temperature.

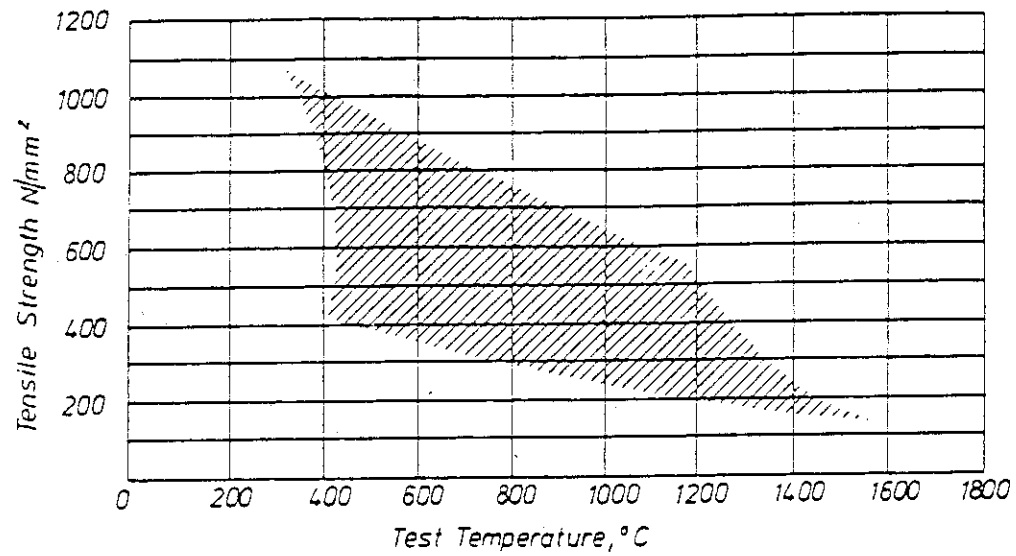


Fig. 14.9 Tensile strength of 1 mm thick tungsten sheet at elevated temperatures, strain rate 15% / minute. The upper limit corresponds to stress relieved and the lower to recrystallized sheet.

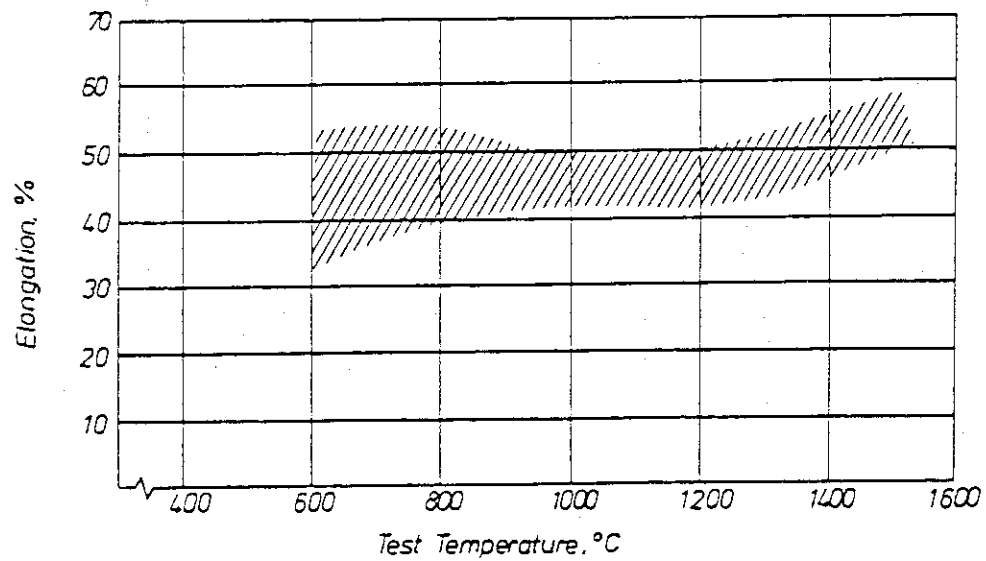


Fig. 14.10 : Elongation of recrystallized tungsten sheet in relation to the test temperature.

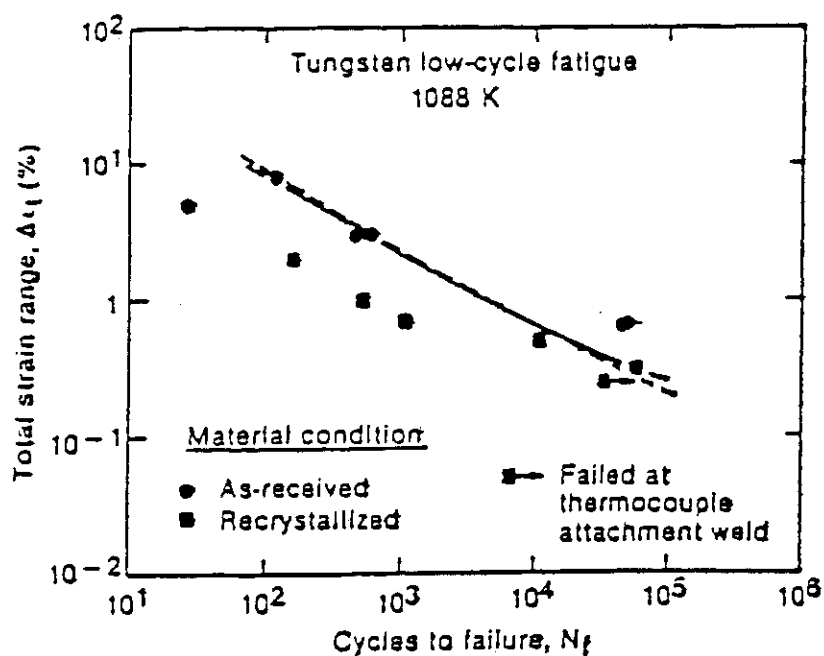
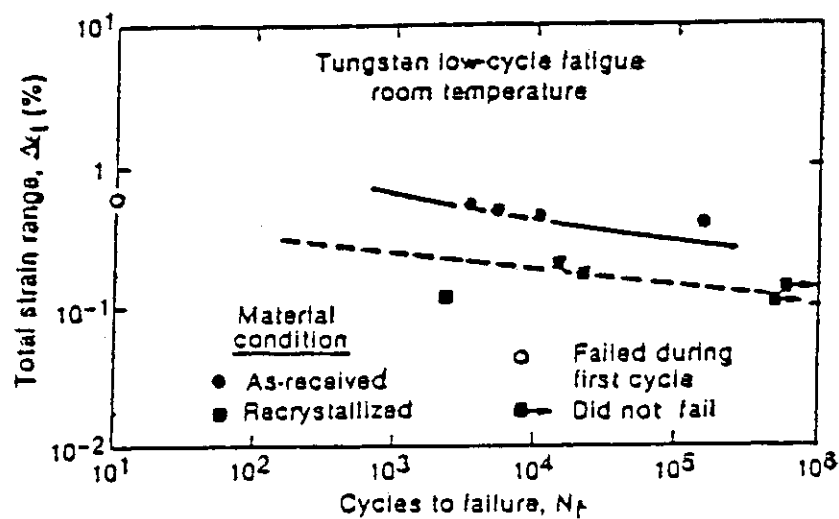


Fig. 14.11 Low cycle fatigue of cross rolled tungsten
R.E. Shmunk and G.E. Korth, "Tensile and
low-cycle fatigue measurements on cross-rolled
tungsten", J.Nucl.Mater. 103 & 104 (1981) 943

Data	W (tungsten)
Title	Solution and diffusion of hydrogen in tungsten
Author	R. Frauenfelder
Literature	The journal of vacuum science and technology, 6(1969) 388

$$D = 4.1_{-2}^{+5} \times 10^{-3} \exp \left(- \frac{9 \pm 2 \frac{\text{kcal}}{\text{gatom}}}{RT} \right) \text{ cm}^2/\text{sec}$$

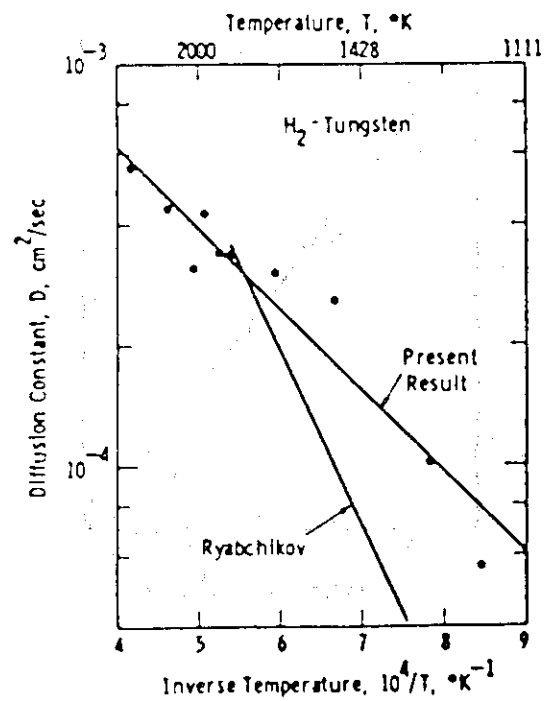


Figure 14.12 Diffusion constant for hydrogen in tungsten.

Data	W (tungsten)
Title	Solution and diffusion of hydrogen in tungsten
Author	R. Frauenfelder
Literature	The journal of vacuum science and technology, 6(1969) 388

$$S = 2.9_{-1.3}^{+2.8} \times 10^{-1} \exp \left(- \frac{24 \pm 4 \text{ kcal/gatom}}{RT} \right) \text{ Torr.liter/cm}^3 \text{ Torr}^{\frac{1}{2}}$$

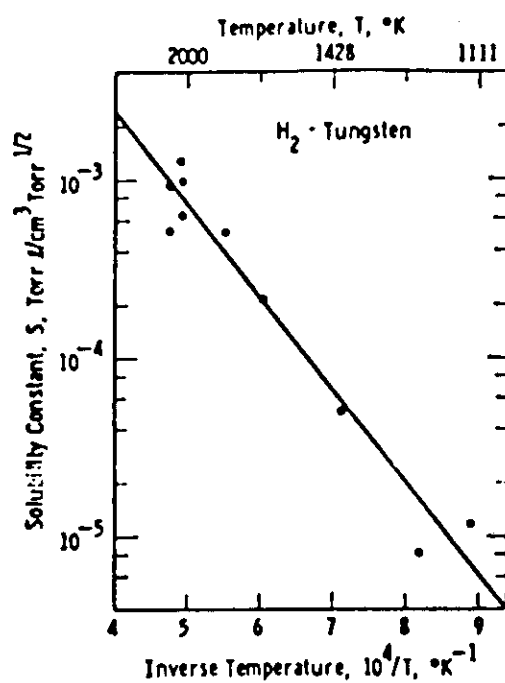


Figure 14.13 Solubility constant
for hydrogen in tungsten.

Data	Graphite
Title	Hydrogen diffusion and solubility in pyrolytic carbon
Author	R.A. Causey, T.S. Elleman and K. Verghese
Literature	Carbon, 17(1979) 323

$$S = 5.1 \times 10^{-8} \exp \left(\frac{33.3 \text{ kcal/mol}}{RT} \right) \text{ atoms/atoms atm}^{0.49}$$

Deuterium solubility in laminar PyC

Material	$S_o \left(\frac{\text{Deuterium Atoms}}{\text{Carbon Atoms}} \right)$	s_o^+	s_o^-	Q	Pressure Dependence
Laminar Pyrolytic Carbon	5.1×10^{-8}	2.6×10^{-7}	9.9×10^{-9}	-33.3 ± 5.1	$.49 \pm .06$

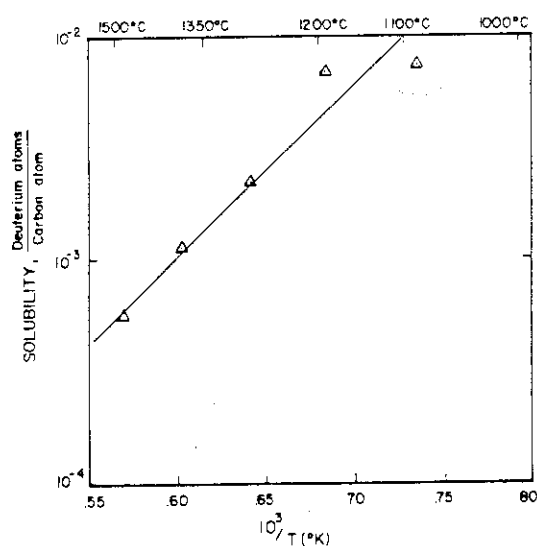


Fig. 14.14 Deuterium solubility at one atmosphere in laminar pyrolytic carbon as a function of temperature.

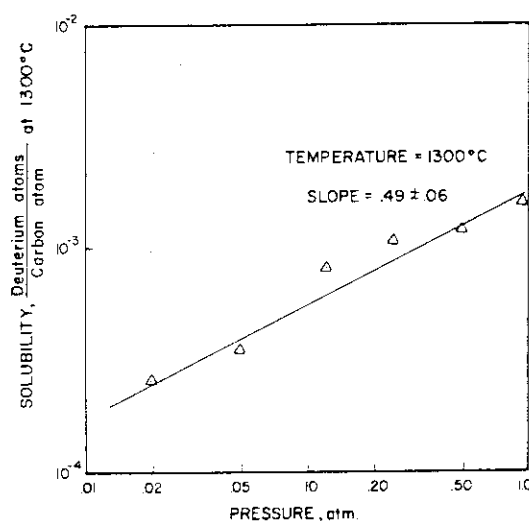


Fig. 14.15 Deuterium solubility at 1300°C in laminar pyrolytic carbon as a function of pressure.

Data	Graphite
Title	Hydrogen diffusion and solubility in pyrolytic carbon
Author	R.A. Causey, T.S. Elleman and K. Verghese
Literature	Carbon, 17(1979) 323

Tritium diffusion results for laminar PyC and Si-doped PyC (D_O^+ and D_O^- are the upper and lower limits on D_O as obtained by least squares fitting)

Material	D_O (cm ² /sec)	D_O^+ (cm ² /sec)	D_O^- (cm ² /sec)	Q(kcal/mole)
Laminar PyC	3.3×10^{-2}	2.0×10^{-4}	5.4×10^{-1}	98.4 ± 5.7
Si-Doped PyC	1.1×10^{-3}	3.9×10^{-3}	3.1×10^{-4}	53.6 ± 3.5

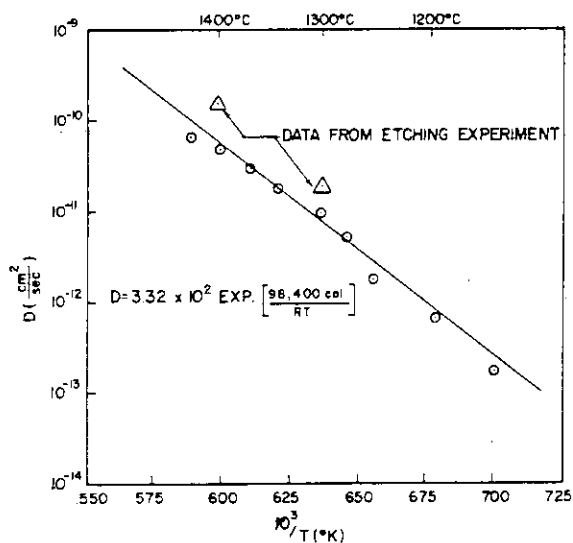


Fig. 14.16 Tritium diffusion coefficients in laminar pyrolytic carbon over the temperature range 1150-1425°C

Data	SiC
Title	Hydrogen transport and solubility in nonmetallic solids
Author	T.S. Elleman, L.R. Zumwalt and K. Verghese
Literature	Proc. Top. Meet. Technol. Controlled Nucl. Fusion Vol. 3-2(1978) 763

MEASURED TRITIUM DIFFUSION COEFFICIENTS

$$D = D_0 \exp(-Q \pm \sigma)/RT) \quad (\text{cm}^2/\text{sec})$$

Material (S.C.=Single Crystal)	D_0 (cm ² /sec)	Q (kcal/mole)	σ (kcal/mole)	Temp. Range °C
Al ₂ O ₃ S.C.	3.26	57.2	2.4	600-1000
Al ₂ O ₃ sintered	7.35×10^{-2}	43.8	2.5	600- 900
BeO S.C.	1.11×10^{-2}	52.5	4.7	650-1200
BeO sintered	7.00×10^{-2}	48.5	3.6	500- 950
Lucalox	39.8	41.8	3.2	360- 570
α SiC S.C.	1.09×10^{-2}	54.9	2.5	700-1300
β SiC S.C.	28.0	65.0	4.1	750-1000
Al-doped α -SiC S.C.	4.04×10^{-4}	34.0	4.2	450- 950
Al-doped hot- pressed SiC	0.904	48.2	3.5	500- 800
SCB glass	2.95×10^{-4}	30.2	1.2	350- 800
Y ₂ O ₃ hot-pressed	0.431	39.1	4.3	420- 620
Yttralox	3.87	39.5	3.1	350- 600
Laminar pyrolytic Carbon	3.3×10^2	98.4	5.7	1100-1450
β -Vapor deposited SiC	1.6	73.6	2.0	900-1300
Si-doped pyrolytic Carbon	1.1×10^{-3}	53.6	3.6	900-1400
Boron Carbide	1.1×10^{-6}	16.8	1.6	300- 700

Data	SiC
Title	Hydrogen transport and solubility in nonmetallic solids
Author	T.S. Elleman, L.R. Zumwalt and K. Verghese
Literature	Proc. Top. Meet. Technol. Controlled Nucl. Fusion Vol. 3-2(1978) 763

MEASURED HYDROGEN SOLUBILITY COEFFICIENTS

$$S = S_0 \exp(-Q/RT) P^\alpha (\text{atoms/g})$$

Material	S_0 (atoms/g atm. $^\alpha$)	Q (kcal/mole)	α	Pressure Range (atm.)	Temp Range (°C)
β -Vapor deposited SiC	1.3×10^{14}	-36.9	0.61	.02-1.0	1000-1400
Laminar Pyrolytic Carbon	2.6×10^{15}	-33.3	0.49	.02-1.0	1100-1500
Al ₂ O ₃ powder*	5.9×10^{20}	18.1	unknown	-	700- 800

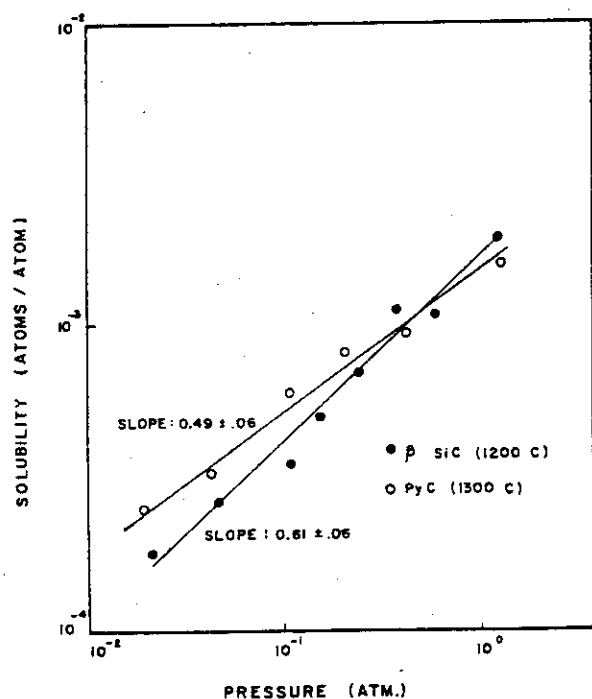
* Results for 1 atm. H₂ partial pressure

Figure 14.17 Deuterium Solubility in Silicon Carbide and Pyrolytic Carbon as a Function of Deuterium Partial Pressure

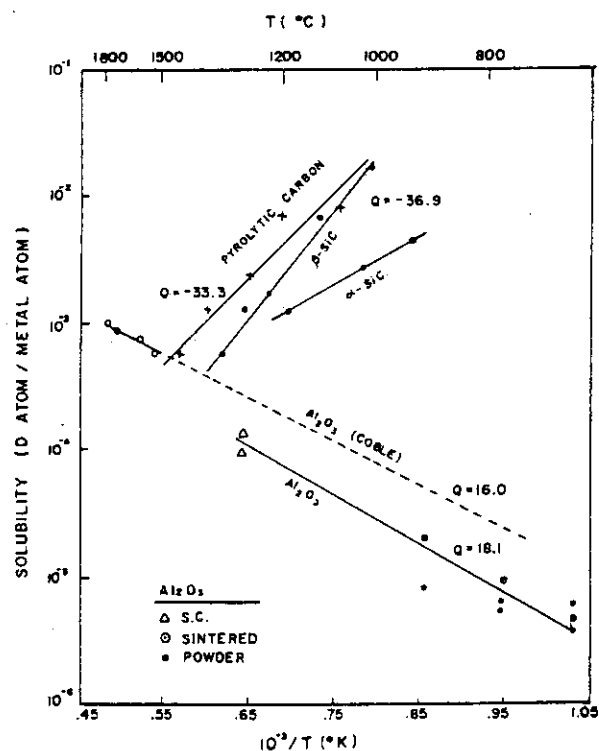


Figure 14.18 Deuterium Solubility versus Temperature (One Atmosphere Hydrogen Pressure)

Data	SUS 304
Title	The diffusivity of tritium in 304 stainless steel in the temperature range 100° to 300°C
Author	K.F. Chaney and G.W. Powell
Literature	Metallurgical transaction, 1(1970) 2356

$$D = 1.24 \times 10^{-2} \exp\left[-\frac{13600}{T}\right] \text{ cm}^2/\text{sec}$$

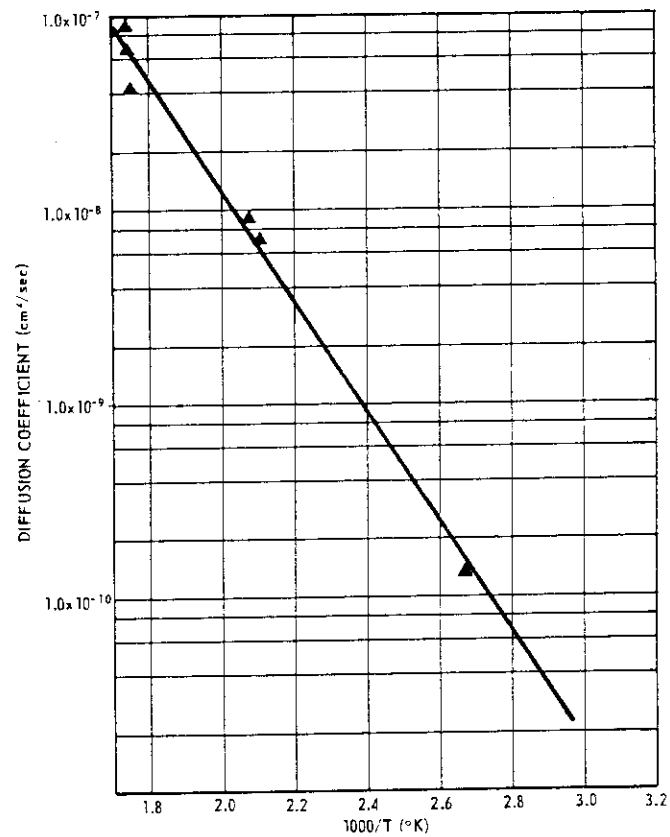


Fig. 14.19 Arrhenius plot of the diffusivity

Data	SUS
Title	Tritium group report-3 Tritium permeation into the coolant
Auther	JAERI
Literature	"Group D summary report Tritium", INTOR Workshop, Phase IIA, Session III (1981)

$$S = 6.78 \times 10^{-2} \exp(-1094.7/T) \text{ STP cc-T}_2/\text{cc-steel Torr}^{\frac{1}{2}}$$

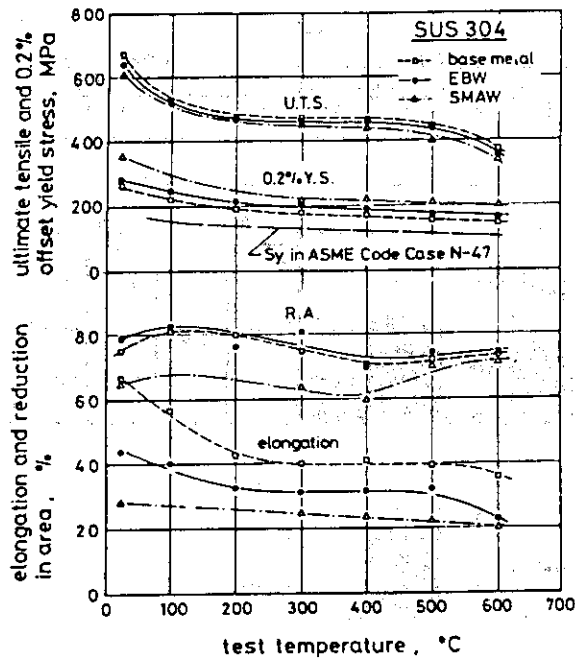


Fig. 14.20 Tensile properties of type 304 stainless steel and the welded joints

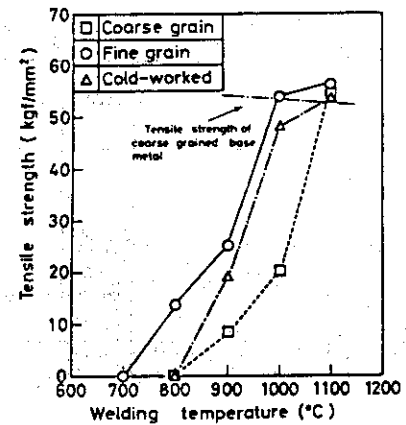


Fig. 14.21 Effect of welding temperature on tensile strength of diffusion welds. (Welding pressure = 1 kgf/mm², Welding time = 30 min.)

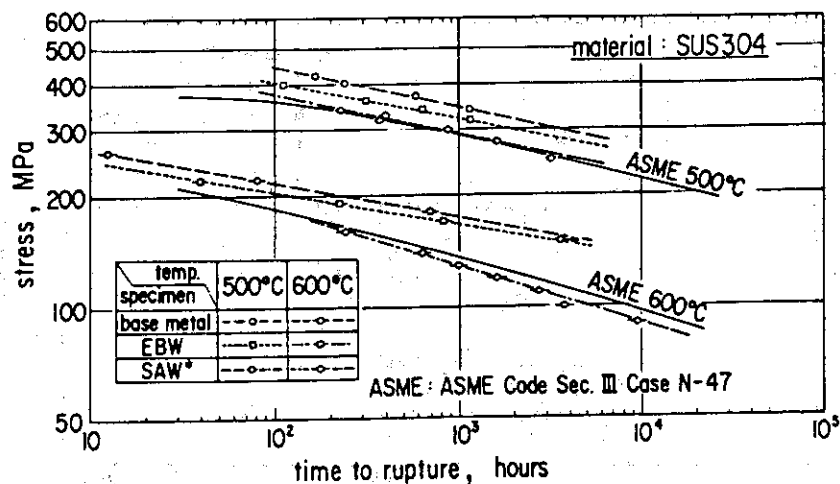


Fig. 14.22 Creep rupture strength of type 304 stainless steel and the welded joints

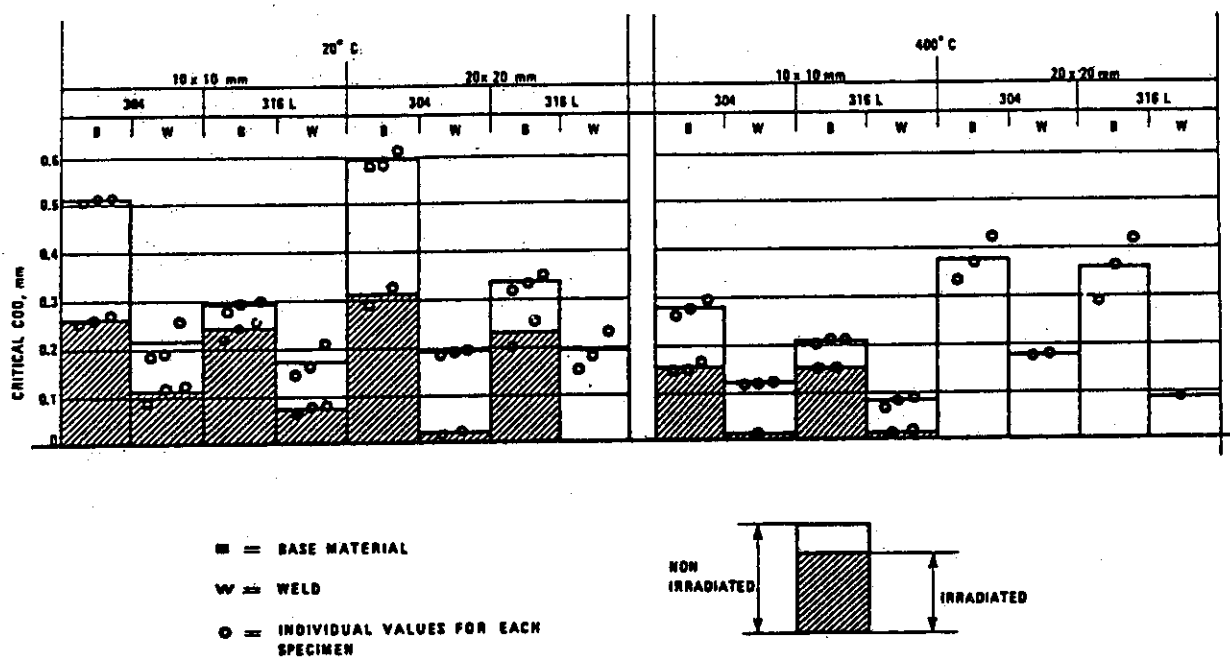


Fig. 14.23 Critical crack opening displacement values (initiation of stable crack growth)

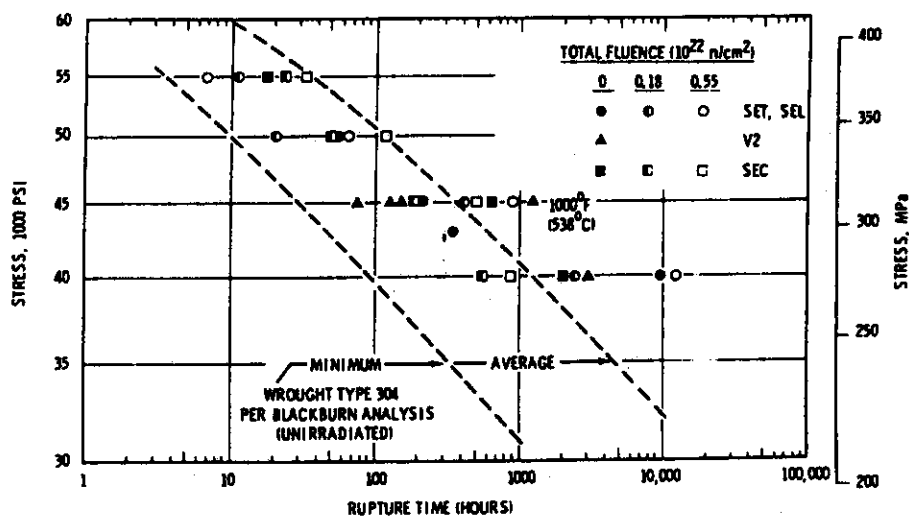


Fig. 14.24 Pre- and post-irradiation stress versus rupture life relationship for control residual element type 308

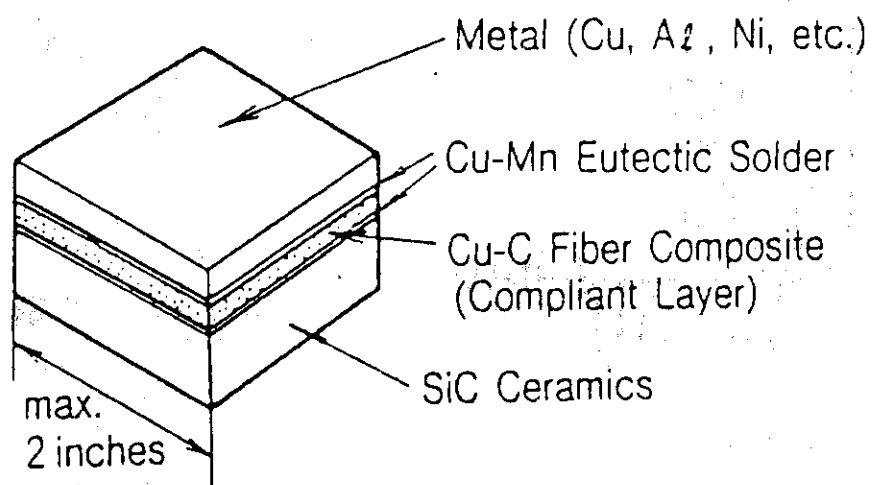


Fig.14.25 The structure of silicon carbide bonded to metal substrates

A. Coating Method

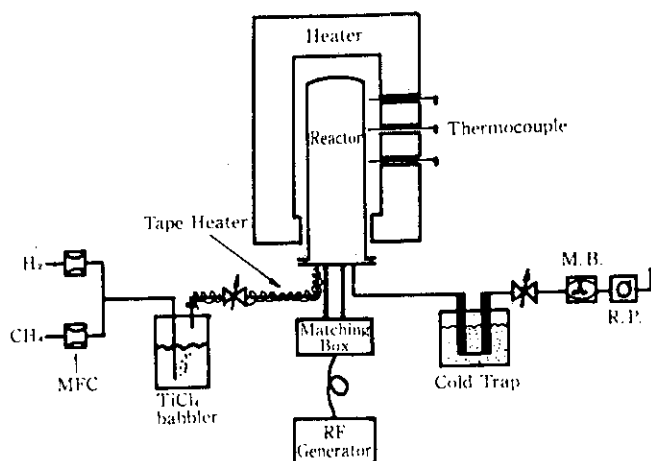


Fig 14.26 Schematics of apparatus.

Table 14.9 Condition for TiC Film Deposition by TP-CVD.

Substrate temperature	900°C
Pressure in vessel	2 Torr
H ₂ : CH ₄ : TiCl ₄	77 : 21 : 2
RF power	300 W
RF frequency	13.56 MHz
Deposition rate	2.5 m/hour

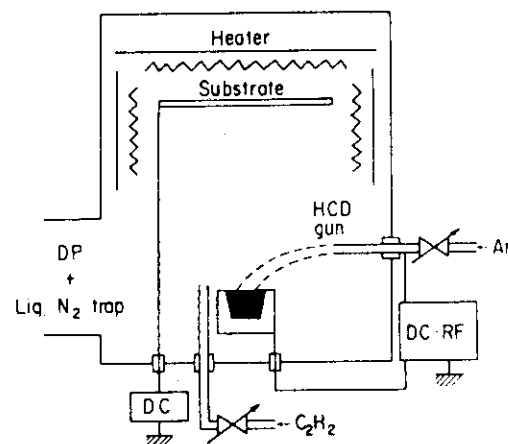


Fig 14.27 Schematic view of HCD-ARE system.

Table 14.10 Condition for TiC film deposition by HCD-ARE.

Distance of source-substr.	450 mm
Substrate temperature	500°C
Hollow cathode discharge	-30 V, 200 ~ 300 A
Substrate bias voltage	≥ -200 V
Ar gas flow rate	20 cc/min (STP), >99.99%
C ₂ H ₂ gas flow rate	140 cc/min (STP), >99.0%
Deposition rate	0.3 μm/min
Titanium	99.7% pure

B. ESCA Spectrum of TiC Film

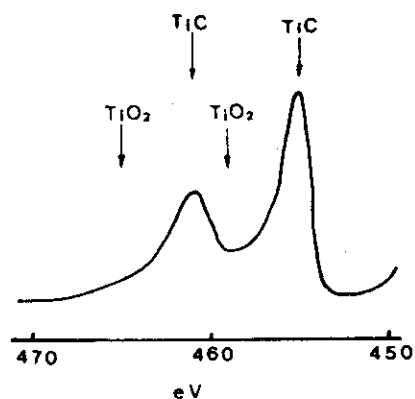


Fig 14.28 ESCA spectra of Ti(2S) from TiC film.

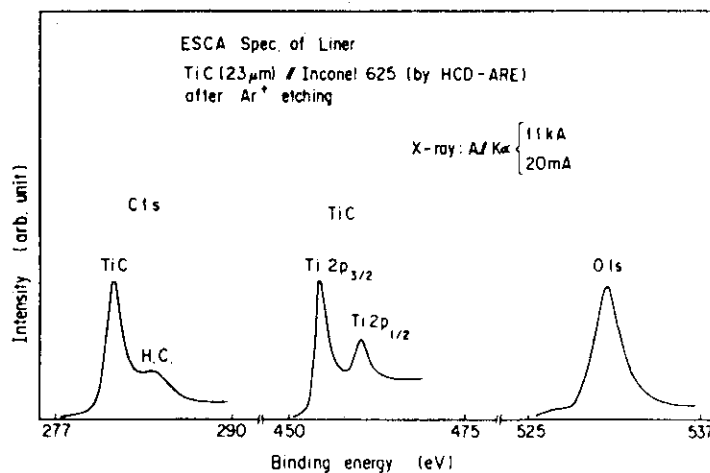


Fig 14.29 ESCA spectrum of the film deposited on Inconel 625 liner.

C. Outgassing Rate

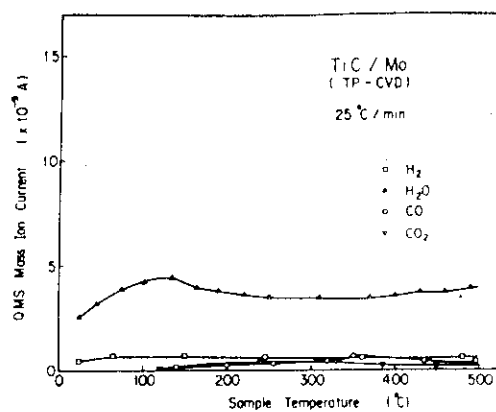


Fig 14.30 Thermal desorption spectra obtained for TiC-coated Mo

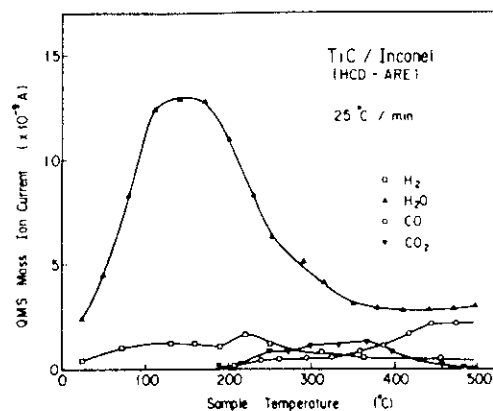


Fig 14.31 Thermal desorption spectra obtained for TiC-coated Inconel

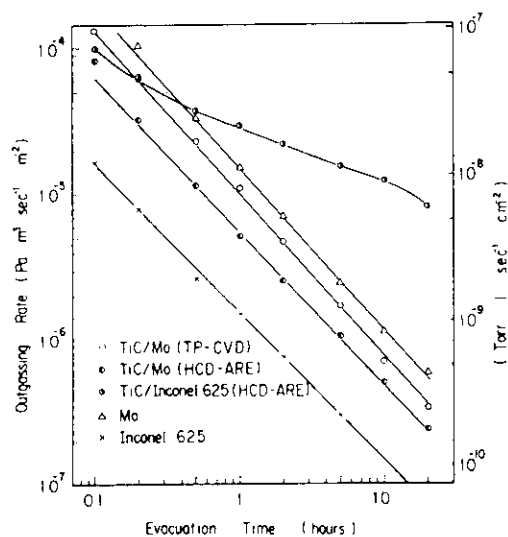


Fig 14.32 Evacuation time vs. outgassing rate curves obtained for five different materials

Table 14.11 Summary of the outgassing rate of five different materials prior to and after 250°C baking

	before baking	after baking
TiC/Mo (TP-CVD)	$8.8 \cdot 10^{-7}$	$2.6 \cdot 10^{-8}$
TiC/Mo (HCD-ARE)	$4.8 \cdot 10^{-7}$	$1.1 \cdot 10^{-8}$
TiC/Inconel (HCD-ARE)	$1.2 \cdot 10^{-6}$	$8.8 \cdot 10^{-8}$
Mo	$1.1 \cdot 10^{-7}$	$8 \cdot 10^{-8}$
Inconel	$1.5 \cdot 10^{-7}$	$8 \cdot 10^{-8}$

(Pa · m³ / s · m²)

D. Emissivity

Table 14.12 Emissivity of TiC coated surface

Substrate	Molybdenum			Inconel 625	
	Electrolytic polishing	TiC (HCD-ARE)	TiC (TP-CVD)	Chemical etching	TiC (HCD-ARE)
Emissivity	0.075	0.141	0.378	0.175	0.142

E. Mechanical Characteristics

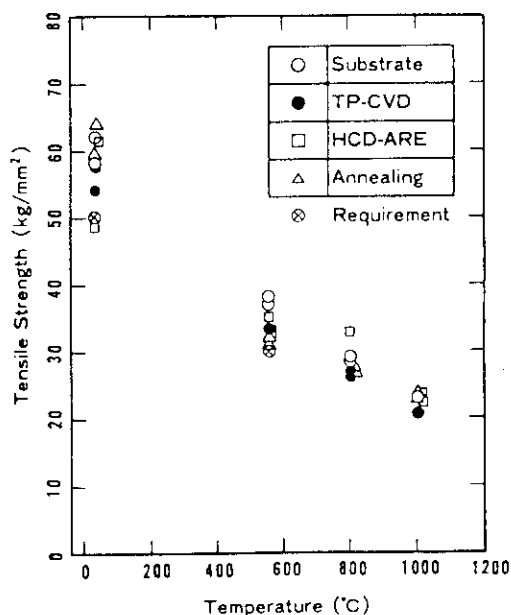


Fig 14.33 Tensile strength of hot rolled pure molybdenum of 20 mm thickness

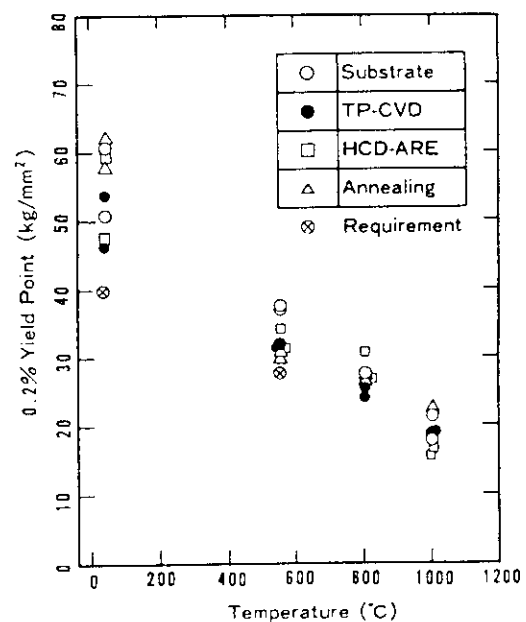


Fig 14.34 0.2% yield point of hot rolled pure molybdenum of 20 mm thickness

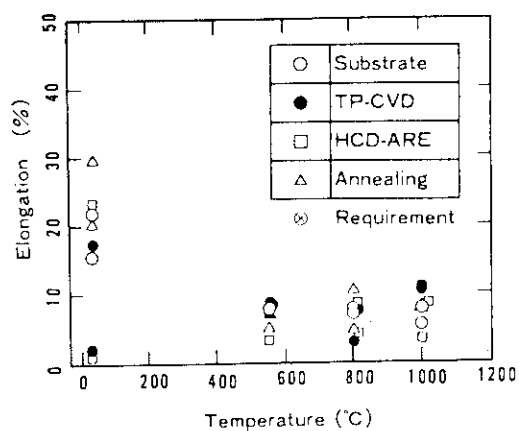


Fig 14.35 Elongation of hot rolled pure molybdenum of 20 mm thickness

Table 14.13 Mechanical properties of TiC coated Inconel 625

	T.S. (kg/mm ²)		0.2% Y.P. (kg/mm ²)		Elongation (%)	
	R.T.	550°C	R.T.	550°C	R.T.	550°C
Requirement	≥84.4	—	≥42.2	—	≥30.0	—
Inconel 625	101.6	88.7	49.8	36.0	49.6	43.3
TiC coated Inco. 625	101.6	85.2	67.8	38.3	42.7	41.9

15. Conclusions and Recommendations

In the course of the Phase 2A, part 2 sessions, our efforts have been mainly focused on "Low edge temperature divertor design", and "Data base assessment".

The major conclusions and recommendations are summarized as follows:

(A) Low edge temperature divertor

- 1) The geometry of the divertor plate and the divertor chamber depends on the plasma configuration (the magnetic field lines). Two plasma configurations have been considered for the engineering study. The first plasma configuration is the same as the Phase I design. The second plasma configuration is based upon the Japanese physics prediction. More physics information is needed to establish the best solution of the divertor geometry.
- 2) Under the Phase I divertor configuration, the maximum heat flux is 7 MW/m^2 on the inner plate. The maximum heat flux is reduced to 5 MW/m^2 , if the inner plate is placed at an angle of 20° to the field lines. The other divertor configuration has been considered in order to limit the peak heat flux to about 2 MW/m^2 . The angle between the divertor plate and the separatrix is 8° for the inner channel, and 6° for the outer channel.
- 3) The divertor chambers for the long channel length divertor and the reduced channel length divertor have been compared. The length of divertor channel has been taken to be 40 cm for the reduced channel length divertor. The peak heat flux has been taken to be either 5 MW/m^2 or 7 MW/m^2 for both long and reduced channel length divertor. The reduced channel length divertor gives the decrease of 0.45 to 0.6 m in the height of divertor chamber compared with the long channel length divertor.
- 4) The divertor collector plate is composed of a protective material, heat sink, and supporting structure. The protective material is 1 mm or 3 mm thick tungsten. The heat sink is pure copper or a copper alloy, and the support structure is stainless steel. The protective tile is brazed or plasma-sprayed to the heat sink.
- 5) Stress and fatigue analyses of the divertor plate indicate that the peak heat flux less than 2 MW/m^2 is required to reduce the thermal fatigue stress range to an acceptable level. An unacceptably short lifetime results under the peak heat flux of 5 MW/m^2 . The plasma spraying is preferred to the brazing from the standpoint of heat sink fatigue life. However, the strength and fatigue life of tungsten appear to be critical for the plasma spraying.
- 6) The stress in the divertor plate is quite sensitive to the deposition thickness of 316 SS. The stress increases with increasing the deposition thickness. Deposition of 316 SS on the divertor plate could result in significantly reduced life.
- 7) The bulk mechanical property data base for the protective material and the heat sink is small, and there are great uncertainties in the interface bond strength. Further studies are needed for the accurate lifetime estimation and the selection

of reference bonding method.

(B) Additional studies

- 8) The first wall is composed of Type 316 stainless steel. If the melt layer is stable, the thickness with an allowance for erosion of first wall is only 6.9 mm, and the first wall is expected to survive the reactor lifetime in terms of fatigue damage accumulation. Using the assumption that the entire melt layer is lost, the first wall has to be replaced at least once.
- 9) Thermo-hydraulic analyses were made on a helium-cooled first wall. The results indicate that a practical design of the first wall is possible with helium coolant.
- 10) Thermal response of the divertor plate covered with thin stainless steel layer were calculated for the reference disruption energy flux of 230 J/cm^2 with the duration of 5 ms or 20 ms.
 - i) Tungsten does not melt for either of the conditions.
 - ii) Melt layer and vaporized thicknesses increase with increasing thickness of the stainless steel.
 - iii) In the case of 1 m deposition layer, the SS layer completely melts for 5 ms disruption. Thus if all the melt layer is lost, stainless steel cannot accumulate on the tungsten surface thicker than 1 m.
 - iv) Judging from these results, a certain deposited thickness exists which melts completely for 20 ms disruption.
- 11) Melt layer stability was analysed with the aid of the hydrodynamic linear stability theory. As long as the theory is applicable, the melt layer is predicted to be unstable. Further studies are required.
- 12) The first wall is composed of Type 316 stainless steel. If the melt layer is stable, the thickness with an allowance for erosion of the first wall is only 6.9 mm, and the first wall is expected to survive the reactor lifetime in terms of fatigue damage accumulation. Using the assumption that the entire melt layer is lost, the first wall has to be replaced at least once.
- 13) The lifetime of the divertor plate and the first wall has been analysed for the long pulse operation, and has been compared with that in the reference operation. The advantages of the long pulse operation are:
 - i) The fatigue life of the divertor plate is 5 times longer than that in the reference operation. For the long pulse operation, the fatigue life of heat sink is 3.3 year in the Case 1, and 1.6 year in the Case 2.
 - ii) The lifetime of the first wall is expected to be more than the full reactor lifetime. On the other hand, it would be necessary to exchange the first wall at least once for the reference operation of Case 2.
- 14) The limiter is composed of either Be or C bonded to Cu heat sink and support structural material (316 SS: 40 mm thick). 3-D thermomechanical calculations were performed for four cases of 10/20 mm thick Be and 5/10 mm thick C. The stress intensity in the Cu heat sink is below the 3Sm limit for all cases.
- 15) The lifetime considerations for the limiter plate were made in terms of the erosion and fatigue. The conclusions are that:

- i) the Be-Cu and C-Cu limiter plates are expected to survive the reactor lifetime in terms of fatigue damage accumulation,
- ii) the consideration of the erosion results in an unacceptably short lifetime, at most 0.1 y in the case of 20 mm thick Be, and
- iii) further analysis should be made with consideration of the erosion/redeposition for the leading edge.